THE UNIVERSITY OF
SYDNEY

COPYRIGHT AND USE OF THIS THESIS

This thesis must be used in accordance with the provisions of the Copyright Act 1968.

Reproduction of material protected by copyright may be an infringement of copyright and copyright owners may be entitled to take legal action against persons who infringe their copyright.

Section 51 (2) of the Copyright Act permits an authorized officer of a university library or archives to provide a copy (by communication or otherwise) of an unpublished thesis kept in the library or archives, to a person who satisfies the authorized officer that he or she requires the reproduction for the purposes of research or study.

The Copyright Act grants the creator of a work a number of moral rights, specifically the right of attribution, the right against false attribution and the right of integrity.

You may infringe the author's moral rights if you:

- fail to acknowledge the author of this thesis if you quote sections from the work
- attribute this thesis to another author
- subject this thesis to derogatory treatment which may prejudice the author's reputation

For further information contact the University's Director of Copyright Services

sydney.edu.au/copyright

School of Chemical and Biomolecular Engineering

The University of Sydney

Experimental Study of Fluid Flow and Heat Transfer in Tortuous Microchannels

A thesis submitted in fulfilment of the requirements for the degree of

DOCTOR OF PHILOSOPHY

by

Zhenhui Dai

March 2014

Declaration

I hereby declare that the work presented in this thesis is solely my own work and that, to the best of my knowledge, the work is original except where otherwise indicated by reference to other authors. No part of this work has been submitted for any other degree or diploma.

Zhenhui Dai

March, 2014

Acknowledgements

One of the joys of completion is to look over the journey past and remember all the friends and family who have helped and supported me along this long but fulfilling road.

First and foremost, I would like to express deepest gratitude to my supervisors Professor Brian S. Haynes and Adjunct Professor David F. Fletcher. They have provided a rich and fertile environment to study and explore new ideas. The powerful and insightful thinking of Brian has not only been instrumental in the realisation of this work, but will also help enormously in my future endeavours. David has helped me immensely in CFD simulations and thesis drafting. This thesis would not have been possible without their invaluable guidance and continuous support. I could not have asked for better role models, each inspirational, knowledgeable, supportive, and patient.

I would like to thank the technicians and workshop staff of School of Chemical and Biomolecular Engineering, particularly Dr. Bogumil Eichstaedt, Gary Towell, Dr. Jeffrey Shi, and Alex Farago for their support in construction of the experimental apparatus as well as expanding my knowledge of practical issues beyond the textbooks. The support and help from Professor Tim Langrish and the administrative staff of the school are also gratefully acknowledged.

My sincere thanks go to Dr. Raghvendra Gupta, and Dr. Yang Liu, for their guidance and invaluable help during the early days of my PhD, Dr. Sharon Leung, for mentoring and sharing her research experience with me, Dr. Zhanying Zheng, for the help on CFD simulations and discussions on the subject.

Many thanks to members in the combustion group past and present: Dr. Alejandro Montoya, Marta Kremky, Sergio Londono, Dr. Ryan Zhou, Dr. Christian Renk, Dr. Xiao Liang, Dr. Maximilian Warner, Dr. Asanka Rahubadda, Christopher Jazrawi, Sisi Zheng, Kambiz Shojaee, Mohammad Zangouei, Simon Guo, Conrad Harvey Ralph Gillard, Ali Zafaranloo and Juan David Gonzalez Calderon. I am very grateful for the friendship and help of all of the members of this group, especially Yin Cao, Yaya He and Jason Mann, for so much humour and entertainment to make my life joyful and enjoyable.

I am also very grateful to Shane Kirwan from Lapping Services, Dr. Harald Fiedler from microParticles GmbH and Lino Montuno from SciTech Pty Ltd. In addition to their technical services and resources, I greatly value the practical suggestions and skills they shared.

The financial support from the University of Sydney International Scholarship (USydIS) granted by the University of Sydney is gratefully acknowledged.

I also owe thanks to Mary and her family whom have taken good care of me and give me a home away from China.

Finally, and most importantly, I would like to express my deepest gratitude to my family for their unconditional love, constant encouragement and support throughout my life. Without whom I could not have made it here.

Abstract

The growing importance of compact heat exchangers for use in chemical plants and electronic cooling has led to enormous interest in flow in tortuous microchannels due to their great potential to enhance fluid mixing and heat transfer. The design and application of tortuous passages is raising the importance of understanding the fluid dynamics and transport behaviour in micro-structured systems.

While the fluid flow and heat transfer in wavy microchannels have been studied extensively in a numerical fashion, experimental studies in the field are very limited due to the technical difficulties of making accurate measurements in micro-scale flows. This thesis provides insights into thermohydraulics of tortuous microchannels by developing experimental techniques and performing systematic visualisation and heat transfer experiments.

This work focuses on channels relevant to printed circuit heat exchangers, having a semi-circular cross-section with a diameter of 2 mm and following zigzag or sinusoidal pathways (comprising typically 9 repeating units). The channels were mechanically milled in Kovar plates and then sealed with glass covers through an anodic bonding technique. This arrangement allows simultaneous heating and good optical access to the flow. Flow visualisation using high-speed Micro-Particle Image Velocimetry (micro-PIV) techniques and heat transfer experiments for single-phase flow of water were carried out in five wavy channels having different geometries for Reynolds numbers ranging from 50 to 900.

A numerical model was also developed using the ANSYS CFX package to simulate steady flow and heat transfer in test sections identical to those used in the present experiments. Simulations were carried out for water flow (Prandtl number = 6.13) with the corresponding experimental conditions to validate the experimental approaches and to provide data to compare with experimental results.

A transition from a steady flow to a time-dependent oscillatory flow having a dominant frequency and subsequently to a complex transient flow was observed in the wavy channels through time-resolved velocity measurements. The critical Reynolds number (Re_c) for the onset of unsteadiness depends on the channel geometry, with higher values of Re_c being observed in smoother geometries. However, the transition to a transient flow occurs at much lower Reynolds numbers than predicted numerically. The early transition is believed to be

triggered by the small inlet flow disturbances in the experiments, since the flow is very sensitive to the inlet conditions at a high enough Reynolds number. This hypothesis is supported by results from transient simulations with fluctuating inlet boundary conditions.

The detailed flow patterns in wavy channels were identified and were found to be affected greatly by geometrical parameters. Recirculation zones form immediately after the inner corner with their size and strength increasing with increasing Reynolds numbers. Flow recirculation occurs more easily in zigzag channels than sinusoidal passages which have relatively smoother pathways. The recirculation size and strength are bigger in channels with higher bend angle (θ) or amplitude to half-unit length ratio (A/L).

The ability of the present two-dimensional micro-PIV to measure three-dimensional velocity fields through scanning-based visualisation and 3D reconstruction techniques was explored. Three-dimensional maps of the complex flow show that Dean vortices formed in the cross-sections promote fluid mixing transverse to the main flow direction in both zigzag and sinusoidal channels. The spatial and temporal evolution of secondary flow (Dean vortices) play an important role in enhancing fluid mixing and heat transfer.

The three-dimensional conjugate heat transfer simulations enabled the complex thermal behaviour present in the current experimental design to be understood and interpreted. They showed that the microchannels do not correspond strictly to any standard thermal boundary condition even though the perimeter-averaged wall heat flux is approximately constant in the heating zone. Since the wall thermal conditions inside the microchannel cannot be measured directly, the experimental Nusselt number was determined based on a simplified model which was shown to provide values consistent with the CFD simulations.

Results show that significant heat transfer enhancement can be achieved in wavy channels compared with the equivalent straight channel, although an increased pressure-drop penalty is also observed. Both the heat transfer enhancement and pressure-drop penalty increase with increasing Reynolds number, but the heat transfer augmentation at higher Reynolds number rises relatively faster when compared with the increase in pressure-drop penalty for most channels considered in this thesis. A heat transfer enhancement which is 2.1 times higher than the pressure-drop penalty can be achieved in a sinusoidal channel with $A/L = 0.5$ and $L/d = 3.5$ at $Re = 400$.

The effect of geometrical parameters on the heat transfer performance and pressure-drop penalty was examined. Higher bend angle (θ) or amplitude to half-unit length ratio (A/L) generally led to an increased heat transfer enhancement, as well as a relatively greater friction factor increase due to stronger and larger flow recirculation. In addition, the heat transfer performance of the sinusoidal channels is as good as the corresponding zigzag channels (with the same amplitude and half-unit length), while the pressure drop is smaller in the sinusoidal channels. Based on the fluid dynamic study, the high heat transfer enhancement at the expense of low pressure-drop penalties is mainly due to the absence of recirculation formation and the presence of Dean vortices that promote cross-sectional mixing without incurring great pressure drop. In general, measured data are in good agreement with computed pressure losses and Nusselt numbers from the CFD simulations.

Extension of this work to the design of compact heat exchangers requires evaluation of not only the thermohydraulics of the channel but also the stackability of channels on a plate. It is found that zigzag channels provide significant heat transfer enhancement with much higher surface area densities (e_A = 0.91-0.99) than sinusoidal channels (e_A = 0.81-0.89), as their shape is conducive to stacking, and therefore represent a more appropriate passage design for use in microchannel devices.

A significant component of the research in this thesis has been the development of experimental techniques to measure local heat transfer rates in microchannels. A novel non-intrusive technique based on Laser Induced Fluorescence (LIF) was developed to measure the fluid temperatures in micro-devices, using two fluorescent dyes (Kiton Red and Rhodamine 110) and a colour camera with a colour enhancement filter. Demonstrations of this technique in single-phase flow and Taylor flow indicate that the micro-LIF technique using dissolved fluorescent dyes has poor resolution in the optical direction and reports more-or-less un-weighted average values over the depth of the samples since volume illumination is applied in the system. It provides a better estimation of the local temperature when the temperature variation is negligible across the fluorescence collecting depth, such as the liquid film in Taylor flow.

To increase the depth-wise resolution of the micro-LIF technique, temperature sensitive particles (TSPs) with promising characteristics for local temperature measurement were developed. The evaluation of different particles was undertaken. The calibrations have proved the applicability of certain two-dye particles for making temperature measurements

with an uncertainty of 2.5 °C for a single shot image analysis. A simultaneous measurement strategy was proposed to link the velocity and temperature measurements through the combined micro-PIV/LIF using the TSPs. The uncertainties and corresponding challenges of using TSPs were also presented.

In summary, this thesis contributes to an improved understanding of the thermohydraulics of single-phase flow in tortuous microchannels. The high quality experimental data collected through non-intrusive optical techniques provide a new perspective on flow behaviour and heat transfer performance in wavy microchannels, filling an important gap in the experimental field. The results presented in this thesis deliver valuable information for the validation of numerical models and for the design and optimization of micro-reactors and heat exchangers using wavy channels. Additionally, the advanced experimental techniques developed in this thesis provide important tools for the investigation of thermohydraulics of various micro-devices in the field of engineering.

Table of Contents

List of Figures

List of Tables

Nomenclature

Symbols

A	Channel amplitude, area (m^2)
A_{adj}	Plate area between two adjacent channels (m^2)
$A_{c,p}$	Channel project area (m^2)
A_e	External surface area of the test section (m^2)
A_p	Surface area of the plate (m^2)
A_s	Surface area (m^2)
A_w	Channel wall surface area (m^2)
$\hat{c}_p$	Fluid heat capacity (J kg^{-1} K^{-1})
C	Molecular concentration of the fluorescent dye (mol m^{-3})
Ca	Capillary number, $Ca = \mu_L U_{TP}/\sigma$
d	Channel diameter (m)
d_h	Hydrodynamic diameter (m)
d_p	Particle diameter (m)
Dn	Dean number, $Dn = Re(d/R_c)^{1/2}$
e	Internal energy (J kg^{-1})
e_A	Area utilisation
e_f	Relative pressure-drop penalty
e_{Nu}	Heat transfer enhancement
E	Heating power (W)

f	Fanning friction factor
$f_{n,i}, f_{t,i}$	Frame numbers when the i^{th} bubble nose and tail appear on the video image
f_s	Sampling frequency (Hz)
h	Heat transfer coefficient (W m^{-2} K^{-1}) or enthalpy (J kg^{-1})
h_{loss}	Heat loss coefficient (W m^{-2} K^{-1})
i_A	Heat transfer intensification
I	Current (A)
I_b	Background noise intensity (a.u.)
I_f	Fluorescent intensity (a.u.)
I_L	Incident laser light intensity (a.u.)
I_n	Normalized intensity
k	Thermal conductivity (W m^{-1} K^{-1})
K_{opt}	Optical constant
K_{spec}	Spectral constant
L	Half-unit length (m)
L_B	Bubble length (m)
L_h	Heater length (m)
L_{hy}	Hydrodynamic entrance length (m)
L_p	Overall path length (m)
L_S	Liquid slug length (m)
L_{th}	Thermal entrance length (m)
$\dot{m}$	Mass flow rate (kg s^{-1})

n	Channel unit number, bit depth, refractive index
N	Sampling number
NA	Numerical aperture
N_s	Moving step
Nu	Nusselt number, $Nu = hd_h/k$
P	Cross-sectional perimeter length (m)
Pr	Prandtl number, $Pr = \mu\hat{c}_p/k$
ΔP	Pressure-drop (Pa)
ΔP_{bend}	Pressure-drop due to bends (Pa)
ΔP_{con}	Pressure-drop due to contraction (Pa)
ΔP_{exp}	Pressure-drop due to expansion (Pa)
ΔP_{extra}	Pressure-drop due to extra sources (Pa)
ΔP_{in}	Pressure-drop due to inlet portion (Pa)
ΔP_{out}	Pressure-drop due to outlet portion (Pa)
q_s	Surface heat flux (W m^{-2})
$\dot{q}_w$	Wall heat flux (W m^{-2})
Q_f	Heat transferred to the fluid (W)
Q_{in}	Total power input (W)
Q_{loss}	Heat loss to the environment (W)
R	Channel radius (m), thermal resistance (m^2 K W^{-1}), signal ratio
R_c	Radius of curvature (m)
Re	Reynolds number, $Re = \rho u_m d_h/\mu$

s	Channel axial location (m)
S	Temperature sensitivity (% K^{-1})
$\dot{S}$	Volumetric heat generation rate (W m^{-3})
S_0	Channel axial path length in one unit (m)
S_f	Fluorescence signal (a.u.)
St	Strouhal number, $St = fd_h/u_m$
t	Time (s), wall thickness (m)
t_{acq}	Acquisition time (s)
T_a	Ambient temperature (K)
T_b	Bulk mean fluid temperature (K)
T_h	Heater temperature (K)
T_{in}	Inlet temperature (K)
T_G	Glass temperature (K)
T_M	Metal temperature (K)
T_{out}	Outlet temperature (K)
$\bar{T}_w$	Peripherally-averaged wall temperature (K)
u_m	Mean fluid velocity (m s^{-1})
U_B	Bubble velocity (m s^{-1})
U_G	Superficial gas velocity (m s^{-1})
U_L	Superficial liquid velocity (m s^{-1})
U_{TP}	Two-phase mixture velocity, $U_{TP} = U_G + U_L$ (m s^{-1})
V	Voltage (V)

$\dot{V}$	Volumetric flow rate (m^3 s^{-1})
V_{em}	Collection volume (m^3)
z	Depth (m)
ΔZ	Distance moved by the bubble nose in a time of τ (m)

Greek symbols

β	Temperature sensitivity (% K^{-1})
δ_F	Film thickness (m)
ε_L	Molar extinction coefficient of fluorescent dye (m^2 mol^{-1})
η	Quantum efficiency
θ	Channel bend angle (°)
λ	Wavelength (nm)
μ	Dynamic viscosity (Pa s)
ρ	Density (kg m^{-3})
σ	Surface tension (N m^{-1})
τ	Frame period (s)
τ_p	Particle response time (s)
$\emptyset$	Fluorescence quantum efficiency
Ω	Solid angle

Subscripts

c	Channel

G	Glass
h	Heater
i	Inner surface
in	Inlet
m	Measured value
M	Metal
o	Outer surface
out	Outlet
s	Value at the axial location s
str	Straight channel
w	Wall, wavy channel
x, y, z	x, y, z coordinate

Chapter 1

Introduction

“The water just rushes out against the outer bank of the river at the bend and so washes the bank away [. . .] it allows deposition to occur at the inner bank [. . .] the question arose to me: Why does not the inner bank wear away more than the outer one?”

Thomson (1876)

Recent technological developments in areas such as microfluidic devices and microelectronics have led to process miniaturization and a near exponential growth in applications of micro-technology. Micro-structured devices are finding evermore industrial applications where high rates of heat transfer are required in a compact space, such as compact heat exchangers, micro-reactors and electronic cooling devices.

In the chemical process industries, micro-structured devices have brought new developments that go beyond “traditional” chemical engineering. Significant research has focused on novel equipment and techniques that potentially could transform the concept of chemical plants and lead to compact, safe, energy-efficient and environment-friendly sustainable processes. Ramshaw (1983), one of the pioneers in the field, defined process intensification as a strategy for making dramatic reductions in the size of a chemical plant. These reductions can come from shrinking the size of individual pieces of equipment and also from cutting the number of unit operations or apparatuses involved. Later on, Stankiewicz and Moulijin (2000) provided a broader definition: process intensification consists of the development of novel apparatuses and techniques that, compared to those commonly used today, are expected to bring dramatic improvements in manufacturing and processing, substantially decreasing equipment-size/production-capacity ratio, energy consumption, or waste production, and ultimately resulting in cheaper, sustainable technologies. A typical example to meet this need is compact heat exchangers, which have developed quickly because of their advantages of the higher duties that are achieved in smaller sizes than shell and tube heat exchangers. This compactness is achievable through higher surface area densities (i.e. heat transfer surface area per unit volume of heat exchanger) and enhanced mass/heat transfer.

In order to meet the increasing demand for more efficient and effective heat transfer devices, significant research has been focused on flow and forced convection heat transfer in mini-/microchannels which are widely used in micro-devices. However, due to the reduced length scale in these devices, the flow in microchannels is usually laminar or transitional, so that turbulent mixing is absent. Some of the simplest arrangements that can be used for heat transfer enhancement involve using single-phase forced convection, two-phase gas-liquid flow or flow boiling in small channels. For the single phase flow, a higher heat removal rate can be achieved with flow following tortuous passages (Rosaguti et al., 2006, Geyer et al., 2007, Zheng et al., 2013b), using micro-fin structures (Foong et al., 2009), and mechanical aids (Kumar et al., 2011) to promote fluid mixing.

Curved microchannels present great potential to provide enhanced heat exchanger performance, where Dean vortices due to the recirculation in the cross-section induced by flow around bends, is of critical importance and can be seen as a means to process intensification. The printed circuit heat exchanger (PCHE) produced by Heatric, which is a successful industrial example for compact plate heat exchanger, has been employed all over the world, because of its advantages of compactness, high-pressure endurance and high heat transfer performance. The channels used in PCHEs are small semi-circular in cross-section with a typical diameter from 0.5 to 2 mm and they are usually shaped into a herringbone, or zigzag pattern, as presented in Figure 1.1 (a). The metal plates including the flow channels are then stacked and diffusion-bonded together to generate a core of heat exchanger Figure 1.1 (b)).

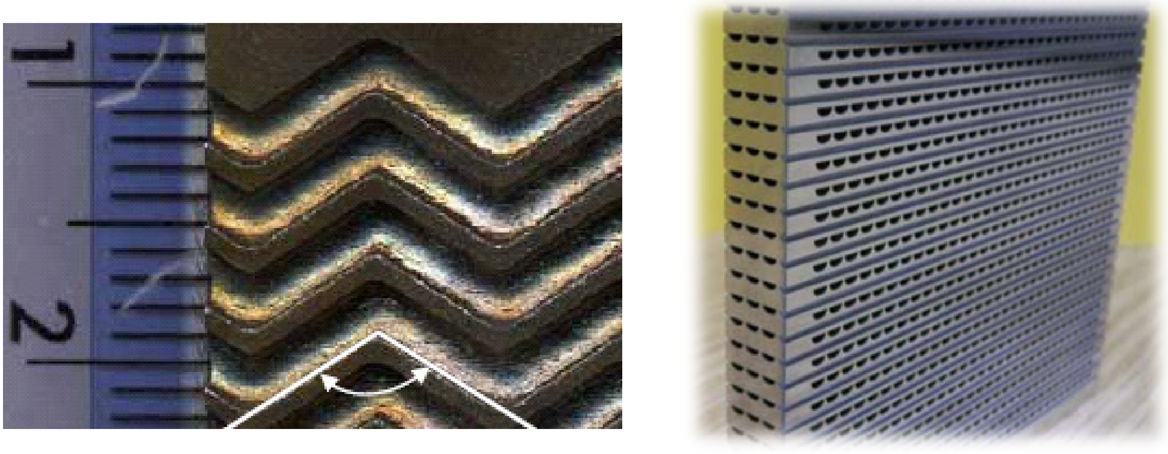

(a) (b)

Figure 1.1: **(a)** Zigzag channels used in PCHEs; and **(b)** Heat exchanger core of PCHEs. Taken from http://www.heatric.com.

Due to the relative simplicity of the channel structure, flow mechanisms for enhanced fluid mixing and thus improved heat transfer in wavy channels has become an important research field and have driven a considerable number of theoretical, numerical and experimental studies. The tortuous features from the wavy patterns have been shown to enhance heat transfer coefficients considerably but also is accompanied by an increase in pressure drop, in comparison with flows in straight channels (Rosaguti et al., 2006, Geyer et al., 2007, Zheng et al., 2013b). As the geometrical configurations strongly influence both the hydraulic and thermal performance, the final heat exchanger design is certainly dependent on the choice of the channel geometry.

In order to develop technology for producing efficient compact heat exchangers, a thorough understanding of the fundamentals of thermohydraulics in wavy microchannels is necessary. Although the fluid flow in wavy microchannels has been studied extensively numerically, very few experimental data are available to validate the numerical models. The technical difficulties due to the restrictions imposed by the small length-scales involved in obtaining accurate, microscale measurements are the main obstructions that have hindered the progress towards understanding the thermohydraulics in such systems experimentally. For the experimental validation of flow dynamics and heat transfer performance in wavy microchannels, novel experimental techniques for velocity and temperature measurements in microscale are urgently needed.

1.1 Objectives

The present work attempts to fill the existing gap in validation studies, with specific objectives as follows:

1. To develop experimental techniques for velocity and temperature measurements in microscale devices. The techniques could be used to understand the fluid dynamics and heat transfer characteristics in various fields of engineering and to validate numerical models.
2. To conduct flow visualisation and heat transfer experiments in tortuous microchannels across a range of Reynolds numbers. Firstly, data should be collected at low Reynolds numbers where the flow is steady to validate the steady-state simulations. Then, techniques could be extended to higher Reynolds number to confirm the existence of massive recirculation and unsteady flows. In addition, as the transient and turbulent

regime is an important Reynolds number regime for heat exchangers, the experimental data could be obtained for exploration and validation of turbulence transition models.

3. To understand the fundamental mechanisms responsible for the heat transfer enhancement observed in wavy microchannels, assisting with channel design and optimization.

1.2 Thesis structure

The chapters in this thesis are organised as follows:

Chapter 2: Literature Review provides a review of flow behaviour in tortuous channels and the associated heat transfer performance. The currently available computational studies on single-phase flow in wavy microchannels and the relevant literature on established experimental techniques to investigate flows behaviour in microchannels are assessed with identification of some gaps in the knowledge-base.

Chapter 3: Experimental Apparatus and Method Validation describes the experimental setup and techniques employed in this study. Data acquisition and reduction procedures are provided together with the results of the single-phase validation experiments in straight channels.

Chapter 4: Heat Transfer in Straight Microchannels presents the experimental results for heat transfer in straight channels. The computational methodology for the CFD modelling to study the conjugate heat transfer problem is presented. Simulation predictions are compared with experimental data to validate the experimental setup and methodology.

Chapter 5: Hydrodynamics in Wavy Microchannels presents a comprehensive study of the flow dynamic behaviours in wavy microchannels, including flow instability and pressure-drop penalty. The three-dimensional flow patterns which reveal both flow recirculation and Dean vortices are obtained. The impacts of geometric variations are also discussed.

Chapter 6: Heat Transfer in Wavy Microchannels studies the heat transfer characteristics of wavy microchannels through heat transfer experiments and conjugate simulations. The interactions between flow instability, heat transfer and pressure drop penalty are discussed.

Chapter 7: Non-intrusive Temperature Measurements describes a new non-intrusive technique (two-dye Laser Induced Fluorescence (LIF) using a colour camera) for temperature measurement in micro-devices. The applications of the developed technique in fluid temperature measurements in single-phase flow and Taylor flow are presented.

Chapter 8: Temperature Sensitive Particles and Simultaneous Measurement of Temperature and Velocity presents technique development for temperature sensitive particles with promising characteristics for local temperature measurement and the capability for simultaneous measurement of temperature and velocity fields in microscale systems.

Chapter 9: Conclusions and Recommendations discusses the conclusions from the current study and provides some suggestions for future research.

Chapter 2

Literature Review

Micro-structured devices are finding evermore applications where high rates of heat transfer are required in a compact space. The flow in wavy microchannels presents great potential to enhance fluid mixing and heat transfer compared with straight microchannels. Over the last few decades, a lot of effort has devoted to the understanding of flow and heat transfer characteristics in these types of channels with various geometrical structures. In this chapter, a review of the flow behaviour in tortuous channels and the associated heat transfer performance is presented. A discussion on limitations of current computational studies is provided. Subsequently, the current state-of-the-art of techniques for whole-field velocity and temperature measurements is summarized and discussed. The currently available experimental data for single-phase flow in wavy microchannels are assessed with identification of some gaps in the knowledge-base.

2.1 Thermohydraulic behaviour of tortuous microchannels

The enhancement in heat transfer can be achieved by increasing the heat transfer surface, disrupting the flow velocity and promoting flow mixing/turbulence. Compact heat exchangers using smaller channels provide high surface area density as compared with conventional heat exchangers. However, the flow in these microchannels is usually laminar or transitional due to small hydraulic diameters, so it is difficult to achieve turbulent mixing. It is well-known that when liquid flows through curved passages, secondary flows known as Dean vortices may be generated, which will improve the mixing and heat transfer. Several protocols for fluid mixing based on this mechanism have been proposed and demonstrated in micro systems, for example, microchannels with helical/spiral geometry (Yang et al., 1995, Jiang et al., 2004), twisted tapes (Ray and Date, 2001, Ray and Date, 2003), channel bends (Chang et al., 1983, Sudo et al., 1998, Nikolaidis and Mathioulakis, 2002, Rosaguti et al., 2005, Geyer et al., 2006b, Rosaguti et al., 2006, Xiong and Chung, 2008), surface waviness (Metwally and Manglik, 2004, Zhang et al., 2004, Islamoglu, 2008, Giron-Palomares et al., 2009), and complicated configurations such as three-dimensional C-shaped channel (Liu et al., 2000). The fundamentals involved in enhancing the mixing performance and local phenomena in curved channels are discussed in the following sections, to better understand how mixing and heat transfer proceed for single-phase flow.

2.1.1 Development of flow fields

The complexity of fluid dynamics occurring in curved channels has driven extensive research efforts in the last few decades. Unlike the flow in a straight pipe, fluid motion in a curved passage is not parallel to the axis of the pipe, owing to the presence of flow instabilities and secondary flow caused by the curvature.

2.1.1.1 **Flow instabilities**

For flow in wavy passages, there is a progression, with increasing Reynolds number, from steady laminar flow to chaotic flow (which may or may not be steady), then to transient flow and finally to fully-developed turbulent flow. The flow behaviour in tortuous channels is found to be characterized by the generation of fluid recirculation, reattachment, deflection, impingement, roller vortices or lateral swirl in the trough regions of the wavy channels (Rush et al., 1999, Comini et al., 2002, Guzman and Del Valle, 2006, Vashisth et al., 2008). The critical Reynolds number for flow transition to unsteadiness can be significantly lower than that in straight channels. Rush et al. (1999) have studied experimentally the flow and heat transfer for laminar and transitional flows in sinusoidal passages with large aspect ratios. Unsteady flow was observed at Reynolds numbers as low as 200 near the channel exit and with an increase in the Reynolds number, the location of the onset of unsteadiness moved towards the channel entrance. The critical Reynolds number for onset of unsteadiness depends critically on the channels geometry, as well as the total channel length in the flow direction. Curvature-induced lateral vortices were observed in the trough of the wavy profiles, as can be seen in Figure 2.1. These flow instabilities result in macroscopic or significant mixing between the core fluid and near-wall fluid, thereby disrupting and thinning the boundary layers to enhance the heat transfer.

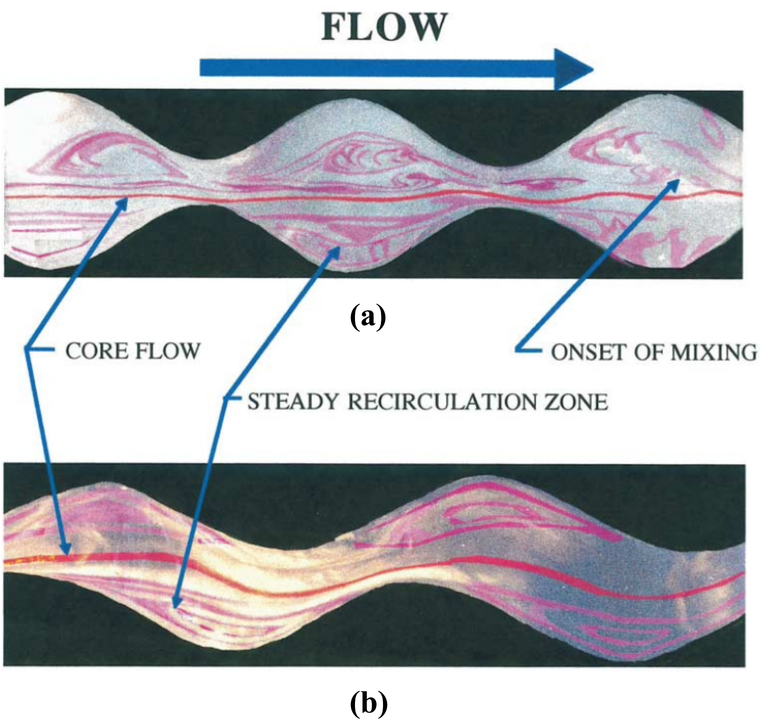

Figure 2.1: Typical images showing recirculation zones and the onset of mixing for phase shift ψ: **(a)** ψ = 180°; **(b)** ψ = 90°, as investigated by Rush et al. (1999).

Numerous authors have analysed the flow pattern in detail and the conditions for the appearance of instabilities and chaos in the flow within corrugated and converging-diverging plate channels, with various shapes such as sinusoidal (Amon et al., 1996, Oviedo-Tolentino et al., 2008, Oviedo-Tolentino et al., 2009, Ramgadia and Saha, 2013) and V shape (Islamoglu and Parmaksizoglu, 2006, Naphon, 2007, Naphon, 2008) . A two-dimensional (2-D) representation of the wavy plate channels as a parallel-corrugated-plate channel with heat transfer at the wavy walls, which is an idealization of the three-dimensional model had been considered in many of the earlier studies (Wang and Vanka, 1995, Yang et al., 1997, Comini et al., 2002, Metwally and Manglik, 2004, Zhang et al., 2004). An important observation made from these studies is that these wavy passages do not provide significant heat transfer enhancement if the flow remains steady. However, when the flow transitions to an unsteady state, remarkable heat transfer enhancement is observed. Wang and Vanka (1995) studied the heat transfer rates numerically for flow through a periodic array of wavy channels. The flow was observed to be steady up to a Reynolds number of around 180, above which self-sustained oscillatory flow was observed. The self-sustained oscillations lead to complex interactions between the core fluid and the boundary layer fluid through shear-layer destabilization, and thus provided a natural mechanism of heat and mass transfer enhancement. They reported that the average Nusselt numbers for the wavy wall channel were only slightly larger than those for a parallel-plate channel in the steady-flow regime, while in the transitional flow regime, the enhancement of heat transfer was about a factor of 2.5. Friction factors for the wavy channel were found to be about twice those for the parallel-plate channel in the steady flow region, and remained almost constant in the transitional regime. Comini et al. (2004) revealed similar results and pointed out that as the Reynolds number increases above a critical value, Re_{cr}, the transverse vortices, whose axis of rotation is normal to the main flow, start detaching periodically and moving downstream, leading to a time-periodic behaviour of both the velocity and temperature fields. The transverse vortices significantly enhance convection only above the critical Reynolds number. Using the three-dimensional plots, they found that longitudinal vortices, whose axis of rotation is aligned with the main flow, can produce mixing of fluid from the wall region to the core of the flow, and vice versa, even in stationary conditions.

Self-sustained oscillatory flow at higher Reynolds number has been observed in many studies on two-dimensional grooved and wavy channels (Amon et al., 1996, Nishimura et al., 2000, Hossain and Islam, 2004, Guzman and Del Valle, 2006, Ramgadia and Saha, 2012, Guzman et al., 2013, Ramgadia and Saha, 2013), and the flow subsequently becomes chaotic resulting in higher heat and mass transfer. Transition scenarios from laminar to transitional flows, with one, two or more dominate frequencies in different geometric channels configurations were demonstrated. The heat transfer rate increases due to flow mixing enhancement after the flow bifurcation, which is accompanied by an increase in pressure drop. The transitional Reynolds number for the onset of these oscillations was found to vary with channel geometry.

However, the 2-D models cannot fully capture the physics of the problem as there is mounting evidence that three-dimensional flows often develop in tortuous channels. The revealed Dean vortices in cross-sections (as discussed in the next section) have then attracted more attention when three-dimensional (3-D) models were used. Manglik et al. (2005) provided a summary of relevant literature available for two- and three-dimensional wavy-walled passages, and they themselves investigated the steady, fully-developed laminar flow and heat transfer in 3-D wavy-plate-fin heat exchanger cores with rectangular cross-sections (as shown in Figure 2.2), declaring 2-D results as instructive only. They detailed the effect of fin density and cross-section aspect ratio on flow and heat transfer. It was found that the wavy-wall-surface produces a secondary flow pattern that is made up of multiple counter-rotating vortices in the flow cross-section of the trough region, and their magnitude and spatial coverage increases with Reynolds number and fin spacing ratio. This significantly enhances the overall heat transfer coefficient as well as the pressure drop penalty, when compared with those in a straight channel of the same cross-section.

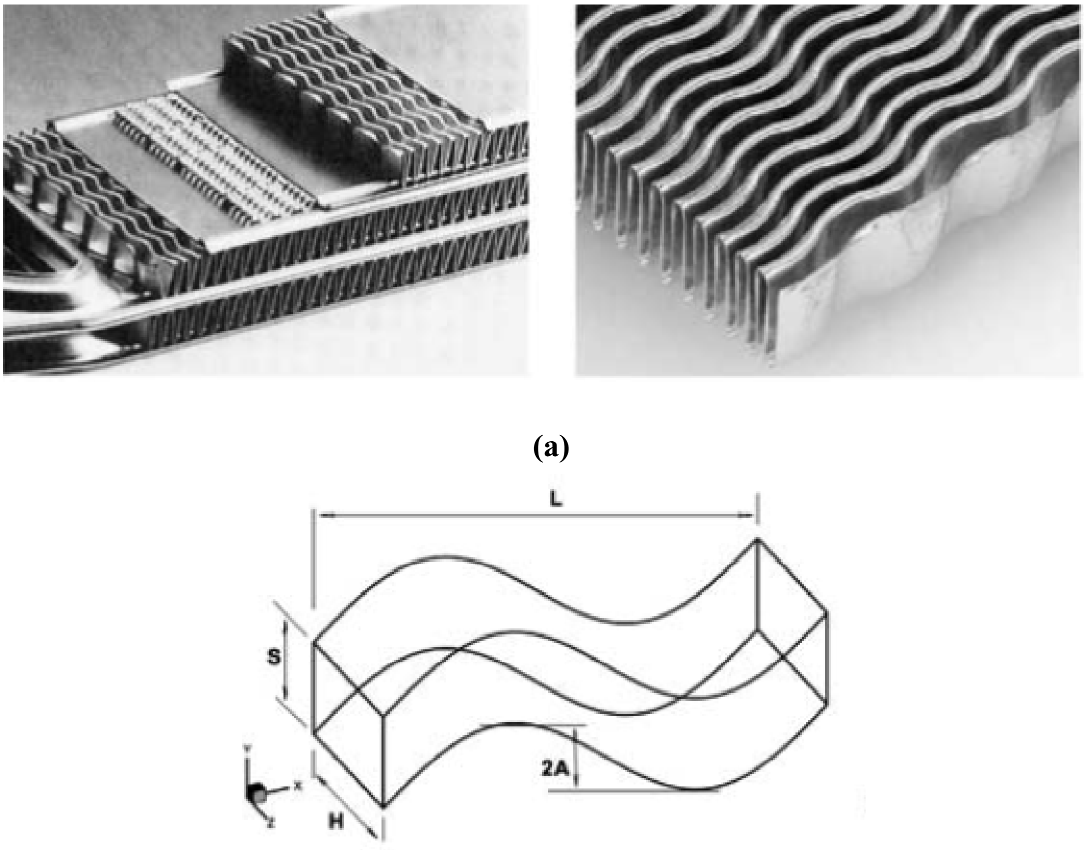

(a)

(b)

Figure 2.2: **(a)** Typical wavy-plate-fin cross-flow heat exchanger core; and **(b)** geometrical description of three-dimensional sinusouidal wavy-pate-fin. Taken from Manglik et al. (2005).

Recently, Sui et al. (2012) performed numerical simulation of fluid flow and heat transfer in periodic sinusoidal channels with rectangular cross-sections. They found that with increasing Reynolds number, the flow transitions from steady to time periodic with a single frequency, and subsequently to quasi-periodic flow with two distinct fundamental frequencies. A further increase in the Reynolds number leads to aperiodic behaviour of the flow, which suggests chaotic flow. A periodic oscillation was also found in the study of Oosthuizen (2008), who did simulations of a mini-channel with a square cross-section and a centre-line path composed of a series of circular arcs. He found that the critical Reynolds number at which unsteady flow develops decreases with decreasing bend radius. The development of this unsteadiness can lead to an increase in the pressure drop in the channel and significant increase in the heat transfer rate.

2.1.1.2 **Dean vortices**

When fluid flows through curved passages, the more rapidly flowing central parts of the flow are forced outwards by centrifugal action, while the slower parts along the wall are forced inwards where the pressure is lower, and a so called "secondary flow" takes places at right angles to the main flow. The earliest observation of secondary flow in curved pipes was found by Williams et al. (1902) and Eustice (1910, 1911). These rotating secondary flow features (see Figure 2.3 for an illustration of the flow structure) were subsequently named Dean vortices after Dean (1928) developed an analytical solution for fully-developed laminar flow in a curved tube of circular cross-section. Dean characterised the behaviour of these vortices in helical passages by defining a non-dimensional number *Dn* (known as the Dean number) given by

$$Dn = Re\left(\frac{d}{R_c}\right)^{1/2} \tag{2.1}$$

where *Re* is the Reynolds number, *d* is the channel diameter and R_c is the radius of curvature.

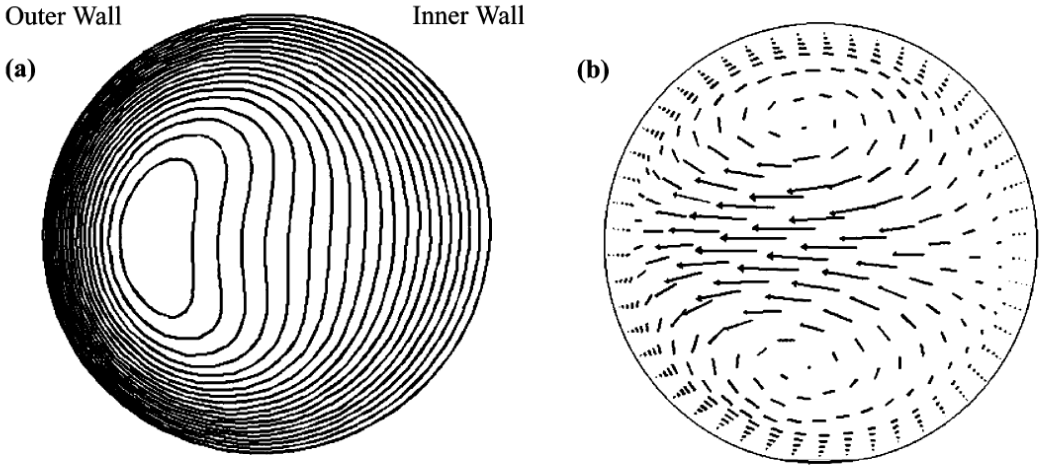

Figure 2.3: **(a)** Velocity streamlines; and **(b)** Dean vortices in a curved tube. Taken from Vashisth et al. (2008).

A large amount of research was carried out on fluid flow for various geometrical parameters (curvature ratio and tube pitch), with attention given to Dean vortices over a wide range of Dean numbers. A review work can be found in Vashisth et al. (2008) and Naphon et al.

(2006). It was reported that for low Dean numbers, the axial velocity profile was parabolic and unaltered from the fully-developed straight channel flow. As the Dean number is increased, the maximum velocity begins to be skewed toward the outer periphery. Similarly, for low values of curvature ratio (ratio of radius of curvature to channel dimension), the secondary flow intensity is very high, while for high values of curvature ratio the secondary flow intensity is much less.

The pattern of the secondary flow was found to change with Dean number. Sugiyama et al. (1983) clarified the phenomena of a secondary flow in a fully-developed laminar flow region in curved rectangular channels by visualizing the flow pattern. As shown in Figure 2.4, in the laminar stable region at a low Dean number, only main secondary flow vortices appear, and as the Dean number increases, a retarded layer occurs near the outer wall. With a further increase of the Dean number, two pairs of additional secondary flow vortices are set up. However, Cheng et al. (1976) found that the additional secondary vortices disappeared above a critical value, which is around *Dn* = 500.

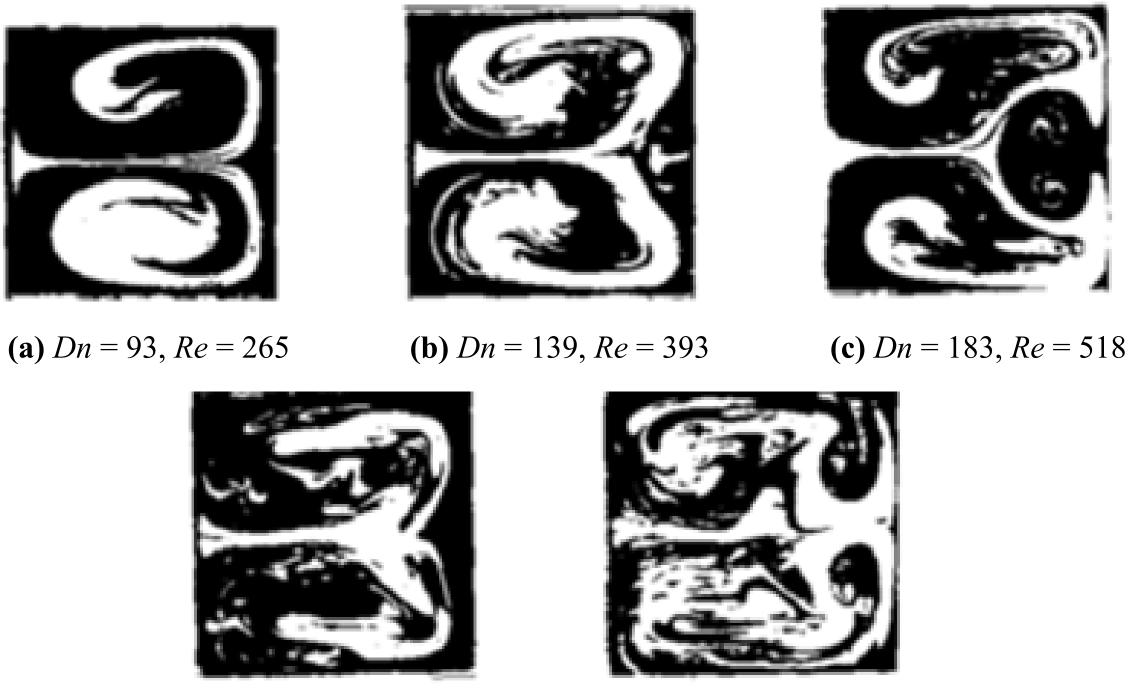

(a) *Dn* = 93, *Re* = 265 **(b)** *Dn* = 139, *Re* = 393 **(c)** *Dn* = 183, *Re* = 518

(d) *Dn* = 383, *Re* = 1083 **(e)** *Dn* = 527, *Re* = 1489

Figure 2.4: The flow patterns in the channel of aspect ratio 1.0 and curvature ratio 8. Taken from Sugiyama et al. (1983).

The critical Dean number, above which value the additional counter-rotating vortices appear, has been determined numerically in curved channels at various flow rates and geometrical parameters (Joseph et al., 1975, Cheng et al., 1976, Dennis and Ng, 1982). However, the effect of curvature on the bifurcation of the flow was not clearly understood as conflicts still exist among different studies (Nandakumar and Masliyah, 1982, Cheng, 1986). The additional pair of vortices was confirmed in Laser Doppler Anemometry (LDA) experiments of Hille et al. (1985). They pointed out that the differences in the literature with regard to the Dean number range of the second vortex pair may be attributed to different curvature ratio and claimed results may be only comparable if both the Dean number and curvature ratio are identical.

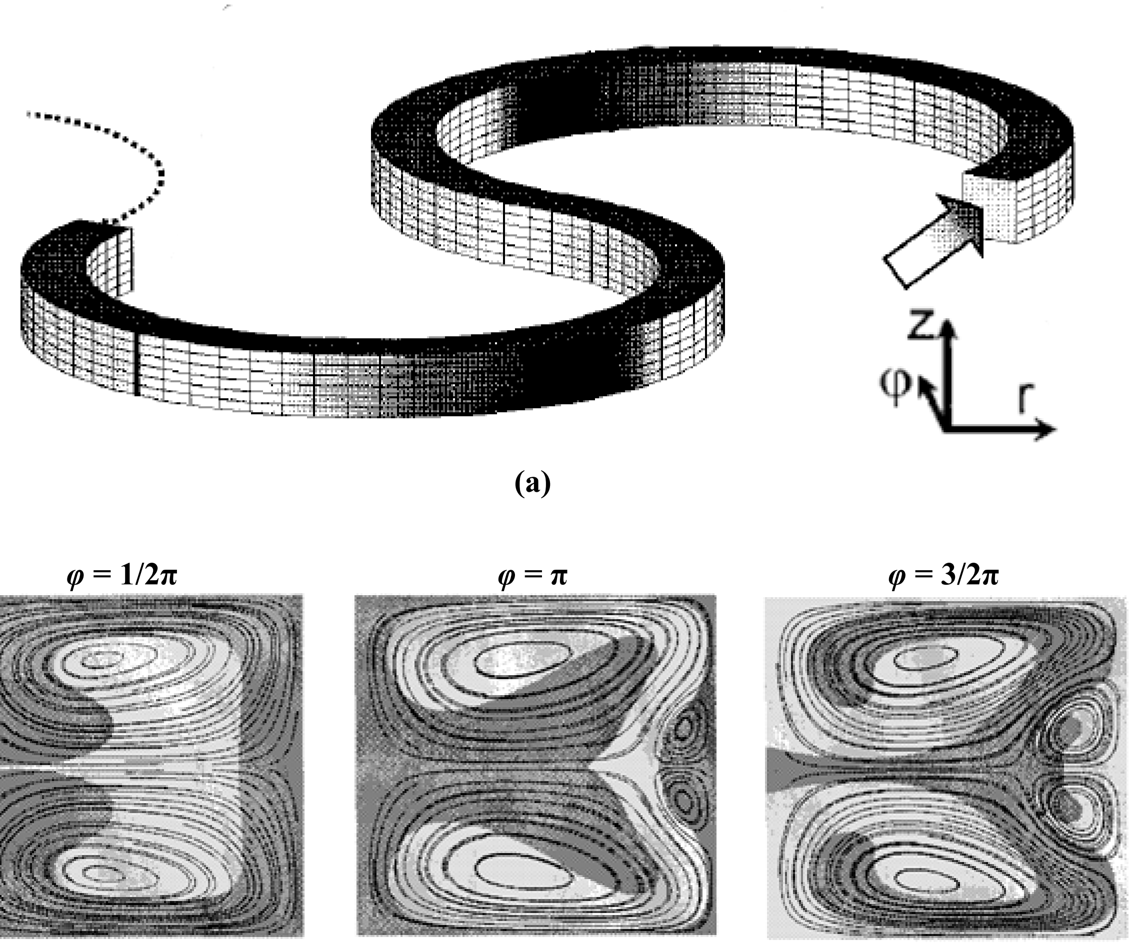

(a)

***φ* = 1/2π** **φ = π** **φ = 3/2π**

(b)

Figure 2.5: (a) Model geometry of the meandering channel; and **(b)** velocity fields of the secondary flow at different cross sections for Dean number *Dn* = 300. Taken from Schöenfeld and Hardt (2004).

The Dean vortex arises not only in conventional curved channels with constant curvature, but also in various channels with tortuous features, such as sinusoidal, serpentine, trapezoidal channels or curved channels with varying curvature (Schönfeld and Hardt, 2004, Geyer et al., 2006b, Gong et al., 2011b, Anxionnaz-Minvielle et al., 2013). These channels are used widely in practical applications for enhanced flow mixing and heat transfer. Compared with constant curvature channels, the flow in tortuous passages are often far more complicated and may show specific flow features for different geometries. In the numerical work of Schöenfeld and Hardt (2004), Dean vortices were generated in a meandering channel, which consists of several connected three-quarter circular ducts with curvature changing sign at the connections (shown in Figure 2.5 (a)). The quantity and the location of the Dean vortices were found to change along the flow direction, as seen in Figure 2.5 (b). Accordingly, chaotic flows are generated by periodic "switching" between one and two pairs of vortices, respectively.

Most recently, Sui and co-workers (Sui et al., 2010, Sui et al., 2012) investigated numerically the fully-developed flow in a periodic wavy channel with rectangular cross-section for increasing Reynolds numbers ranging from the steady laminar to transitional flow regimes. They also found that the number and the location of the Dean vortices undergo drastic changes along the flow direction. Further increase in the Reynolds number leads to very complex patterns of Dean vortices which evolve temporally and spatially along the flow direction, and the flow symmetry may even be lost. The spatial evolution of the flow patterns was caused by the changing direction of the centrifugal force along the wavy channel with curvature changing sign. Anxionnaz-Minvielle et al. (2013), who studied the wavy channels based on plate-type heat exchanger/reactor, found that the intensity of the counter-rotating vortices is highest at the bend outlet and then decreases along the channel length before disappearing. They also pointed out that the Dean number, more than the Reynolds number, seems to govern the flow in the wavy channels.

2.1.1.3 **Chaotic advection**

Another flow behaviour that has attracted increasing attention is chaotic advection. This term was first proposed by Aref (Aref, 1984) in his study of a "blinking vortex model" for describing a special flow regime in which the fluid particle trajectories became chaotic and fluid mixing was achieved very efficiently. The study was conducted for a two-dimensional, unsteady flow system and it was then proved theoretically that chaos could also be generated in a three-dimensional, steady flow. The appearance of chaotic particle trajectories have been observed in laminar flow in various of geometries, such as B-shaped channels (Lasbet et al., 2007), twisted curved channels (Peerhossaini et al., 1993), three-dimensional serpentine microchannels (Liu et al., 2000) and bent coil configurations (Kumar and Nigam, 2005), as shown in Figure 2.6. The emergence of chaotic advection can help to stir the fluids very efficiently and consequently enhance the heat transfer rate.

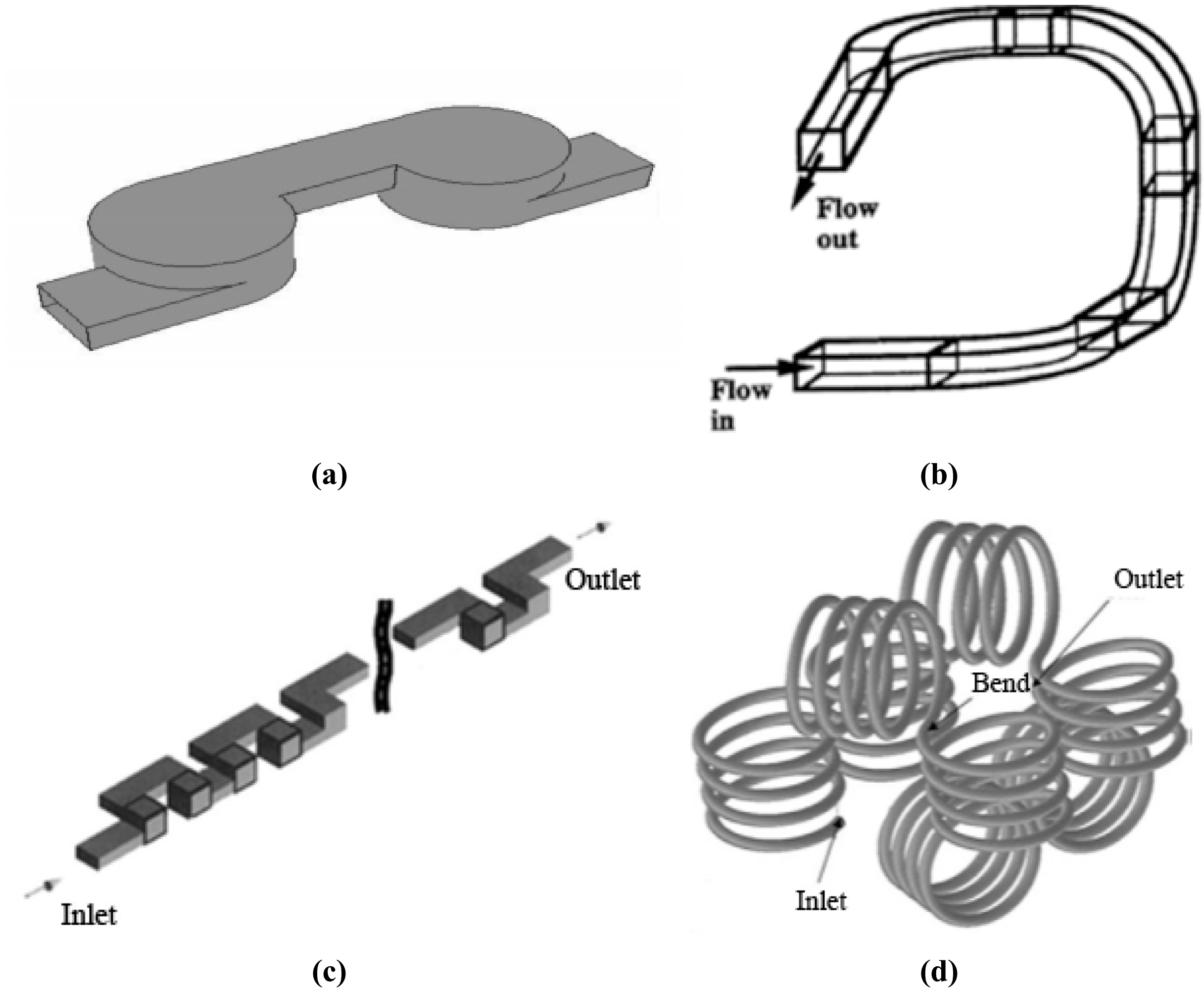

Figure 2.6: Channel structures designed to promote chaotic advection: **(a)** B-shaped channel from Lasbet et al. (2007); **(b)** twisted curved channel from Peerhossaini et al. (1993); **(c)** three-dimensional serpentine channel from Liu et al. (2000); and **(d)** bent coil configuration from Kumar and Nigam (2005).

Similar studies have been made for planar-based geometries, which can be easily etched on plate surfaces. However, planar channels do not generate chaotic advection as readily as three-dimensional geometries, as indicated by Yamagishi et al. (Yamagishi et al., 2007) and Aref (Aref, 2002). Chaotic advection in planar-based channel was observed by many researchers together with Dean vortices (Jiang et al., 2004, Schönfeld and Hardt, 2004, Sui et al., 2010). Jiang et al. (2004) found that the mixing performance in the planar-based channel is enhanced substantially relative to a straight channel. Sui et al. (Sui et al., 2010) gave another example using simple periodic wavy channels with rectangular cross-sections and found the generation of secondary flow (Dean vortices) and chaotic advection by use of Poincaré sections. Most recently, Zheng et al. demonstrated that chaotic advection is able to be generated in simple planar-based zigzag channels with square (Zheng et al., 2013a) and semi-circular cross-sections (Zheng et al., 2013b). They pointed out that the spatially periodic flow patterns were no longer seen due to the existence of chaotic fluid particle trajectories. Fluctuations of unit-based heat transfer enhancement and pressure-drop penalty were also observed and their mean value on a per unit basis increased gradually with increasing Reynolds number in the chaotic advection flow regime. It was concluded that this flow behaviour must be common in channels which share geometric similarities with these zigzag channels.

2.1.2 Heat transfer and pressure drop

Based on the study of the flow field development (flow instabilities and secondary flows), the heat transfer performance and pressure drop were investigated in detail for the design of heat exchange devices. Although the material, shape and size of the small passages vary widely across the literature, some general conclusions can be made.

It is concluded that the heat transfer performance of the wavy microchannels is always better than that of straight microchannels with the same cross-section. The facts concerning the working principle of curved channels and reasons for its enhanced performance can be explained in terms of flow mechanisms as mentioned in the following: (a) generation of secondary flow (Dean vortices) due to unbalanced centrifugal forces; (b) flow separation and reattachment; (c) destabilization and thinning of thermal boundary layer; (d) enhanced cross-sectional mixing; and (e) chaotic advection generated in two-dimensional unsteady flow or three-dimensional steady flow. The extent of enhancement increases with increasing Reynolds number. At low Reynolds numbers, the viscous forces become more important and act to suppress secondary flow formation. The flow tends towards the straight pipe solution and no heat transfer enhancement or pressure drop can be expected at low Reynolds number (Xin and Tao, 1988, Rosaguti et al., 2006). As the Reynolds number increases and inertial forces become more significant, secondary flows and flow separation establish and they enhance the interactions between the core flow and the boundary layer and result in a significant increase in fluid mixing and thus the heat transfer. Different tortuous geometries provide different degrees of disruption to the flow and temperature fields and therefore different effectiveness of enhancement. Other factors, such as the thermal boundary conditions and fluid Prandtl number, also influence the heat transfer performance in tortuous passages (Shah and London, 1978, Geyer et al., 2006a, Zheng et al., 2013b).

The studies of heat transfer in various curved channels are often accompanied by a discussion of the increased pressure-drop compared with the equivalent straight channel. Pressure drop penalties have been attributed not only to secondary flows but also to the recirculating regions established as the flow separates from the channel walls. The additional pressure drop due to the bend is commensurate with the strength of the vortices around the outer and inner walls of the bend (Xiong and Chung, 2007, Xiong and Chung, 2008). However, Dean vortices formed within channels were found to retard the onset of flow separation, unsteady flow and turbulence (Rosaguti et al., 2006). The absence of recirculation zones accounts for the small increase in friction factor. Increased heat transfer performance may therefore be obtained with a surprisingly low pressure drop penalty.

An interesting observation reported by Popiel and van der Merwe (1996) is that when the friction factor is plotted against the Reynolds number, there is either no definite transition from laminar to turbulent flow or a delayed transition relative to that of a straight pipe. This is also reflected in the work of Johnston and Haynes (Johnston and Haynes, 2002), whose results demonstrated a smooth transition from laminar to turbulent flow in plots of the fraction factor and Colburn *j*-factor versus the Reynolds number. They hypothesized that smooth transition to turbulence occurs due to the secondary flows produced in the complex geometries.

In spite of the pressure drop increase, the heat transfer enhancement significantly exceeds the increase in friction factor (Metwally and Manglik, 2004, Manglik et al., 2005, Sui et al., 2010, Gong et al., 2011b, Gong et al., 2011a, Sui et al., 2012). Gong et al. (2011a, 2011b) have shown that the heat transfer enhancement can exceed the relative pressure drop penalty by factors of two or more for laminar flows of water with constant axial heat flux and peripherally uniform temperature. In the study of Rosaguti et al. (2007b), the heat transfer enhancement exceeds the relative pressure-drop penalty by factors as large as 1.5 and 1.8 for the circular and semi-circular cross-sections, respectively. It was pointed out that this is mainly due to the establishment of Dean vortices whose axes were aligned with the flow direction and so promoted cross-stream mixing without causing a large pressure-drop.

2.1.3 Effects of geometrical parameters

As the geometric configurations influence greatly both hydraulic and thermal performance, a large diversity of channel geometries (pathways and cross-sections) has been examined. The passages following pathways of serpentine, sinusoidal, zigzag and trapezoidal represent an interesting model flow path for various applications, such as compact heat exchangers and chemical reactors.

In serpentine passages with sharp corners (Choi and Anand, 1993, Choi and Anand, 1995, Chintada et al., 1999, Xiong and Chung, 2007, Xiong and Chung, 2008), it was found that the flow separation and formation of vortices appears around the sharp corner and develops with increasing Reynolds number. These vortices increase in strength with increasing Reynolds number, causing the bend pressure drop to increase sharply with Reynolds number. The sharp corners can be rounded, for example by sweeping a set cross-section along an axial pathway (Rosaguti et al., 2005, Rosaguti et al., 2006, Rosaguti et al., 2007b). Such passages are easy to manufacture for small-scale heat exchangers in practice and bring benefits of high heat transfer rate with comparatively low friction factors. This is because that sharp corners are more likely to generate recirculation regions that lead to increased pressure drop without the desired heat transfer enhancement. While the serpentine passage represents an interesting model flow path, it is not ideal for application in plate structures because of the poor stackability (passages cannot be placed close together and so it makes poor use of the available plate area).

Sinusoidal channels are found to be more stackable than the serpentine channels. This kind of channel was not studied too much using plate-based concepts as more studies were carried out on parallel-plate channels with sinusoidal corrugated walls (Rush et al., 1999, Islamoglu and Parmaksizoglu, 2003, Metwally and Manglik, 2004, Zhang et al., 2004, Mohammed et al., 2011). The effects of Prandtl number, Reynolds number and geometrical parameters (e.g. channel amplitude and corrugation angle) on the friction factor and the local and overall heat transfer were investigated. Typically, the improved performance is more significant in a much more compressing channel (lowering the wavelength or increasing the amplitude). This is attributed to thinning of the hydrodynamic boundary and thermal boundary layers due to the compounding effect of geometry and the flow velocity.

Focusing on the compact heat exchanger based on a plate structure, considerable efforts have been made by Haynes and co-workers (Rosaguti et al., 2005, Geyer et al., 2006a, Geyer et al., 2006b, Rosaguti et al., 2006, Geyer et al., 2007, Rosaguti et al., 2007a, Rosaguti et al., 2007b, Gupta et al., 2008, Zheng et al., 2013a, Zheng et al., 2013b, Zheng et al., 2014) to build a database covering a wide range of cross-sections, pathways and boundary conditions with consideration of stackability for application to plate structures. Systematic numerical study was performed on fully-developed, chaotic and transient flow and heat transfer in wavy microchannels with circular, semi-circular, triangular, trapezoidal and square cross-sections following the pathways ranging from regular square serpentine to a zigzag. The concept of area efficiency was introduced to define the stackability of channels on a plate (Geyer et al., 2007, Gupta et al., 2008). It was found that the zigzag pathway which was used widely in PCHEs provides the greatest heat transfer intensification of all the paths investigated, while the serpentine passages are not suitable because of their poor stackability. The results obtained for different cross-sections are qualitatively similar. The triangular duct was shown to be the optimum choice (best heat transfer augmentation compared with increased pressure drop) compared with the channels of circular, semi-circular, and square cross-sections. Rounding the corner of the triangle does not offer any advantage in terms of the heat transfer enhancement for triangular tortuous channels. Mohammed et al. (2011) also investigated the effect of various channel shapes numerically, such as zigzag, curved and step channels, with rectangular cross-section on the overall thermal and hydraulic performance of water flow. Similarly, the zigzag channel was found to have the greatest heat transfer coefficient among various channel shapes, but also the highest values of pressure drop.

Most recently, some new flow channel configuration models have been proposed to improve heat transfer performance with reduced pressure drop. Kato and co-workers (Ngo et al., 2006, Nikitin et al., 2006, Ngo et al., 2007, Tsuzuki et al., 2007, Tsuzuki et al., 2009) suggested a flow channel with S-shaped fins, as shown in Figure 2.7 (a). They found that the S-shaped fin channels were able to enhance the heat transfer with a much smaller increase in pressure drop when compared with the conventional zigzag channels. Sui et al. (2010) proposed two novel designs, as seen in Figure 2.7 (b), which the relative wavy amplitude (wavy amplitude/wavy length) of the microchannels along the flow direction is varied without decreasing the compactness of the wavy microchannels. They found that the heat transfer was enhanced by increasing the relative waviness along the flow direction. The relative waviness was also tailored to be locally higher at high heat flux regions to increase the local heat transfer performance and is thus invaluable for applications involving hot spot mitigation.

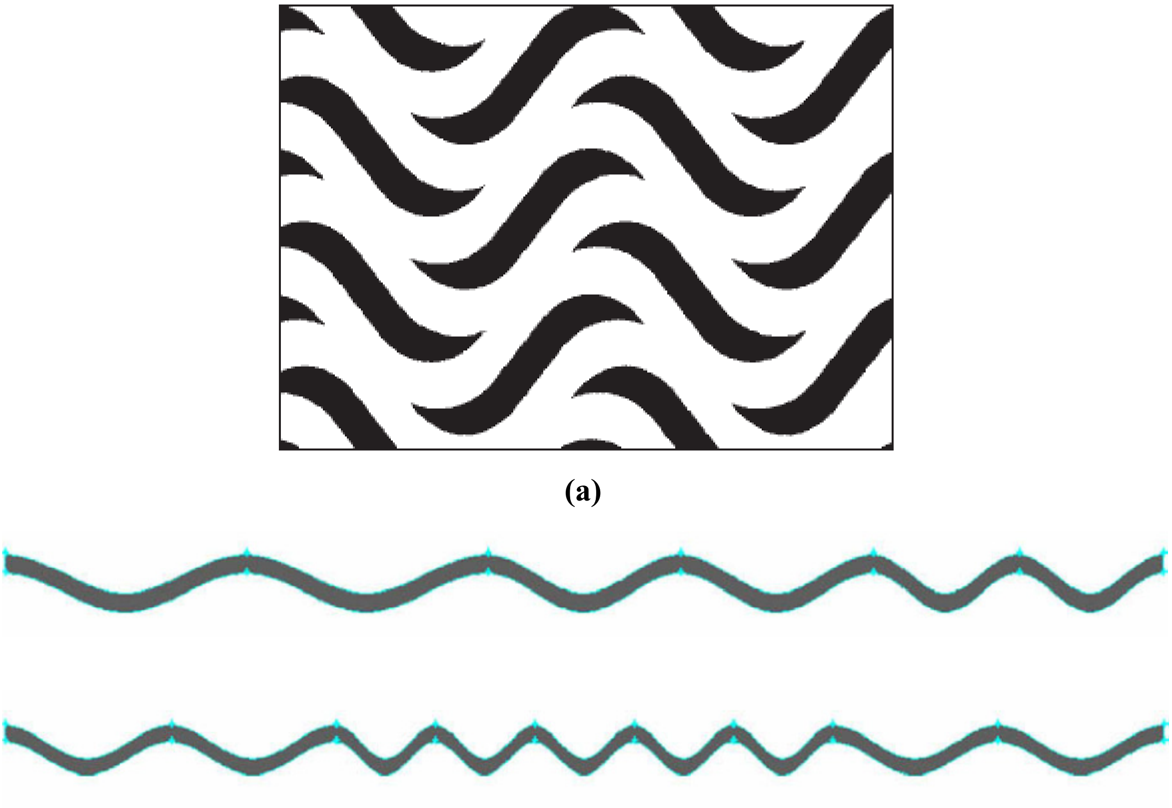

(a)

(b)

Figure 2.7: **(a)** S-shaped fins geometry proposed by Kato and co-workers, taken from (Tsuzuki et al., 2009); and **(b)** planar illustration of wavy microchannels with decreasing wavelength (top) and shorter wavelength in certain regions along the flow direction (bottom), proposed by Sui et al. (2010).

2.2 Limitations of computational studies

The previous studies on flows in the tortuous passages employed in compact heat exchangers were mostly carried out by using Computational Fluid Dynamics (CFD) simulation. CFD gives an insight into the detailed flow dynamics and heat transfer characteristics of the flow that are difficult, expensive or impossible to study using traditional (experimental) techniques. In spite of these advantages, there are some limitations to study the thermodynamics in wavy microchannels by using CFD methods.

1. Lack of experimental validation

Single phase flow behaviour in wavy channels at low Reynolds number has been well understood by CFD simulations. For steady, fully-developed laminar flow of an incompressible, Newtonian fluid such as water in wavy channels, the velocity and temperature fields can be fully described theoretically by solving the Navier-Stokes equations. Although the results are believed to be accurate, they have not been validated by experimental data. In addition, the behaviours of the flow field and heat transfer in the unsteady flow at higher Reynolds numbers (> 200-500), where chaotic advection and unsteady characteristics may occur in tortuous channels (Zheng et al., 2013a, Zheng et al., 2013b), have not been completely clarified due to the limitations of the CFD modelling.

2. Limitations of turbulence models

Most compact heat exchangers are also designed to work under high Reynolds number such as transition or even turbulent flow. Previous numerical studies on tortuous channels assumed a spatially periodic flow pattern without considering the fact that the flow may become non-periodic with an increase of the Reynolds number (Korichi and Oufer, 2007, Li et al., 2008, Korichi et al., 2009, Sui et al., 2012). Some limitations related to the numerical approach used were observed in laminar-turbulent transitional regime and in the transient prediction through the comparison results for periodic and non-periodic configurations (Mereu et al., 2013). Therefore, the relevant conclusions from the investigation of the transition of the flow remain doubtful.

For turbulent flow, it is believed that this can be described well through the use of the Navier–Stokes equations (Direct Numerical Simulation (DNS)). The main difficulty in modelling turbulent flow comes from the wide range of spatial length-scales and timescales. As a result, very small computational meshes and time steps are needed meaning that DNS is computationally very demanding, which makes such simulations impractical for engineering simulations. The present CFD techniques for turbulent flows, based on the Reynolds-Averaged Navier-Stokes (RANS) equations were developed with different applications in mind and have not been validated for this type of application due to the shortage of experimental data. The deficiencies in the turbulence models may cause differences between simulation results and experimental data.

2.3 Experimental difficulties and advances

The above review shows that a considerable number of numerical investigations have been conducted on the flow regime and heat transfer performance in wavy microchannels. There has been significant progress, especially in the identification of Dean vortices, but because of the limitations of CFD methods, the fundamental mechanisms are still not completely understood. Thus, experimental examinations are required to investigate both steady and unsteady flow phenomena and to evaluate the heat transfer performance.

The development of experimental methods has been an important topic of interest to understand the fluid dynamics and heat transfer characteristics in various fields of engineering and to validate numerical models. However, experimental studies on tortuous microchannels are very rare. A number of experimental difficulties have hindered the progress towards understanding the thermohydraulics in tortuous microchannels. The main difficulty has been the absence of sensitive and quantitative experimental techniques capable of measuring the fundamental dynamical variables: the velocity field, temperature field, vorticity, etc. in microscale systems. It becomes more challenging to analyse a three-dimensional thermal flow field due to the restrictions imposed by the small length-scales involved in obtaining accurate, microscale measurements over the entire thermal flow field. Furthermore, when the flow becomes unsteady, the time-dependence of the variables has to be obtained to achieve a fundamental understanding of the onset of unsteadies. A second difficulty has been an inadequate degree of control over boundary conditions and other experimental parameters. For the experimental validation of flow dynamics and heat transfer performance in wavy microchannels, measuring techniques for velocity and temperature fields in microchannels are urgently needed.

2.3.1 Velocity measurements and flow visualisation

Flow visualisation, as one of the most used experimental methods in micro-systems, is of key importance for the fundamental understanding of fluid flows, to analyse and investigate the velocity field and flow behaviour. In previous experimental studies, flow patterns or mixing characteristics could be observed by means of the aluminium dust method (Nishimura and Matsune, 1998) and direct smoke injection (Rush et al., 1999, Hwang et al., 2006). However, the qualitative appearance of a flow is not necessarily a reliable indicator of its fundamental behaviour.

Local measurements can be made by the old technique of hot wire anemometry, in which the heat transport from a small resistively heated wire (or film) is used to infer the local velocity perpendicular to the wire (Sudo et al., 1998, Sudo et al., 2001). However, the small length-scale of the measurement region in microchannels makes it difficult to use this technique directly without introducing significant experimental errors.

Laser Doppler Anemometry (LDA), also known as Laser Doppler Velocimetry (LDV), is an optical technique ideal for non-intrusive point measurement of velocity and turbulence distribution in both free flows and internal flows. Using LDV, several representative investigations of early studies on macroscale curved ducts were conducted by Chang et al. (1983) and Hille et al. (1985).

Most recently, with the rapid development of modern imaging and optical diagnostic instrumentation, a number of techniques have emerged to provide a more detailed quantitative study. Specifically, Particle Tracking Velocimetry (PTV) and Particle Image Velocimetry (PIV) permit the measurement of the instantaneous velocity distributions across a plane defined by a laser sheet, based on the movement of small tracer particles carried by the flow. Extensive reviews of the PIV technique and applications have been proposed by Lindken et al. (2009) and Williams et al. (2010). In 1998, Santiago et al. (1998) introduced micron-resolution Particle Image Velocimetry (micro-PIV) where an epi-fluorescent microscope with a volume illumination was employed and the velocity field was calculated by cross-correlating the acquired images. Different from the conventional PIV technique, the entire flow field is illuminated by a volume of light (cone of light) and the measurement plane is determined by the focal plane of a microscope objective (Figure 2.8). Thus, the depth-of-field (DOF) of the microscope plays a significant role in micro-PIV. In the last 10 years this method has become the standard tool for fluid velocity measurements in micro-devices (Bottausci et al., 2004, Kim et al., 2004, Shinohara et al., 2004, Ahmad and Hassan, 2010). Kim (2001) experimentally studied the developing and fully-developed flows in wavy channels, examining the onset position of the transition and the global mixing by the Correlation Based Correction PIV (CBC PIV). The micro-PIV technique was applied to obtain the detailed velocity vector field in serpentine microchannels with mitre bends by Xiong and Chung (2007, 2008). The vortices around the outer and inner walls of the bend were found to change with Reynolds number. The experimental results agreed well with theoretical and numerical predictions.

Although micro-PIV is already a powerful flow analysis tool at present to measure the velocity distributions of microscopic fluid flow both spatially and temporally with high resolution, it is not suitable for investigation of three-dimensional flow field such as internal flows in wavy microchannels. There remain two major critical issues to be solved in micro-PIV method for three-dimensional measurement, improvement of spatial resolution in the vertical direction and acquisition of the out-of-plane velocity component. Recently, emphasis has been on those approaches that provide three-dimensional images of stationary or unsteady flows. A few of today's most widely used methods make it possible to obtain the three velocity components from micro-PIV data, such as confocal micro-PIV (Kinoshita et al., 2007, Oishi et al., 2011), stereoscopic micro-PIV (Bown et al., 2007), defocusing micro-PIV (Willert and Gharib, 1992) and tomographic micro-PIV (Elsinga et al., 2006) methods. However, these techniques are typically based on the reconstruction of particle images, followed by either 3-D cross-correlation or particle tracking analysis that limits maximum spatial resolution. Furthermore, these techniques are very expensive and require additional or modified hardware not required for traditional PIV (Fouras et al., 2009).

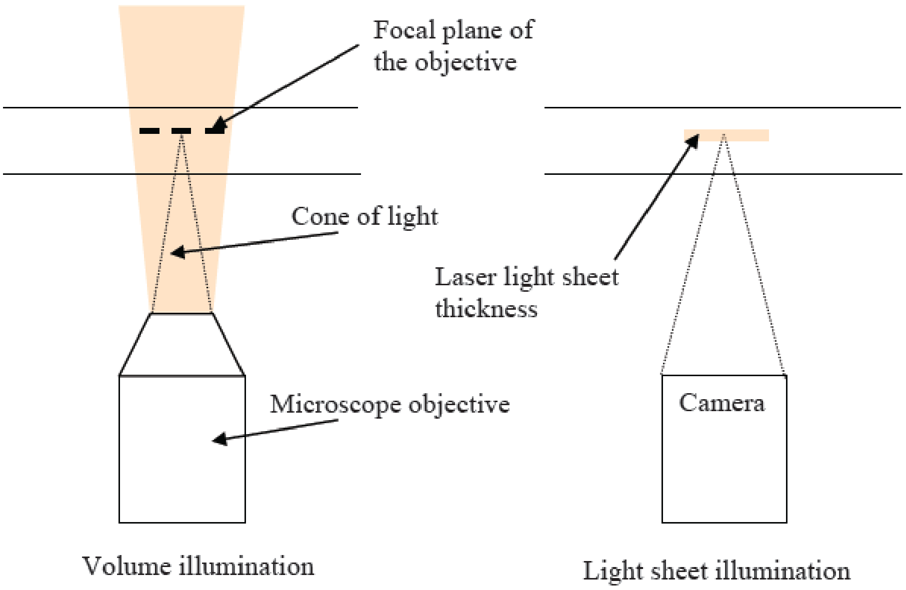

Figure 2.8: Difference between volume illumination and light sheet illumination. Taken from Fouilland (2008).

Another method used widely to obtain the three-dimensional flow structure is to acquire 2-D velocity distributions in contiguous planes of the flow field, and then determine the out-of-plane velocity field using the continuity concept. This technique was pioneered at the macroscopic scale by Robinson and Rockwell (1993), who made a critical assessment of this procedure using synthetic flow fields. Bown et al. (2007) compared its performance with that of the stereomicroscopic PIV technique in a micro-device. The results showed that the continuity based data agreed well with an independent computational fluid dynamics solution and had a smaller experimental uncertainty than the stereoscopic technique at a better spatial resolution.

The technique is gaining popularity and has achieved some considerable success recently. Lang and Limberg (1999) used this method successfully to reconstruct the 3-D flow field over a delta wing Elliptic Aerodynamic Configuration (ELAC). Primary and even secondary vortices were detected with the help of this technique, suggesting accurate reconstruction. Using a two-dimensional implementation of digital PIV and this continuity based technique, Sousa (2002) obtained three-dimensional maps of the turbulent flow around a surface-mounted cube, and undertook identification and localization of vortical structures. In Marakkos and Turner's study (2006), the three-dimensional streamline patterns were determined to examine the classical horseshoe vortex system created when boundary layer flow was incident on a circular cylinder mounted on an end-wall.

The micro-PIV system together with 3D reconstruction technique has been a useful and powerful flow measurement technique available for a wide variety of microfluidics research. However, the experimental data for fluid flow in wavy microchannels are very limited. Only a few studies have reported PIV measurements in wavy channels of large scale or only two-dimensional velocity fields in planes parallel to the flow direction (Kim, 2001, Xiong and Chung, 2007, Xiong and Chung, 2008). To the best knowledge of the author, very few attempts have been made to investigate experimentally three-dimensional flow behaviour, such as Dean vortices in the cross-section of wavy microchannels.

2.3.2 Temperature measurements

While progress has been made with regard to velocity field measurement techniques (e.g. micro-PIV), the scalar field of temperature has received less attention. Commonly used temperature measurement techniques often prove inadequate for microscale applications. Thermocouples or resistance temperature detectors (RTDs) are usually applied to microscale flows by mounting the sensors onto the microchannel base or surface. Infrared (IR) thermography can be used for surface temperature measurements in microchannel heat sinks and micro-evaporators (Hetsroni et al., 2011). However, IR thermometers lack good spatial resolution and their precision depends on the properties of the subject studied. Also IR radiation does not penetrate glass walls and thus cannot be used for thermometry in combination with microscopes or in most microfluidic devices.

Until recently, most temperature measurements in microfluidic systems were limited to measurements of bulk fluid temperature at the inlet and outlet of microfluidic sections or measurements of the substrate temperature. The direct local measurements of the bulk temperature of the fluid in microchannels and the direct measurements of temperature at the interface between fluid and solid are very difficult to implement using conventional methods. In addition to being intrusive, these probes can suffer from poor spatial and temporal resolution, since most probes have a characteristic size comparable with that of the microchannels under consideration.

Generally, the researchers involved in the experimental estimation of convective heat transfer coefficients apply a heat conduction model to estimate the inner wall temperature. The local temperature difference between the wall and the fluid is then calculated, either by choosing a linear variation for the bulk temperature of the fluid in the axial (flow) direction (Tso and Mahulikar, 2000, Lelea et al., 2004), or by choosing the logarithmic mean temperature difference considering an extrapolation of the parallel flow heat exchanger model (Peng and Peterson, 1996). Another assumption consists of considering this bulk temperature to be constant and equal to the inlet bulk temperature (Wang and Peng, 1994). However, these assumptions may not be valid for mini-/micro-channels, especially for complex geometries, when the axial bulk temperature profile of the fluid is not linear. Therefore, most researchers deal with the flow and average heat transfer characteristics of wavy channels, but not with the local heat transfer characteristics.

A non-intrusive temperature measurement technique developed in the past uses thermo-sensitive liquid-crystals (TLC). It was commonly used to visualize temperature qualitatively due to the unique optical properties of the crystals which are dependent on temperature. When TLC is illuminated, it selectively reflects light at a visible wavelength characterized by the local temperature. This relationship of colour to temperature has allowed researchers to quantitatively map temperature distributions (Pehl et al., 2000, Fujisawa et al., 2008). The major shortcoming in using TLC is that the calibration process is quite tedious as it has to be done at each point of the test field and repeated at each different test section in order to compensate for the influence of the illuminating light variations and location differences. Furthermore, the accuracy relative to the temperature range is not high, e.g. an error of 0.6 °C for 6 °C temperature range was reported in Sillekens et al. (1998).

Another non-intrusive and instantaneous technique, Laser Induced Fluorescent (LIF), was introduced to measure whole-field scalar properties (species concentration, temperature or pH) of fluids. It has been used successfully to measure the fluid temperature when a temperature sensitive fluorescent dye is excited by laser light. A great advantage of LIF over TLC is the better accuracy relative to the temperature range which is typically 1.5 °C for a 40 °C temperature range (Sakakibara et al., 1997).

The use of LIF as a temperature tool, started with the single-dye/colour LIF technique (Coppeta and Rogers, 1998, Ross et al., 2001). However, this technique has been shown to have significant errors related to the non-temperature dependent parameters, such as non-uniform illumination, fluctuation of light, non-uniform dye concentration and photo-bleaching. To correct for this problem, a ratiometric technique (two-dye/colour LIF) based on the detection of the fluorescence signal in two distinct spectral bands is used quite extensively to eliminate the effects of the non-uniformity in the illumination (Sakakibara and Adrian, 1999, Lavieille et al., 2001, Funatani et al., 2004, Sutton et al., 2008, Chamarthy et al., 2009, Natrajan and Christensen, 2009, Shafii et al., 2010, Estrada-Perez et al., 2011).

In macroscale environments, an arrangement of spherical and cylindrical lenses was usually used to obtain a laser sheet that illuminates the dye in the region of interest (Coolen et al., 1999, Shafii et al., 2010). However, in a typical microfluidic experiments, the entire volume of the channel is illuminated because of difficulties arising in the thin laser sheet illumination and low fluorescence signal intensity. Similar to micro-PIV, microscale laser induced fluorescence (micro-LIF) was proposed when the LIF technique was used in a volume-illuminated microfluidic system. The method can be used to measure fluid temperatures with micrometer spatial resolution and millisecond time resolution (Ross et al., 2001). The efficacy of the method was demonstrated by Ross et al. (2001) by measuring temperature distributions resulting from Joule heating in a variety of microfluidic circuits that are electrokinetically pumped, as shown in Figure 2.9. The indicator Rhodamine B in an aqueous buffer was used to visualize thermal changes within the microfluidic channels with a precision of 0.03-3.5 °C and a spatial resolution down to 1 μm limited by the optical setup. A solution of Rhodamine B along with a second less temperature sensitive rhodamine derivative (Sulforhodamine 101) were used by Natrajan and co-authors (Natrajan and Christensen, 2009, Natrajan and Christensen, 2010, Natrajan and Christensen, 2011) for referenced two-colour LIF temperature mapping in microfluidic devices. The spatially resolved fluid temperature fields in microchannels were reported with uncertainties of up to 0.5 °C.

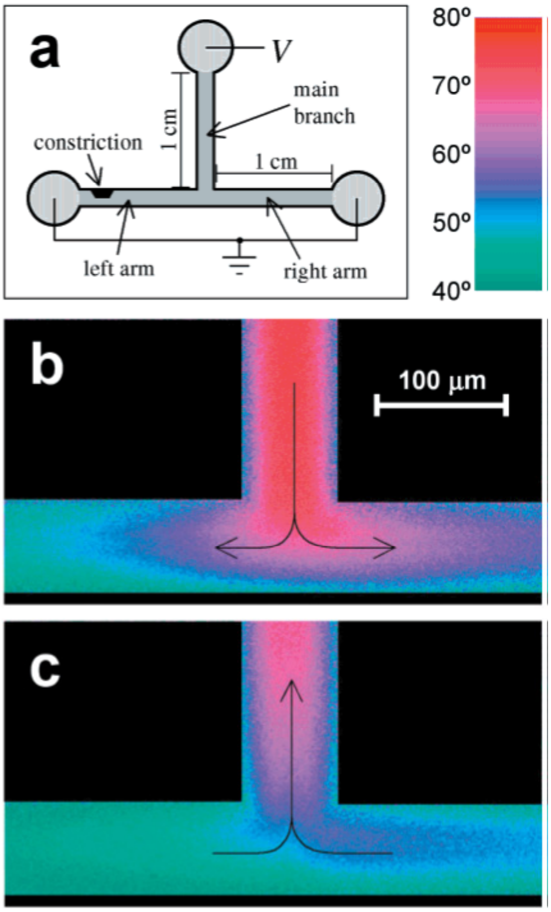

Figure 2.9: Thermal pseudo-color-images of Joule heating of electrokinetically pumped buffered solutions in a T-shaped microfluidic system. Taken from Ross et al. (2001).

Based on the temperature measurement techniques, many experimental studies on heat transfer characteristics of a straight channel have been conducted. For example, Natrajan and co-authors (2010, 2011) applied a microscale adaptation of two-dye LIF thermometry to investigate the spatially resolved fluid temperature fields under constant heat flux conditions at three of the four microchannel walls. The thermal-transport characteristics of both laminar and transitional flow were investigated. An unbiased comparison of measured Nusselt number to macroscale correlations could be made using this non-intrusive methodology. Bogild et al. (2012) used planar laser induced fluorescence to determine the temperature gradient at the wall of mini-channels, which was used to determine the convective heat transfer coefficient. The experiment data showed good agreement with the conventional correlation. However, the applicability of LIF over the whole geometry is not found to be satisfactory, as optical disturbances were found.

Notwithstanding the capabilities of LIF, we have to keep in mind that this fluorescence technique has a limitation on depth resolution. In the conventional micro-LIF system, an epi-fluorescent microscope illuminates the entire flow field, that is, both in- and out-of-focus fluorescence is captured by the camera, and, thus, is linked to the depth-averaged scalar field (Matsumoto et al., 2005, Barz et al., 2008). The out-of-focus fluorescence causes a thick depth-of-field, so that it is difficult to measure the temperature gradient in the depth-wise direction. Consequently, for devices such as tortuous microchannels where three-dimensional flows develop, the conventional micro-LIF technique may have inherent limitations and excessive measurement errors.

Due to the limitation in depth-wise resolution using a conventional microscope, a confocal microscope with the ability to capture only the in-focus fluorescent image was developed by many researchers (Ismagilov et al., 2000, Park et al., 2004, Ichiyanagi et al., 2007, Ichiyanagi et al., 2009, Ichiyanagi, 2012). With the application of micro-LIF with confocal microscopy, Ismagilov et al. (2000) visualized the concentration distribution of the calcium ions produced by a chemical reaction at the interface between two aqueous solutions in a Y-shaped microchannel. Ichiyanagi et al. have applied this technique to measurement of pH distribution (Ichiyanagi et al., 2007) and dissolved CO_2 concentration distribution in a liquid flow field (Ichiyanagi, 2012). Another way to improve the depth-wise resolution is the particle-based LIF, which is discussed in detail in Chapter 8.

2.3.3 Simultaneous study of fluid flow and heat transfer characteristics

In previous studies, velocity and temperature were usually measured separately through different techniques. The relationship between the flow development and heat transfer performance is hardly ever discussed. In order to study the heat and mass transfer in tortuous microchannels, the simultaneous measurement of temperature and velocity plays an important role in determining the physical properties in the transport phenomenon and understanding the mechanisms of heat transfer enhancement.

The TLC method is one of the most used methods for the simultaneous study of thermal flow fields (Dabiri and Gharib, 1991, Ozawa et al., 1992, Park et al., 2001). The movement of a liquid crystal tracer pattern during a constant time interval gives a velocity vector and its colour indicates a temperature. Using the same technique, the 2-D temperature measurement was extended to a 3-D temperature field by rotating the test section (Kimura, 1998) or by using the scanning light sheet technique described by Fujisawa and Funatani (2000). Due to the limited colour characteristics of the liquid crystals, this technique was only applied to study fluid flows with a relatively small temperature range.

Taking the advantage of the LIF technique which can measure a relatively large temperature range, simultaneous measurement of temperature and velocity has been actively carried out by LIF in combination with LDV or PIV in recent years. Lemoine and co-workers (Lemoine et al., 1999, Lavieille et al., 2000, Lavieille et al., 2001) performed simultaneous measurements of passive scalars (temperature and concentration) and velocity of turbulent transport, by means of combined LDV/LIF and PIV/LIF. Using scanning PIV measurement combined with LIF, Syuto (2010) successfully obtained the 3-D structure in the near-field of buoyant jet. A micro-PIV and micro-LIF technique system has been setup by Kim (2005) to accomplish the comprehensive measurements of velocity and temperature fields for buoyancy driven flow in a heated channel. The experimental measurements showed fairly good agreement when compared with numerical results. Asthana et al. (2011) used the same technique to study convective heat transfer in microchannels with segmented liquid-liquid flows. Grafsronningen and Jensen (2012) carried out experimental investigation of the simultaneous temperature and velocity fields above an evenly heated horizontal cylinder. Ensemble averaged two-dimensional velocity and temperature fields, velocity fluctuations, temperature variance and velocity-temperature correlations were obtained from simultaneous LIF and PIV. In addition, the simultaneous measurement was also used in studies of chemical reaction, convection and diffusion with the LIF signal representing concentration (Barz et al., 2008, Ichiyanagi, 2012) and pH (Ichiyanagi et al., 2007). For example, Barz et al. (2008) investigated the pressure-driven flow within the twice-folded microchannel by employing the micro-LIF and micro-PIV, which allows access of both height-averaged concentration fields and 3-D profiles of the axial velocity. The secondary flows were identified through the concentration variations and evolution of the contact interface between the seeded and the unseeded liquid through the microchannel. They suggested that the potential of these methods appears to be comparable with confocal fluorescence microscopy, but is achieved at much lower costs.

Fujisawa and co-authors (Fujisawa et al., 2008) made great strides on simultaneous measurements using combined TLC/PIV system and combined LIF/PIV system. They indicated that the former method is capable of measuring the thermal flow over a relatively small temperature range with a low cost, and the later method is applicable to that of relatively large temperature range with reasonable accuracy. They (Funatani et al., 2004) also demonstrated the use of two-colour LIF together with PIV technique to study the turbulent buoyant plume for the first time using a colour camera. The statistical results based on the this measurement technique approached those reported in the literature (Sakakibara and Adrian, 1999).

In the combined LIF/PIV applications, fluorescent dye solutions were usually used for temperature measurement while additional PIV particles were added for velocity measurement (Funatani et al., 2004, Kim, 2005, Asthana et al., 2011, Grafsronningen and Jensen, 2012). The system separates the signals spectrally and samples them simultaneously: the PIV camera detects particle displacement and the LIF camera detects the fluorescence levels. The limitation of this technique is that the particles would deteriorate the accuracy of temperature measurement by influencing the fluorescence intensity used for temperature calculation if they cannot be filtered out from the LIF images. While the seeding density of the particles was increased to improve resolution and accuracy for velocity measurement, a decrease of accuracy for the temperature measurement was observed (Funatani et al., 2004). Furthermore, in some cases of LIF and PIV combined measurement techniques, these strategies have necessitated the use of separate light source and several cameras, especially in order to combine two-colour LIF and PIV techniques. In addition, as mentioned before, the temperature measurement will be limited to depth-averaged values when the entire flow field is illuminated.

To overcome the problem associated with volume illumination, simultaneous measurement can be achieved by using particles which act as both temperature indicators and PIV tracers. Very recently Someya et al. (Someya et al., 2009, Someya et al., 2010, Someya et al., 2011) successfully obtained the velocity field and temperature distribution in a fluid flow simultaneously based on luminescent particles doped with europium complex (EuTTA). The temperature field was measured based on the temperature-dependent decay time of the particles, and the velocity distribution was evaluated from the same images by PIV. Different from the intensity-based LIF, the luminescence lifetime approach eliminates many of the problems associated with the intensity-based approach, such as intensity fluctuation of the light source. This method shows great potential for accurate high-resolution measurements, but also requires highly sophisticated equipment, such as high speed camera with a frame rate of 15 kHz. Furthermore, the lifetime of the luminophor should be long enough to enable detection by a high-speed camera without an image intensifier which suffers from an intrinsic delay time of its own.

Vogt and Stephan (2012) demonstrated a further particle-based technique using microencapsulated fluorescent dyes for high-resolution temperature and velocity measurements. They demonstrate two different setups with laser light sheet illumination and volume illumination, respectively. Very high seeding density with a low magnification was used in the setup with laser light sheet illumination, and the particles cannot be detected separately. The temporal and spatial resolution was therefore traded off against measurement accuracy through temporal and spatial averaging. Using the microscope setup with volume illumination, they studied the flow inside a small capillary tube and achieved a resolution of 8 × 8 μm^2. The applicability in this case was limited to stationary fluids due to the low particle seeding density and temporal averaging.

Recently, interest has peaked in the use of semiconductor nanocrystals or quantum dot (QDs) for both velocity and temperature measurements. QDs are single fluorophores, with fluorescence lifetimes similar to conventional fluorophores, but with significantly higher quantum efficiency, resistance to photobleaching and, of capital importance, size-tunable absorption and emission colours. In general, the luminescence intensity of QDs decreases with an increase in temperature, and this is accompanied by a widening and a red shift of the emission spectra. Several authors have measured the temperature sensitivity of QDs emission close to ambient conditions. Walker et al. (2003) reported a temperature sensitivity of –1.3%/K between 278 and 313 K for (CdSe)ZnS core-shell QDs embedded into poly(lauryl methacrylate) (PLMA) matrix, and Liu (2006) measured a similar temperature sensitivity of –1.1%/K between 280 and 350 K for bulk emission water-soluble CdSe/ZnS core-shell QDs in a phosphate buffered saline solution for use as a bio-probe.

Local temperature measurements were therefore proposed by virtue of their small sizes, and favourable photostability based on changes in the fluorescence intensity (Guasto and Breuer, 2008) and/or peak position (Li et al., 2007). Li et al. (2007) evaluated temperature profiles of a microheater under different input voltages based on the spectral shift of QDs on the heater. A spatial resolution of 230 nm was reported which was limited by the optical setup, while the theoretical resolution of this technique could go down to the size of a single quantum dot using far-field optics. As well as using individual QDs, composite particles or hydrogels doped with QDs were also investigated by many authors, such as Generalova et al. (2013) and Hardison et al. (2008).

Some researchers demonstrated the use of single quantum dots (QDs) as simultaneous temperature and velocity probes at the microscale. Guasto and Breuer (2008) used ensemble-average of single QDs to achieve simultaneous temperature and velocity measurements in the very near-wall region (within 200 nm) of microchannels. A two-colour, time-averaged temperature sensing technique based on the ensemble intensity changes of single QDs as compared with that of a reference dye (Rhodamine 110) was presented. However, the nanometer sized single QDs have a low signal-to-noise-ratio due to their high diffusivity and low emission intensity, as result of which intensified CCD cameras are needed. High intensifier gain produces significant noisy artefacts due to effects like blooming and cross-talk (Guasto et al., 2006), which can appear similar in shape, size and intensity profile to real tracer particles. This leads to false particle images and errors in the velocity measurements. QDs are currently mainly used in nano-scale measurements or near-surface velocimetry (Pouya et al., 2005, Guasto et al., 2006, Guasto and Breuer, 2008).

Despite the progress in the experimental techniques, direct measurements of the local temperature and velocity of the 3-D flows in wavy microchannels and the resulting local heat transfer performance are not reported in the literature to date.

2.4 Summary

Through this review of the existing literature on single-phase flows in tortuous microchannels, it can be concluded that there are a number of areas where it is necessary to carry out future work. Several knowledge gaps for the study of thermohydraulic characteristics in tortuous passages are identified below:

1. While the thermohydraulic behaviour in tortuous microchannels at low Reynolds numbers has been well understood by CFD simulations, to date few experimental data can be found due to technical difficulties in detailed velocity and temperature measurements in microscale devices. Due to the limitations of CFD models, the behaviours of the flow field and heat transfer in unsteady flow at higher Reynolds number have not been completely clarified.

2. The effects of various geometrical parameters on the flow and heat transfer of planar-based geometries have been investigated in computational studies and a few preliminarily experimental studies. Systematic experimental data to show the importance

of geometrical effects on flow and heat transfer characteristics are required for heat exchanger designs and operations.

3. The heat transfer enhancement brought about by tortuous geometries is reported and the mechanisms of this enhancement are proposed based on various special flow behaviours. It would be worthwhile to identify the fundamental mechanisms and effects of various parameters on heat transfer, especially when the flow becomes chaotic or transient.

4. The difficulty in measuring three-dimensional velocity and temperature fields in microchannels is noteworthy. The currently available experimental data are limited to averaged heat transfer coefficients and two-dimensional flow patterns; they do not unequivocally identify the fundamental mechanism of heat transfer. For the experimental validation of flow dynamics and heat transfer performance in wavy microchannels, novel experimental approaches, especially simultaneous measurement of velocity and temperature fields in microchannels are urgently needed.

In this thesis, the flow characteristics and heat transfer in planar-based tortuous passages are studied experimentally together with technique development. In the next chapter the experimental methodology and apparatus used in this study are described in detail.

Chapter 3

Experimental Apparatus and Method Validation

As discussed in the previous chapter, there are very few experimental data available for wavy microchannels, due to technical difficulties. The development of experimental methods is required to understand the fluid dynamics and heat transfer characteristics in tortuous channels and to validate numerical models. In this chapter, the experimental apparatus and procedures used for studies of the flow pattern, pressure drop and heat transfer in tortuous microchannels are presented. Test sections which allow simultaneous study of flow visualisation and heat transfer measurements are first designed and manufactured. Whole-field velocity measurements in a three-dimensional domain are achieved by flow visualisation and image processing, bringing new insights to the understanding of the thermohydraulics of wavy passages. Pressure drop and heat transfer measurements along with data reduction procedures are also presented.

3.1 Test section design and manufacture

3.1.1 Choice of channel geometry

Wavy channels with different cross-sections and pathways have been applied in industrial devices for enhancing heat and mass transfer efficiency because of their ability to promote vortex formation and turbulence. The channels used in Heatric Printed Circuit Heat Exchangers (PCHEs) are approximately semi-circular in cross-section with typical diameters ranging from 0.5 to 2 mm. These small channels have the benefit of creating a large heat transfer area for a given heat exchanger volume. The PCHE channels have flow paths that follow a herringbone, or zigzag pattern (Johnston and Haynes, 2002, Tsuzuki et al., 2007). Secondary flows (Dean vortices) due to the recirculation in the cross-section are generated in the these tortuous channels, which is of critical importance and can act as a means to process intensification. Many studies have found that considerable heat transfer enhancement has been achieved for a relatively small increase in pressure drop, in comparison with flows in straight channels. However, no systematic experimental study has been reported on how these types of geometries induce changes to the flow field and promote heat transfer. To further understand the underlying mechanisms controlling heat transfer, detailed thermohydraulic characteristics of wavy channels were studied experimentally in the present work.

Wavy channels with semi-circular cross-section were designed to study the geometric effect on flow and heat transfer characteristics. The main interest of this study is to examine flow in channel geometries of relevance to typical compact heat exchangers. While the serpentine passage represents an interesting model flow path, it is not ideal for application in plate structures because the passages cannot be placed close together, that is they have poor stackability or packing density (Geyer et al., 2007). Sinusoidal and zigzag channels were selected in this study with consideration of stackability to make good use of the available plate area. These kinds of channel have not been studied, whereas a number of studies have been carried out on parallel-plate channels with corrugated walls (Rush et al., 1999, Islamoglu and Parmaksizoglu, 2003, Metwally and Manglik, 2004, Zhang et al., 2004, Mohammed et al., 2011).

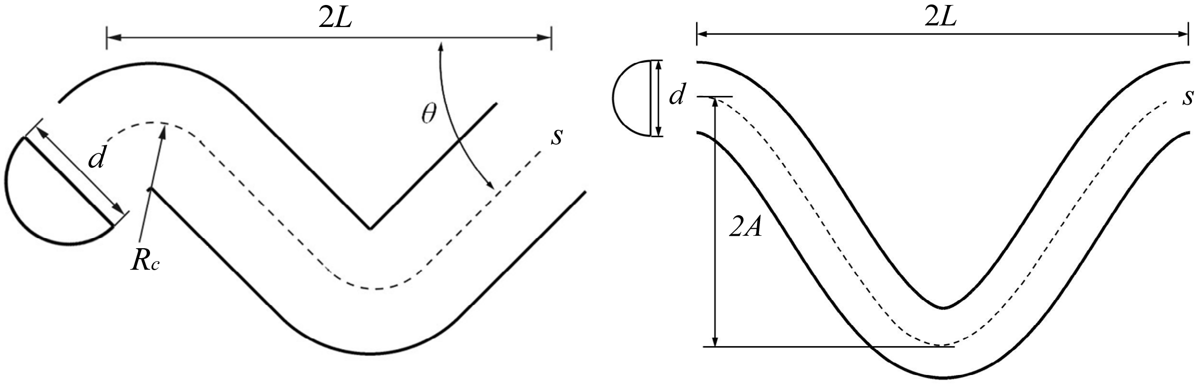

(a) **(b)**

Figure 3.1: Schematic of a repeating unit of a: **(a)** zigzag channel; and **(b)** sinusoidal channel.

The geometry of a zigzag channel is characterised by the half-unit length, L; the diameter of the semi-circular cross-section, d; the radius of curvature of the bends, R_c; and the channel bend angle, θ. Similarly, a sinusoidal channel is characterised by L, d and the amplitude, A, as can be seen in Figure 3.1. Five wavy channels with different geometries were used in this study and their dimensions are listed in Table 3.1. All the microchannels have a diameter of 2 mm and were cut on plates with a size of 140 mm × 17 mm. This was the maximum plate size that could be used due to manufacturing restrictions, i.e. size limitation of the anodic bonder plate. The overall path length, L_p, was calculated for each channel. Figure 3.2 shows the photograph of the test sections with different channel patterns. A straight channel was also selected as a base channel for comparison and technique validation.

Table 3.1: Geometrical parameters of wavy microchannels.

Channel	**Diameter d (mm)**	**half-unit length L (mm)**	**Bend curvature R_c (mm)**	**Bend angle θ (°) or Amplitude A (mm)**	**Overall path length L_p (mm)**
Straight	2	-	-	-	124.0
Zigzag 1	2	3.5	1.02	45°	156.3
Zigzag 2	2	6.06	1.02	30°	136.0
Sine 1	2	3.5	-	1.75	173.6
Sine 2	2	6.06	-	1.75	143.9
Sine 3	2	7	-	3.5	163.2

Figure 3.2: Photograph of test sections with different channel patterns. The size of the plates is 140 mm × 17 mm (length × width).

3.1.2 Test section manufacture

Flow visualisation and heat transfer measurements are required to understand the thermohydraulic characteristics of wavy channels. Therefore, the design of the test section has to be suitable to carry out experimental work for both purposes, that is, it has to provide a heating source to the fluid while maintaining good visual access to the flow.

In the previous literature, flow observation and heat transfer measurements were usually carried out in two different test sections separately, by viewing the flow in a transparent part and taking heat transfer measurement in a metallic part downstream or upstream of the visualisation section (Huo et al., 2004, Revellin et al., 2006). Apart from missing the ability to connect the flow behaviour and heat transfer performance directly, they also encountered optical distortion caused by the combined effect of the channel curvature and the refractive index mismatch between the test fluid and the channel wall. With the development in material and manufacture fields, some researchers have recently succeeded in investigating the flow structure and heat transfer rate simultaneously by using test sections coated with Transparent Conductive Oxide (TCO) (Owhaib et al., 2006, Yen et al., 2006) or channels made of sapphire (Fouilland, 2008), due to their combined transparency and high thermal conductivity. However, an issue associated with the TCO coating method is the compromise between transparency and heating power.

Another means of channel manufacture, the so called “hybrid channel”, has been used widely in microfluidic devices, such as silicon integrated circuits, drug delivery, micro-reactors and micro-mixers. These “hybrid” channels are generally made by bonding two different materials (typically a transparent one like glass and a machinable one like silicon) (Tuckerman and Pease, 1981, Natrajan and Christensen, 2010). The test sections are heated from their bottom surface and have a transparent cover for visualisation purposes. Therefore, in this study, “hybrid channels” were used to achieve simultaneous study of flow visualisation and heat transfer measurements.

3.1.2.1 **Anodic bonding principle**

Anodic bonding is a commonly used technique to bond two dissimilar materials (mainly metal/semiconductor and sodium-rich glass) electrostatically, involving little alteration in the shape, size and dimensions of the materials. The basic mechanisms of anodic bonding were set out in the early work of Wallis and Pomerantz (1969) with little change since then. The materials are typically heated to a temperature in the range of 300-500 °C, so that the cations (mainly Na^+) become mobile and allow the glass to behave as an electrolyte. Once the materials are at the bonding temperature, a voltage typically between 200 and 2,000 V is applied over the stack of the two materials, with the glass attached to the cathode and the metal/semiconductor to the anode. The applied potential drives the migration of mobilized sodium ions from local points of contact at the interface to the negatively charged cathode, leaving less mobile negatively charged oxygen ions in this sodium depletion region. The space charging of the depletion layer then generates a large interfacial electric field and the resulting electrostatic forces pull the two surfaces into intimate contact for the formation of permanent bond. The bond formed is irreversible in nature as a permanent chemical bond is formed at the glass/metal interface involving an intermediary metal oxide interface layer, approximately 10-20 nm thick (Rogers and Kowal, 1995, van Helvoort et al., 2004).

3.1.2.2 **Substrate materials**

In glass-to-metal anodic bonding, it is important to ensure the coefficients of thermal expansion (CTE) of both components are similar at least in the range of the glass set point and room temperature. This is because a large difference in the CTE between the materials will cause unacceptable levels of stress during the sample's cooling process and these stresses can induce premature failure of the bonding.

A metallic material of Kovar, which is a nickel-cobalt ferrous alloy, was selected as its coefficient of thermal expansion is close to that of borosilicate glasses. It consists of 29% Ni, 17% Co with the balance being Fe with a CTE = $5 \times 10^{-6}\ K^{-1}$ between 25 and 400 °C. Pyrex Corning 7056 is a borosilicate glass widely used as a Kovar sealing glass. It has a CTE of $5.1 \times 10^{-6}\ K^{-1}$ between 25 and 350 °C.

3.1.2.3 **Manufacture details**

An anodic bonding rig purchased from Applied Microenginneering Ltd (AML) was used to perform anodic bonding. This bonder is capable of providing 300-2,500 V with a maximum 40 mA current flow, 20-400 °C, 0-3,000 N clamping force, and high vacuum ($< 1 \times 10^{-5}$ mbar) conditions for anodic bonding. Process conditions including temperature, voltage and sealing time have been found to have important effects on the strength of formed bonds. Generally, a higher temperature and/or voltage results in a greater bond strength (Knowles and van Helvoort, 2006). A higher voltage can reduce the bonding time at a particular bonding temperature while the voltage necessary to complete the bonding process at constant time decreases with increasing temperature (Sim et al., 1996, Briand et al., 2004). The upper voltage limit for anodic bonding is suggested to be 2,000 V due to the need to inhibit sparking. The operating conditions used in this study to achieve good bonding between Kovar and Pyrex plates are listed in Table 3.2.

Of all the process variables, surface flatness, surface smoothness and the matching of the CTEs are the most critical parameters to determine whether anodic bonding can be performed successfully. When the surface is not smooth or flat, the two materials will not be in intimate contact over the whole interface. Newton interference rings and fringes will be visible through the Pyrex glass, highlighting the presence of an air gap between the materials to be bonded across the surface of contact. The electrostatic force that is needed to pull the two surfaces into intimate contact is dependent on the inverse square of the distance across the air gap (Wallis and Pomerant, 1969). When the electrostatic force is larger than the mechanical rigidity of the structure (the necessary force to bring the two surfaces into contact), the structure will bond. However, if the electrostatic force is lower, the structure will not bond. High values of surface roughness will prevent full scale hermetic sealing. Hence, lapping and polishing were employed to smooth the surface in advance of the bonding process.

Table 3.2: Conditions for anodic bonding process.

Materials	Temperature (°C)	Applied voltage (V)	Clamping force (N)	Bonding time (min)
Kovar Pyrex 7056	350	1,900	2,000	30

Due to the limited size of the bonder plate, the Kovar plate was cut into strips with a size of 140 mm × 17 mm × 3 mm (length × width × thickness). The Kovar strips were cut, lapped and highly polished by Kemet Australia Pty Ltd before anodic bonding. The surface flatness of the samples was then measured by an optical flat with a monochromatic light and the surface roughness was measured by a profilometer. Very flat and smooth surfaces suitable for anodic bonding were obtained, with the variation in flatness between 0.885 and 2.065 μm and the surface roughness, *Ra*, (the arithmetic mean roughness which represents the average of all peaks and valleys) between 0.02 and 0.15 μm. The channel was then ground into the Kovar plate by a diamond cutter on a CNC machine by Heller Enterprises Pty Ltd. The speed of the grinding wheel and the grit size were adjusted to get an optimum surface finish based on the material, so that channel surface was smooth and free of irregularities that could adversely affect the flow behaviour of the liquids. Holes were drilled at the inlet and outlet on the Kovar plate. Finally, a fine polishing was carried out to remove any surface scratches induced by grooving and drilling. The Kovar strips and glass substrates were ultrasonically cleaned in acetone for 1-2 hours. The glass plate with size of 140 mm × 15 mm × 2 mm (length × width × thickness) was then anodically bonded to the metal in order to seal the channel whilst still allowing optical access to the interior of the microchannel. The inlet and outlet holes on the plate were connected by two NanoPort assemblies (N-333, IDEX® Health & Science). Figure 3.3 shows the photograph of test sections with straight and zigzag microchannels. This channel configuration is of a form similar to that used in typical PCHEs. Furthermore, the flat optical surface does not cause any optical distortion during observation.

The bonding strength was tested by immersing the test section in a food dye solution at a nitrogen pressure of 2 bars. The sealing gap could be visualized by observing the dye penetration into the interface of Kovar and glass. Good bonding was achieved without detection of the dye in the interface.

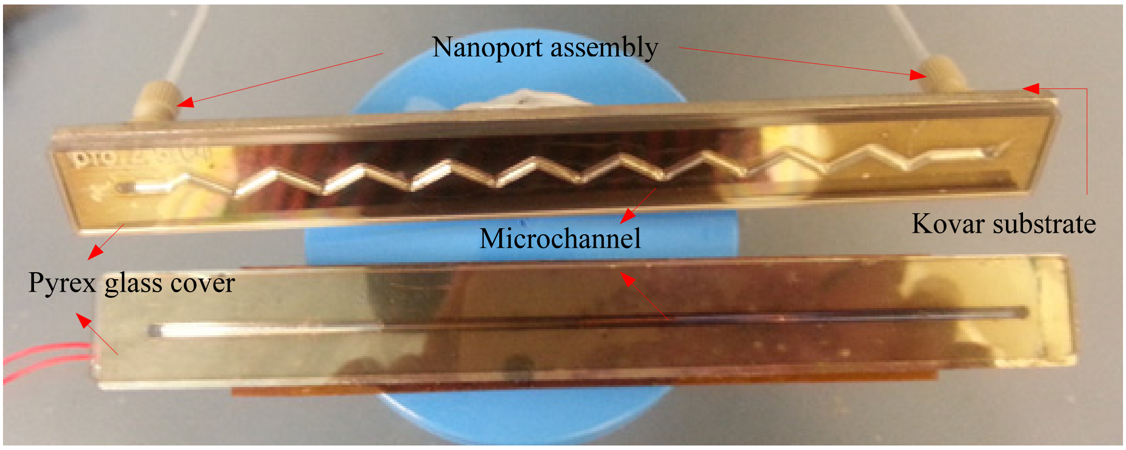

Figure 3.3: Photograph of test sections with straight and zigzag channels.

3.1.2.4 **Channel quality check**

The fabrication of channels is extremely important in microscale thermal fluid experiments. There are many machining processes that can be used to create mini or microchannels. These processes include micromechanical machining, X-ray micromachining, chemical etching, rapid prototyping, and surface proximity micromachining. However, controlling surface roughness still represents a significant challenge because most methods of fabrication leave behind surface irregularities that could potentially impact both the flow and heat transfer behaviour of a microscale device. To check the quality of CNC grooving, the surface roughness of each channel wall was measured before anodic bonding, through a 3D laser measuring microscope (LEXT OLS4000) at the Australian Centre for Microscopy & Microanalysis (ACMM). The surface roughness, *Ra*, was typically less than 5 μm so that the wall roughness effect can be neglected. However, the channel depth is beyond the working distance of the 3D laser measuring microscope, and the refractive metal surface made it difficult to get a whole profile of the cross-section. In order to solve this problem, the channel was replicated by making a PDMS mould using the Sylgard 184 Silicone Elastomer Kit (Dow Corning). The mould was then cut into thin segments across the channel so that the cross-section of the channel could be visualized under a back-lit illumination. Figure 3.4 shows an image of a segment of the channel mould for a sinusoidal channel under the microscope. The channel profiles were checked at different locations from the inlet ($L_1 = 25$ mm, $L_2 = 70$ mm, $L_3 = 100$ mm) and calibrated from the microscope images. As can be seen, compared with the semi-circular profile with radius of 1 mm, the channel has very uniform profiles along the whole length.

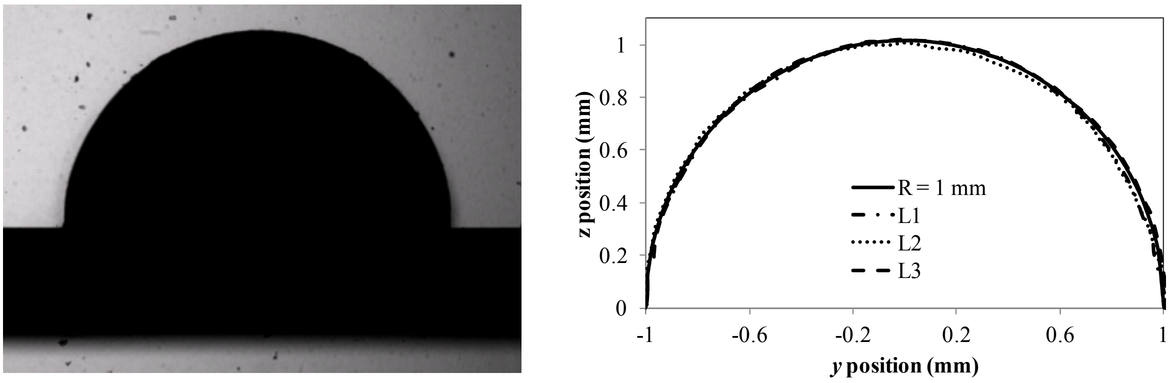

(a) **(b)**

Figure 3.4: **(a)** A microscope image of a channel mould segment; and **(b)** channel profiles at different axial locations.

3.2 Flow loop

The flow loop used for both flow visualisation and heat transfer measurements is shown in Figure 3.5. Degassed and deionised water seeded with fluorescent particles was delivered from a liquid tank into the test section using a variable-speed progressing cavity pump

(Seepex MD 0005-24). A heat exchanger together with a chiller (MRC300DH2-DV, Laird Technologies) was inserted after the outlet of the pump in order to maintain a stable inlet fluid temperature. A differential pressure transmitter (UNIK 5000, 250 mbar) with accuracy of ±0.04% full scale was mounted across the test section to measure the pressure drop. The pressure data were recorded using a data-logger (USB-1608FS) which allows a measurement frequency up to 10,000 Hz. The liquid flow rate was monitored by weighing the liquid discharged to a container with an electronic balance (A&D HP320) over a pre-set period of time. The experimental apparatus used to visualize the flow and measure the heat transfer rate will be described in details in the following sections.

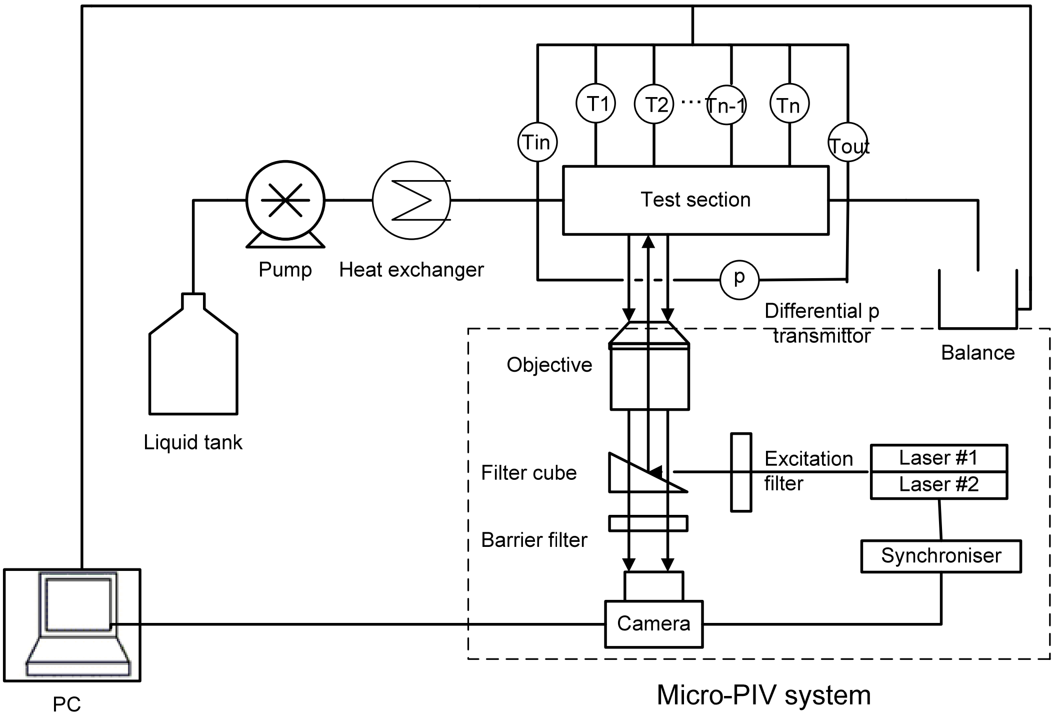

Figure 3.5: Schematic of the experimental setup.

3.3 Micro-PIV system

3.3.1 Micro-PIV configuration

A high-speed micro-Particle Image Velocimetry (micro-PIV) system was used to measure the whole-field of velocity distribution. As shown in Figure 3.5, a double pulse high power high speed laser (Darwin-Duo, Quantronix) with a wavelength of 527 nm was used as the light source. The light was directed through an epi-fluorescent microscope (Olympus IX71) after being reflected by a dichroic mirror (540DRLP, Omega optical) to illuminate the test section with fluorescence particles (7 μm, Ex/Em = 542/612 nm, Duke Scientific). The fluorescence emission was then collected by the objective and transmitted through the dichroic mirror followed by a long-pass filter (540LP, Omega optical) that removes all remaining incident light. The imaging was performed with a high-speed CMOS camera (1024 PCI, Photron) which is capable of taking up to 1000 frames per second (fps) at full 1024 × 1024 pixels resolution, and a maximum of 109,500 fps at reduced resolution. A control system composed of a synchroniser (ILA) and a PIV workstation was used to synchronise the camera with the firing of the laser pulses for high speed measurements, and for image acquisition and PIV post-processing. The image recordings were made under the conditions when the flow became steady and the stable pressure reading were observed. All experiments were carried out at room temperature (around 21 °C) and ambient pressure.

Two objectives (UPLFN 4×, Numerical Aperture (N.A.): 0.13, Working Distance (W.D.): 17.0 mm, Field Number (F.N.): 26.5 and UPLFN 10×, N.A.: 0.30, W.D.: 10.0 mm, F.N.: 26.5) were used in this study depending on the field of view and resolution required. The objective providing 4× magnification was used for most of the micro-PIV measurements as it gives a $4.35 \times 4.35 \text{ mm}^2$ area observation window. The 10× objective provides an area of view of $1.74 \times 1.74 \text{ mm}^2$ at full 1024 × 1024 pixels resolution and was employed to resolve smaller-scale fluctuations.

The frame rate of the camera is always twice the sampling rate, which determines the time resolution (measurement frequency) of the measurement. The camera was synchronized with the high-speed laser pulses and the frame straddling technique was used, which has been well demonstrated in our laboratory (Fouilland, 2008, Liu, 2011). A laser pulse duration of 10 ns was used in all experiments, which froze the motion of the particle sufficiently without making particle streaks. The time between two successive laser pulses was set to between 10 μs to 1000 μs according to the flow rate, so that the particle displacement between the two images was smaller than the size of the interrogation window used for the velocity calculation. The VidPIV software, which is the micro-PIV analysis software from ILA, was used to determine the velocity field. A standard cross-correlation followed by an adaptive cross-correlation method was used to obtain a higher spatial resolution and higher accuracy of the velocity field. Due to the volume illumination which was used in the micro-PIV system, high background noise and out-of-focus particles might contribute significantly in the images leading to erroneous velocities from the PIV analysis. Therefore, the recorded images were pre-processed using the ImageJ software before being imported into VidPIV to improve the image contrast by removing out-of-focus particles with low intensities. Finally, the velocity data could be exported to Excel or Tecplot for further analysis.

The micro-PIV system was modified into a system which combined micro-PIV with Laser Induced Florescence (LIF) which is described in Chapter 7.

3.3.2 Technical considerations regarding the seeding particles

The seeding particles are a critical component of the micro-PIV system (Meinhart et al., 2000). In order to obtain the correct kinematic properties of the flow, the particle size, particle concentration and the particle dynamics should be considered.

3.3.2.1 **Particle size**

A number of considerations must be taken when selecting the size of the particles. Generally, the seeding particles should obviously be small enough to follow the flow faithfully, and as well they should be small enough not to clog the microchannel. On the other hand, the fluorescent particles have to be large enough to emit a sufficient amount of light in order to be detectable for PIV correlation analysis. They also need to be of a sufficient size to minimise the effects of Brownian motion, which is the random thermal motion of particles suspended in a fluid.

3.3.2.2 **Particle response time**

The PIV technique relies on the assumption that tracer particles follow the same motion as the flows. The response time of a spherical particle was examined using a Stokes drag-law analysis as described in Eq. 3.1 (Wereley and Meinhart, 2005).

$$\tau_p = \frac{\rho_p d_p^2}{18\mu_f} \tag{3.1}$$

where d_p and ρ_p are the diameter and density of the particle, respectively and μ_f is the fluid dynamic viscosity. It is obvious from Eq. (3.1) that the particle diameter and density are critical parameters to ensure accurate particle tracing. For example, for 6 μm diameter polystyrene particles immersed in water, the particle response time is approximately 2 μs, which is much smaller than the typical time scales of the flow field used in the present study.

3.3.2.3 Particle density

While particle density is a significant parameter in determination of particle response time, it is also of importance in relation to buoyancy. Most commonly, tracer particles with a density similar to the fluid are added to a fluid flow, which gives neutral buoyancy.

3.3.2.4 Particle concentration

The concentration of seeding particles is a critical aspect in micro-PIV measurements. Due to the application of volume illumination, high background noise in the images is more severe in the micro-PIV technique than in the conventional PIV technique. Therefore, the particle concentration needs to be balanced to provide high spatial resolution and good particle visibility to ensure particle detectability. A lower particle concentration is required to obtain a high signal-to-noise ratio by minimising the background noise (Wereley and Meinhart, 2005), however, it leads to an undesirable poor spatial resolution and high uncertainties for PIV correlation.

3.3.2.5 Pixel locking

One problem that may be encountered during PIV measurements is called pixel locking (or peak locking). Although well known, this effect has not been paid enough attention in many previous studies. Pixel locking is the biasing of particle displacements toward integer pixel values. The magnitude of peak locking can be ascertained by inspecting the velocity histogram. True displacements that exist between integer pixel values are pushed toward the nearest integer pixel displacement, severely degrading the accuracy of the sub-pixel estimate. As can be seen in Figure 3.6, peaks occur at integer pixel displacements and troughs exist in between (Christensen, 2004).

Peak locking is attributable to both the choice of sub-pixel resolution peak-fitting algorithms and under-resolved optical sampling of the particle images. Westerwell (1997) showed that a Gaussian sub-pixel estimator is superior to both centroid and quadratic fits in terms of mitigating pixel locking effects. Roesgen (2003) proposed a “sinc”-kernel (nearest-neighbour interpolation performed with a top hat kernel) to compute a bias-free sub-pixel estimate of the correlation peak. The use of “sinc” interpolation was claimed to suppress the peak locking error in the most efficient manner. When the particle images are under-resolved (particle diameters smaller than 2 pixels), peak locking can be a significant bias error that is independent of the choice of sub-pixel estimator. In such cases, the resulting correlation peak is not adequately resolved and the sub-pixel estimator cannot faithfully determine the sub-pixel displacement of the particles. This effect is more apparent for smaller particles, with lower numbers of particles in the interrogation window and with smaller fill ratios of the sensor (light sensitive area/ sensor area) (Prasad et al., 1992, Nogueira et al., 2001, Roesgen, 2003).

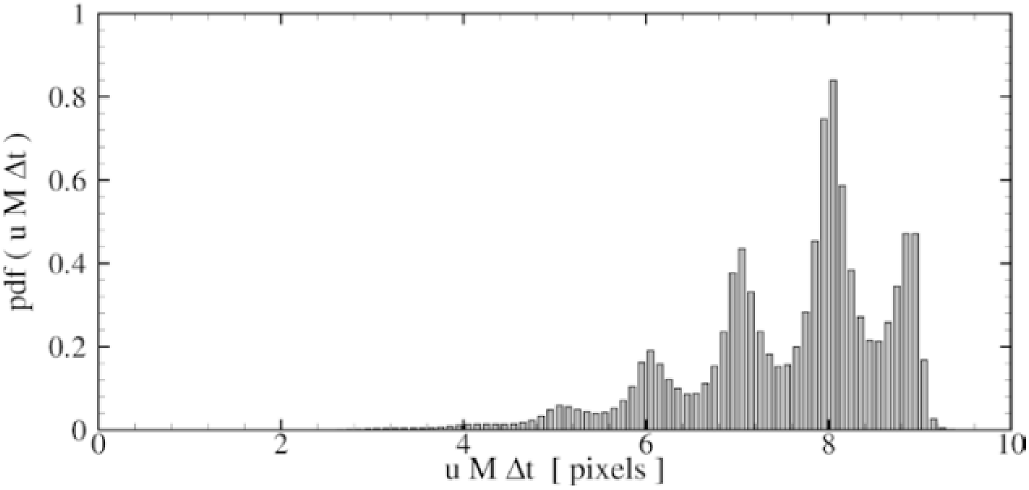

Figure 3.6: Ensemble-averaged probability density function of particle-image displacement illustrating pixel-locking effects (Christensen, 2004).

A variety of solutions has been studied to decrease the effect. Raffel, Willert and Kompenhans (1998) discussed the optimization of particle image diameter. It was found that the optimum particle image diameter to minimize this uncertainty was 2 pixels. In addition, a higher particle density can reduce the measurement uncertainty substantially, which can be explained by the simple fact that more particle image pairs increase the signal strength of the correlation peak. Very high seeding densities, however, can alter the characteristics of the flow being measured and increase the background noise. An alternative is to increase the size of the interrogation window. This increases the number of tracer particles in the interrogation region without increasing the seeding density. However, large interrogation windows perform poorly when there are strong gradients in velocity at the scale of the interrogation window during the time interval. Consequently, there is an upper limit to both the seeding density and the interrogation size used to process PIV data.

3.3.2.6 **Final particle selection**

Based on the above considerations, 7 µm particles with a density of 1.05 g cm^{-3} (Duke Scientific) were used to make sure the particles emitted a sufficient amount of light to be detectable, especially when using the low magnification objective. The camera used in the PIV system has a very large CMOS sensor with 17 µm square pixels. Therefore, the particle size had to be selected carefully to avoid the particles being under-resolved. According to the configurations in the micro-PIV system, 7 µm particles would occupy more than 2 pixels in diameter under 4× objective and 4 pixels under 10× objective. Examination of the velocity histogram confirmed the absence of pixel locking in this study.

A particle concentration of ~0.03% w/v was used to give enough spatial resolution and avoid any clumps in the channel. This concentration also ensured sufficient particles were present within the interrogation window to give a good peak for the PIV correlation.

The particles were tagged with a fluorescent dye that absorbs at a wavelength of 542 nm and emit at a peak of 612 nm. However, the fluorescence particles were found to stick on the glass surface of the test section. Surfactant (Igepal 60) was added into the particle solution to stop the particles from aggregating and being absorbed by the glass. The particle solution was placed in an ultrasonic bath for at least 3 hours before each run to breakup any remaining aggregates and to ensure a good distribution of the particles in the solution.

3.3.3 Whole-volume velocity measurement

3.3.3.1 **Scanning-based visualisation technique**

In micro-PIV, the measurement was taken in the focal plane of the objective where a planar velocity field was obtained. The focusing knob of the microscope was motorised using a stepper motor with each step corresponding to 18.4 nm vertical displacement. Velocity data at different depths (z) could be achieved by moving the focusing plane of the objective.

The planar measurement could be extended to a volume measurement by scanning the focal plane across the whole depth of the channel. Figure 3.7 illustrates the scanning-based technique used for the whole-volume visualisation. A large number of successive images of the flow were recorded at different depths (z) closely spaced by moving the focal plane from the bottom of the channel to the top. PIV analysis was carried out independently for each set of images taken at different depths. Velocity fields in the whole volume of observation could then be reconstructed, by stacking and interpolating the velocity data measured at different measuring planes. As a flat glass cover was used in our test section, a full field view of velocity across the entire cross-section could be achieved without any optical distortion. However, this scanning-based technique is only valid for steady flow as the measurements at different depths were taken at different times. It was used to analyse the time-averaged flow field in this study.

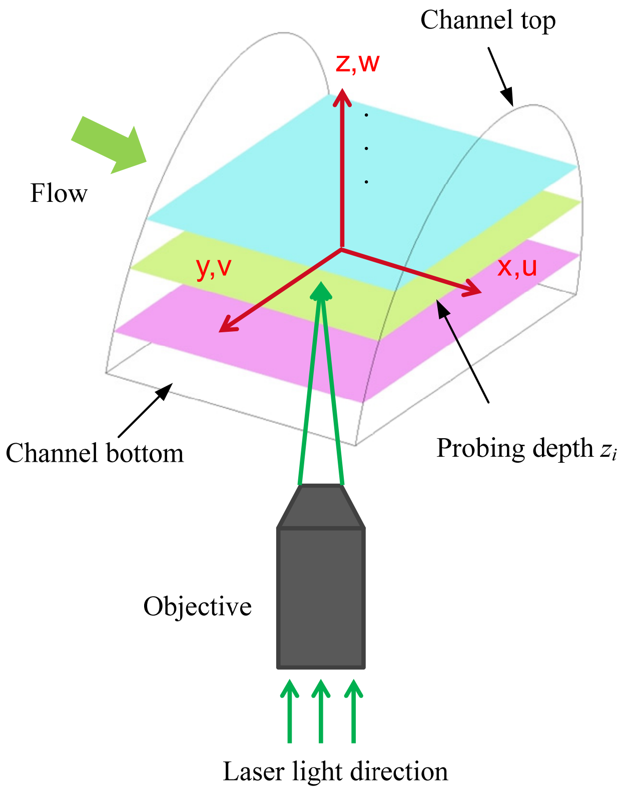

Figure 3.7: Illustration of the scanning-based visualisation technique.

Two in-plane velocity components could be obtained in the three-dimensional space (3D-2C) through the scanning-based technique. In order to get all three components of the velocity in the whole volume, a three-dimensional, three-component (3D-3C) reconstruction technique based on the continuity equation was used, which are described in Chapter 5.

The test section was held horizontally by a customized clamp that was connected to a 3D mechanical stage over the microscope. The test section can be moved precisely with the step down to 10 μm in the x and y directions. For micro-PIV measurements in this study, different locations were examined to visualize the flow development along the wavy channel as well.

3.3.3.2 **Determination of the depth**

The depth of field (DOF) of the microscope plays a significant role in micro-PIV measurement. Meinhart et al. (2000) defined the measurement depth as the out-of-plane measurement resolution of micro-PIV, which depends on the tracer particle diameter and numerical aperture of the objective lens. Only the particles within the measurement depth affect the PIV analysis, whereas the out-of-focus particles do not contribute to the evaluation. Consequently, the obtained velocity data are regarded as a two-dimensional projected planar velocity field in the focal plane.

The total measurement depth δz_m was given by Meinhart et al. (2000), considering the effects of diffraction, geometric optics, and finite particle size:

$$\delta z_m = \frac{3n\lambda_0}{NA^2} + \frac{2.16nd_p}{NA} + d_p \tag{3.2}$$

where n is the refractive index of the fluid between the microfluidic device and the objective lens; λ_0 is the wavelength of light in a vacuum being imaged by the optical system; *NA* is the numerical aperture of the objective and d_p is the particle diameter.

With 7 μm particles used in this study, Eq. (3.2) results in a measurement depth, δz_m, of 232 μm and 78 μm for the 4× and 10× objectives, respectively. The objective with a lower magnification, which usually has a lower numerical aperture, results in a larger depth of field and the velocity calculated from the correlation peak is a weighted average over the depth of focus.

For a semi-circular channel, the channel width becomes smaller as the probing depth goes deeper from the flat surface. Due to the background noise induced by the volume illumination, the channel wall location is relatively difficult to determine as the wall edge in the particle images tend to be blurry. It is important to be able to determine the position of the bottom surface where a few stationary particles stick on the glass surface could be clearly observed. The location of the measurement plane (z) was then determined based on the moving steps (N_s) of the focusing knob of the microscope from the bottom surface, using the following equation:

$$z = 1.33 * 18.4 \times 10^{-3} * N_s \tag{3.3}$$

where 1.33 is the refractive index of water to correct the real position of the particles. The channel width ($2y$) at depth z was then calculated through a semi-circular curve function.

$$y^2 + z^2 = R^2 \tag{3.4}$$

3.3.4 Micro-PIV validation

Based on the configuration and method discussed above, micro-PIV system validation was performed in a straight channel. The fully-developed laminar flow in a straight channel with semi-circular cross-section can be obtained analytically and predicted accurately by CFD simulation. However, analytical solutions are not available for the non-straight passages. Therefore, in this study, CFD simulation using the commercial software package ANSYS CFX 14.5 (ANSYS Inc.) was used for technique validation and comparison.

Velocity profiles were measured using both the 4× and 10× objectives for Re = 102. Fourteen different depths were selected by changing the focusing positions for the 4× objective, while eleven depths were examined using the 10× objective. All measurements were taken at 100 mm downstream from the inlet of the test section. The hydrodynamic entrance length required for a fully developed flow at Re = 102 is about 6.7 mm which is estimated through $L_{hy} = 0.054 Re . d_h$ (Shah and London, 1978). Therefore, the length was sufficient for complete flow development.

Figure 3.8 shows images of instantaneous velocity vectors obtained from the micro-PIV system using the 4× and 10× objectives. The focal plane was located at z = 0.481 mm above the flat surface of the channel. As mentioned earlier in this Chapter, the observation area of 4× objective can cover the whole cross-section of the channel, while that of 10× objective only covers 1.73 mm. The channel was located slightly away from the middle of the viewing window of the 10× objective so that at least one side of the channel wall could be detected. The velocity profiles were determined using a multiple-pass interrogation algorithm with a 32 pixels × 32 pixels interrogation window (50% overlap both horizontally and vertically). The corresponding spatial resolutions are 68 µm × 68 µm for 4× objective and 27 µm × 27 µm for 10× objective. The separation size (grid size) displayed in Figure 3.8 is 70 pixels × 12 pixels in order to show the parabolic profile clearly. The uniformity of velocity vectors along the streamwise direction indicates that the flow was fully developed.

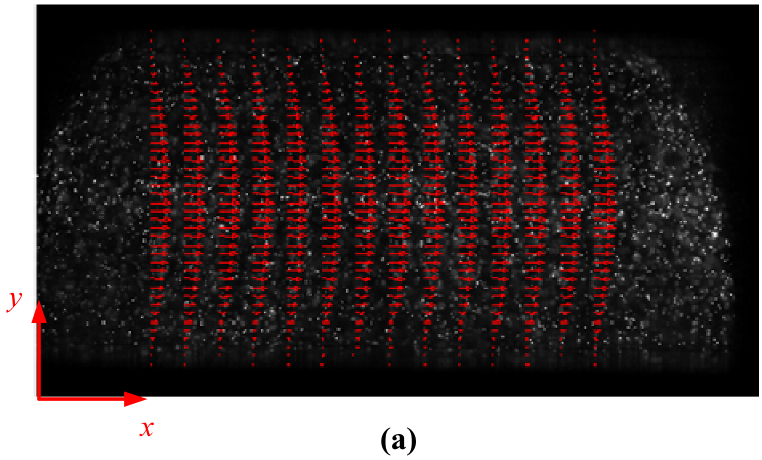

(a)

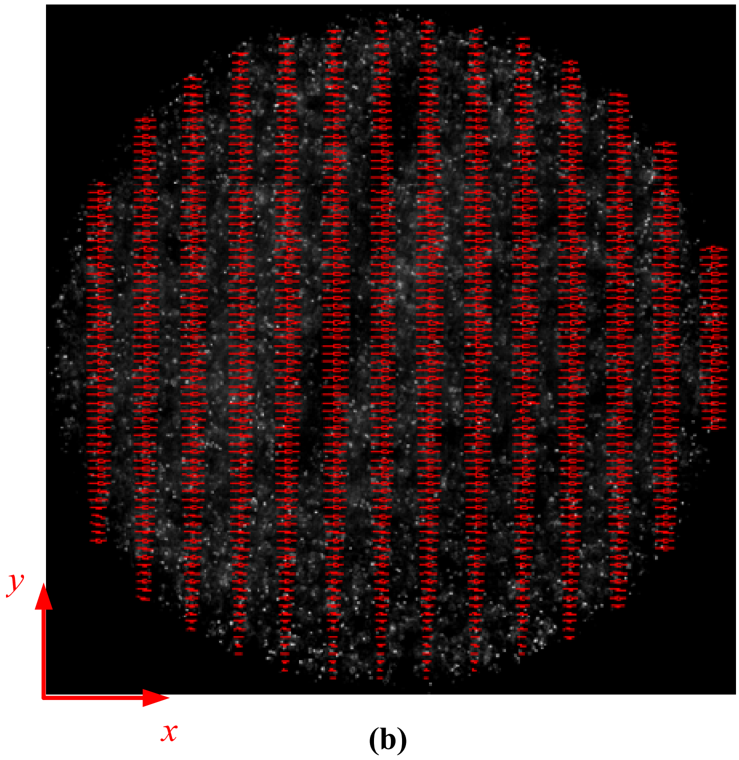

(b)

Figure 3.8: Instantaneous velocity vectors at z = 0.481 mm for Re = 102 using: **(a)** 4× objective; and **(b)** 10× objective.

The time-averaged velocity was obtained by averaging the velocity values over multiple PIV images (e.g. 200 images) taken at separated times. The time-averaged velocity data at different depths are plotted in Figure 3.9. It can be seen that there is overall a very good agreement between the experimental and computational velocity profiles. However, the experimental velocity data appear to deviate from the simulations for the measurements located very close to the glass wall (Figure 3.9 (a)). The possible reason for the disparity is that the particles will migrate away from the wall due to the Saffman effect. Moreover, the contribution of out-of-focus particles is probably more significant near the wall as the main contribution is due to particles located behind the focal plane. Therefore, the evaluated velocity values are inconsistent with the actual position in the channel and they are greater than the one expected at these locations near the wall. Using 7 µm particles as a tracer, the velocity can be resolved satisfactorily as close as 90 µm from the channel wall. This resolution can be improved by using smaller particles, such as 3 µm (Fouilland, 2008). However, particles smaller than 7 µm might not emit sufficient light to be detected by the camera under low magnifications. It can be also seen from Figure 3.9 that the velocity values measured using the 4× objective are basically the same as those measured by the 10× objective, which also indicates that the integrated effect of seed particles over the depth of field was negligible.

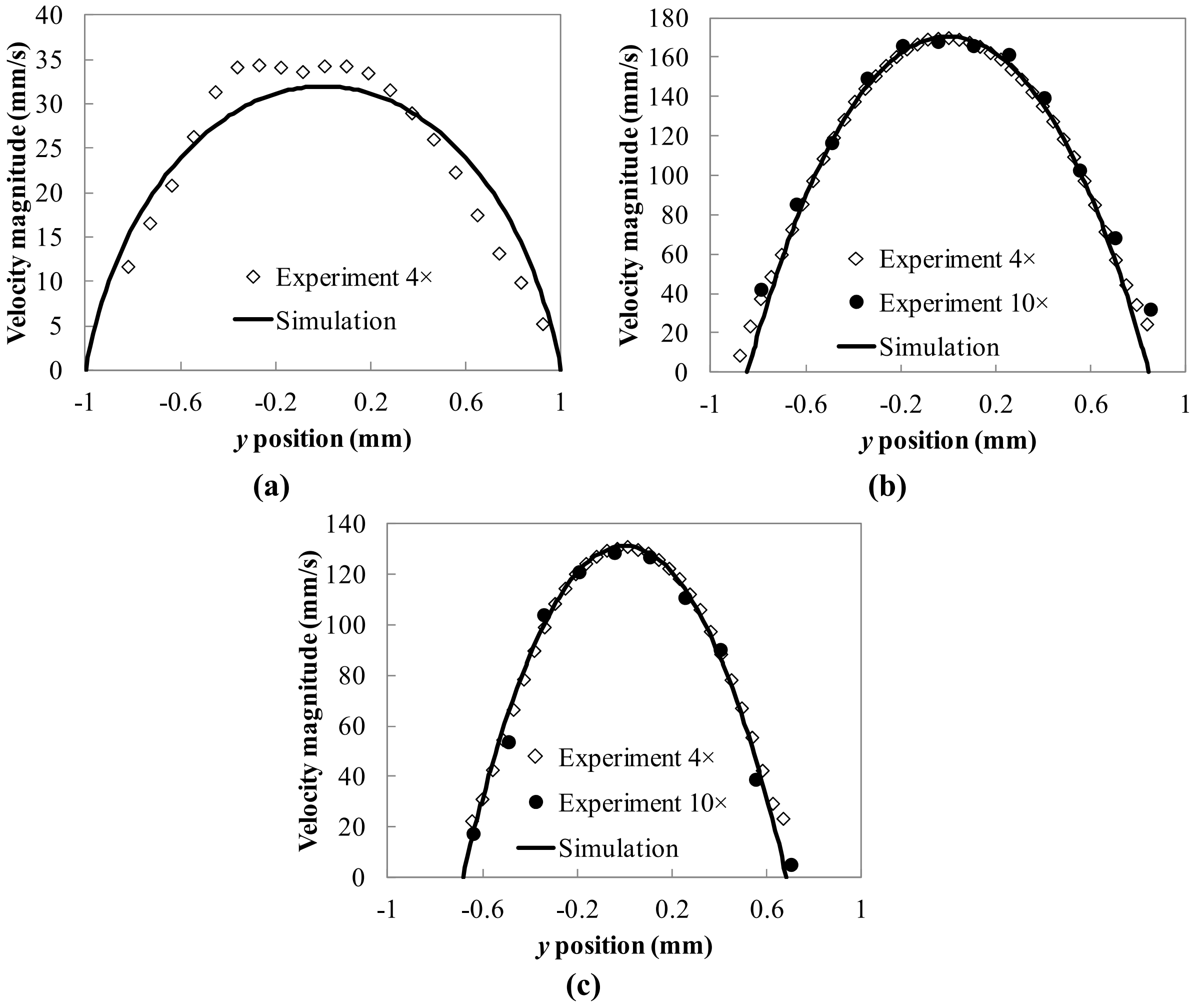

Figure 3.9: Comparison of the measured velocity profiles with those predicted by simulation for *Re* = 102 at: **(a)** $z = 0.045$ mm; **(b)** $z = 0.534$ mm; and **(c)** $z = 0.731$ mm in a semi-circular straight channel.

The centre-line velocity profile, which was reconstructed from different depths in *z* direction, is plotted in Figure 3.10. The vertical bar indicates the standard deviation of the instantaneous velocity variations. Again, as shown in Figure 3.10, the experimental results agree well with the numerical predictions for both objectives. The discrepancy between the PIV measurements and the calculated velocities is usually less than 5%. The Root Mean Square (RMS) uncertainties are 4.8 mm s^{-1} and 5.9 mm s^{-1} for measurements at *Re* = 102 using the 4× and 10× objectives, respectively.

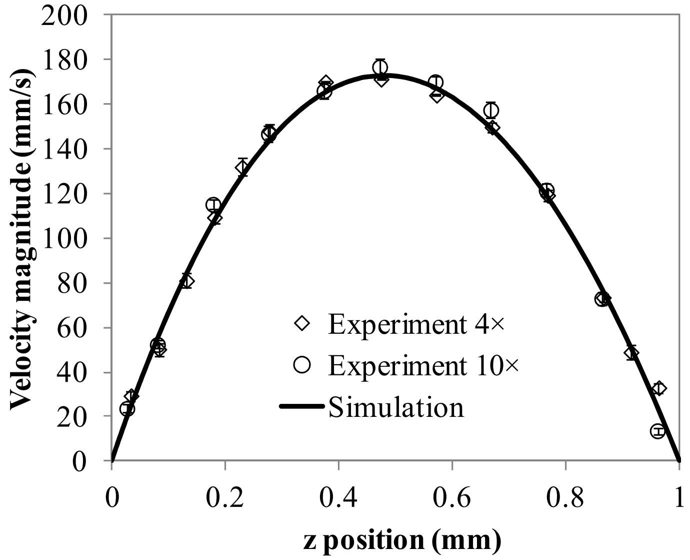

Figure 3.10: Comparison of measured centre-line velocity with that predicted by simulation for *Re* = 102.

3.3.5 PIV uncertainties

The overall measurement accuracy in PIV is a combination of a variety of aspects extending from the recording process through the methods of evaluation (Raffel, 1998). The PIV data carry a measurement noise inherent to the method. This noise is introduced during recording due to optical distortion, light illumination non-homogeneity, transfer function of CCD, particle characteristics, speckle etc. As PIV is based on the statistical correlation of imaged sub-regions to determine local flow velocities, it is subject to inherent errors that arise from finite tracer particle numbers, sample volume size and image resolution. Furthermore, systematic errors are induced during the data processing, including the peak fitting algorithm, image interpolation and peak deformation (Westerweel, 1997). The effects of many of these were discussed in some detail in the recent book by Adrian and Westerweel (2011) based on their earlier work. The accuracy of PIV algorithms and the pixel locking effect were addressed by many other researchers by examining the bias and/or random error (Keane et al., 1995, Huang et al., 1997, Gui and Wereley, 2002). In this study, PIV data noise was reduced by using high resolution imaging equipment and carefully controlling seeding density and interrogation size. The PIV algorithm embedded in VidPIV software had been shown to provide good accuracy through the validation procedures above. Therefore, the uncertainties during experimental measurements are discussed in detail here.

An important step that determines the success of PIV is the calibration of the pixel dimensions into physical dimensions. In this study, a micro-rule was imaged by the camera to determine the scale of the image under different objectives. However, the camera does not have an infinite resolution, and the ruler line edge is usually smeared over several pixels. This makes it difficult to determine exactly where the edge of the line is and therefore brings uncertainty on the velocity calibration. This error was reduced by repeating calibration several times and was found to be negligible.

Similarly, the uncertainty propagation to the measurement target position is also considered. Due to the blurry edge of the channel during experiments, uncertainties exist in the determination of wall location and the estimation of the measurement depth. The location of the measured velocity field could therefore be different from the exact physical space. The possibility of this bias was found to be in the range of 3 pixels which corresponds to 13 μm using the 4× objective.

Based on the validation of flow in a straight channel, the PIV technique suffers larger errors in the measurements near the wall. The evaluation errors which correspond to the standard deviations obtained with 2,000 displacement vectors in the straight channel at Re = 645 are given in Figure 3.11. As shown in Figure 3.11, the evaluation error has a relatively flat distribution in the middle of the channel with standard deviation less than 3% and it is much larger at the position close to the wall. Two main phenomena, Brownian motion and the Saffman effect, primarily give rise to this error by preventing the seed particles from following the flow.

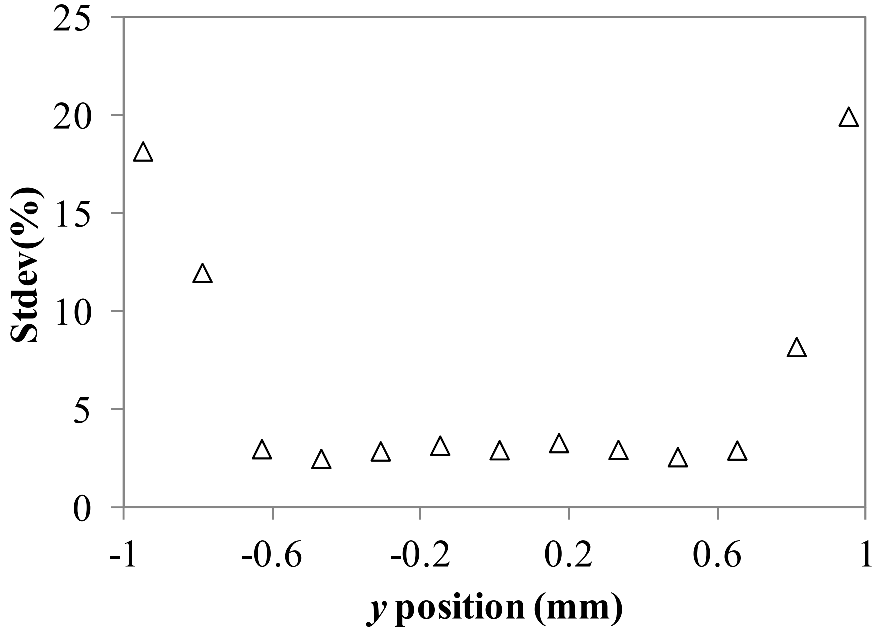

Figure 3.11: Evaluation errors across the straight channel at depth of $z = 0.245$ mm for $Re = 645$.

Brownian motion is the random thermal motion of a particle suspended in a fluid. It is typically much more significant in micro-PIV applications where small seed particles and low velocities are encountered. It has been established that the relative error in the measured particle displacement due to Brownian motion increases as the particle size and the velocity of the flow decrease (Wereley and Meinhart, 2005). Brownian motion is found to influence the signal strength of the correlation function, making it more difficult to find the signal peak from among the noise peaks (Olsen and Adrian, 2000). The signal strength can be increased by reducing the magnitude of the Brownian motion by either increasing the particle diameter or decreasing the time intervals between two consecutive laser pulses.

Many authors (Wereley et al., 2005) reported that particle migration should be considered as a possible source of error when using the micro-PIV technique. The Saffman effect can become large in the case of particles very near a boundary. It was noticed in the experiments that particle concentration reduced near the walls with fewer particles observed. The errors became bigger because fewer particles fell into the interrogation window for PIV correlation.

Lastly, out-of-focus particle images degrade the image by producing background noise, decreasing the discrimination of the in-focus particles, and ultimately affecting the correlation. It was not possible to obtain satisfactory cross-correlation peaks using a simple cross-correlation method directly on the raw images. In order to obtain reliable measurements, the raw images were pre-processed using the ImageJ software to attenuate the background noise. Measurement noise was also reduced by applying an adaptive cross-correlation after the standard cross-correlation. The adaptive cross-correlation uses a smaller interrogation window and a smaller grid spacing, which overall gives higher spatial resolution and higher accuracy.

3.4 Pressure drop measurements

In many previous studies, the pressure drop measurement was taken between the inlet and exit wells of a microchannel and the inlet and outlet effects were neglected in the calculations. Due to the relatively short length of the microchannels used in this work, these additional pressure losses cannot be neglected. These pressure losses were estimated by some empirical formulae in some studies, which may not be accurate enough (Li et al., 2003, Lelea et al., 2004). To achieve the accurate measurement of frictional pressure drops, a straight channel was used to calculate the additional pressure losses.

In the present experiments, the total pressure drop along the test section was measured using a differential pressure transmitter mounted across the two NanoPort assemblies. The total pressure drop includes the pressure drop through the test channel, ΔP_c , pressure drop at the inlet and outlet portion of the experimental setup, ΔP_{in} and ΔP_{out} , pressure drop due to the contraction and expansion of the cross-sectional area, ΔP_{con} and ΔP_{exp}, and the pressure drop caused by connection bends, ΔP_{bend}. Therefore, the total pressure drop measured in a straight channel, $\Delta P_{str,m}$, can be expressed with the following equation:

$$\Delta P_{str,m} = \Delta P_{str,c} + \Delta P_{in} + \Delta P_{out} + \Delta P_{con} + \Delta P_{exp} + \Delta P_{bend} = \Delta P_{str,c} + \Delta P_{extra} \quad (3.5)$$

Similarly, the measured pressure drop in a wavy channel, $\Delta P_{w,m}$, can be expressed by:

$$\Delta P_{w,m} = \Delta P_{w,c} + \Delta P_{in} + \Delta P_{out} + \Delta P_{con} + \Delta P_{exp} + \Delta P_{bend} = \Delta P_{w,c} + \Delta P_{extra} \quad (3.6)$$

where ΔP_{extra} is the pressure loss induced by all the additional sources. Both the straight channel and wavy channel were connected to the exactly same inlet and outlet assemblies. At the same flow rate, the straight and wavy channels have the same Reynolds number and therefore the same extra losses (ΔP_{extra}). For fully-developed laminar flow in a semi-circular straight channel, the theoretical prediction of fanning friction factor was report by Shah and London (1978) and expressed as

$$f_{str}Re = 15.767 \tag{3.7}$$

$$\Delta P_{str,c} = 4f_{str}\frac{L_{str}}{d_h}\frac{\rho u_m^2}{2} \tag{3.8}$$

The Reynolds number (Re) is defined as:

$$Re = \frac{\rho u_m d_h}{\mu} \tag{3.9}$$

where ρ is the fluid density , u_m is the mean flow velocity, d_h is the hydraulic diameter and μ is the fluid dynamic viscosity.

By substituting Eqs.(3.5), (3.7) and (3.8) into Eq. (3.6) and assuming the flow development length to be negligible, the pressure drop in a wavy channel can be obtained by

$$\Delta P_{w.c} = \Delta P_{w,m} - \Delta P_{extra} = \Delta P_{w,m} - \left(\Delta P_{str,m} - 4\frac{15.767}{Re}\frac{L_{str}}{d_h}\frac{\rho u_m^2}{2}\right) \tag{3.10}$$

In order to assess the performance of various wavy channels, the relative pressure-drop penalty is calculated by comparing friction factors with those occurring in straight channels with the same semi-circular cross-section and the same overall path length:

$$e_f = \frac{\Delta P_{w,c}}{\Delta P_{str,c}} = \frac{f_w}{f_{str}} \tag{3.11}$$

3.5 Heat transfer measurements

3.5.1 Heating methods

Taking advantage of the “hybrid channel”, different heating methods can be applied for heat transfer measurements. First, the test section was heated by an electric current through the Kovar plate via a DC power supply that could provide low voltage but high current. In this way the required power could be achieved despite the low resistance of the Kovar plate. The heat flux to the fluid could be calculated from the applied electrical power, accounting for the heat losses to the environment. However, a large amount of heat loss was found through the electrode heads and power wires due to the high current applied. Very thick connection wires had to be used to reduce the connection resistance, so as to reduce the heat generated in the wires, which made it very inflexible to move the test section on the mechanical stage.

So it is imperative to use a heating method that has efficient use of power and flexibility. Thermofoil heaters are thin, flexible components consisting of an etched-foil resistive heating element laminated between layers of flexible insulation. The thin construction provides close thermal coupling between the heater element and heat sink. The test section was then heated by a thermofoil heater (Kapton heater, Minco) with a thickness of 0.3 mm and uniform heat pattern attached on the back of the Kovar substrate. Using a pressure-sensitive adhesive (PSA) on the back of the heater, the heater is affixed in intimate contact with the surface beneath it, as any gaps are avoided to block heat transfer or cause a hot spot. The thermofoil heater has a specific resistance. Its power output in Watts can be determined knowing the supplied voltage.

3.5.2 Temperature measurements

The room temperature was measured using a 1/16 inch K-Type thermocouple probe (Merlin Marlox series). The fluid inlet and outlet temperatures were measured using miniature K-Type thermocouples with 0.25 mm diameter inserted into the inlet and outlet assembly ports of the test section. Eight miniature flexible platinum RTD sensors (RdF 29223) were attached on the top of the heater to measure the longitudinal wall temperature distribution over the metal plate. Similarly, another eight RTDs were attached on the glass side. The RTDs were located with uniform spacing between 15 mm and 125 mm from the entrance of the microchannel. Each temperature sensor was calibrated using an ice water bath and a boiling water bath at atmospheric pressure and an accuracy of better than ±0.15 ˚C was found in the temperature calibration experiments. All temperature data were acquired by a data acquisition system (Agilent 34970A). The local fluid temperature in the channel could be measured through the micro-PIV/LIF system as will be explained in detail in Chapter 7. All experiments were conducted at room temperature and under atmospheric pressure conditions.

As the heater must be affixed in intimate contact with the metal surface to provide a uniform heat flux, the RTD sensors had to be attached on the top of the heater rather than the metal surface. The measured temperature (T_h) does not represent the real metal surface temperature accurately due to the thermal resistance between the heater and the Kovar plate. The temperature distribution across the heater can be solved by a one-dimensional heat diffusion equation with energy generation and boundary conditions:

$$k\frac{d^2T}{dx^2} = \dot{S} \qquad (3.12a)$$

$$\frac{dT}{dx} = 0, \qquad x = 0 \tag{3.12b}$$

$$-k\frac{dT}{dx} = q_s, \qquad x = L_h \tag{3.12c}$$

where $\dot{S}$ is the volumetric heat generation rate; k is the thermal conductivity of the heater; L_h is the heater film thickness and q_s is the surface heat flux. The energy source generated by the heater can be defined as:

$$E = VI = \dot{S}\,A_s L_h = q_s A_s \tag{3.13}$$

where V and I are the input voltage and current supplied by the power source; A_s is the surface area of the heater.

The boundary conditions (Eqs. 3.12b and 3.12c) are obtained when the test section is well insulated, so that the outer surface of the heater is taken as an adiabatic boundary and the inner surface has a constant surface heat flux boundary. The temperature difference between the metal surface and heater outer surface, $T_h - T_M$, can be obtained by solving the heat diffusion equation:

$$T_h - T_M = T_{L_h} - T_0 = \frac{\dot{S}}{2k}{L_h}^2 = \frac{VI}{A_s}\frac{L_h}{2k} = q_s\frac{L_h}{2k} \tag{3.14}$$

It can be seen from Eq. (3.14) that the temperature difference is proportional to the heat flux. A constant thermal resistance between the metal surface and heater outer surface can be obtained as $R_{h,M} = \frac{L_h}{2k}$. Based on the properties of the heater materials, the thermal resistance was found around 9×10^{-4} m^2 K W^{-1}. This thermal resistance is important especially for high heat flux (q_s > 2,000 W m^{-2}) when the temperature difference between the heater and the metal surface could be higher than 1 °C. It would induce very large errors in the heat transfer calculations if this resistance were not taken into account. Hence, the metal outer surface temperature, T_M, is calculated by subtracting the temperature drop across the heater from the measured heater temperature, as expressed in Eq. (3.14).

3.5.3 Data reduction

Mass flow rate

The mass flow rate is calculated as

$$\dot{m} = \dot{V}\rho \tag{3.15}$$

where $\dot{V}$ is the volumetric flow rate and ρ is the fluid density.

Heat flux

The heat flux is the net heat flux added to the fluid and is calculated using the surface area of the inner wall of the channel. From an energy balance, the inner wall heat flux $\dot{q}_w$ can be expressed as

$$\dot{q}_w A_w = h A_w (\bar{T}_w - T_b) = \dot{q}_s A_s - Q_{loss} \tag{3.16}$$

where $A_s = L_x \cdot L_y$ is the surface area of the heater, and $A_w = L_x P = L_x(\frac{\pi d}{2} + d)$ is the inner wall surface area of a straight channel; Q_{loss} is the heat loss to the environment. It can be obtained from heat loss calibration experiments and the details are discussed in Chapter 4.

Heat transfer coefficient and Nusselt number

In order to accurately interpret the experimental data and to compare the measured data with the calculated results, it is necessary to properly define the heat transfer rate and Nusselt number especially when only limited data (substrate wall temperature and the inlet and outlet fluid temperatures) could be obtained experimentally.

Numerical simulations using ANSYS CFX 14.5 were performed in this study to assist experimental analysis and system validation. In the simulations, the peripherally-averaged heat transfer coefficient at a given axial location *s* is defined as

$$h_s = \frac{\dot{q}_w}{\bar{T}_{w,s} - T_{b,s}} \tag{3.17}$$

where $\bar{T}_{w,s}$ is the perimeter-averaged wall temperature and $T_{b,s}$ is the bulk mean fluid temperature at an axial location *s*.

The perimeter-averaged wall temperature and bulk mean fluid temperature are defined as

$$\bar{T}_{w,s} = \frac{1}{P_s}\int_{P_s} T_w \mathrm{d}L \tag{3.18}$$

$$T_{b,s} = \frac{\int_{A_{X,s}} \rho \left| u_{x,y} \right| \hat{c}_p T_{x,y} \mathrm{d}A}{\int_{A_{X,s}} \rho \left| u_{x,y} \right| \hat{c}_p \mathrm{d}A} \tag{3.19}$$

where P_s is the cross-sectional perimeter length, $\hat{c}_p$ is the heat capacity of the fluid, $u_{x,y}$ is the velocity component parallel to the channel direction, and $T_{x,y}$ is the local temperature at the point (x, y) of the cross-sectional plane.

The corresponding peripherally-averaged Nusselt number (Nu_s) can be expressed as

$$Nu_s = \frac{h_s D_h}{k} \tag{3.20}$$

where k is the thermal conductivity of the fluid.

To evaluate the overall heat transfer performance, the average Nusselt number is calculated by averaging the local Nusselt number along the channel.

$$Nu = \frac{1}{s} \int_S Nu_s ds \tag{3.21}$$

To assess the heat transfer performance of various wavy channels, the heat transfer enhancement, e_{Nu}, is defined as

$$e_{Nu} = \frac{Nu_w}{Nu_{str}} \tag{3.22}$$

where Nu_{str} is the Nusselt number for a straight channel.

In the experiments, the peripherally-averaged wall temperature, bulk mean fluid temperature and corresponding Nusselt number are calculated based on the measured temperatures and a model associated with the thermal boundary conditions. The details are described in Chapters 4 and 6 on heat transfer studies.

Chapter 4

Heat Transfer in Straight Microchannels

Single phase heat transfer in straight microchannels with various geometries has been reported in numerous studies, both experimental and numerical. However, many early experimental investigations claimed that the behaviour of fluid flow and heat transfer in microchannels is different from that which typically occurs in conventionally-sized channels (Sobhan and Garimella, 2001, Guo and Li, 2003, Hetsroni et al., 2005). There appears to be considerable variation in the experimentally-determined heat transfer coefficients obtained by various researchers. Some studies revealed an increase in convective heat transfer with reduction in the hydraulic diameter for different channel geometries (Choi et al., 1991, Adams et al., 1998, Rahman, 2000), while other works found a decreased convective heat transfer rate in microscale channels (Wang and Peng, 1994, Qu et al., 2000, Tso and Mahulikar, 2000, Gao et al., 2002). In addition, some experimental studies observed good agreement with the theories conventionally used in macrochannels (Qu and Mudawar, 2002, Lelea et al., 2004, Lee et al., 2005, Mokrani et al., 2009). Several special phenomena, including surface roughness effect (Qu and Mudawar, 2002, Kandlikar et al., 2003), entrance effects, viscous dissipation effect (Koo and Kleinstreuer, 2004) and the effect of axial conduction within the walls and the fluid (Celata et al., 2006) have been suggested to interpret these deviations. The phenomenon may be also related to the discrepancy between the actual conditions of a given experiment and the assumption made to generate the theoretical or numerical solution used for comparison (Li et al., 2004). In many studies, the heat flux is not applied to all of the sides of the channel, while, for comparative analysis, a uniformly applied heat flux is invoked. Furthermore, the measurement accuracy in various parameters, especially the wall temperatures and hydrodynamic diameter, may be the most important factor that causes this discrepancy (Yang and Lin, 2007, Mokrani et al., 2009).

It is important to note that in practical applications, convective heat transfer in microchannel systems is coupled with significant conduction effects existing within the substrates, which is called a conjugate problem. It is important to note that in plate-based heat exchanges, microchannels are fabricated as an integral part of the substrates. The conductive material for the test section consists of a large volume to be heated and the heat can conduct in all directions, including the axial direction (Fedorov and Viskanta, 2000). This coupling becomes more significant in a "hybrid channel" with two different materials and when the heat source is located on only one side of the channel, as opposed to the case where the perimeter of the channel is heated symmetrically. The effects of conjugate heat transfer in microchannels can induce a multi-dimensional temperature distribution and the wall heat flux becomes non-uniform along the microchannel (Maranzana et al., 2004).

Therefore, in this chapter, heat transfer simulations and experiments are conducted in a straight channel using the "hybrid test section". Numerical simulations which present detailed distributions of the local heat flux and temperature at the fluid-wall interface are performed to study the conjugate effects and provide information for experimental calculations. Single-phase heat transfer experiments are carried out for a wide range of Reynolds numbers to validate the established system and data processing procedures.

4.1 Numerical simulations

4.1.1 Computational methodology

A numerical model was developed using the ANSYS CFX version 14.5 package to analyse the three-dimensional heat transfer characteristics of the present test section by solving the conjugate heat transfer problem. Different from the previous studies in our research group (Geyer et al., 2007, Rosaguti et al., 2007b, Zheng, 2013, Zheng et al., 2013b) where a channel with zero wall thickness was simulated, the model in the present study is a complete modelnof the experimental device that includes the Kovar and glass substrates, as shown in Figure 4.1. The properties of the test section materials at room temperature are listed in Table 4.1.

Table 4.1: Physical properties of the test section materials.

Property	Kovar	Pyrex 7056
Density (g cm^{-3})	8	2.23
Thermal conductivity (W K^{-1} m^{-1})	17	1.13
Electrical resistivity (Ω mm^{2} m^{-1})	0.49	N/A
Specific heat capacity (J g^{-1} K^{-1})	0.46	0.75

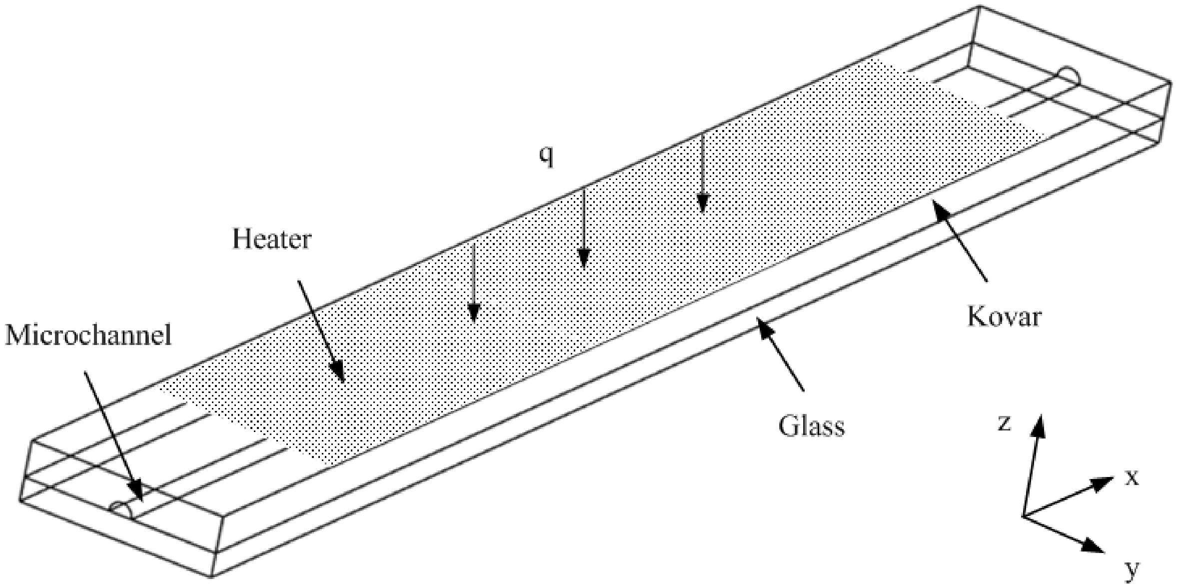

Figure 4.1: Simulation model of the test section with a straight channel.

4.1.1.1 **Conservation equations**

In the simulation, the model was constructed making the following assumptions:

- the fluid in the channel is incompressible and Newtonian,
- the viscous dissipation is neglected,
- the fluid properties, such as density, dynamic viscosity and thermal conductivity are independent of temperature,
- properties of Kovar and Pyrex glass at room temperature are specified for the test section.

Using the stated assumptions, the continuity, momentum and energy equations that govern laminar flow and heat transfer are written as follows:

Continuity:

$$\nabla \cdot (\rho \boldsymbol{u}) = 0 \tag{4.1}$$

Momentum:

$$\nabla \cdot (\rho \boldsymbol{u} \otimes \boldsymbol{u}) = -\nabla p + \nabla \cdot (\mu(\nabla \boldsymbol{u} + \nabla \boldsymbol{u}^T)) \tag{4.2}$$

Energy:

$$\nabla \cdot (\rho \boldsymbol{u} h) = \nabla \cdot (k \nabla T) \tag{4.3}$$

where ρ is the density, μ is the dynamic viscosity and k is the thermal conductivity. $\boldsymbol{u}$ denotes the velocity vector; p, e, h and T denote the pressure, internal energy, enthalpy and temperature, respectively.

4.1.1.2 **Boundary conditions**

The CFD model was formulated with the necessary boundary conditions to simulate the experimental setup:

- no-slip boundary conditions at all solid walls,
- constant mass flow rate at the inlet,
- an area-averaged pressure of 0 Pa at the outlet,
- at all external surfaces of the test section (including Kovar top, glass bottom and all side surfaces), the heat losses were specified as $q_{loss} = h_{loss}(T_w - T_a)$, with the heat loss coefficient, h_{loss}, calibrated from experiments,
- the heating source was modelled as a boundary condition with a specified heat flux into the surface of the test section,
- continuity of temperature and heat flux is automatically set in the code to couple the energy equations for the fluid and solid phases.

4.1.1.3 **Solution methodology**

The conservation equations for mass, momentum and energy were solved using the finite-volume based CFD code ANSYS CFX 14.5 via the method detailed in Zheng (2013). A modified Rhie-Chow algorithm was used to link the pressure and velocity fields, which were solved via a coupled solver. All the calculations were carried out using a second-order bounded differencing scheme for the convective terms. The system was regarded as having reached a converged state once all the scaled residuals fell below 10^{-6} and the global imbalances, representing overall conservation, fell below 10^{-3}.

4.1.1.4 **Model discretization**

In this model, fluid and solid domains have different mesh configurations to reduce the number of mesh elements and to increase the performance at the same time. The straight channel was defined by sweeping a semi-circle along the path. The cross-sectional mesh was constructed to provide the greatest resolution close to the channel walls where fluid velocity and temperature gradients are the highest, as shown in Figure 4.2 (a), with mesh on the inlet being swept along the channel. The mesh in solid domains (Kovar and glass), shown in Figure 4.2 (b), was set such that the node groups were distributed relatively evenly along the plate, with a slightly higher density towards the channel wall and the interface between the Kovar and glass.

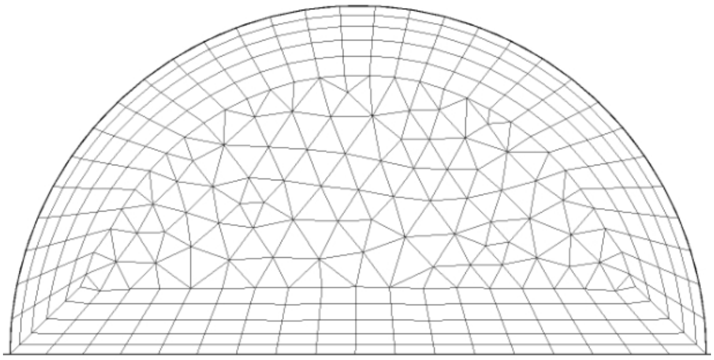

(a)

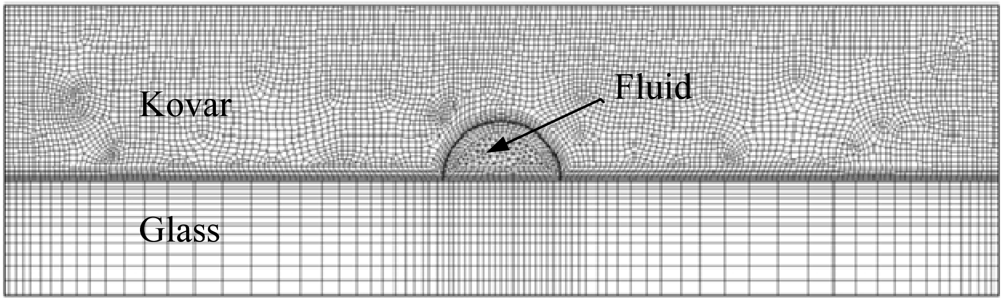

(b)

Figure 4.2: Illustration of the computational mesh for the straight channel on the cross-section in: **(a)** fluid domain; and **(b)** solid and fluid domains.

4.1.1.5 **Grid independence study**

Grid independence studies were conducted to ensure that the mesh generated for the test section, especially the fluid domain, is refined to the extent that the resulting solution is no longer influenced by the size of the grid. The mesh used in the fluid domain contains approximately 360 elements on the channel cross-section with 80 elements in the axial direction. The mesh density in the fluid domain was increased in both the cross-section and axial directions, while the mesh in solid domains was kept the same. The local Nusselt number (Nu_x) was assessed within the geometry for increasing mesh densities. Figure 4.3 shows the Nusselt number plot for different grids in the fluid domain for Re = 406. With the mesh refined from 29,000 to 130,000 elements, the average Nusselt number for the straight channel changed by less than 0.1%.

In this study, the 3-D computational domain consists of 651,000 hexahedral and prism cells, with 622,000 and 29,000 elements in the solid and fluid, respectively. A large number of elements were generated in the solid domains due to the relatively large total volume of the plates compared with the channel (fluid) domain.

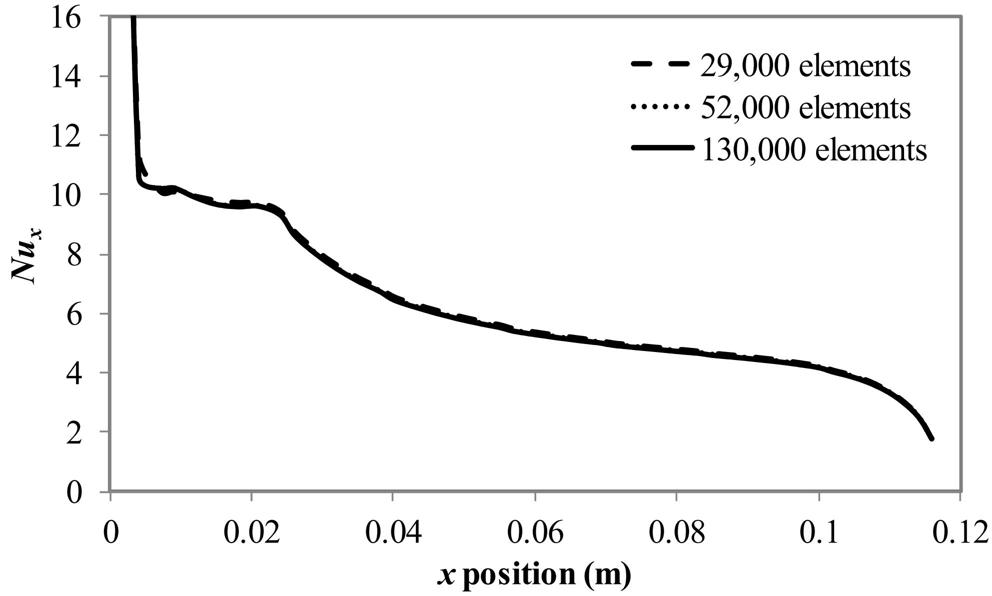

Figure 4.3: The circumferentially-averaged Nusselt number in the flow direction of the straight channel at $Re = 406$. Three meshes in the fluid domain were tested, comprising 29,000, 52,000 and 130,000 volume elements, respectively.

4.1.2 Effect of heating method

As the heat transfer rate was calculated at the interface where the fluid and the channel wall are in direct contact, a key factor that determines the accuracy of the heat transfer prediction is the thermal boundary condition that is used at the inner wall of the channel. Due to the complexity of the conjugate problem induced by using the “hybrid channels”, the thermal boundary condition was first examined numerically. Simulations were conducted for four cases using different heating methods and their effect on the thermal boundary condition at the channel wall was assessed.

Four heating methods were considered: (a) a current applied at the two ends of the metal plate (Current heating); (b) a constant heat flux distributed on the metal surface (Metal heater); (c) a constant heat flux distributed on the glass surface (Glass heater); and (d) a constant heat flux distributed evenly on both the metal and glass surfaces (Metal and Glass heater 1:1). The input power energy in four cases was the same and the Reynolds number for all cases was 102.

Figure 4.4 provides contour plots of the wall heat flux along the channel. As these plots show, the heat flux is not uniform in either the axial or the peripheral direction. This is due to the heat losses specified on the external surfaces that are a function of channel wall temperature, which in turn changes the wall heat flux. The heat flux distribution patterns, however, are quite similar for the different heating methods. Figure 4.5 shows the peripheral distribution of heat flux and temperature in the middle section of the channel (x = 0.07 m). It can be seen that temperature and heat flux are not constant around the cross-section. The metal wall has more uniform profiles than those of the glass wall. The temperature and heat flux of the glass surface are much lower than those of the metal surface no matter whether the glass is heated or not. The ratio of heat flux applied to the glass and metal surfaces was adjusted to different levels. However, the patterns stayed basically the same. The glass did not act as an effective conductor as the Kovar due to its high thermal resistance. However, this thermal resistance is not high enough to take the glass as an insulator.

Similar trends are found in Figure 4.6, which presents the axial heat transfer and temperature distribution at the middle of the metal and glass surfaces (y = 0.001 m). It is clear that both the heat flux and temperature of the glass wall are lower than that of the Kovar wall. The distributions of heat flux and temperature are the same for all heating methods. It is noted that heating through applying current and sticking a heater on the metal surface gives almost the same results because of the relatively high thermal conductivity of Kovar. However, as mentioned in Chapter 3, current heating is actually not suitable in the present experimental set-up.

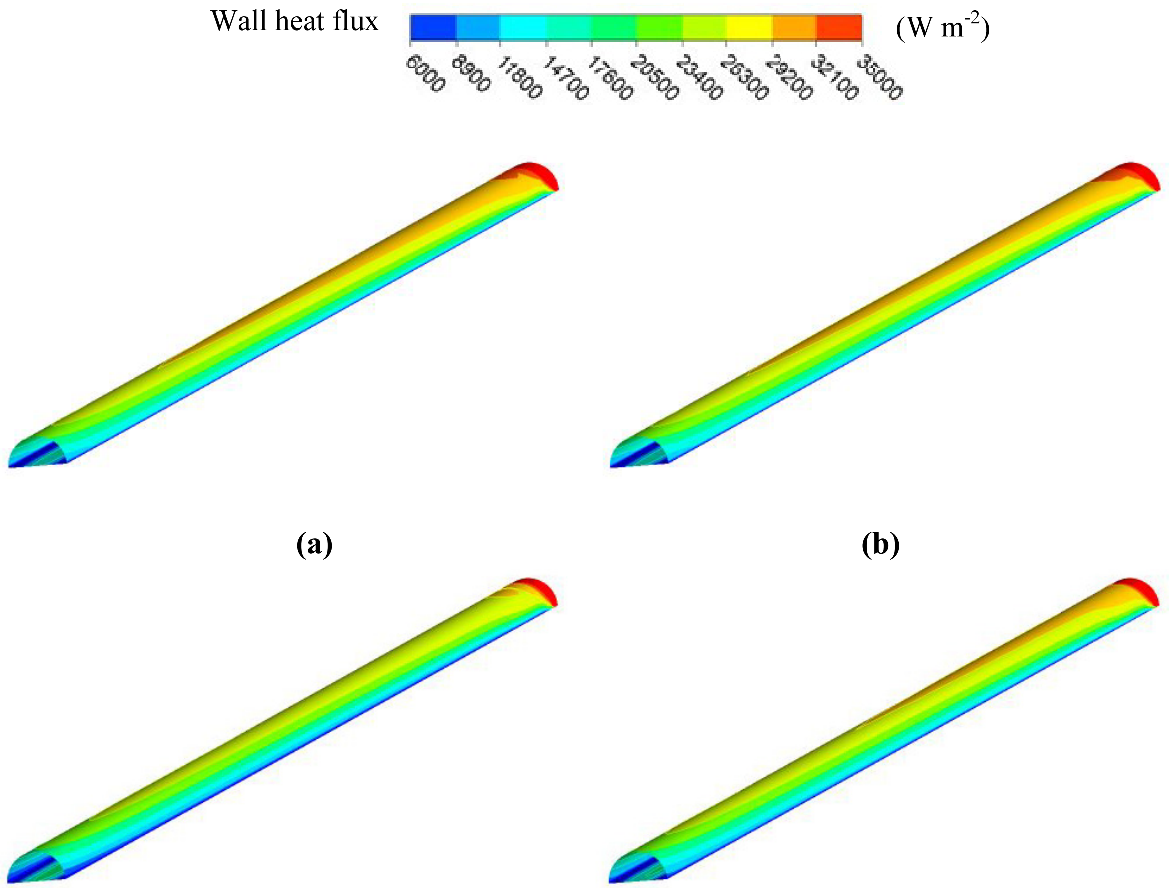

(a) **(b)**

(c) **(d)**

Figure 4.4: Wall heat flux distribution along the channel under different heating methods: **(a)** Current heating; **(b)** Metal heater; **(c)** Glass heater; and **(d)** Metal and Glass heater 1:1.

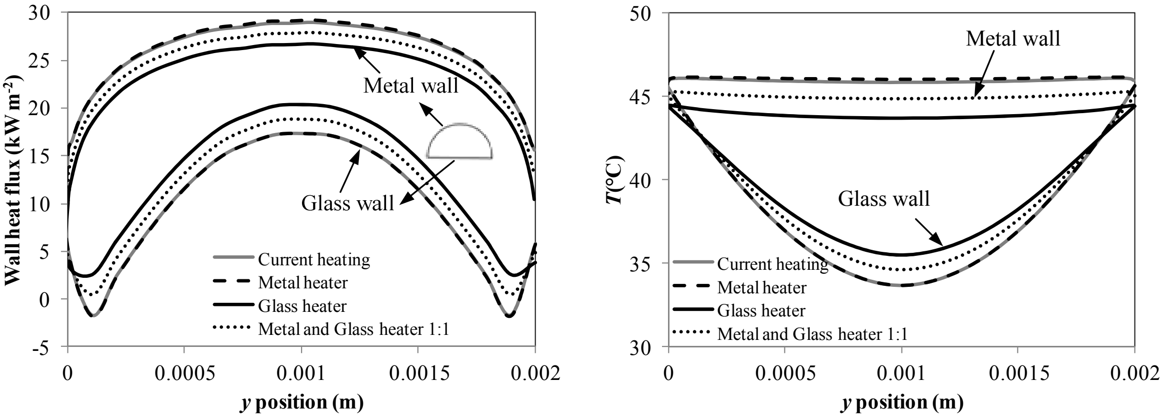

(a) **(b)**

Figure 4.5: Peripheral distributions of: **(a)** wall heat flux; and **(b)** temperature at x = 0.07 m for different heating methods.

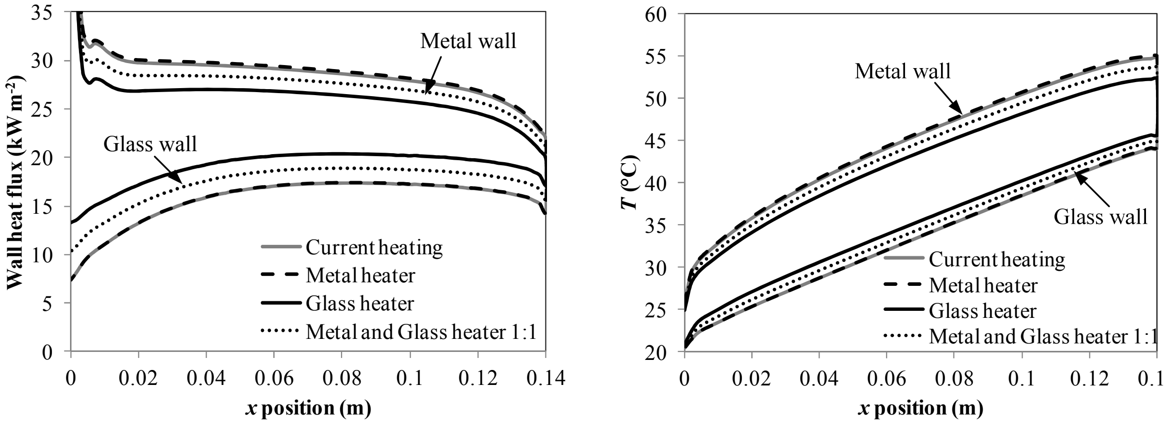

(a) **(b)**

Figure 4.6: Axial distributions of: **(a)** wall heat flux; and **(b)** temperature at $y = 0.001$ m for different heating methods.

4.1.3 Effect of metal thickness

In conjugate problems the heat transfer in both the solid substrate and the fluid is considered, so the thickness of the substrate may play an important role in the heat conduction of the test section (Kosar, 2010). Heat transfer in test sections with different Kovar thicknesses (1.5 mm, 3 mm and 4 mm) was studied to examine the effect of the substrate thickness on the thermal boundary condition at the wall-fluid interface.

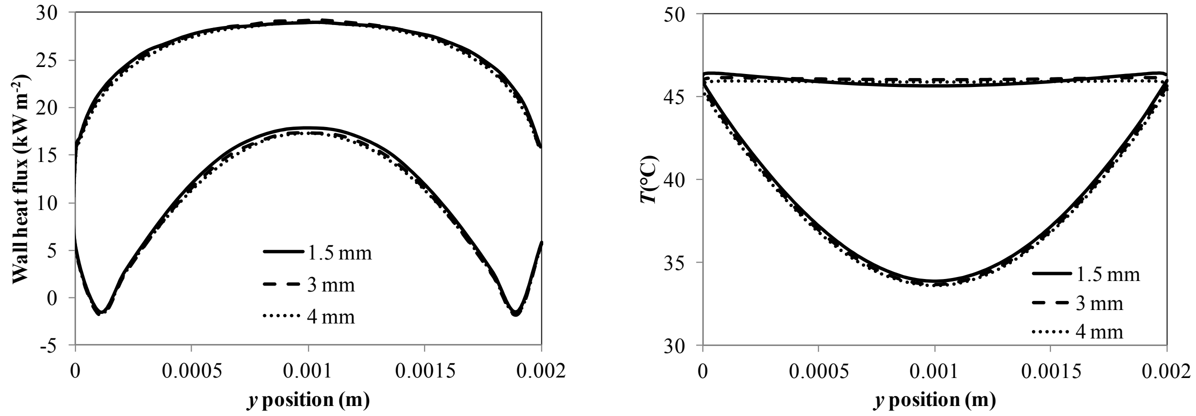

(a) **(b)**

Figure 4.7: Peripheral distributions of: **(a)** wall heat flux; and **(b)** temperature at $x = 0.07$ m for different metal thicknesses.

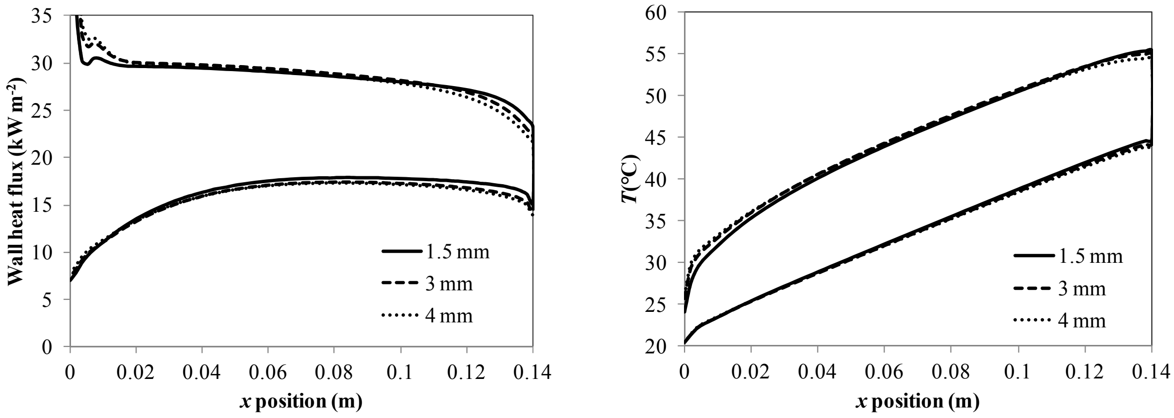

(a) **(b)**

Figure 4.8: Axial distributions of: **(a)** wall heat flux, and **(b)** temperature at $y = 0.001$ m for different metal thicknesses.

Figures 4.7 and 4.8 show the peripheral and axial distributions of heat flux and temperature for different metal thicknesses. As can been seen, the distribution patterns stay the same for all of the cases. However, in the thick substrate test section, the temperature distribution along the metal wall is slightly more uniform than that in the thin substrate test section. But the influence of substrate thickness on the thermal boundary condition at the wall-fluid interface is very weak.

From the simulation results, it is confirmed that the conjugate effects cannot be neglected for the current experimental design. Neither a constant heat flux nor a constant temperature boundary condition can be attained even by adjusting the plate thickness and heating methods. Therefore, in the present study the microchannels do not correspond strictly to any standard thermal boundary condition for laminar flow.

4.2 Heat transfer experiments

Based on the simulation results, heating through the metal surface (Metal heater) was selected due to its flexibility and simplicity. As mentioned in Chapter 3, a thermofoil heater with a size of 17 mm × 93 mm was attached on the back of the metal plate to provide a uniform heat flux on the metal surface. In the simulation, the thin thermofoil heater was modelled as a boundary condition with specified heat flux into the Kovar top surface. The heating area was set to be the same as that applied in the experimental device, as seen in Figure 4.1.

Experimental data were compared with simulation results to validate both the numerical model and experimental procedures.

4.2.1 Heating zone calibration

Due to the fact that flow visualisation has been done separately without heat transfer measurements, the test section was wrapped in closed cell foam insulation to minimize ambient heat loss and the effect of environmental changes, and also to reduce the measurement uncertainty.

Heat loss calibration with an empty test section was first conducted to estimate heat losses due to free convection, conduction, and radiation. The heat loss coefficient between the heating zone and the environment is defined as:

$$h_{loss} = \frac{Q_{loss}}{A_e(\bar{T}_{w,s} - T_a)} \tag{4.4}$$

where $\bar{T}_{w,s}$ is the average surface temperature of the test section, T_a is the ambient temperature, and A_e is the external surface area of the test section.

Due to the fact that no working fluid is employed in this case, all the input power is transferred to the ambient environment

$$Q_{loss} = Q_{in} = VI \tag{4.5}$$

where V and I are the input voltage and current supplied by the power source.

The average temperature of the whole test section was calculated by averaging the temperatures measured on the heater surface and those of the Pyrex glass surface.

$$\bar{T}_{w,s} = \frac{\sum_{i=1}^{i=n} T_{hi} + \sum_{i=1}^{i=n} T_{Gi}}{2n}, n = 8 \tag{4.6}$$

where T_{hi} and T_{Gi} (i =1,…,8) are the temperatures measured by RTD sensors attached on the heater and the glass, respectively.

A series of calibration experiments was conducted under different power levels using the straight channel test section. The heat loss coefficient is found to increase slightly with increasing temperature difference between the plate and the environment, as shown in Figure

4.9. By fitting the data points with a second order polynomial, the heat loss coefficient for the present test section was obtained, as expressed by Eq. (4.7).

$$h_{loss} = -0.0004(T_w - T_a)^2 + 0.0558(T_w - T_a) + 6.4863 \tag{4.7}$$

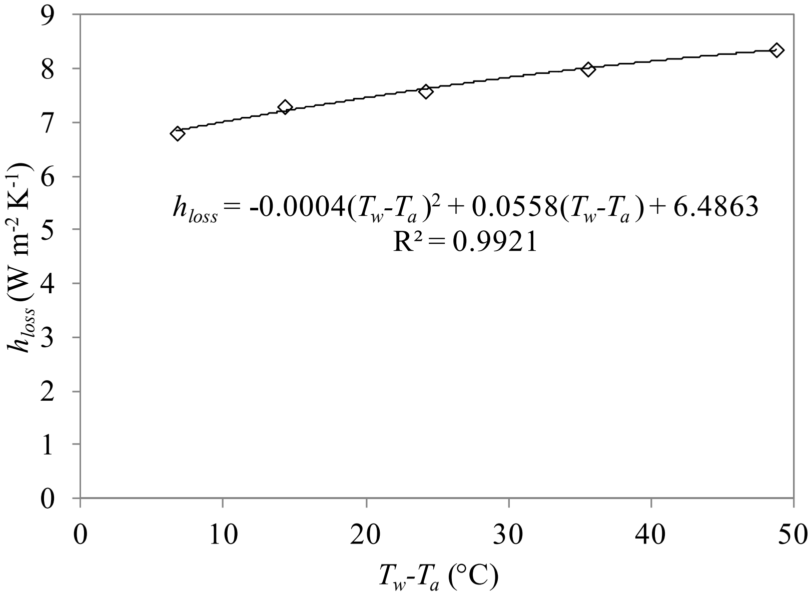

Figure 4.9: Heat loss coefficient calibration.

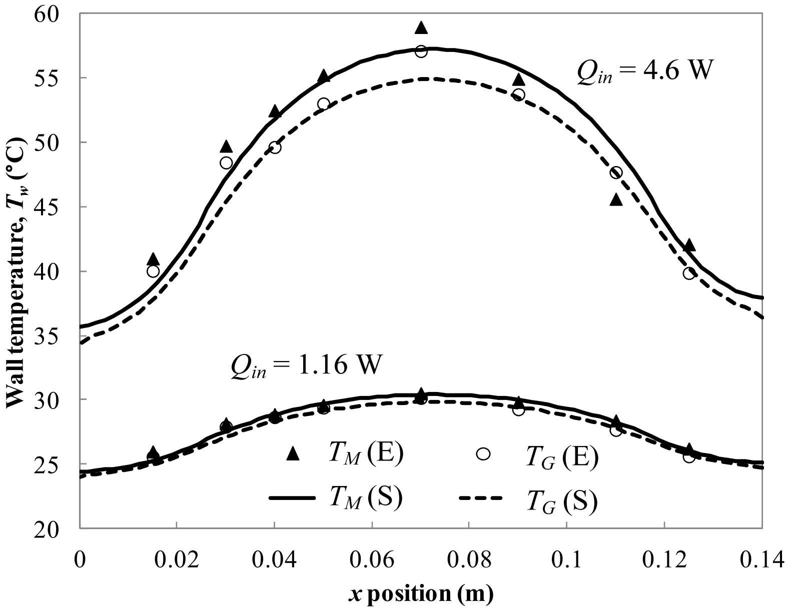

Figure 4.10: Typical wall temperature distributions obtained from experiments (symbols) and simulations (lines) under no flow conditions.

The accuracy of the values of the heat loss coefficient was verified by comparing the wall temperatures predicted by simulation with the measured wall temperatures. Figure 4.10 shows the typical wall temperature distributions on the Kovar and glass outer surfaces obtained from the zero flow experiments under different input power (Q_{in}). As can be seen, good agreement is found between the predicted and measured values, with the largest deviation being less than 5%.

4.2.2 Heat transfer of single-phase laminar flow

4.2.2.1 **Data reduction**

A series of single phase water flow heat transfer experiments were conducted in a straight channel for Reynolds numbers varied from 51 to 935 to validate the established system. For each run, the pump was set to provide the desired flow rate and the electrical power to the heater was adjusted to the desired level by the power supply. The system was then allowed to reach a steady state, which was achieved within 5-10 min from the time the flow conditions had stabilized.

The overall heat transfer balance at steady-state can be expressed as

$$Q_{in} = VI = Q_f + Q_{loss} \tag{4.8}$$

where Q_f is the heat transferred to the fluid and Q_{loss} is the power dissipated due to heat losses. Due to different properties of the glass and Kovar, there was a large temperature difference between the two outer surfaces. The heat loss coefficient was calculated for the heater and glass separately using the average temperature of each surface.

$$Q_{loss} = h_{loss,h} A_h (\bar{T}_h - T_a) + h_{loss,G} A_G (\bar{T}_G - T_a) \tag{4.9}$$

The heat transferred to the fluid can be estimated as

$$Q_f = \hat{C}_p \dot{m} (T_{out} - T_{in}) \tag{4.10}$$

However, the numerical simulation results show that Eq. (4.10) is not very accurate, because of the uncertainty of measuring the outlet temperature. The measured temperature taken near the Nanoport assembly can be a few degrees lower than the fluid temperature at the exit of the channel, as shown in Figure 4.11. Thus, Eq. (4.10) provides only a rough estimation of Q_f. In general, the heat loss to the environment, Q_{loss}, was less than 5% of the total power input for most cases (with a few falling in the 5-15% range), indicating that the heat input was transferred predominately into the fluid. Therefore, Q_f was estimate by subtracting the heat loss from the input energy using Eqs. (4.8) and (4.9). This provides rather high accuracy due to the small amount of heat loss. The outlet fluid temperature was then given by Eq. (4.11):

$$T_{out} = T_{in} + \frac{Q_{in} - Q_{loss}}{\dot{m}\hat{C}_p} \tag{4.11}$$

As mentioned before, conjugate effects exist in the current experimental design. Figure 4.12 presents the numerical result of the perimeter-averaged wall heat flux as a function of axial position for the case of *Re* = 902 and Q_{in} = 19.1 W. The active length of the heater is smaller than the channel length. As a result, the channel walls were not heated in the end parts of the test section and the heat flux decreases at the ends of the test section. It is apparent that in the axial region between 0.022 m to 0.115 m where the heating is applied, the wall heat flux is very uniform. The low values of the heat flux near the two ends are due to axial conduction.

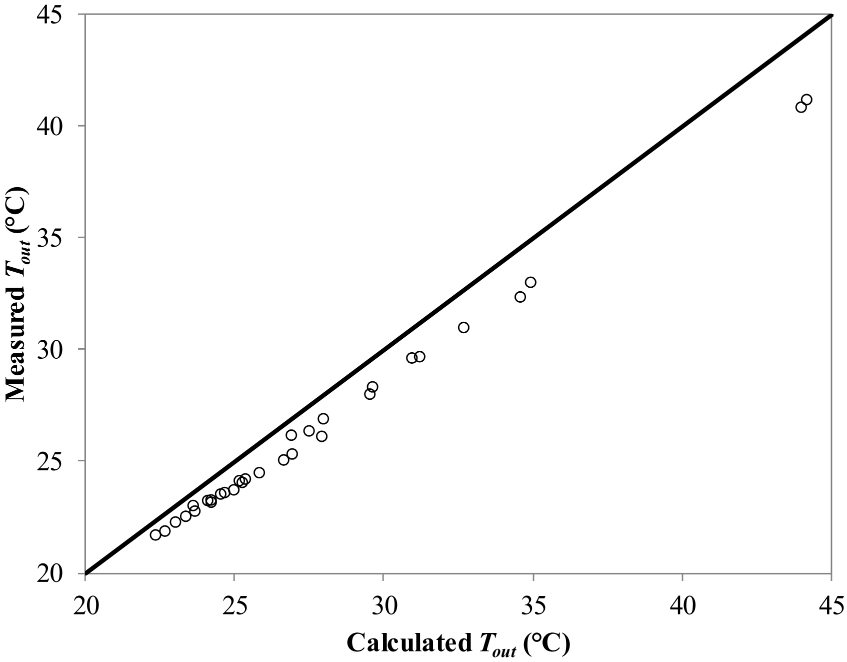

Figure 4.11: Comparison of the measured outlet temperature with the calculated values using Eq. (4.11).

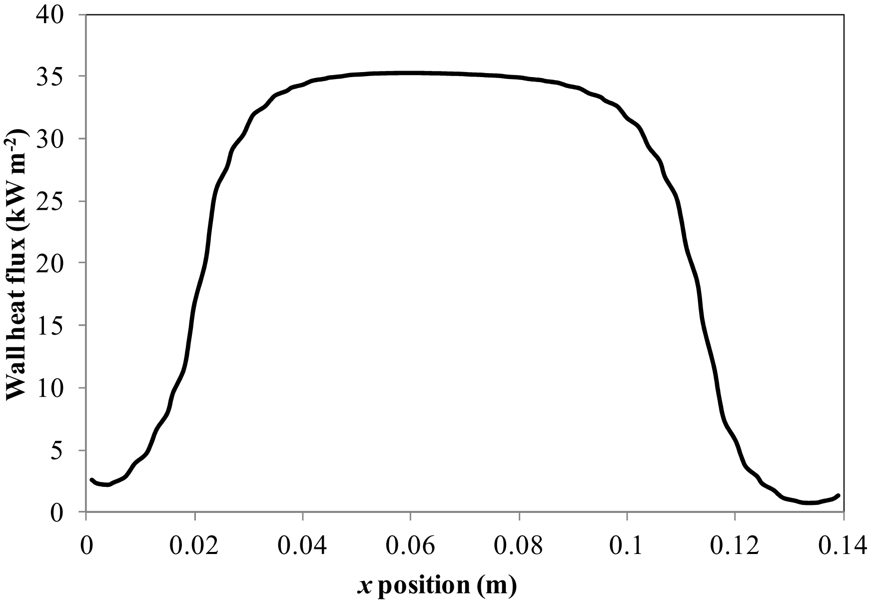

Figure 4.12: Perimeter-averaged wall heat flux along the straight channel for *Re* = 902 and Q_{in} = 19.1 W obtained from simulation.

Figure 4.13 shows the Kovar cross-section averaged value of axial heat flux in the streamwise direction. The axial heat flux is normalized by the surface heat flux supplied by the heater. As can be seen, the axial heat flux has two peaks at distances about 0.03 m and 0.11m from the inlet, where is near the edge between the heating (0.022-0.115 m) and non-heating regions. The negative values indicate the heat flux acts in the direction opposite to the flow (x) direction. Simulations were performed for a large range of Reynolds numbers which show that the lower the Reynolds number the larger the axial conduction effects become. However, the axial heat flux is less than 8% of the total input energy for the worst case near the ends. Therefore, the axial conduction can be neglected in the main part of the heating zone, which agrees with the results shown in Figure 4.12.

The simulated temperature profiles of the outer wall and inner wall of the metal and glass at y = 0.001 m are plotted in Figure 4.14. It is clear that the wall temperatures do not change linearly along the longitudinal x-direction. The temperature variations have different gradients, especially near the inlet and outlet parts where no heat flux is applied. This is a consequence of axial conduction effects. The bulk temperature is shown to vary in a quasi-linear manner along the flow direction, except near the two ends. In addition, there are several degrees of temperature difference between the outer surface of the substrate and the inner wall of the channel, especially in the glass side due to its relatively low thermal conductivity (k = 1.13 W K^{-1} m^{-1}). The peripheral-averaged wall temperature (T_w) that was obtained from Eq. (3.18) does not correspond to any temperature of the metal or glass wall due to the non-uniform distribution in the channel cross-section, as shown in Figure 4.5 (b).

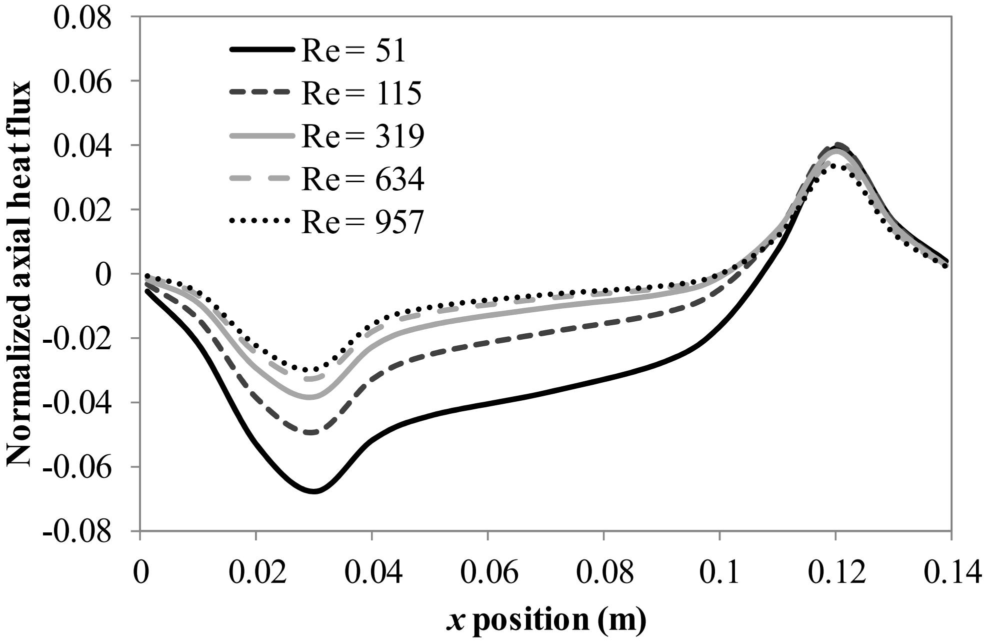

Figure 4.13: Normalized axial heat flux in the flow direction.

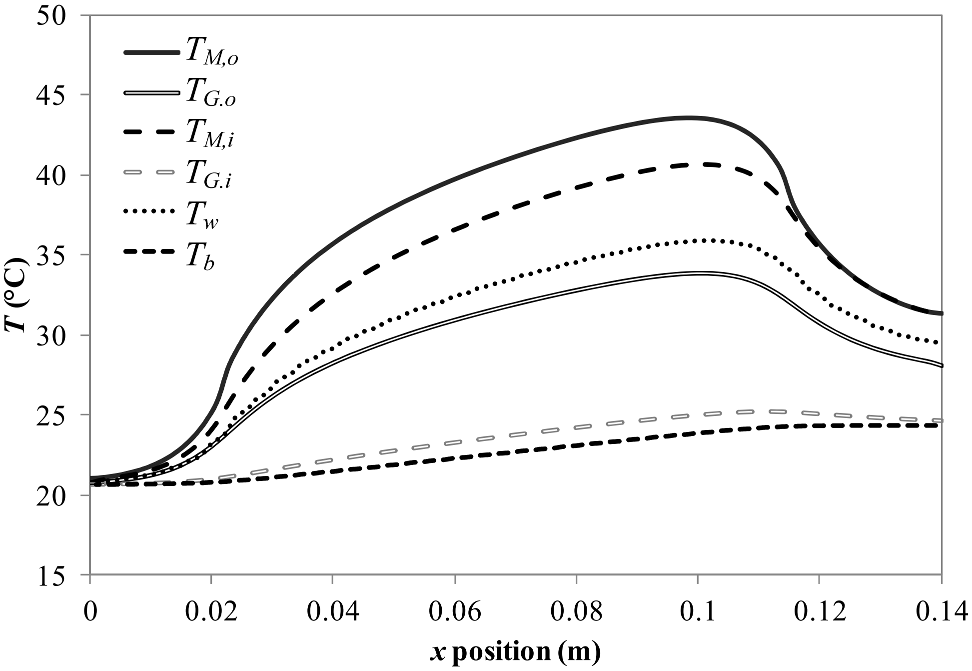

Figure 4.14: Wall temperature distributions along the straight channel for *Re* = 902 obtained from simulation. $T_{M,o}$ and $T_{G,o}$ are the outer wall temperature of the metal and glass, respectively. $T_{M,i}$ and $T_{G,i}$ are the inner wall temperature of the metal and glass, respectively. T_w and T_b are the peripheral-averaged wall temperature and bulk mean fluid temperature, respectively.

Experimentally, direct measurements of temperature and wall heat flux at the interface between fluid and solid are very difficult to implement. For simplicity, the perimeter-averaged wall temperature of the channel was calculated from Eq. (4.12), assuming uniform temperature distributions for the metal and glass inner surfaces at a certain cross-section.

$$\bar{T}_{w,x} = \frac{1}{P}\int_P T_w dL = \frac{1}{(L_M + L_G)}\left(\int_{L_M} T_{M,i} dL + \int_{L_G} T_{G,i} dL\right) \approx \frac{T_{M,i}L_M}{(L_M + L_G)} + \frac{T_{G,i}L_G}{(L_M + L_G)} \tag{4.12}$$

where $T_{M,i}$ and $T_{G,i}$ are the inner wall temperatures of the metal and glass, respectively; L_M and L_G are the cross-sectional perimeter lengths of the metal and glass parts, respectively. Therefore, the temperature difference between the channel wall and fluid can be written as:

$$\bar{T}_{w,x} - T_{b,x} \approx \left(T_{M,i} - T_{b,x}\right)\frac{L_M}{(L_M + L_G)} + \left(T_{G,i} - T_{b,x}\right)\frac{L_G}{(L_M + L_G)} \tag{4.13}$$

The glass can be taken as an adiabatic boundary since a very small fraction of the heat (< 5%) is lost from the surface. Therefore, the second term in Eq. (4.13) can be neglected.

The inner wall temperature of the metal was calculated based on one-dimensional heat conduction using the measured wall temperature at the outer surface, $T_{M,o}$, which was obtained from Eq. (3.14) as described in Chapter 3.

$$T_{M,i} = T_{M,o} - q_s R_M \tag{4.14}$$

where R_M is the thermal resistance of the metal substrate.

Therefore, Eq. (4.13) can be rewritten as

$$\bar{T}_{w,x} - T_{b,x} \approx \left(T_{M,i} - T_{b,x}\right)\frac{L_M}{(L_M + L_G)} = \left(T_{M,o} - q_s R_M - T_{b,x}\right)\frac{\pi}{\pi + 2} \tag{4.15}$$

The accuracy of Eq. (4.15) was investigated using simulation data without measurement uncertainty for a wide range of heat input (3.2 W < Q_{in} < 23.7 W) and Reynolds numbers (100 < Re < 900). Figure 4.15 compares the actual temperature difference, $\bar{T}_{w,x} - T_{b,x}$, from simulations with the predicted values from Eq. (4.15) and a good agreement is achieved, with the broken lines indicating values of ±10% of the prediction.

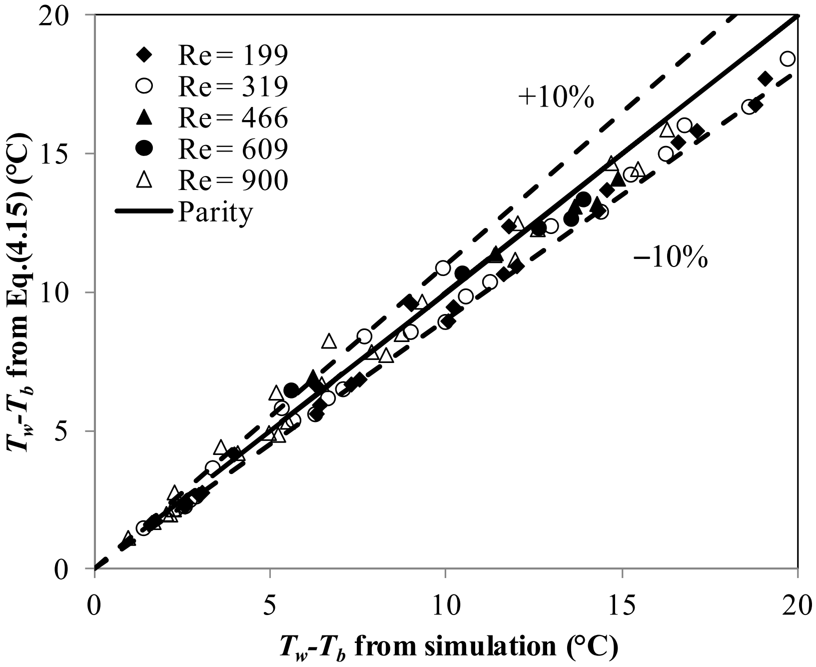

Figure 4.15: Comparisons of the temperature difference, $T_w - T_b$, between the simulation data and the predicted values obtained from Eq. (4.15).

Since the axial heat conduction can be neglected in the heating zone, a constant wall heat flux is assumed in the heating area. The bulk mean fluid temperature at location x ($T_{b,x}$) was calculated as

$$T_{b,x} = T_{in} + \frac{\dot{q}_w l_x P}{\hat{C}_p \dot{m}} \tag{4.16}$$

where l_x is the axial location from the start of the heating point.

4.2.2.2 **Heat transfer**

The single phase laminar flow heat transfer experiments were performed in the straight test section for Reynolds numbers ranging from 51 to 936. The typical temperature profiles measured from experiments are shown in Figure 4.16 and compared with the simulation results. It can be seen that the experimental temperatures of both the metal and glass outer surfaces agree very well with the corresponding numerical predictions. The perimeter-averaged wall temperature (T_w) calculated using Eq. (4.15) approaches the actual numerical values very closely. Also, the bulk temperatures calculated by Eq. (4.16) agree well with the simulation results. Eqs. (4.15) and (4.16) were validated for a wide range of Reynolds number. However, the constant heat flux assumption may not be valid at low Reynolds number (*Re* < 50) when axial conduction becomes significant.

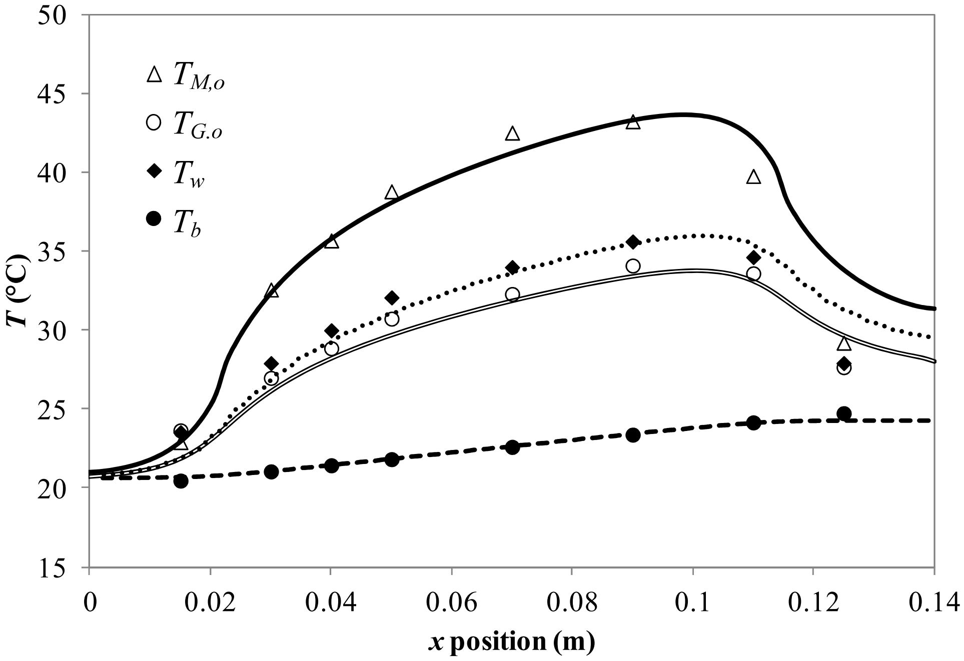

Figure 4.16: Comparison of the temperature distributions obtained from experiments (symbols, T_w is estimated using Eq. (4.15) and T_b is estimated using Eq. (4.16)) and simulations (lines) for *Re* = 902.

The local Nusselt number variation in the flow direction are plotted in Figure 4.17 for *Re* = 288 and *Re* = 902 with different levels of heat flux applied on the plate. As indicated by Incropera and De Witt (Incropera, 1996), the thermal entry length of a circular tube may be calculated from

$$L_{th} = 0.05 Re.Pr.d \tag{4.17}$$

For the semi-circular channels, the thermal entry lengths can be estimated by replacing the tube diameter, *d,* with the hydraulic diameter, d_h, giving a thermal entry length of 0.108 m and 0.338 m for *Re* = 288 and *Re* = 902, respectively. From Figure 4.17, the local Nusselt number in the straight channel obtained from the experiment is in agreement with the simulation value in the heated region (0.022-0.115 m). The large deviation at the two ends is due to axial conduction effects. The Nusselt number is found to be dependent on the Reynolds number due to the entrance effect.

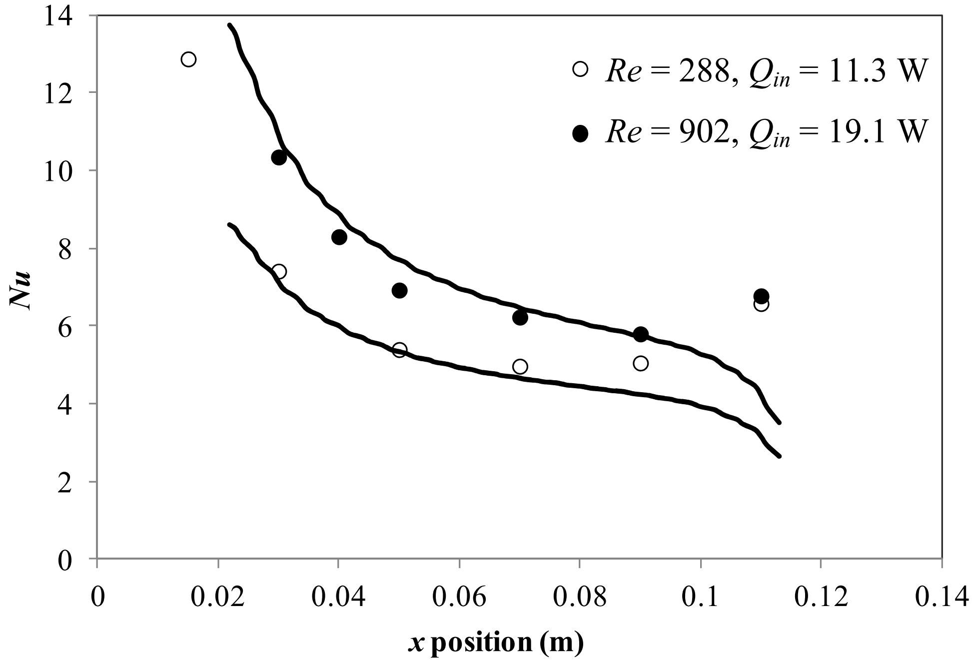

Figure 4.17: Comparison of the local Nusselt number obtained from experiments (symbols) and simulations (lines).

In Figure 4.18, the local Nusselt numbers, Nu_x, expressed as a function of the inverse of the Graetz number ($Gz = \frac{d_h PrRe}{x}$) are compared with the theoretical and numerical results for thermally-developing and hydrodynamically fully-developed laminar flow with different thermal boundary conditions. Shah and London (1978) gave solutions for the thermal developing flows for the semi-circular channel for two H1 boundary conditions. In the axial direction, they considered constant wall heat flux: in the peripheral direction; they considered (1) constant wall temperature along the entire periphery, and (2) constant wall temperature along the semicircular arc and zero heat flux (adiabatic) along the diameter. The simulation solutions for a straight channel with constant temperature boundary condition (T), constant wall heat flux boundary condition (H2) and the boundary condition encountered in the present experiments are also plotted in Figure 4.18.

It is important to specify exact boundary conditions for comparison of data from various sources. While the experimental arrangement does not correspond strictly to any standard thermal boundary condition, it has been shown that the heat transfer coefficients agree closely with theoretical results for H1 boundary conditions. Due to the short length of the test section (0.14 m), the flow was mainly in the thermally-developing region for most of the experiments. Simulation was conducted to obtain the fully-developed value of Nu under the present boundary conditions by extending the channel length. The fully-developed Nusselt number calculated numerically is 3.7, which lies between the values of 3.160 and 4.089 for the two different H1 boundary conditions (Shah and London, 1978).

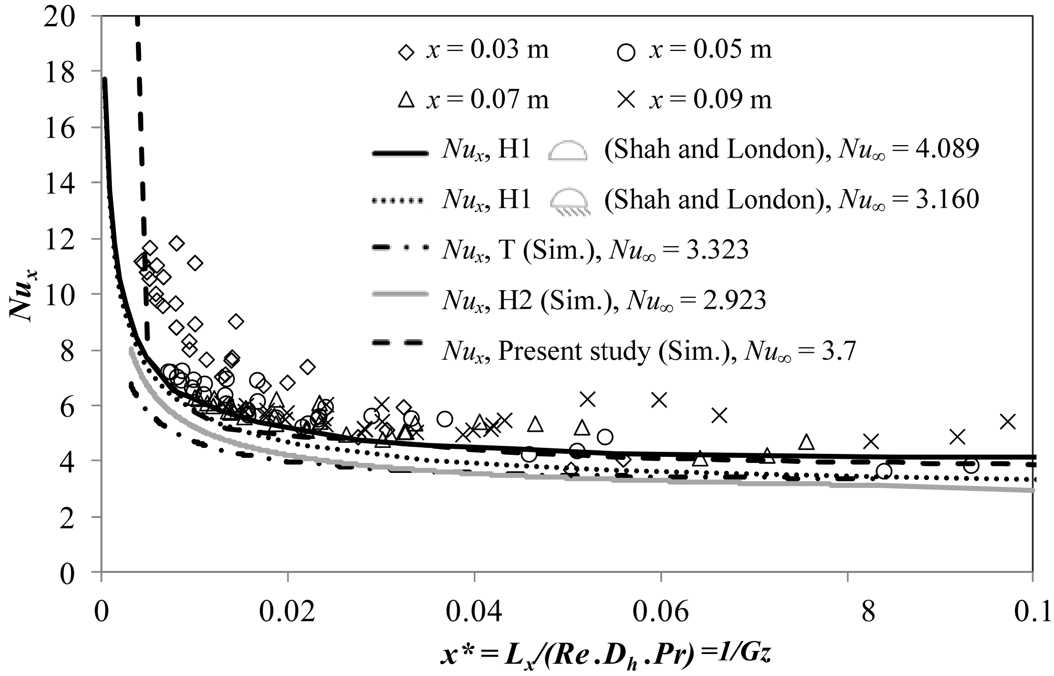

Figure 4.18: Comparison of the experimental straight channel single-phase local Nusselt numbers with theoretical results and simulation results for different thermal boundary conditions.

As seen in Figure 4.18, the Nusselt number approaches a constant as the inverse Graetz number approaches infinity, indicating fully-developed heat transfer. Most of the experimental Nusselt numbers fall within 20% of the standard Graetz solution. Large deviations can be found near the unheated region (e.g. $x = 0.09$ m) where the axial conduction effect is significant. One point to note here is that data for the unheated sections were not included in the comparison due to different thermal boundary condition from the main part. The above results also show that the conventional heat transfer correlation for large tubes can be applied for predicting the heat transfer performance of fluid flow in microchannels. As expected, there is no significant size effect for water flow in channels within the diameter range used in this study.

The average Nusselt number for single-phase flow was determined by averaging the local Nusselt numbers at axial positions along the flow direction. The data for the last location ($x = 0.11$ m) were not used in subsequent analysis due to the large uncertainties in temperature measurement at the channel ends. Figure 4.19 shows the variation of the average Nusselt number with the Reynolds number. The error bars represent one standard deviation for the local Nusselt numbers measured at different locations. As can be seen, the average Nusselt number increases with increasing Reynolds number due to the entrance effects as the channel length is not long enough for fully-developed flow. A good agreement can be found between the experimental data and the simulation predictions over the entire Reynolds number range in this study.

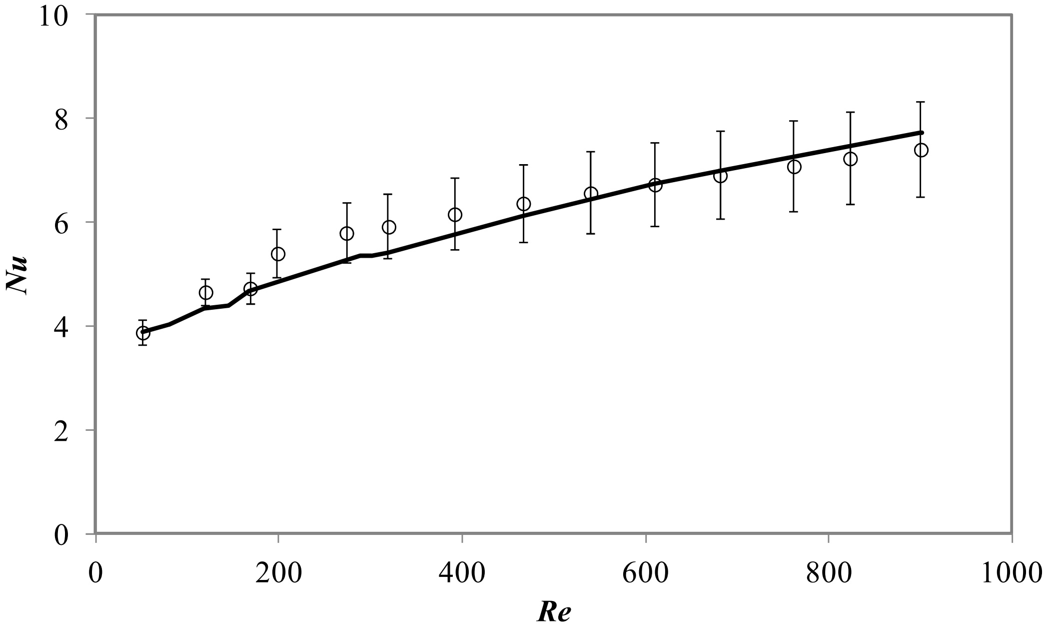

Figure 4.19: Variation of average Nusselt numbers with Reynolds number from experiments (symbols) and simulations (solid line). The error bars represent one standard deviation for the local Nusselt numbers measured at different locations.

4.2.3 Error analysis

Performing a standard error analysis, the average uncertainties in determining the Nusselt number, Nu, are presented in Table 4.2, which also lists the uncertainties in the individual measurements needed to evaluate the Nusselt number. The greatest source of uncertainty in determining the Nusselt number came from the estimation of the inner wall temperature and wall-fluid temperature difference associated with Eq. (4.15), whose uncertainty was estimated to be ±10%. This is caused by the conjugate effect in the present experimental design. Combined with the uncertainties in flow properties, geometry of the test sections, and power calculations, the average uncertainty in the local Nusselt number in the main heating region was estimated to be 14%. The biggest uncertainty of calculated Nusselt number near the channel ends is about 30% due to axial conduction effect.

Table 4.2: Uncertainties of measured parameters and calculated Nusselt number.

Parameter	Uncertainty
Channel diameter (mm)	±1%
Channel length (mm)	±1%
Thermocouple temperature (°C)	±0.15 °C
RTD temperature (°C)	±0.15 °C
Mass flow rate (kg m^{-2} s^{-1})	±2%
Heat flux (W m^{-2})	±5%
Nusselt number	±14%

4.3 Summary

Heat transfer of laminar flow in a semi-circular straight channel embedded in the “hybrid test section” was studied both numerically and experimentally. A numerical model of the complete experimental device was developed to study the conjugate heat transfer problem involved in the current experimental design. It is confirmed that the conjugate effects in microchannels induce non-uniform temperature and heat flux distributions at the channel wall. Changing of heating method and metal thickness had little effect on the heat flux and temperature distributions at the wall-fluid interface.

Calibration of the heating system used in this study was performed carefully. Good agreement was found between the experimental data and the simulation results. Heat transfer experiments for single phase water flow were conducted for a wide range of Reynolds numbers. Verification of the experimental approaches was performed by comparing the experimental data with simulation predictions. Measurements of local Nusselt number in thermally-developing laminar flow agree with simulation predictions within 14% in the main heating region. As the microchannels used in this study do not correspond strictly to any standard thermal boundary condition for laminar flow, the fully-developed Nusselt number (Nu_{str} = 3.7) in the straight channel under the conditions of the present study will be used as a reference for the study of wavy channels.

Chapter 5

Hydrodynamics in Wavy Microchannels

Many researchers have investigated developing and fully-developed flows in wavy channels and detected an early transition from laminar to turbulent flow. However, they have mostly reported velocity data in flat channels with a periodically converging-diverging cross-section. Many more computational studies have been published than experimental ones (Gong et al., 2011a, Ramgadia and Saha, 2012, Ramgadia and Saha, 2013). Recently, Zheng et al. (Zheng, 2013, Zheng et al., 2013a, Zheng et al., 2013b) studied numerically the impact of using tortuous channels to enhance single-phase, laminar heat transfer relative to straight channels. They have shown that for a zigzag path there is a progression, with increasing Reynolds number, from steady, ordered flow (with all repeating units having the same heat transfer behaviour once the flow is developed) to steady, chaotic flow and then transient flow. The heat transfer enhancement was affected greatly by the flow conditions and the geometry of the channel.

In the analysis presented in this chapter, micro-PIV techniques were employed to determine velocity fields in wavy microchannels and the experimental data were compared with CFD results. Extensive flow visualisation experiments were performed on five different geometries for a wide range of Reynolds number. The experiments revealed the complexity of the flows in these channels and showed how the geometry affects the important features of the flow.

5.1 Flow field validation in wavy microchannels

Details of the flow visualisation using the micro-PIV system have been described in Chapter 3. The technique was validated by using a straight channel, showing that detailed velocity profiles can be obtained with high accuracy in most regions of the flow, except near the wall region. The capability of micro-PIV system is further explored by validating the two-dimensional (2D) flow fields in wavy microchannels through comparisons with the simulation results. Details of the computational model for wavy channels are described in Chapter 6.

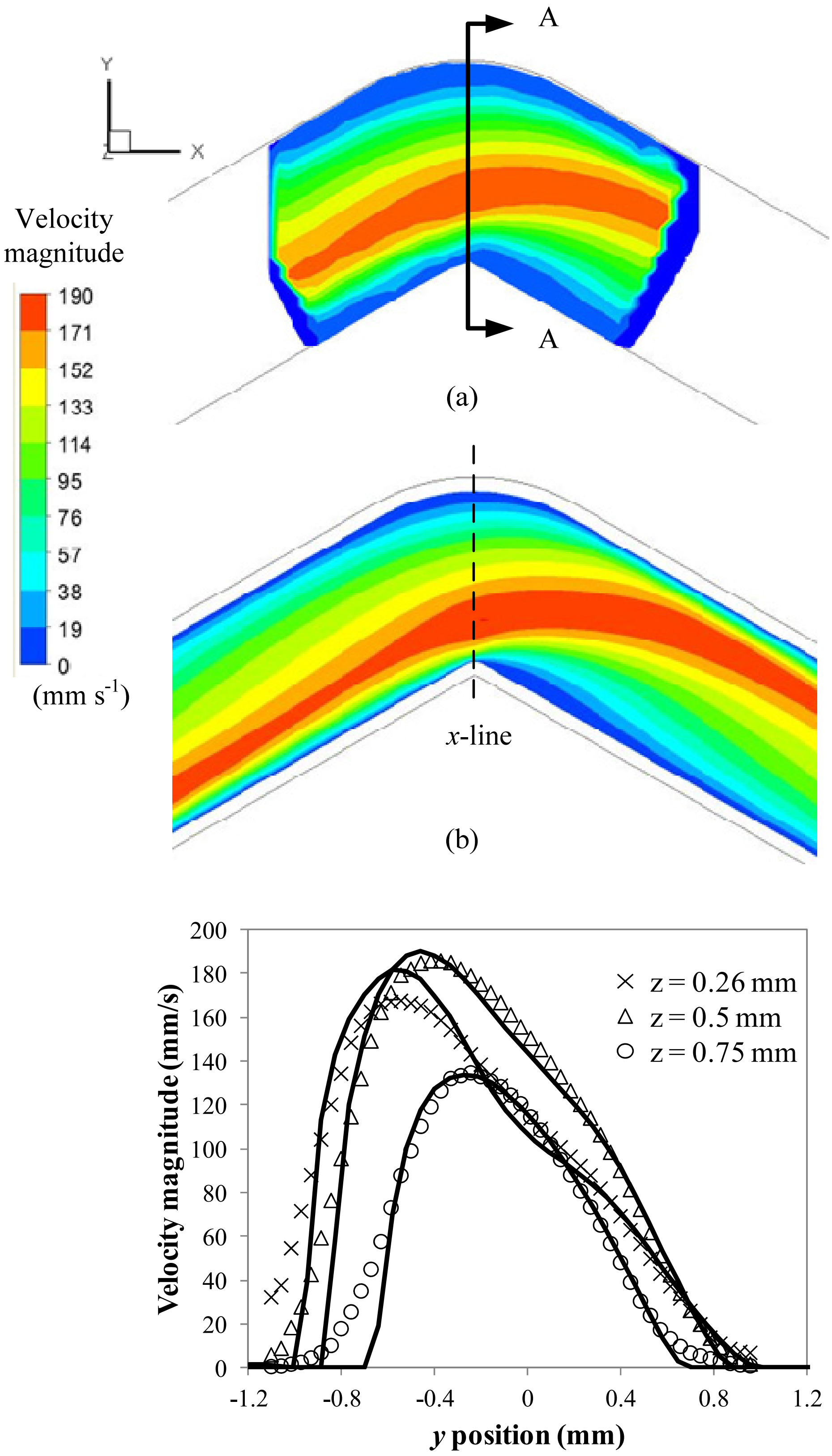

(a)

(b)

(c)

Figure 5.1: 2D velocity fields at z = 0.5 mm at Re = 128 from: **(a)** micro-PIV; **(b)** CFD simulation; and **(c)** velocity profiles of x-lines at different depths (solid lines: simulation, symbols: micro-PIV).

Contour plots of the velocity magnitudes of measured components, *u* and *v*, obtained using the micro-PIV system in a 30° zigzag (Zigzag 2) channel and corresponding simulation plots at *Re* = 128 are presented in Figure 5.1. Figure 5.1 (a) shows the planar velocity field at depth *z* = 0.5 mm (*x*-*y* plane) that was obtained directly from micro-PIV. The numerical solution of the flow field at the same plane is shown in Figure 5.1 (b). It is found that at *Re* = 128, the velocity profiles are different from the straight pipe solution and are no longer symmetric. The measured flow field is in good agreement with the simulation results. A more quantitative comparison between the experimental and numerical results can be seen in Figure 5.1 (c). This figure shows the velocity magnitudes along *x*-lines at three different depths. Discrepancies between the experimental and computational data seem to be found mainly near the wall of the channel. This is similar as what was found in the straight channel measurements.

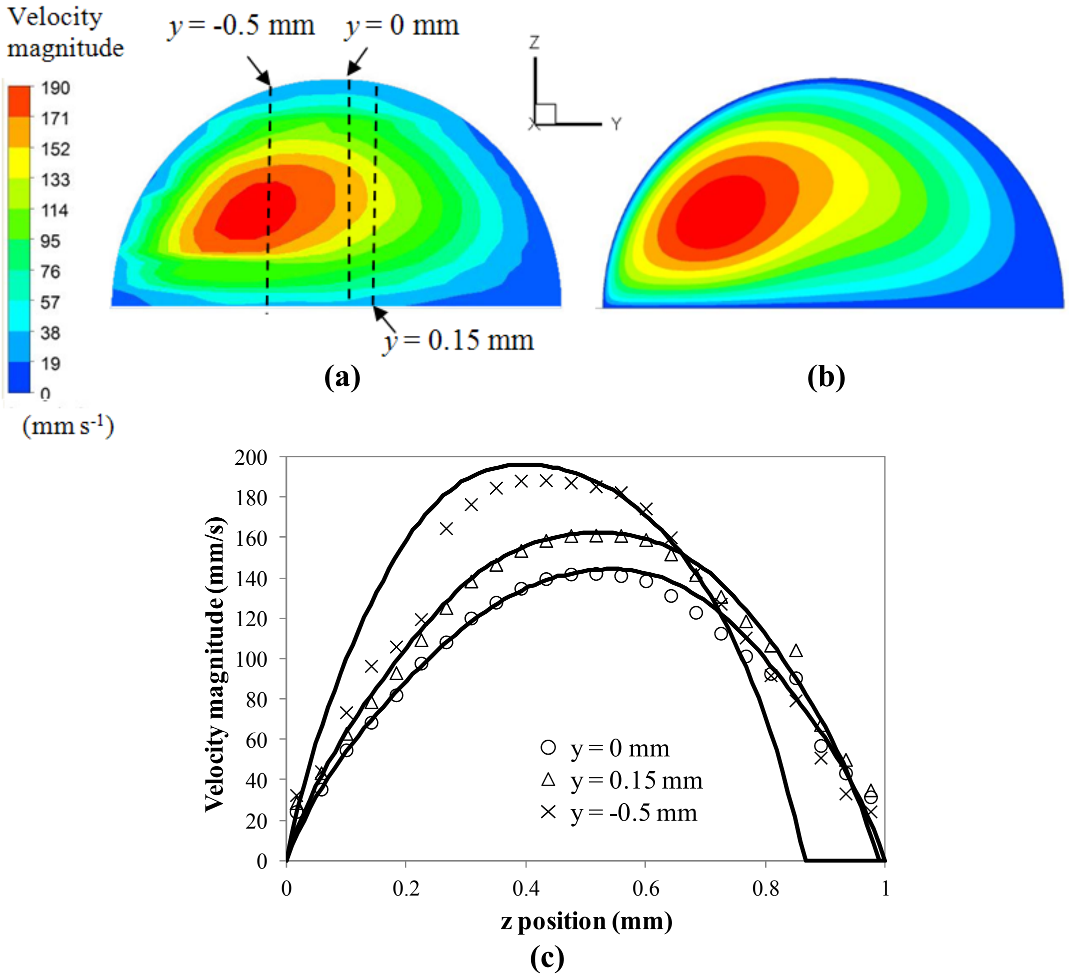

Figure 5.2: 2D velocity fields on the cross-section (plane A-A) at *Re* = 128 from: **(a)** micro-PIV; **(b)** CFD simulation; and **(c)** velocity profiles of different *y*-lines (solid lines: simulation, symbols: micro-PIV).

PIV measurements were taken at 22 different planes in the depth-wise direction of the zigzag channel. The velocity field (u and v components) on the cross-section was obtained by stacking and interpolating the velocity data measured on the 22 planes. The velocity contour plots of plane A-A (indicated in Figure 5.1 (a)) are shown in Figure 5.2 with (a) and (b) obtained from the micro-PIV and simulation, respectively. Figure 5.2 (c) presents the velocity profiles at three different y-lines. Similarly, the velocity peaks shift from the middle of the channel due to the curvature of the bend. A very good agreement between the PIV data and simulation results is again seen in Figure 5.2.

5.2 Flow dynamics of zigzag channels

5.2.1 Time-resolved velocity measurements

A zigzag channel (Zigzag 1) having parameters of $R_c/d = 0.51$, $L/d = 1.75$, and $\theta = 45°$ was used as the base case geometry in this study. Micro-PIV measurements were taken at the tenth bend (Bend 10) to ensure the flow was fully-developed.

As described before, for a steady flow regime, time-averaged velocities were obtained by averaging the velocity values over a series of PIV images (typically 200 images) taken at separate times. In order to investigate the time-dependent characteristics of flow in the zigzag channel, a recording point has been placed in the middle of Bend 10 and the normalized velocity magnitude $\left(\frac{u(t)}{\overline{u(t)}}\right)$ against time at the point was extracted at various Reynolds numbers. As shown in Figure 5.3, at $Re = 135$ and 215, the velocity variations are very small, indicating the flow is steady. At a higher Reynolds number ($Re > 330$), the velocity magnitude starts oscillating irregularly suggesting that the flow is in the transient regime.

The velocity fluctuations are commonly used as an indicator of the onset of this transition. The Root Mean Square (RMS) velocity fluctuations, which correspond to the standard deviation, were used in this study. Velocity measurements were taken at Bend 10 for Reynolds number up to 880. Sequences of images were recorded at 1000 fps which gives a time resolution of 0.002 s. 1000 image pairs were used to get the mean velocity and RMS set. Due to the finite particle concentration, it is not always possible to have particles located at a particular point. Therefore, a very small window was created at the region of interest (ROI) using the masking function in the VidPIV software. The window size was 30 pixels × 30 pixels and corresponded to 127 μm × 127 μm when the 4× objective was used in the experimental setup. The spatial averaged velocity of the ROI represents the local velocity very well due to the small window size while reducing the large noise present if data are collected at a single point.

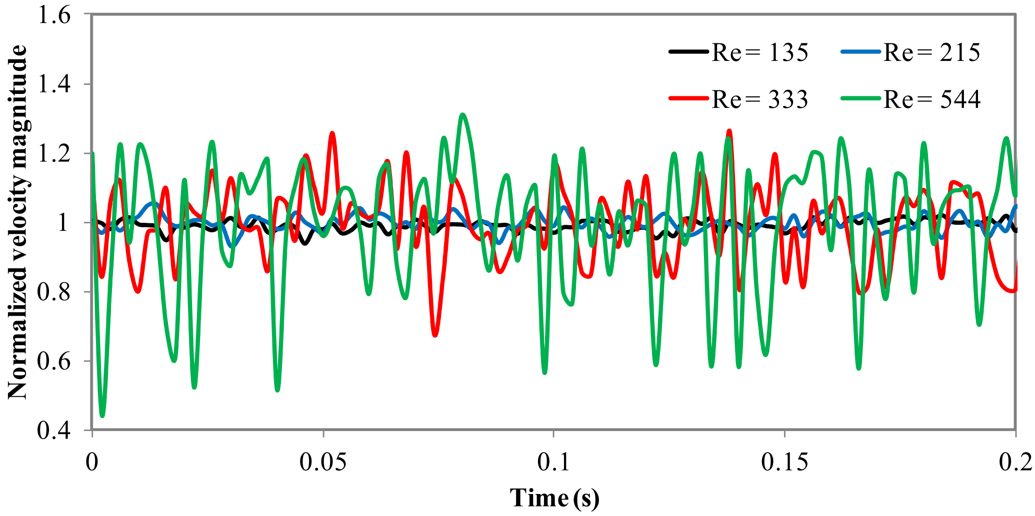

Figure 5.3: Temporal evolution of normalized velocity magnitude at a recording point located in the middle of Bend 10.

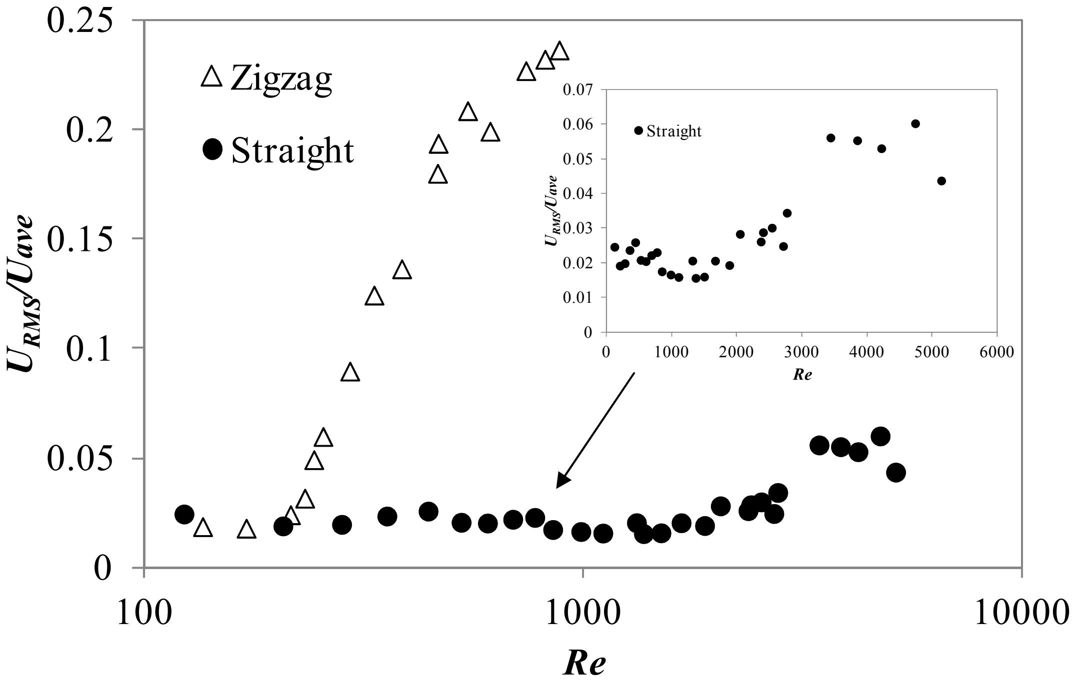

Figure 5.4: Normalized velocity fluctuation for a wide range of Reynolds number.

Figure 5.4 shows the dimensionless profile of RMS velocity fluctuations $\frac{U_{RMS}}{Uave}$ located in the middle of Bend 10. The velocity fluctuations are compared with those in a straight channel. It can be seen that the fluctuation in the wavy channel is much more significant than that in the straight channel, especially at high Reynolds numbers.

For the straight channel, the velocity fluctuations are very small (less than 3%) for $Re < 2000$. At about $Re = 2300$, a slight increase in the RMS fluctuation was observed indicating that the flow is beginning to transition to turbulence, as shown in the non-logarithmic scale plot. As expected, the velocity fluctuations rise sharply at Reynolds number between 2500 and 3500, due to the increasing turbulence of the flow. No obvious early transition to turbulence is observed in the present small passage compared with the experimental data for macroscale pipe flow. For the zigzag channel, two regions are clearly distinguished by a critical Reynolds number (Re_c), which is defined as the point where the fluctuation starts growing sharply. For $Re < Re_c$, which is about 215, the normalized velocity fluctuation is generally less than 3% and does not change much with the Reynolds number. As for the laminar flow region in the straight channel, these fluctuations at low Reynolds numbers correspond to the uncertainties of the micro-PIV technique as mentioned in Chapter 3. When $Re > Re_c$, the velocity fluctuations increase, which indicates flow instability is occurring. The velocity fluctuations grow significantly with a further increase of Reynolds number ($Re > 400$), showing that the flow enters the transient regime. It is obvious that the flow transition from steady to unsteady occurs at a relatively low Reynolds number.

Interesting flow characteristics were observed in the channel when the flow first became unsteady. A typical temporal evolution of the velocity profile at $Re = 215$ and the corresponding Fourier power spectrum of the normalized velocity magnitude are shown in Figure 5.5. Obviously, the velocity was observed to vary regularly showing a temporal periodic oscillation. A dominant fundamental frequency in the vicinity of 50 Hz is evident. A harmonic frequency around 100 Hz with lower amplitude can also be observed.

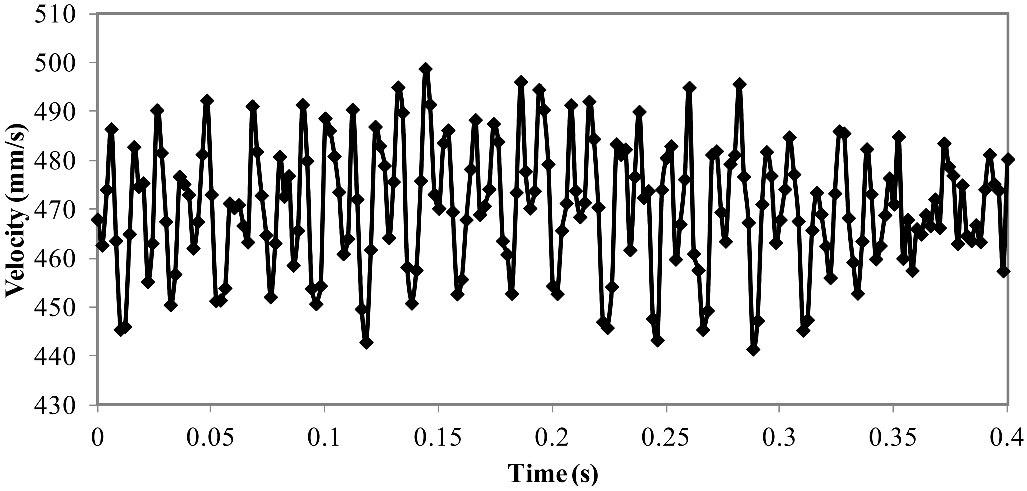

(a)

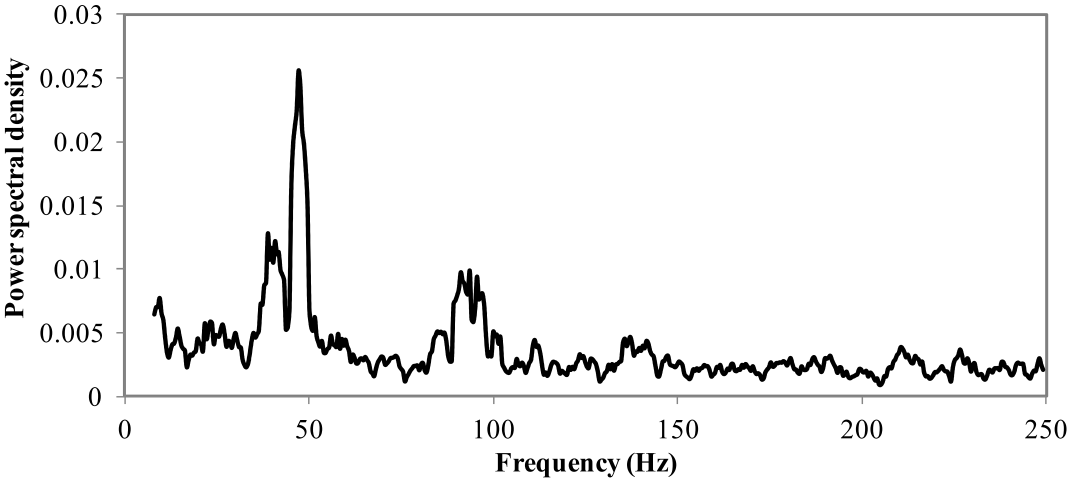

(b)

Figure 5.5: **(a)** Temporal evolution of the velocity; and **(b)** Fourier power spectra of the normalized velocity magnitude for *Re* = 215.

The Fourier power spectra of the normalized velocities at different Reynolds numbers are plotted in Figure 5.6. As can be seen from the plot, for the steady flow regime (*Re* < 215), the spectral energy across the whole frequency range is very low. At Reynolds numbers between 215 and 232, the velocity starts oscillating and there is a distinct frequency peak located at around 50 Hz. With an increasing Reynolds number (*Re* > 300), the Fourier spectrum of the velocity evolution becomes broadband and continuous as no predominant frequency can be observed in the power spectrum.

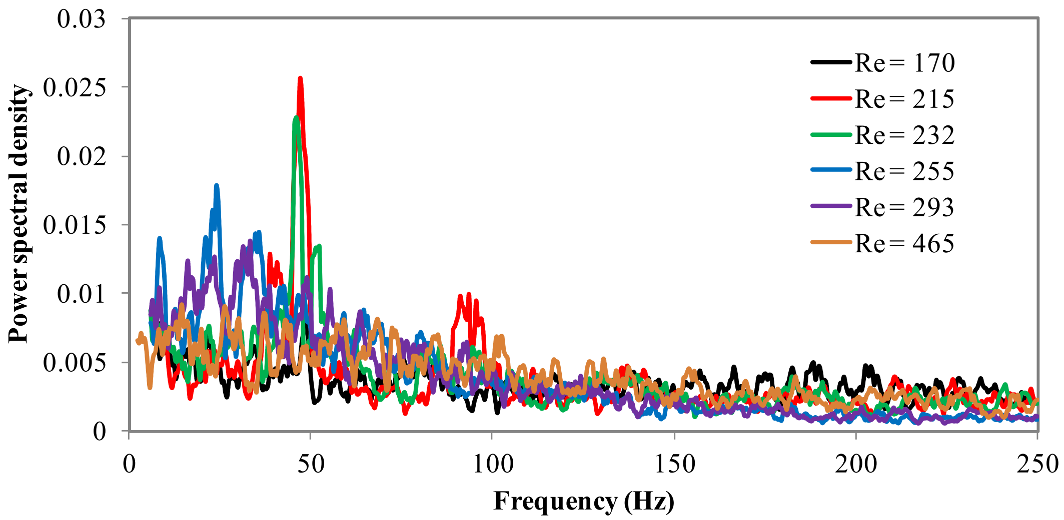

Figure 5.6: Fourier power spectra of normalized velocity magnitude for different Reynolds numbers.

In many studies, the flow was found to be steady in part of the channel and unsteady in the rest of the channel (Rush et al., 1999, Kim, 2001, Zheng et al., 2013b). As the Reynolds number is progressively increased, the onset of unsteadiness occurs much earlier in the channel. To study the flow development along the channel, PIV measurements were taken at three different bends in the channel. Figure 5.7 shows the recording points at which the velocity was measured. These are located at the identical position at each of the bends.

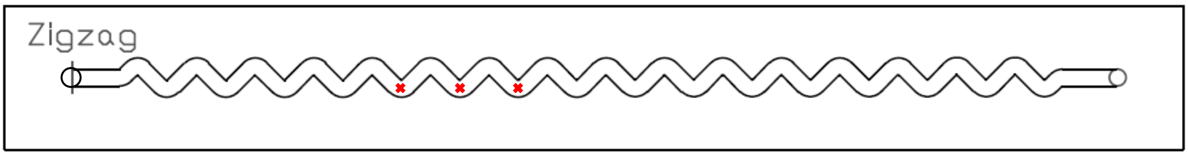

Figure 5.7: Locations of the recording points.

Figure 5.8 shows the standard deviation of velocity variations at the recording points for different Reynolds numbers. It can be seen from the figure that at a low Reynolds number (*Re* < 215) the flow is steady with standard deviation less than 5% and does not vary with the bend location. As the Reynolds number increases, this trend breaks down and the velocities vary along the channel. The flow becomes unsteady at the 7th bend at *Re* = 293 and in the case of *Re* = 465 it is already unsteady at the 5th bend. The bend at which the flow first becomes unsteady moves upstream with increasing Reynolds number. Eventually, at a high enough Reynolds number, the flow is unsteady at the first bend.

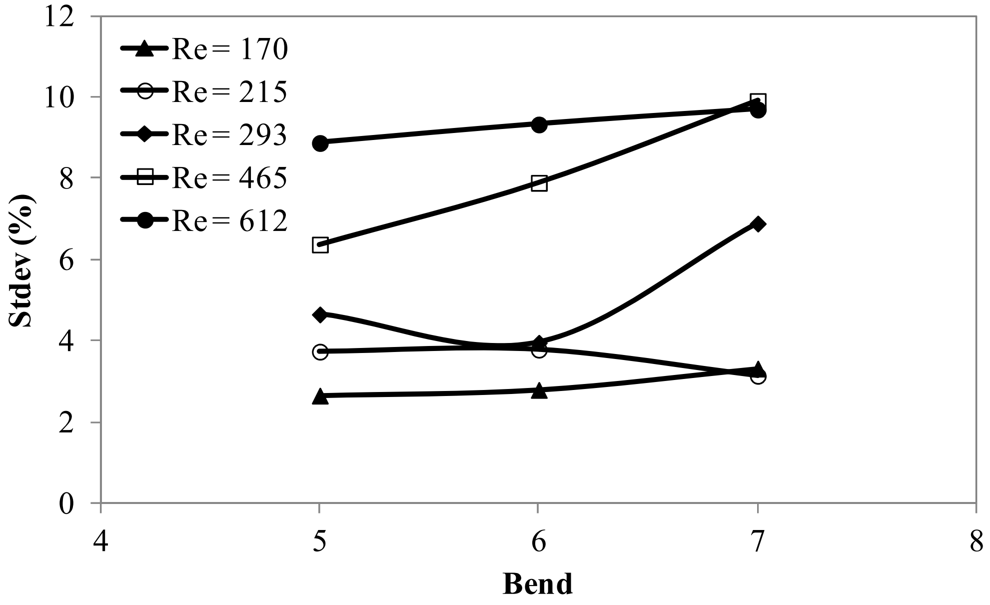

Figure 5.8: Standard deviation of velocities at the recording points for different Reynolds numbers.

5.2.2 Chaotic behaviour

It should be noted that chaotic advection was found in zigzag channels in previous simulations in the steady, laminar flow regime (Zheng, 2013). The flow pattern was not spatially periodic when the Reynolds number is above a certain range, demonstrating the existence of significant chaotic advection. For the same geometry, the simulations showed that chaotic advection occurred at a Reynolds number higher than 200. However, in the experiments time-dependent flow was observed over the range of Reynolds number where steady chaotic advection occurred.

To further study the characteristics of chaotic advection, Zheng (2013) performed simulations of flow in the zigzag channel for Reynolds number varying from 295 to 300. He found that the flow field changes significantly even for a very small variation in the inlet conditions. However, the averaged characteristics was found to change within 3% for the Reynolds number between 295 and 300, indicating that the overall performance remain orderly in this chaotic flow regime. In the experiments, it is found that the inlet flow is never completely steady, the steady regime of chaotic advection would be hard to maintain in practice. This possibly explains the early transition to unsteady flow observed in experiments.

To examine the dynamic behaviour of flow with disturbances, Zheng (personal communication, 2014) conducted a transient computation of Zigzag 1 channel with finite perturbation in the inlet condition.

The mean flow velocity with an inlet flow rate perturbation can be expressed as

$$u_m = u_m^0(1 + F_{tri}(a, f, t)) \tag{5.1}$$

where u_m^0 is the mean velocity without perturbation and F_{tri} is a triangle wave function with an amplitude of a and frequency of f.

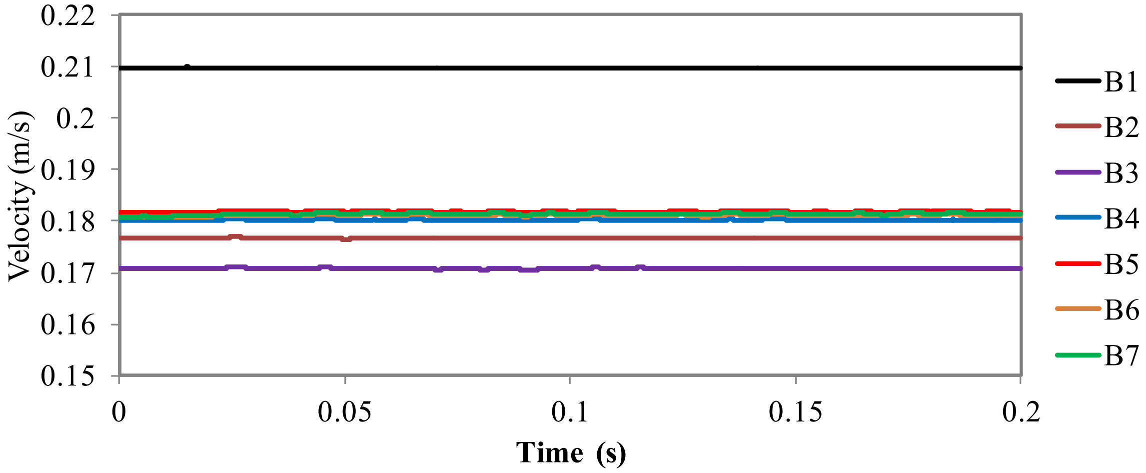

(a)

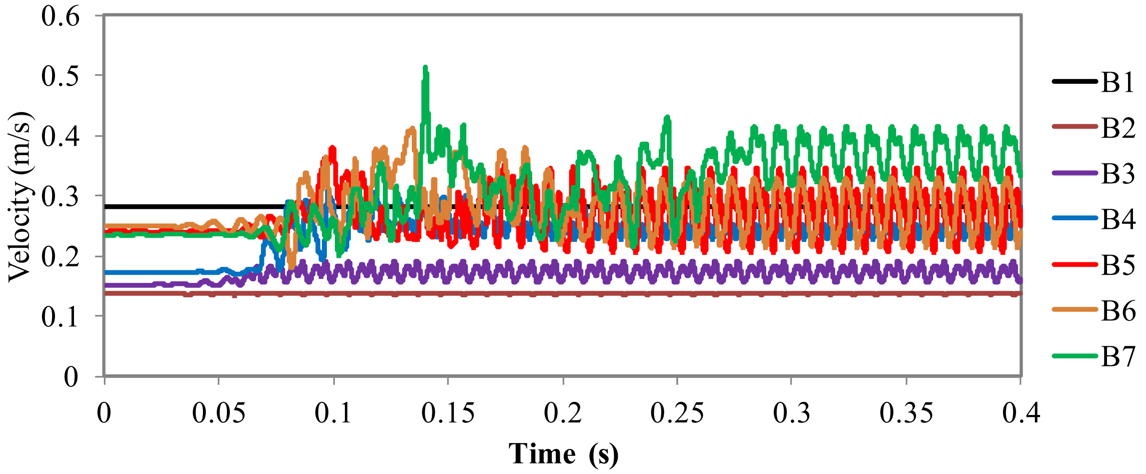

(b)

Figure 5.9: Temporal evolution of velocities at monitor points for: **(a)** *Re* = 200 with perturbation of *a* = 0.01 and *f* = 100 Hz; and **(b)** *Re* = 300 with perturbation of *a* = 0.001 and *f* = 100 Hz.

Without flow rate perturbation, a steady and spatially periodic flow field can be found in the channel at $Re \leqslant 200$, after reaching a “developed” state. The flow is steady at *Re* = 300, however flow patterns are varied in different units, even after sufficient flow development.

When a perturbation of $a = 0.001$ and $f = 100$ Hz was applied to the inlet flow, the flow field remain nearly constant at *Re* = 200. However, significant velocity fluctuations were observed at *Re* = 300. Figure 5.9 (a) shows the temporal evolution of the velocity at monitor points in the middle of the cross-section plane of seven consecutive bends. Velocity variations are within 0.5% at *Re* = 200 even when the perturbation amplitude was increased to a = 0.01. For *Re* = 300, at the first and second points the velocity magnitudes remain constant. However, the velocity fluctuates dramatically after the third point, indicating the flow has transitioned to an unsteady state downstream of the third unit.

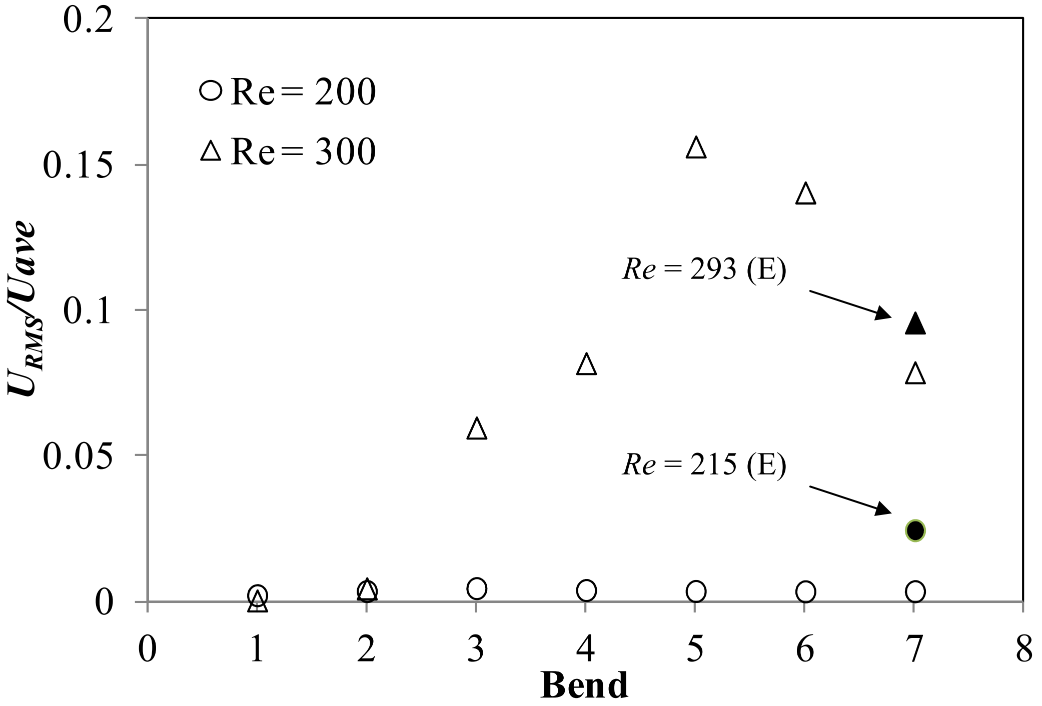

Figure 5.10: Normalized velocity fluctuation for flow with perturbation in the inlet condition.

The dimensionless profile of RMS velocity fluctuations $\frac{U_{RMS}}{Uave}$ at the monitor points are presented in Figure 5.10. As can be seen, the normalized velocity fluctuation is very small at *Re* = 200 since the flow is steady. At *Re* = 300, the velocity fluctuation can be as large as 15% with only 0.1% disturbance in the inlet flow. The fluctuation amplitudes measured in the experiments at the seventh point at *Re* = 215 and *Re* = 293 are also presented in Figure 5.10. A very similar level of fluctuation can be found between the simulation and experimental results. Although the comparison is qualitative rather than quantitative, as the form and amplitude of the experimental fluctuations are unknown, the simulations lend support to the idea that at a high enough Reynolds numbers small fluctuations can trigger transient behaviour. Due to the difficulty in controlling disturbances in experiments, experimental results of instability are essentially for finite random disturbances. It is evident from the simulations that the flow is very sensitive to the inlet conditions in the steady chaotic regime and small disturbances in the inlet flow lead to an early transition to unsteady flow.

5.2.3 Transient behaviour

To investigate the transient flow behavior, a higher sampling rate is required to resolve small-scale structures. For the fast Fourier transform (FFT) method used in this study, the frequency resolution df can be calculated with the following equation:

$$df = \frac{1}{t_{acq}} = \frac{f_s}{N} \tag{5.2}$$

where t_{acq} is the acquisition time; N is the number of samples recorded; and f_s is the sampling frequency. The frequency resolution is determined solely by the acquisition time. The frequency resolution improves as the acquisition time increases.

The sampling rate of a time-series data determines the maximum resolvable frequency. According to the Shannon sampling theorem, the maximum resolvable frequency is half the sampling frequency.

$$f_{max} = f_{Nyquist} = \frac{f_s}{2} \tag{5.3}$$

where f_{max} is the maximum resolvable frequency and $f_{Nyquist}$ is the Nyquist frequency.

The velocity was recorded with a sampling rate of 3000 Hz (camera recording at 6000 fps) which could resolve the frequency up to 1500 Hz. A much higher sampling rate is not practical as the image resolution would be too small to analyze using the VidPIV software.

The power spectra of the normalized velocity magnitudes at the recording point at Bend 10 for different Reynolds numbers are shown in Figure 5.11. For the power spectrum at *Re* = 232, the peak at around 50 Hz clearly corresponds to the regular velocity fluctuations apparent in Figure 5.5. A similar decay trend can be found for three Reynolds numbers with the energy decreasing exponentially at higher frequencies. As the Reynolds number increases, the curves shift to the right with a wider range of frequencies. This is because the instabilities of flow are not sufficiently damped by viscous action and the energy moves to smaller spatial scales before it is dissipated with increasing Reynolds number.

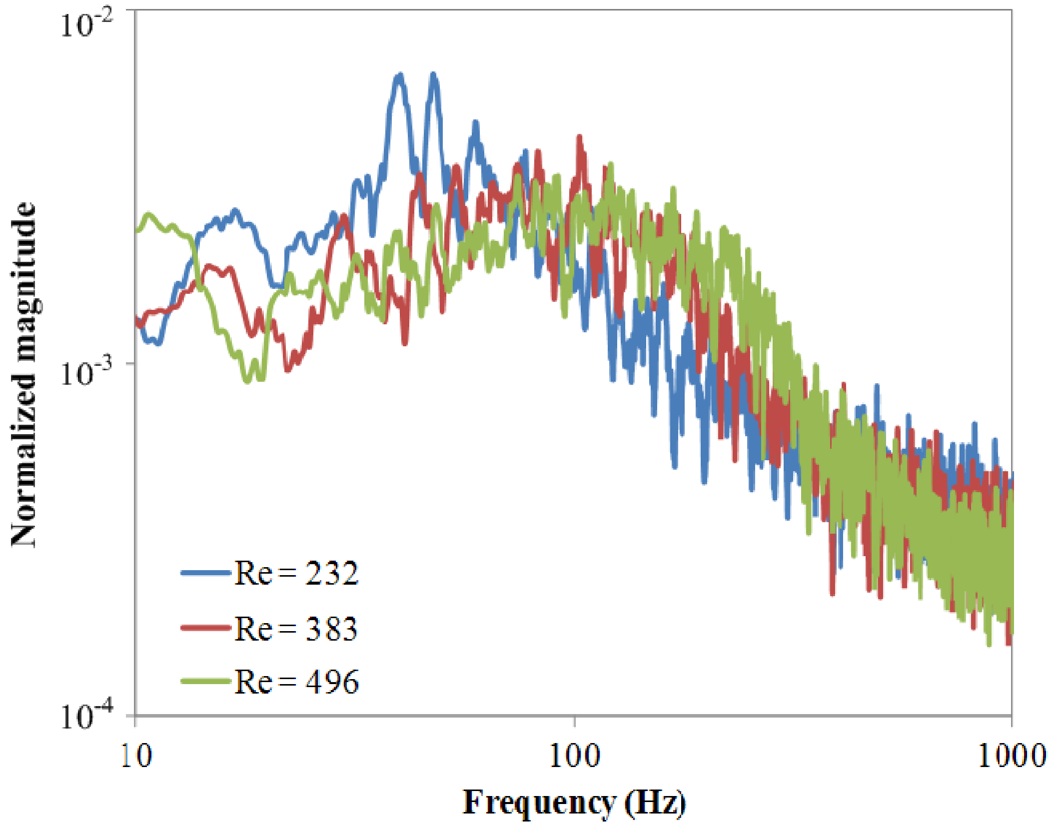

Figure 5.11: Fourier power spectra of normalized velocity magnitudes for different Reynolds numbers (sampling frequency = 3000 Hz).

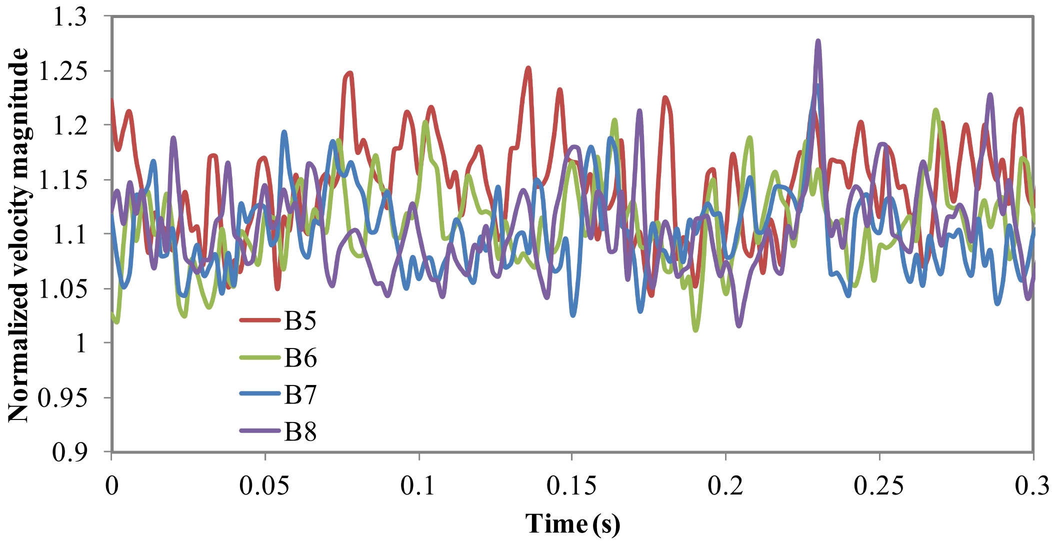

Figure 5.12: Temporal evolution of normalized velocity magnitude at the recording points located at different bends for *Re* = 502.

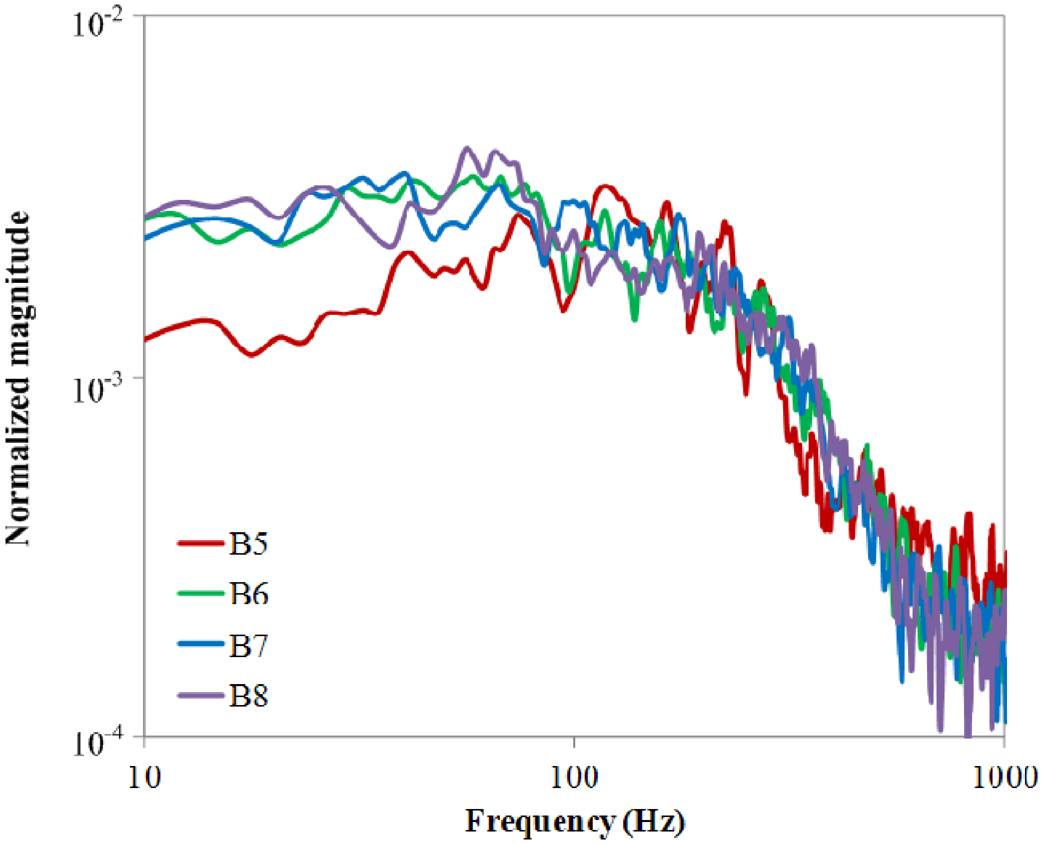

Figure 5.13: Power spectra of normalized velocity magnitude at Bend 5 to Bend 8 for *Re* = 502 (sampling frequency = 3000 Hz).

The Temporal evolution of the normalized velocity magnitudes at the centres of four bends at *Re* = 502 are plotted in Figure 5.12. Irregular velocity variations are evident at each of the four recording points and the flow characteristics are independent of the bend number. Power spectrum analysis was also employed on the velocity signals at different bends. Figure 5.13 shows the power spectra of the normalized velocity magnitudes at Bend 5 to Bend 8 for *Re* = 502. It is found that the flow characteristics are very similar from one bend to the next in the transient flow regime which is indicated by the almost identical spectra.

5.2.4 Two-dimensional (2D) flow pattern in zigzag microchannels

It is known that flow development within a zigzag channel is affected by periodic bends along the passage, which constantly interrupt the development of the boundary layer and induce secondary flows. A detailed visualisation of the flow pattern and discussion of the development of induced secondary flow at the corners for different Reynolds numbers is given below.

Figure 5.14 shows typical time-averaged velocity fields at different Reynolds numbers obtained using the micro-PIV system. All the measurements were taken at a focal depth z = 0.2 mm at Bend 10. It can be seen that flow separation regions have formed immediately after the inner corner, while the flow is turning the corner. The massive role played by the bends in provoking flow separation is clear. Even at a Reynolds number of 160 the region of flow separation is rather large. These vortices continue to develop with increasing Reynolds number. At Re = 420, small-scale vortices are formed around the outer corner as well.

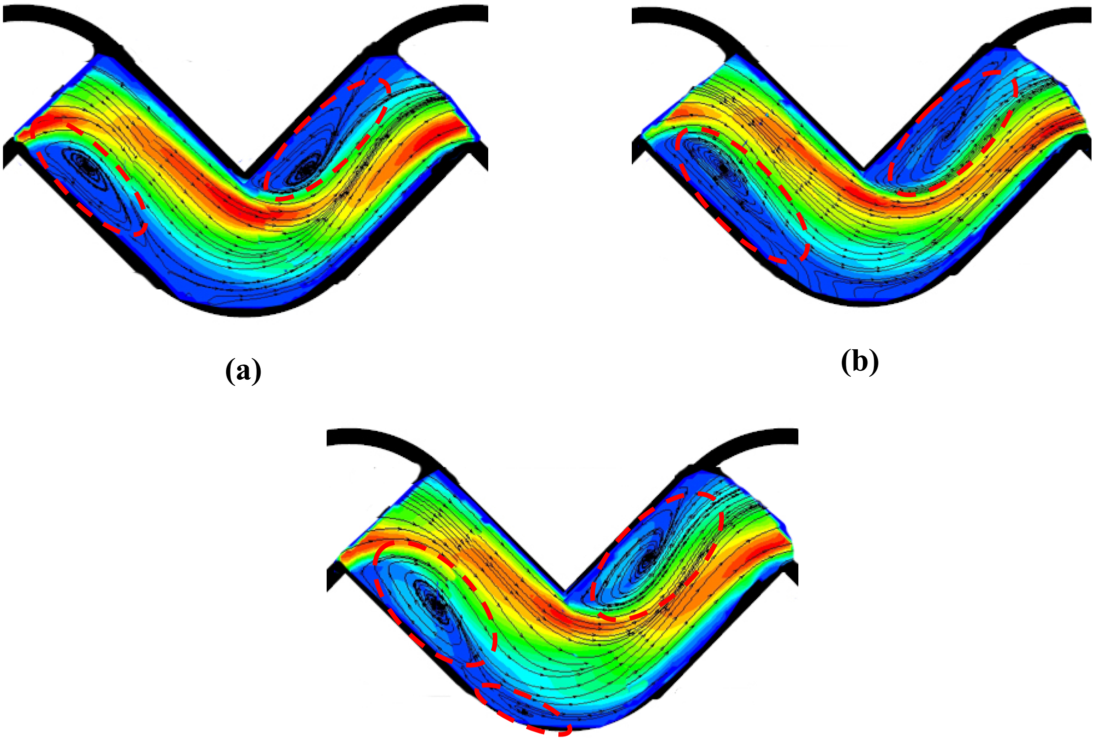
(a) **(b)**

(c)

Figure 5.14: Typical time-averaged velocity fields at Bend 10 at: **(a)** Re = 160; **(b)** Re = 215; and **(c)** Re = 420.

Figure 5.15 (a) - (f) shows enlarged velocity vectors near the bend corner for the Reynolds numbers ranging from 135 to 880. As can be seen, flow recirculation formed at the bend at a very low Reynolds number (Re = 135). As the Reynolds number increases, stronger recirculation can be seen in the separated flow zone. At Re = 293, the vortex is very clear and occupies almost 30% of the channel width. As the Reynolds number is increased further to 612, the vortex grows in size and intensity and occupies up to 50% of the channel width. However, the growth of the vortex seems saturated after Re = 612 as there is no significant difference in the recirculation zone size between Re = 612 and Re = 880; but the strength continues to increase. It is evident that the flow in this geometry is dominated by the existence of large recirculation zones.

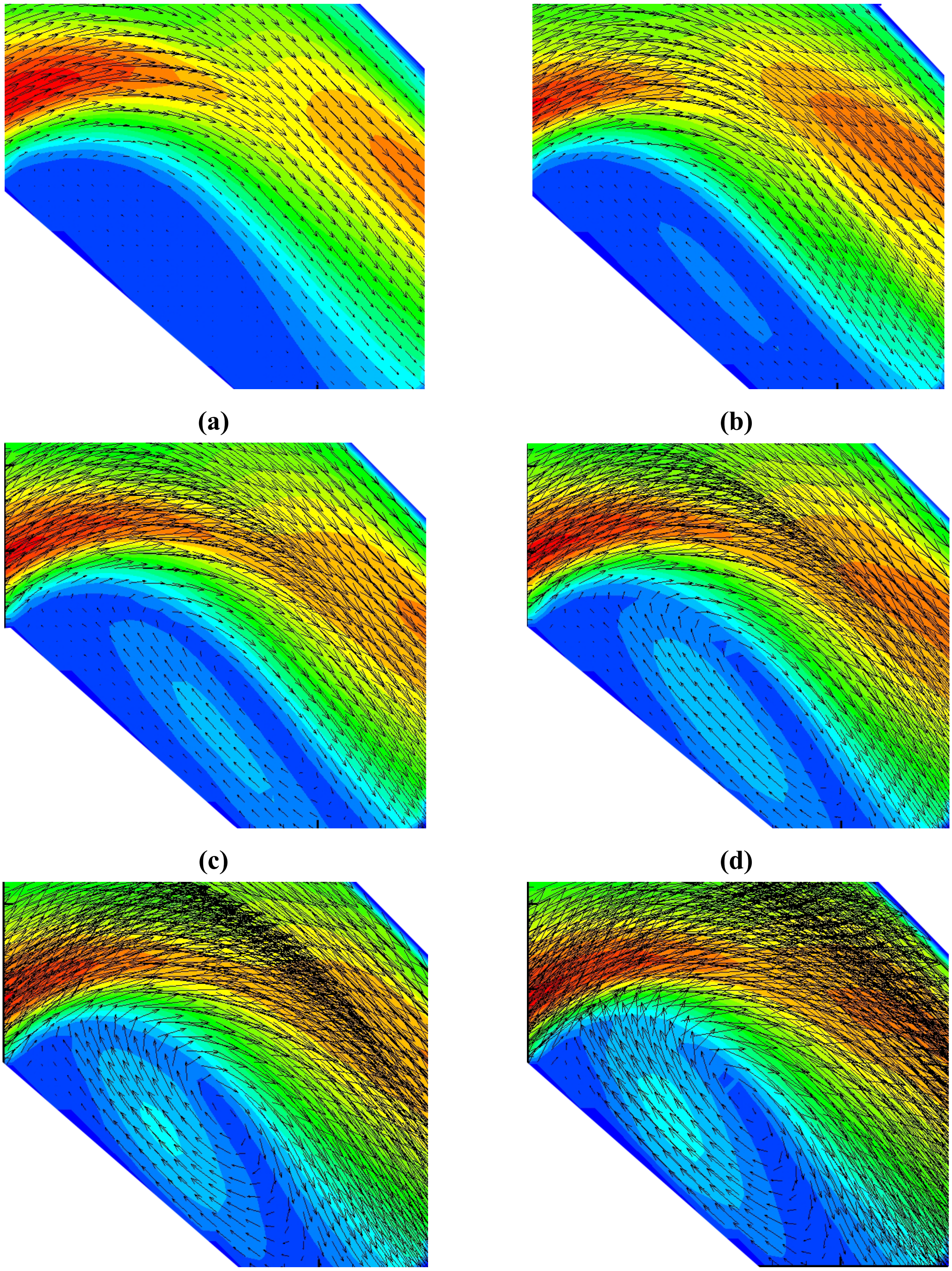

(a) **(b)**

(c) **(d)**

(e) **(f)**

Figure 5.15: Velocity vectors near the corner of Bend 10 for: **(a)** *Re* = 135; **(b)** *Re* = 215; **(c)** *Re* = 293; **(d)** *Re* = 385; **(e)** *Re* = 612; and **(f)** *Re* = 880.

In order to gain greater insight into the flow field in the unsteady flow regime, instantaneous flow fields at Bend 10 are shown in Figure 5.16 for the Reynolds number of 612. It is clear that the flow pattern is very different at different times. The figure shows that the vortices move downstream and simultaneously new vortices are formed near the bend. The number, location and size of the vortices changes dramatically with time, which gives rise to intense fluid mixing, leading to the enhancement of the heat transfer rate. These flow characteristics are in good agreement with the computational results reported by Zheng (2013), who studied the transient behaviour in the zigzag channel, showing that the flow features change dramatically with time.

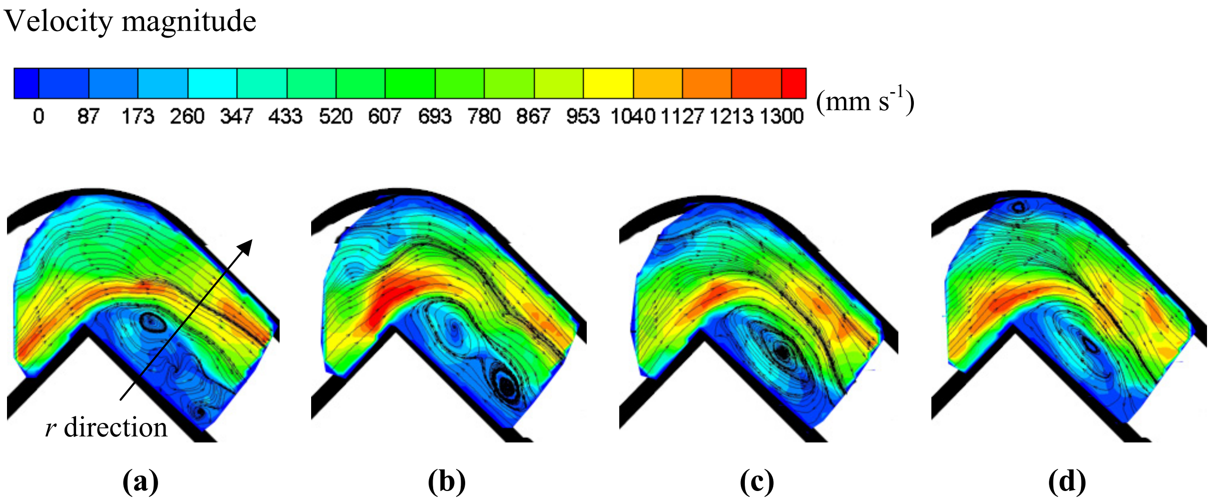

Figure 5.16: Instantaneous flow fields with streamlines at Bend 10 for Re = 612 at: **(a)** $t = t_0$; **(b)** $t = t_0 + 0.01$ s; **(c)** $t = t_0 + 0.02$ s; and **(d)** $t = t_0 + 0.03$ s.

A more complete study was obtained by examining the local flow fluctuations. This allows the exact cause of steady flow breakdown to be investigated. The standard deviation profile of the velocity across the zigzag channel is plotted in Figure 5.17. Thirteen small ROI windows along the line indicated in Figure 5.16 (a) were selected. The profile of the straight channel at Re = 645 when the flow is laminar is also shown in Figure 5.17 for comparison. It can be seen that at a low Reynolds number (Re = 170) the flow is quite steady with very low fluctuations across the whole channel. At Re = 215, higher standard deviation occurs near the inner wall due to the recirculation formed. With an increasing Reynolds number, the flow fluctuates dramatically, especially near the inner corner of the channel. The width of the fluctuating zone and the magnitude of the fluctuations are both increasing, which is in agreement with the results indicated from Figure 5.15. This figure highlights the importance of the recirculation zones in leading to transient flow. The high fluctuations are clearly caused by the evolution of the vortices, including the movement and destruction of the existing vortices, as well as the formation of new ones, as shown in Figure 5.16.

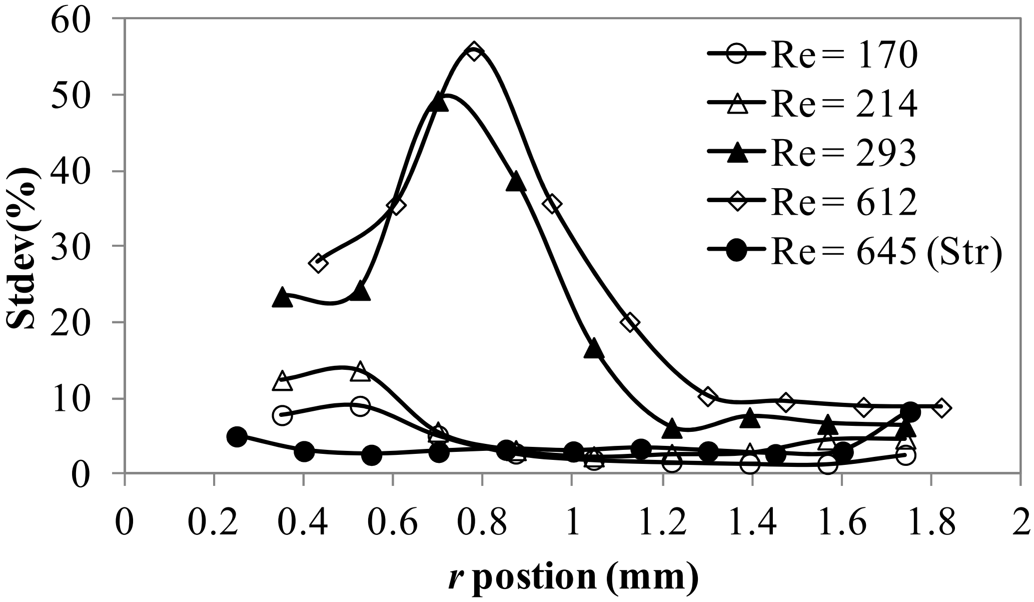

Figure 5.17: Standard deviation of local velocity at Bend 10 for different Reynolds numbers.

5.2.5 Three-dimensional (3D) flow pattern in zigzag microchannels

It is well-known that it is difficult to measure the out-of-plane velocity which is parallel to line-of-sight by using a classical micro-PIV system. Obviously the flow in zigzag channels is three-dimensional and it is also important to understand the fluid behaviour in the direction normal to PIV measuring planes. In order to derive three-dimensional flow maps a continuity based technique was applied to 2D velocity fields recorded in parallel planes. A reliable algorithm for the computation of the continuity based data was developed with the aid of the Matlab software.

5.2.5.1 **3D velocity reconstruction**

The procedure for the continuity based technique is presented below. Using the scanning-based visualisation technique described in Chapter 3, the in-plane velocity components (u and v) could be obtained at different depths (z), as shown in Figure 3.7. The computation of the out-of-plane component w is based on application of the continuity equation gives:

$$\nabla.\boldsymbol{u} = \frac{\partial u}{\partial x} + \frac{\partial v}{\partial y} + \frac{\partial w}{\partial z} = 0 \tag{5.4}$$

Step 1: Computation of the in-plane velocity derivatives

The in-plane velocity derivatives were computed in the *x*-*y* plane, where the velocities, u and v are measured, employing central differences (second-order). Equation (5.5) is used to calculate $\frac{\partial u}{\partial x}$:

$$\frac{\partial u}{\partial x}(x_i, y_j, z) = \frac{u\left(x_{i+1}, y_j, z\right) - u(x_{i-1}, y_j, z)}{2\Delta x} \tag{5.5}$$

The same applies to the calculation of $\frac{\partial v}{\partial y}$. Thus the derivative of the out-of-plane velocity $\frac{\partial w}{\partial z}$ is determined by

$$\frac{\partial w}{\partial z}(x_i, y_j, z) = -(\frac{\partial u}{\partial x} + \frac{\partial v}{\partial y})\,(x_i, y_j, z) \tag{5.6}$$

Step 2: Determination of the out-of-plane velocity field

Integration of Eq. (5.6) in the *z* direction yields the expression to retrieve the *w* component:

$$w(x_i, y_j, z) = w(x_i, y_j, z_0) - \int_{z_0}^{z} (\frac{\partial u}{\partial x} + \frac{\partial v}{\partial y})\,(x_i, y_j, \hat{z})d\hat{z} \tag{5.7}$$

In order to calculate *w* across the depth of the channel, the no-slip boundary condition is necessary where the initial value of *w* can be set to $w(x_i, y_j, z_0) = 0$ for all x_i and y_j. The integral of $\frac{\partial \mathrm{w}}{\partial \mathrm{z}}$ across the channel was obtained using the adaptive Simpson quadrature rule.

5.2.5.2 Validation of 3D reconstruction technique

In order to assess the uncertainties associated with the reconstruction process, numerical experiments were carried out by use of computational velocity data. Three-dimensional reconstructions were performed over a straight exit region of a size of $x \times y \times z$ = 2 mm × 5 mm × 2 mm after a 270° bend channel as shown in Figure 5.18. In the bend channel model, three-dimensional flow with Dean vortices in the cross-section was generated, which can be seen in Figure 5.18.

As shown in Figure 5.18, velocity data (*u, v*) in 10 parallel *x*-*y* planes were extracted from simulation without superimposed noise. The out-of-plane *w* velocity component and velocity field of a cross-sectional plane (Plane A-A) were reconstructed through the continuity based technique.

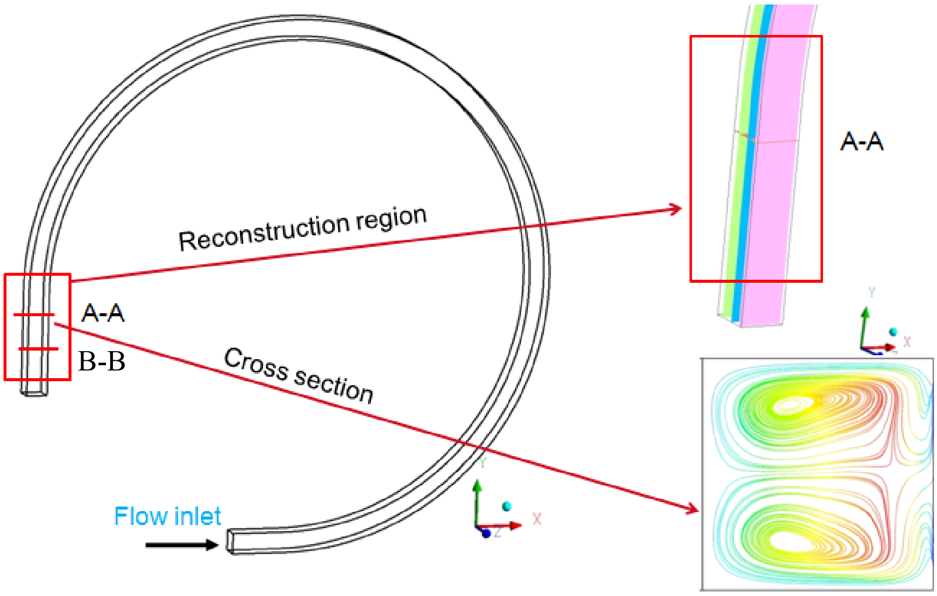

Figure 5.18: Numerical model of a 270° bend channel and the reconstruction region.

In Figure 5.19, the contours of velocity *w* in plane A-A are illustrated in both 3D and 2D views. Comparing the simulation solution and the reconstructed data, it is evident that the velocity component *w* is quite accurately calculated. The reconstructed field is in good agreement with the simulation solution.

In order to estimate the error of the reconstruction procedure, statistical values of the Root Mean Square Deviation (RMSD) and Normalized Root Mean Square Deviation (NRMSD) are defined as following:

$$RMSD = \sqrt{\frac{\sum_{i=1}^{n}(x_{c,i} - x_{s,i})^2}{n}} \tag{5.8}$$

$$NRMSD = \frac{RMSD}{x_{max} - x_{min}} \tag{5.9}$$

They characterise the variability of the constructed values $x_{c,i}$ of $x_{s,i}$, which were obtained by numerical simulation.

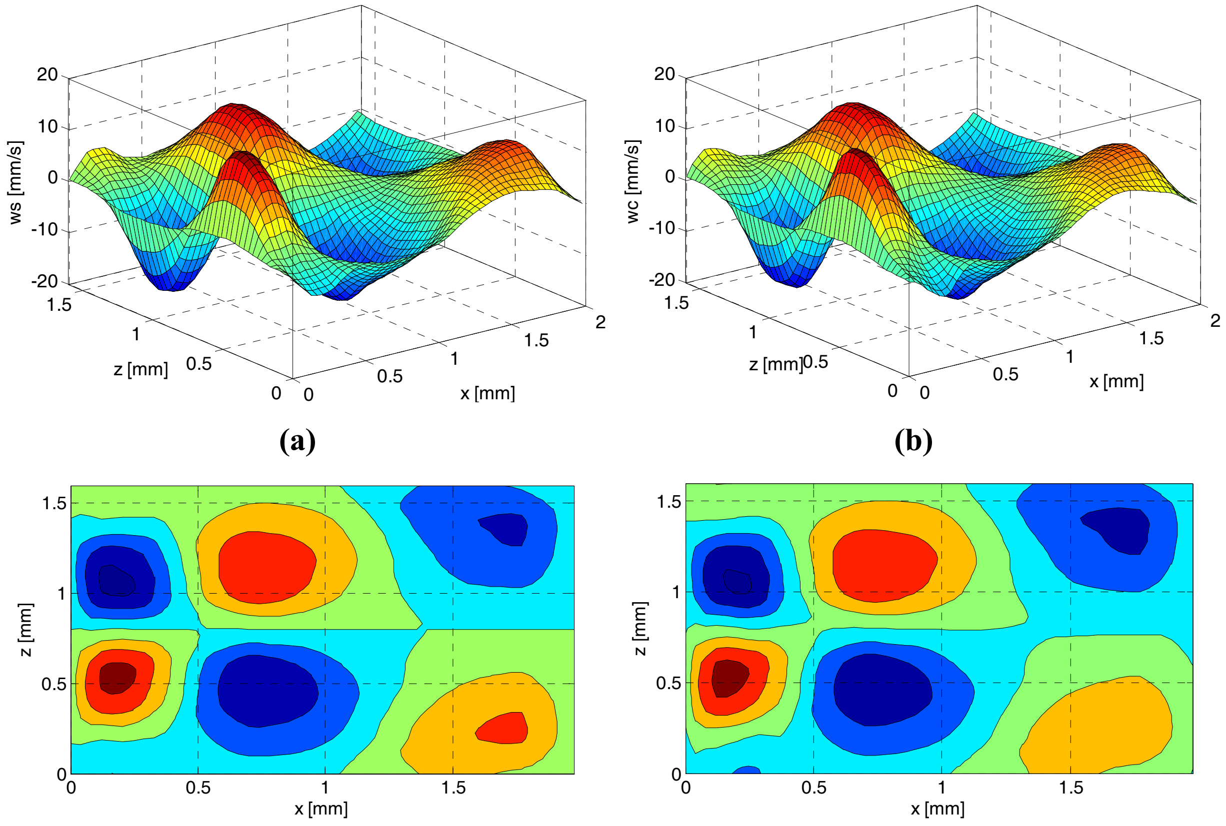

(a) (b)

(c) (d)

Figure 5.19: Comparison of velocity w field in Plane A-A: **(a)** and **(c)** from simulation solution; and **(b)** and **(d)** from reconstruction.

Table 5.1: Uncertainties introduced by reconstruction procedures.

Plane		$\frac{\partial u}{\partial x}$ **(m s^{-2})**	$\frac{\partial v}{\partial y}$ **(m s^{-2})**	$\frac{\partial w}{\partial z}$ **(m s^{-2})**	w **(m s^{-1})**
Plane A-A	RMSD	0.65	0.16	0.61	0.0006
	NRMSD(%)	0.37	0.56	0.34	**1.91**
Plane B-B	RMSD	0.87	0.30	1.68	0.0018
	NRMSD(%)	0.42	1.43	0.80	**5.13**

The values in Table 5.1 present uncertainties introduced by derivative and integral processes and also reflect the overall performance of the processes leading to reconstruction of w velocity component. Important is the fact that even without noise in the original data, the process can give rise to a certain error, in the in-plane derivatives $\frac{\partial u}{\partial x}$ and $\frac{\partial v}{\partial y}$ and integration of w. However, the error in each step is very small. The out-of-plane component w has an error of 1.9% and 5.1% for Plane A-A and Plane B-B, respectively. It should be emphasized that these errors represent the globally-averaged values. At certain locations within the reconstructed region, the errors can be as high as about 70 %.

Here it should be noted that, in this validation, the uncertainties were analysed based on the reconstruction procedure without noise in the original data. In practice, the error of the 3D reconstruction will not only come from the numerical algorithms used but also experimental uncertainty associated with data acquisition.

5.2.5.3 **3D flow field in zigzag microchannels**

Micro-PIV measurements were taken at 18 depth-wise planes to identify the 3D flow pattern in the zigzag channel. Figure 5.20 shows the distributions of two velocity components, *u* and *v*, on four of the measurement planes at Bend 10 of the zigzag channel for Reynolds number of 640. The results show that the flow patterns are quite different at different depths and the recirculation zone is obvious in the bottom half of the channel.

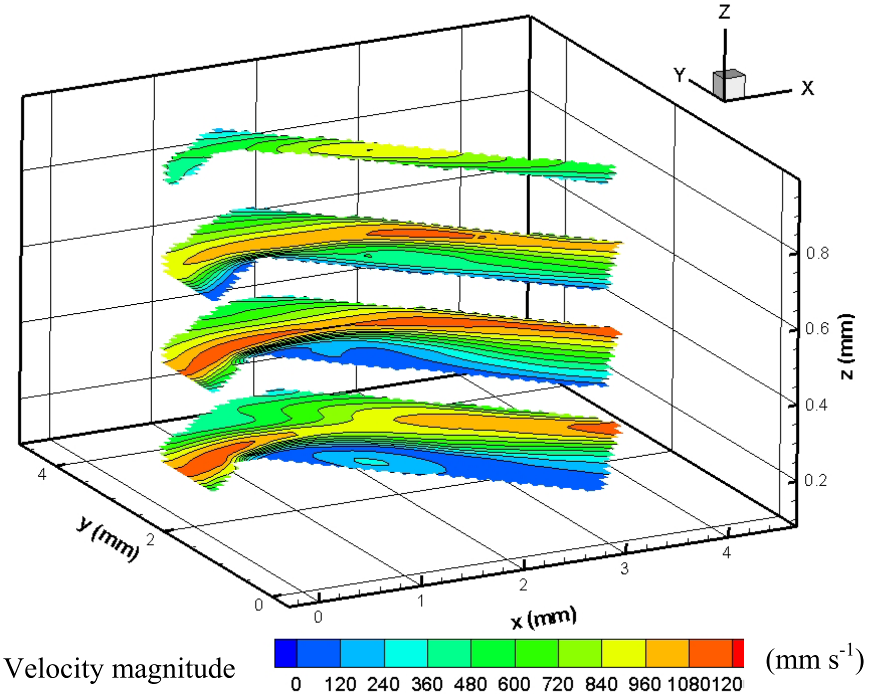

Figure 5.20: In-plane velocity distribution at different depths for *Re* = 640.

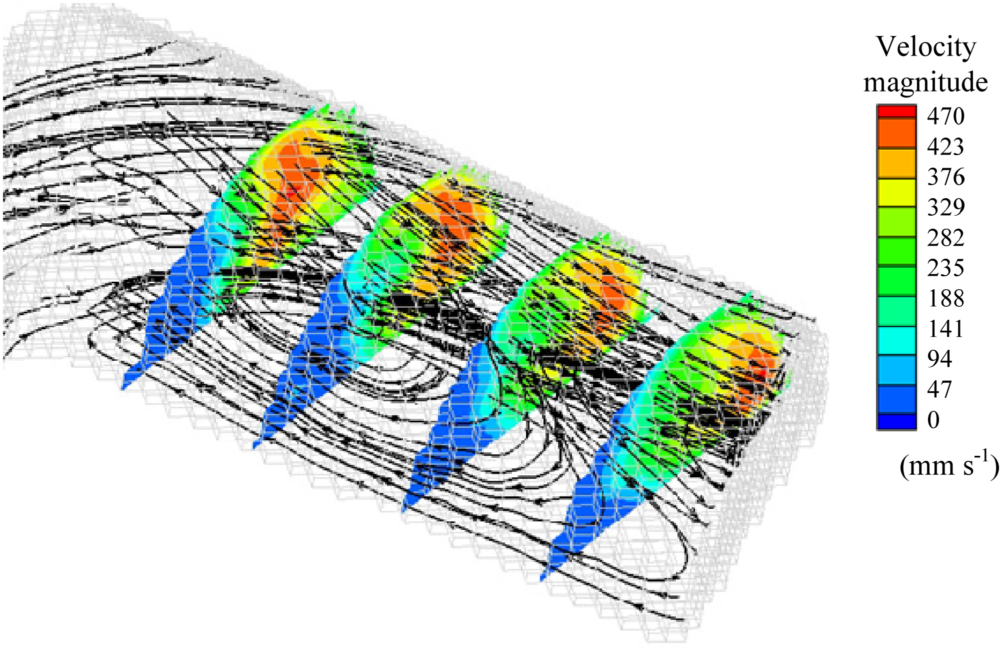

(a)

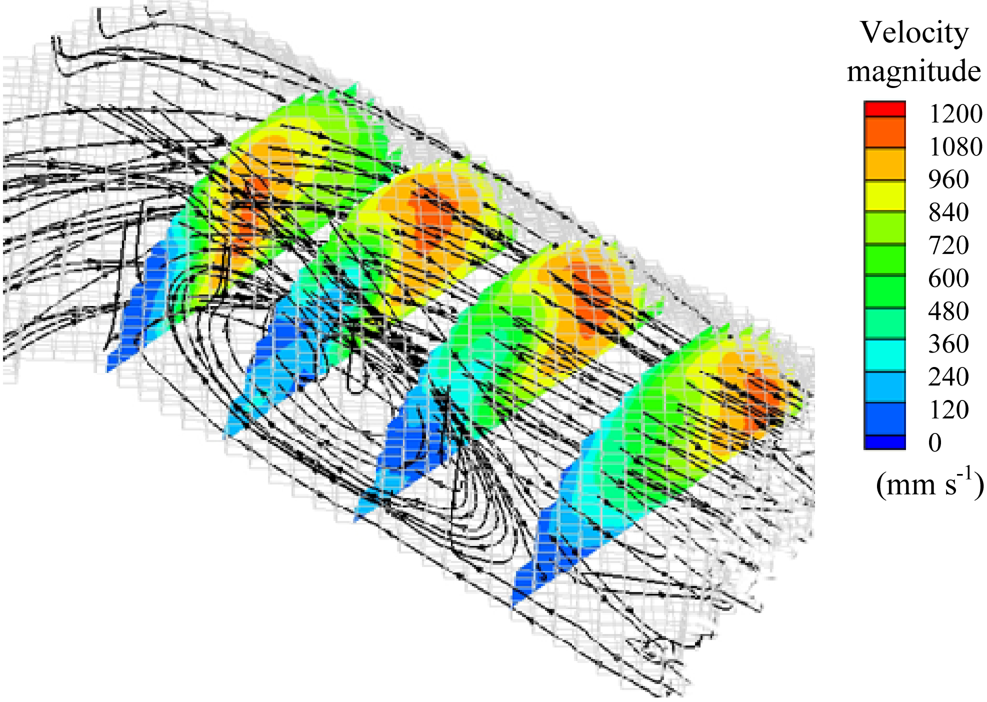

(b)

Figure 5.21: 3D streamline structures and velocity contours at Bend 10 for: **(a)** Re = 236; and **(b)** Re = 640.

Based on the 3D reconstruction technique illustrated above, the 3D geometry of the channel was reconstructed using the 18 PIV measurement planes. The integration started at the flat surface of the channel where the initial value of w was set to zero. The post-processing software Tecplot 360 (Tecplot, Inc. Bellevue, Washington, USA) was used to draw the reconstruction zone. The 3D streamline structure and velocity magnitude (*u*, *v* and *w*) at four cross-sectional planes are shown in Figure 5.21 for *Re* = 236 and *Re* = 640. The shape of the velocity contours at the various cross-sections shows a shift in the maximum fluid speed to the outside of the bend, subsequently producing rotation of the fluid about an axis parallel to the bulk flow, resulting in the formation of vortices. The occurrence of the separated flow regions traps fluid inside the recirculation zone and gives rise to a very obvious reversed flow area in the vicinity of the inside wall. The reverse flow disappears further downstream. It can also be seen that immediately after the bend, the streamlines are twisted and cross over different depths, indicating the fluid is being mixed in the tangential direction and a significant secondary flow is formed. The streamlines at *Re* = 236 are less twisted indicating moderate transverse movement. With an increasing Reynolds number (*Re* = 640), the transverse motion of the flow is more significant and this is in accord with the more pronounced chaotic behaviour for higher Reynolds numbers.

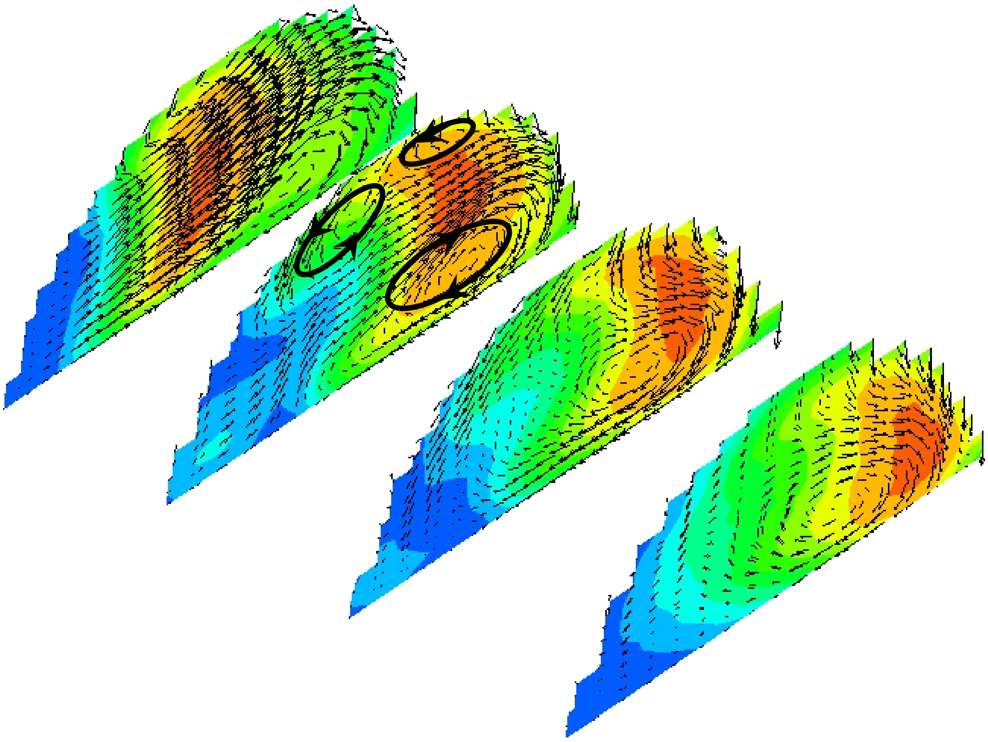

Figure 5.22: Secondary flow vectors and velocity contours on the cross-sectional planes at *Re* = 640.

Figure 5.22 shows the tangential velocity vectors on cross-sections indicated in Figure 5.21 (b) for *Re* = 640. Dean vortices are clearly observed in the flow field after the bend, which provide the means to increase the rate of mixing by transporting fluid away from the walls into the centre of the cross-section and disrupting the thermal boundary layer. It is also found that the number and the location of the Dean vortices change along the flow direction, which can lead to chaotic advection. The direction of rotation of the Dean vortices is expected to alternate after every turning point in the channel as indicated in many simulation studies (Rosaguti et al., 2007b, Sui et al., 2012). These complex flow features have a dramatic effect on the fluid temperature profile and hence the heat transfer rate.

5.2.5.4 **Uncertainties of the reconstruction process**

The 3D reconstruction procedure introduces uncertainties in the values of the recovered velocity component. The error in the processing to get the out-of-plane velocity mainly comes from two sources. One is the truncation error associated with the finite difference scheme used and the other is the measurement or experimental error associated with data acquisition. The former error has been assessed with the aid of a numerically obtained three-dimensional dataset of the flow field, as described in Section 5.2.5.2. The globally-averaged RMS value of the constructed velocity component w was 3.5% when no noise was superimposed on data planes. The experimental error in PIV measurements is estimated to be less than 5% in the majority of the domain of interest with the biggest error occurring near the wall, as illustrated in Chapter 3.

However, the noise in the in-plane velocity components will induce large uncertainties in the calculation of the out-of-plane velocity component. As discussed in Section 5.2.5.1, the unknown velocity component, *w*, is determined by the three-dimensional distribution of $\frac{\partial w}{\partial z}$ when a proper boundary condition for *w* is given. All the data will depend on the quality of the measurements close to the wall. However, it is more difficult to obtain accurate micro-PIV data close to surfaces than in the centre of the domain due to features of the surface appearing in the images and particles interacting with walls. In order to minimize the errors in this approach, it is necessary to ensure that the spacing between adjacent PIV measurement planes is small enough to avoid too large variation in the time-averaged velocity between successive planes.

Robinson and Rockwell (1993) suggested that for particle tracking techniques with low particle density and random velocity vector distribution, it was necessary to carry out an interpolation process in order to bring the vectors to a rectangular grid format. In this study, linear interpolation was applied to the original data. However, no big improvement was found in the reconstruction of *w*. This is possibly because a small interrogation window and close plane spacing have already been used during the measurement and processing stages.

5.3 Effect of channel geometry

The above work has focused on steady and transient flows in the zigzag channel with R_c/d = 0.51, *L/d* = 1.75, and θ = 45°. Experiments were performed for the five different channels (called Zigzag 1, Zigzag 2, Sine 1, Sine 2 and Sine 3 as listed in Chapter 3) to investigate the effect of varying the Reynolds number and the geometric parameters on the flow field and pressure-drop penalty. Two different types of wavy channels were employed: zigzag channels and sinusoidal channels. Both configurations were analysed for different wavelengths, amplitudes and/or bend angles.

5.3.1 Onset of unsteadiness

The RMS velocity fluctuations $\frac{U_{RMS}}{Uave}$ located at the middle of the channel plotted against Reynolds number for the five channel geometries is shown in Figure 5.23. As expected, the flow fluctuations increase with increasing Reynolds number for all wavy channels. At low Reynolds numbers at which the flow is steady, the standard deviation is quite small and does not change with Reynolds number. However, when the Reynolds number is increased to a critical number (Re_c) the standard deviation increases dramatically, demonstrating the existence of significant flow unsteadiness. The critical Reynolds number Re_c depends on the channel geometry. Compared with the straight channel, unsteady flow occurs in wavy channels at a relatively low Reynolds number.

For zigzag channels, the effect of lowering the half-unit length L is analogous to increasing the bend angle θ while keeping the amplitude fixed. This results in sharper corners and shorter straight sections between bends. Clearly, the bend angle has a significant effect on the results. At the same Reynolds number, the standard deviation of Zigzag 1 (θ = 45°) is higher than that of Zigzag 2 (θ = 30°) across the whole range of Reynolds number. Transition happens at a lower Reynolds number for the channel with higher bend angles.

For sinusoidal channels it is evident that fluctuations appear at a lower Reynolds number and are more pronounced for higher amplitude to half-unit length ratio (*A/L*) values. Significant fluctuations ($\frac{U_{RMS}}{Uave} > 0.05$) can be seen at Re = 280 in Sine 1 (*A/L* = 0.5), while the pronounced fluctuations appear later at *Re* = 380 in Sine 2 (*A/L* = 0.289). The flow unsteadiness occurs at a similar Reynolds number (*Re* = 380) in Sine 3 (*A/L* = 0.5, *L/d* = 3.5), which has the same amplitude to half-unit length ratio as Sine 1 (*A/L* = 0.5, *L/d* = 1.75) channel but is scaled up.

The two channel types (Zigzag 1 and Sine 1, Zigzag 2 and Sine 2) have the same wavelength and amplitude but the pathways are much smoother in the sinusoidal channels. The transitions occur at higher Reynolds numbers for sinusoidal channels due to the much smoother geometry.

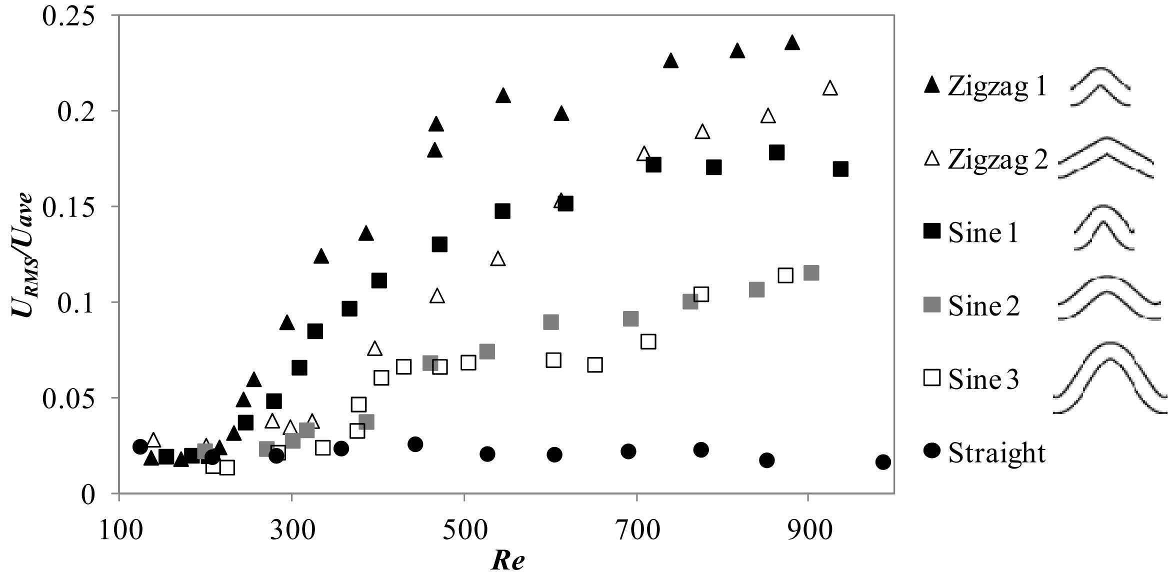

Figure 5.23: Normalized velocity fluctuation against Reynolds number for different channel geometries.

5.3.2 Flow patterns

Figure 5.24 shows the time-averaged streamlines superimposed on the velocity contours for different channels at a Reynolds number around 200. Due to the limited size of the observation view, the flow fields in these figures were generated by combining the results obtained by moving the channel position two or three times. For the zigzag channel geometry, at a small bend angle (Zigzag 2, $\theta = 30°$) the flow separates in only a small region of the channel, while at a higher angle (Zigzag 1, $\theta = 45°$), the flow recirculation occupies a large part of the channel at the same Reynolds number. Both of the recirculation size and strength are bigger in channels with higher bend angle. As θ increases, the bends become sharper with shorter straight sections between consecutive bends, leading to the development of more pronounced recirculation and Dean vortices, which promote fluid mixing in the bends. The comparison between Sine 1 and Sine 2 shows the same trend. On the other hand, recirculation is easier to form in zigzag channels than sinusoidal channels. Figure 5.25 shows the velocity contours for the five channels for Reynolds numbers above 400. Flow complexity, as well as the size and the strength of recirculation zones, increases with Reynolds number. However, this behaviour is absent in sinusoidal channels with smooth pathways, for which the geometry is remarkably resistant to flow separation. For channels Sine 2 and Sine 3, no obvious flow recirculation was found along the channel even at $Re > 900$.

Even though there are no lateral vortices formed in channels Sine 2 and Sine 3, complex secondary flow induced by the bend curvature has been observed through 3D reconstruction. Figure 5.26 shows the secondary flow vectors on the cross-sectional planes at a bend of channel Sine 3 for $Re = 106$. A single pair of Dean vortices, which meet approximately at the centre of the cross-section, are formed in sinusoidal channels. The rotation direction of the Dean vortices changes periodically when the fluid flows through the sinusoidal channel where the curvature periodically switches sign, thus resulting in the spatial evolution of flow patterns. With increasing Reynolds number, the pattern of the Dean vortices evolves spatially and temporally, leading to a chaotic flow and enhanced fluid mixing.

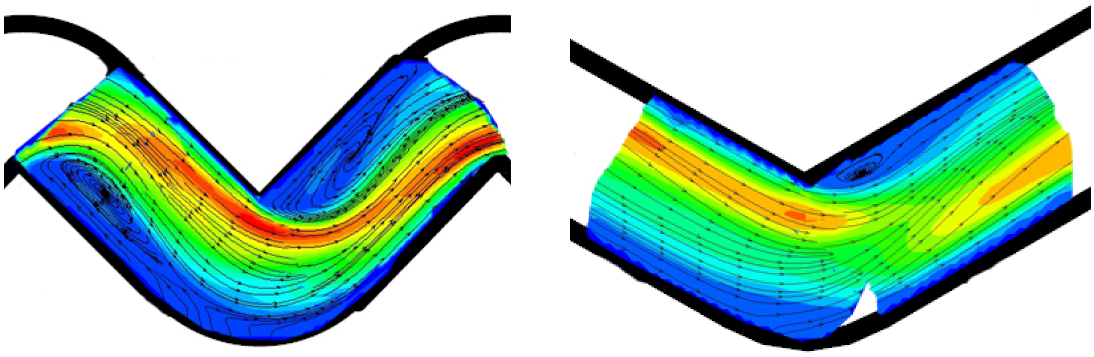

(a) Zigzag 1

(b) Zigzag 2

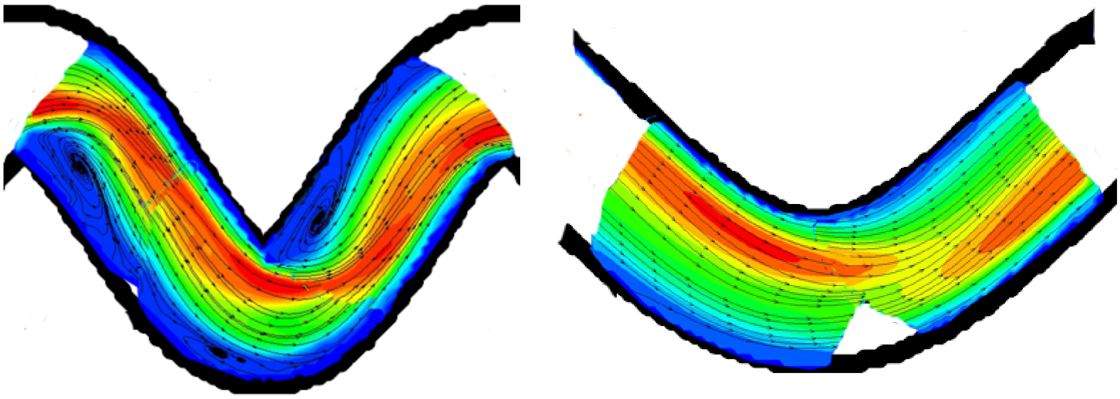

(c) Sine 1

(d) Sine 2

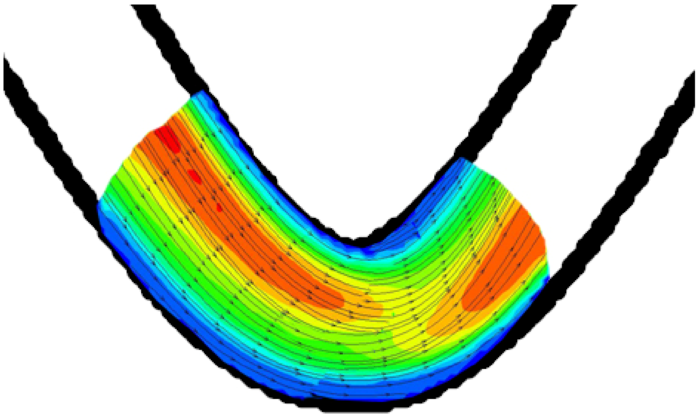

(e) Sine 3

Figure 5.24: Time-averaged velocity fields for: **(a)** Zigzag 1 at *Re* = 215; **(b)** Zigzag 2 at *Re* = 202; **(c)** Sine 1 at *Re* = 208; **(d)** Sine 2 at *Re* = 192; and **(e)** Sine 3 at *Re* = 199.

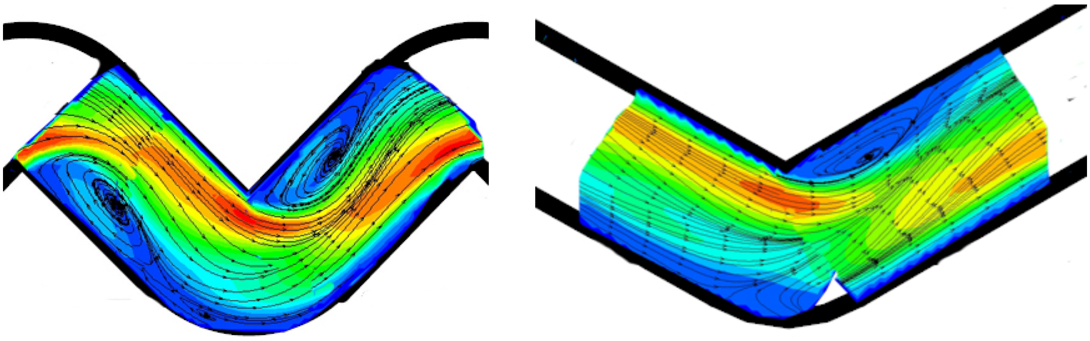

(a) Zigzag 1 **(b)** Zigzag 2

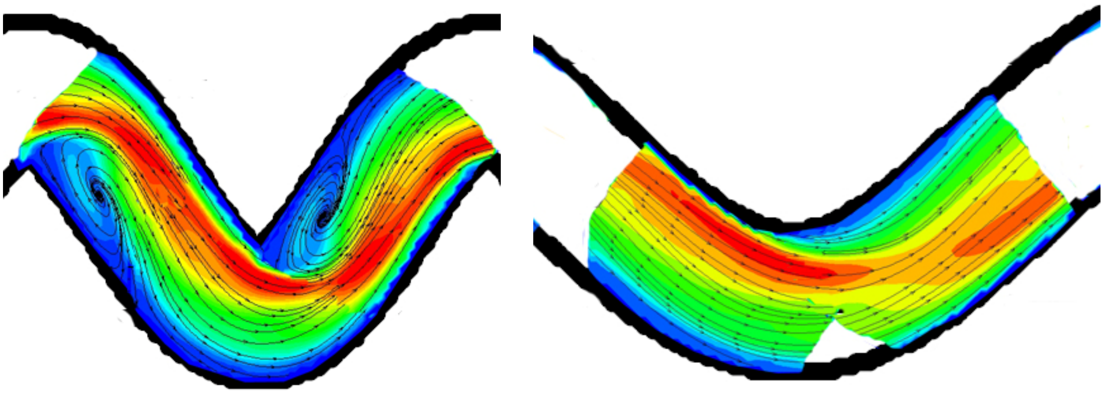

(c) Sine 1 **(d)** Sine 2

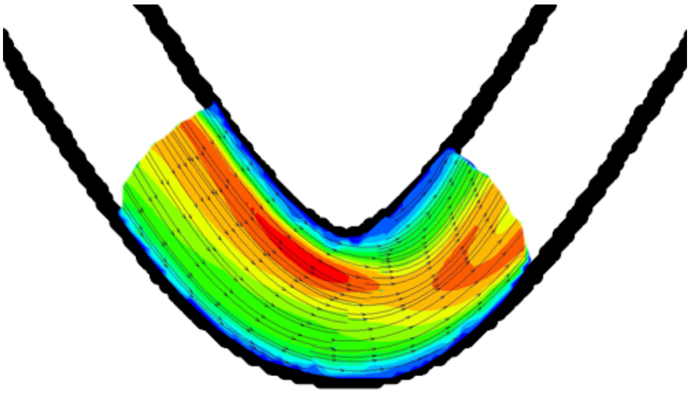

(e) Sine 3

Figure 5.25: Time-averaged velocity fields for: **(a)** Zigzag 1 at *Re* = 420; **(b)** Zigzag 2 at *Re* = 465; **(c)** Sine 1 at *Re* = 498; **(d)** Sine 2 at *Re* = 902; and **(e)** Sine 3 at *Re* = 907.

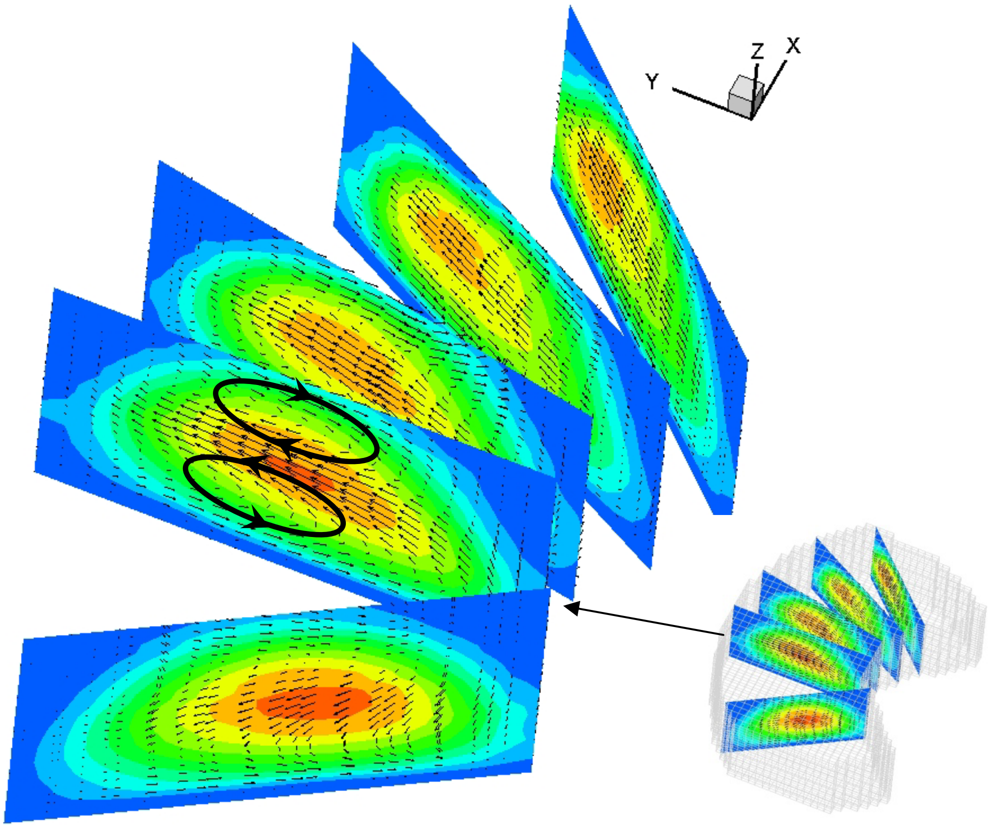

Figure 5.26: Secondary flow vectors and velocity contours on the cross-sectional planes in Sine 3 at $Re = 106$.

Figure 5.27 shows the local flow fluctuation across the channel for all the five geometries. The profile of the straight channel at Re = 645 is also shown in all figures to facilitate comparison. The cross-section for each channel was selected 0.5d after the bend. As shown in the plots, the standard deviations are quite large in the Zigzag 1 and Sine 1 channels which have sharp bends and short straight sections. The flow fluctuation is most pronounced in the recirculation zone near the inner wall immediately after the bend. The recirculation size and strength increase with increasing Reynolds number as expected. For the channels Sine 2 and Sine 3 where the recirculation is hard to form, the flow is relatively steady with the standard deviation usually less than 20%. It is evident that the earlier transition is associated with the effect of the tight bends on the flow fields. These flow fluctuations are responsible for the heat transfer enhancement and augmentation of the pressure drop.

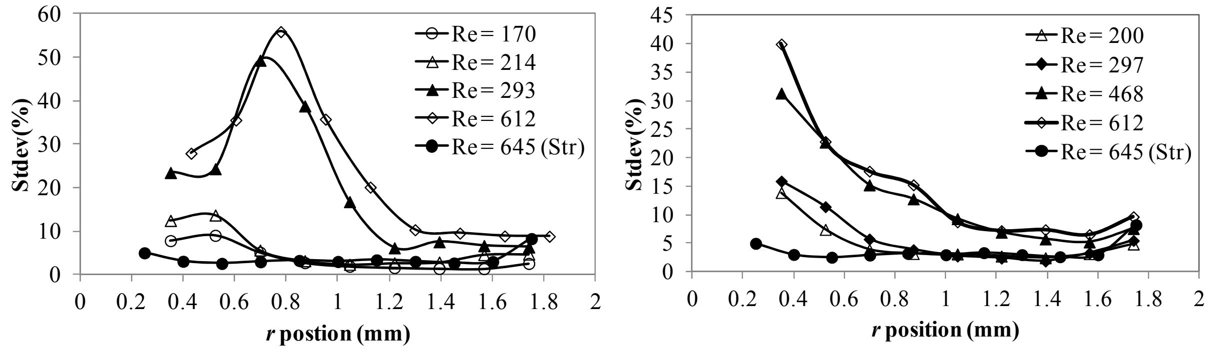

(a) Zigzag 1

(b) Zigzag 2

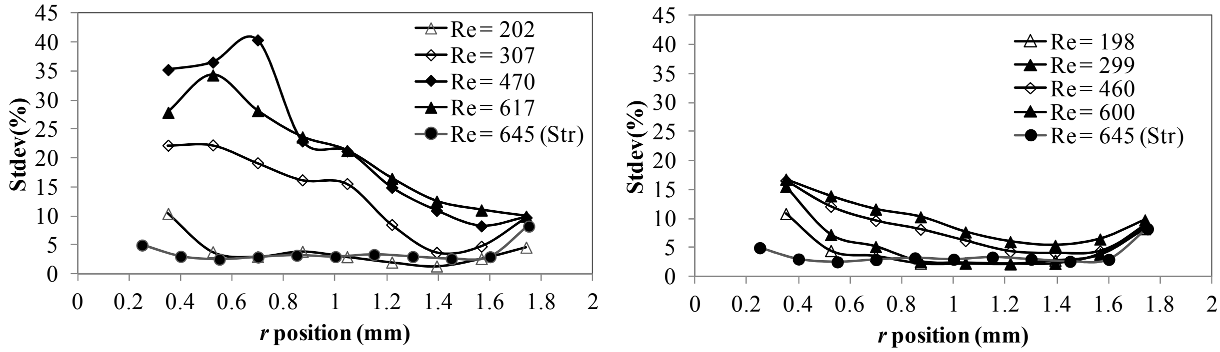

(c) Sine 1

(d) Sine 2

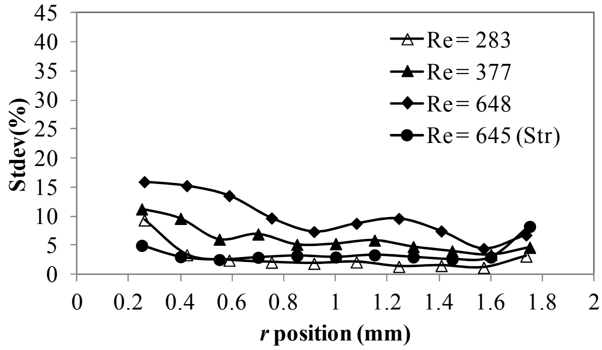

(e) Sine 3

Figure 5.27: Standard deviation of local velocity at different Reynolds numbers for: **(a)** Zigzag 1; **(b)** Zigzag 2; **(c)** Sine 1; **(d)** Sine 2; and **(e)** Sine 3.

5.4 Oscillatory flow in wavy microchannels

Through time-resolved velocity measurements, it has been found that periodic/quasi-periodic flow oscillation occurs in the base zigzag channel (Zigzag 1) over a certain range of Reynolds numbers. This interesting flow behaviour was also found in other channel geometries. The flow in wavy channels has been observed to be steady up to a critical Reynolds number which depends on the geometric configuration. Beyond the critical Reynolds number an oscillatory flow has been observed before the flow becomes transient.

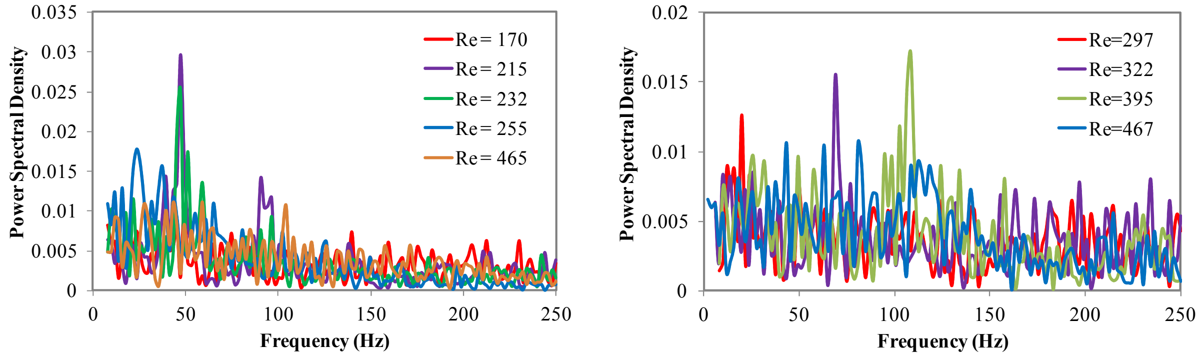

(a) Zigzag 1 **(b)** Zigzag 2

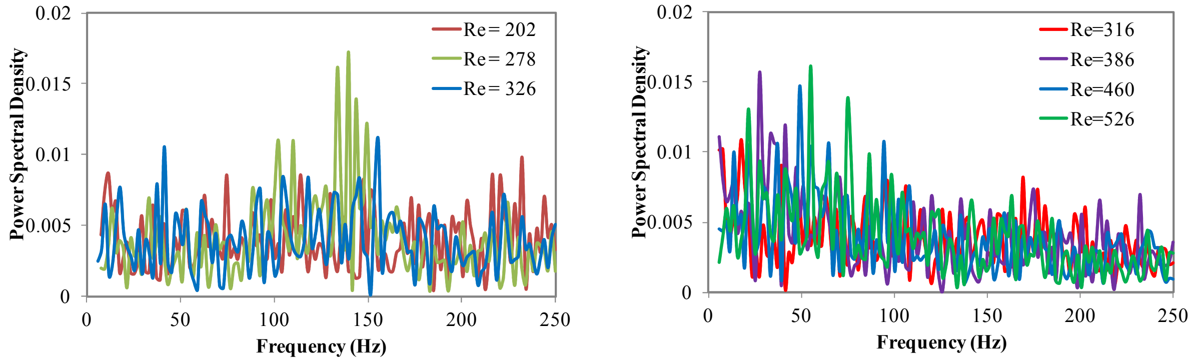

(c) Sine 1 **(d)** Sine 2

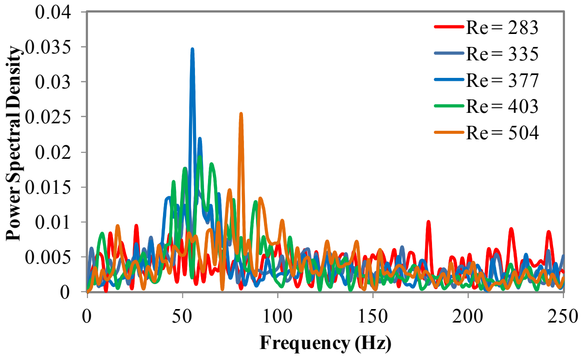

(e) Sine 3

Figure 5.28: Fourier power spectra of normalized velocity magnitudes at different Reynolds numbers for: **(a)** Zigzag 1; **(b)** Zigzag 2; **(c)** Sine 1; **(d)** Sine 2; and **(e)** Sine 3.

Figure 5.28 shows the Fourier power spectra of normalized velocity magnitudes at various Reynolds numbers for the five channels. The Fourier spectrum of the flow confirms that the flow has experienced a transition from a time-independent state to a time-dependent oscillatory flow. It has been discussed above that in Zigzag 1 the velocity was observed to vary regularly at *Re* = 215 with very small fluctuations and a dominant frequency of around 50 Hz. A further increase in Reynolds number leads to quasi-periodic flow. The spectrum shows many spaced peaks with the dominant one slightly lower than the previous fundamental one. For *Re* > 400, the broadband nature of the spectra indicates the onset of chaos.

In Zigzag 2 channel, flow oscillation starts above a Reynolds number of around 320. The predominant frequency moves from 70 Hz to 110 Hz with increasing Reynolds number. However, the oscillation is not quite regular in Sine 1 and Sine 2 channels, as can be seen from the multiple peaks in their power spectra.

The most regular oscillation was found in channel Sine 3, as shown in Figure 5.29, which presents a typical velocity profile against time at *Re* = 377 in the middle of the channel. As can be seen from Figure 5.28 (e), at *Re* = 335 and 377, there is a distinct frequency peak at 55 Hz in the power spectra. At higher Reynolds numbers, for *Re* > 400, multiple peaks in the frequency appear with the main one around 55 Hz. The main peak moves to 80 Hz when the Reynolds number is increased to 504.

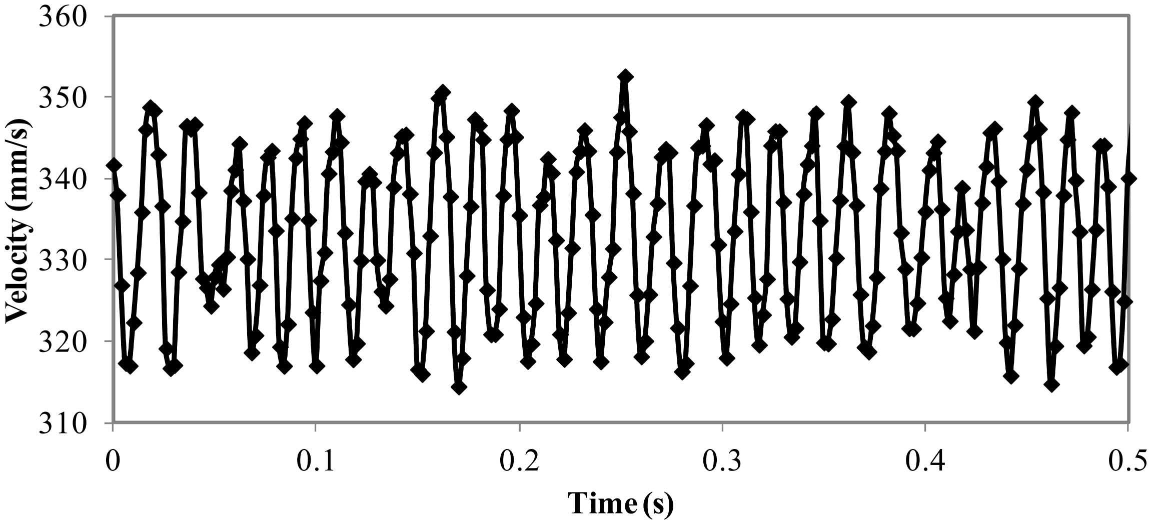

Figure 5.29: Temporal evolution of the velocity for *Re* = 377 in Sine 3.

It is evident that behaviours of the frequencies of the oscillation are different for the five channels. The approximate transition Reynolds number and the dominant frequency of oscillation for the five geometries are given in Table 5.2. The critical Reynolds number for the occurrence of oscillatory flow, that is, the onset of unsteadiness of the velocity field, is lower for channels with sharper bends. Due to the smooth pathway, there is a delay in transition from a steady flow to an oscillatory flow in sinusoidal channels.

Table 5.2: Critical Reynolds number and dominant frequency of oscillation for wavy channels.

Channel	Critical Reynolds number, Re_c	Dominant frequency (Hz)
Zigzag 1	215	50
Zigzag 2	322	70
Sine 1	278	~140
Sine 2	316	-
Sine 3	335	55

To further study the characteristics of oscillatory flow, the non-dimensional frequency or Strouhal number is defined as

$$St = \frac{f d_h}{u_m} \tag{5.10}$$

where f is the dominate frequency of the oscillation, and u_m is the mean flow velocity.

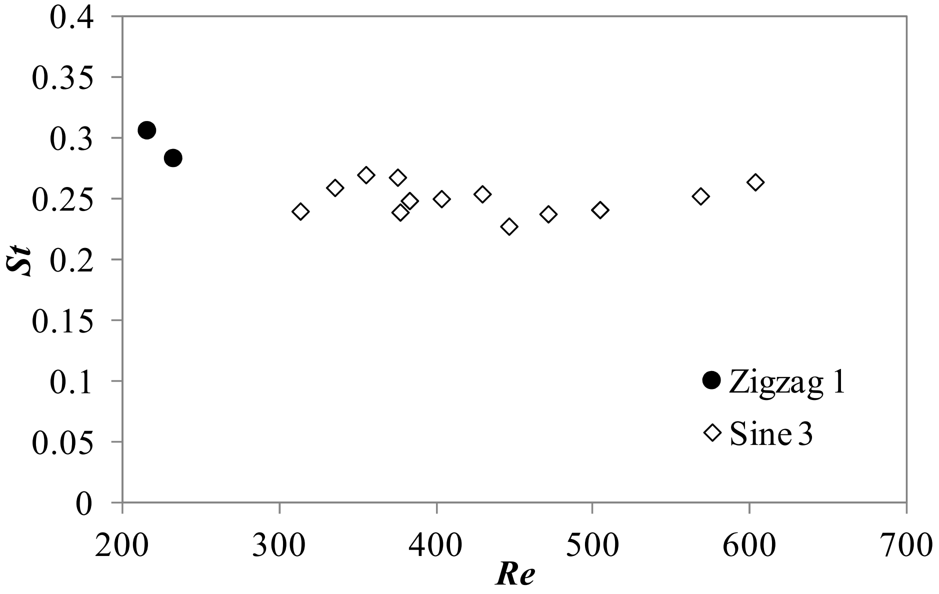

Figure 5.30: Variation of Strouhal number with Reynolds number for Zigzag 1 and Sine 3 channels.

Figure 5.30 plots the *St* number against the Reynolds number for Zigzag 1 and Sine 3 channels. A *St* number around 0.3 can be seen for the oscillatory flow in Zigzag 1 channel. The periodic oscillation turns to chaotic oscillation with no dominant frequency at higher

Reynolds number ($Re > 300$). For Sine 3 channel, the oscillatory flow occurs at a wide range of Reynolds number ($330 < Re < 500$), as seen from Figure 5.28 (e). The power spectra feature a characteristic peak at $St = 0.24$-0.27 in the oscillation regime. Figure 5.30 shows that the St number is relatively constant and is independent of the Reynolds number. Repeating the experiments using a different pump has no noticeable effect on the frequency of oscillation and it concludes that the phenomenon is not induced by the external oscillation such as the rotation of the pump rotor.

A significant number of researchers have observed self-sustained oscillatory flow in many two- or three-dimensional grooved and wavy-walled channels (Amon et al., 1996, Nishimura et al., 2000, Comini et al., 2004, Hossain and Islam, 2004, Guzman and Del Valle, 2006, Ramgadia and Saha, 2012, Guzman et al., 2013). The geometrical parameters considered in these studies, mainly the aspect ratio, relative wavy amplitude, relative channel width and phase shift, are very different from the three-dimensional wavy channels described in this study. Curvature induced transverse or lateral vortices were observed in the crest and trough of the wavy profiles. These vortices detach periodically from the corners and move downstream, leading to time-periodic flow behaviour. The oscillation theory, however, may be different from that of narrowly-spaced passages considered in this study, in which flow mixing is mainly achieved by Dean vortices formed in the cross-section.

Since the early work by Dean (1928), who first demonstrated that curved channel flow is unstable to small amplitude disturbances for Dn number greater than 35.92, many researchers investigated the flow development of fluid flow in curved ducts. A stability analysis of the dual solutions, performed by Yanase et al. (1989), showed the two-vortex flow to be stable to an arbitrary perturbation, while the four-vortex flow was stable to a symmetric perturbation but unstable to an asymmetric perturbation. Sankar et al. (1988) found that it was possible for a four-vortex flow to develop sustained spatial oscillations in the streamwise direction. Through flow visualisation studies of Dean vortex flow, oscillations were observed in the form of vortex pair undulations, vortex pair twisting, and in the form of events where vortex pair split and merge (Finlay et al., 1988, Ligrani and Niver, 1988). Dean vortices with oscillations mostly in the radial direction were believed to strongly depend on the small amplitude disturbances that trigger initial vortex development. Mees et al. (1996) reported detailed experiments and numerical simulations of a fully developed travelling wave state (a form of twisting vortices) in a curved duct of square cross-section. In their experiments, the destabilizing disturbances were created by a pin that was inserted along the horizontal centreline. They suggested that in order to find a travelling wave state, both a steady four-cell flow state and disturbances that destabilize this four-cell state have to be present.

Oscillation of the Dean vortices caused by the switching between a clockwise or counter-clockwise rotation was found in fully developed turbulent flows. Tunstall and Harvey (1968) obtained a bistable flow characterized by a single vortex switching between rotations in the clockwise and counter-clockwise senses in their experiments. The two stable configurations, which are mirror images of each other, are characterized by the inner-corner separation region being displaced into an asymmetric position thus biasing the main flow into the other half of the bend. They noted that the necessary conditions for the switching to occur appear to be that the bend must be acute enough to cause separation at the inner wall. Similar oscillatory phenomena were observed by Rütten et al. (2005), who investigated turbulent flow through 90° pipe bends using large-eddy simulations. They observed the flow spectra exhibit peaks at St ~0.01, which was caused by the two Dean vortices whose strength vary in time and which as such alternately dominate the flow field. This alternating domination lead to a predominance of a clockwise or anticlockwise rotation of the flow close to the wall in the downstream, which is similar to the swirl switching phenomenon found by Tunstall and Harvey. However, they found that the low-frequency oscillation could also be observed when no separation is present. They also found that the spectra exhibited a distinct peak in the high frequency range (St = 0.2-0.3) that is ascribed to shear layer instability. If the shear layer is a result of flow separation, the high-frequency peak is broad and large, while this peak is relatively narrow without separation of the decelerated flow at the inner side.

In this study, as discussed in Section 5.2.2, the flow is very sensitive to the inlet conditions before the flow becomes chaotic. The oscillation might be caused by the unsteadiness of the Dean vortices being trigged by the small disturbances from the inlet. From video recordings of the flow in the oscillation regime, it was seen that the flow flaps up and down with regular frequency when passing the bends. This might be caused by the shear layer instability and variation of the location and strength of the Dean vortices. This seems to share some similarity to the flow observed by Rütten et al. (2005), although the flow is in the laminar regime in this study. It is interesting to note that this oscillation was not observed in simulations with steady inlet conditions. In order to gain further insight into the oscillatory flow and understand the mechanisms, simulations with introduced fluctuating inlet boundary conditions in this flow regime need to be carried out.

5.5 Pressure-drop penalty of wavy microchannels

As a result of the complex flow fields described above, a larger pressure drop is also expected in wavy microchannels. The experimental method to measure pressure drop in wavy channels was described in Chapter 3. The relative pressure-drop penalty defined in Eq. (3.11) is examined and plotted in Figure 5.31. A series of numerical calculations have been conducted and the results are presented in Figure 5.31 for comparison.

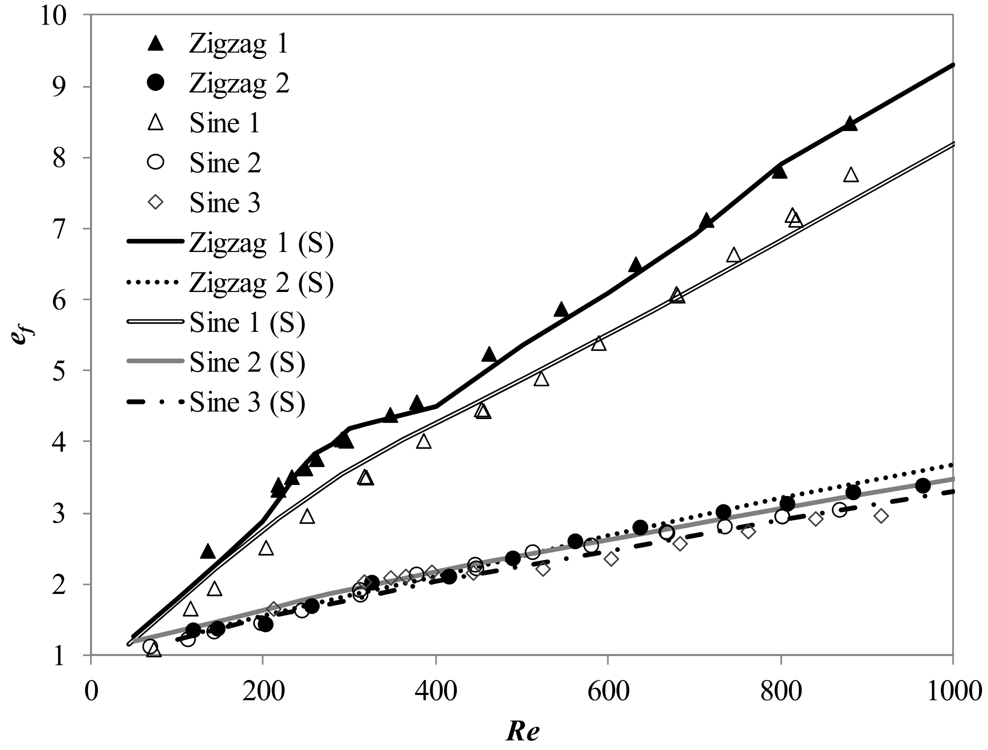

Figure 5.31: Pressure-drop penalty as a function of Reynolds number for different channel geometries (lines: simulation values; symbols: experimental results).

For the base case geometry (Zigzag 1), the pressure-drop penalty is higher than that for a straight channel of the same length since $e_f > 1$. With increasing Reynolds number, the pressure-drop penalty increases dramatically. The investigation of the flow field reveals the dominance of recirculation zones in the zigzag channel with tight bends. These recirculation vortices lead to complex transient flow effects above a Reynolds number of 300. As the Reynolds number is increased, these transient effects become more important as the volume occupied by the recirculation zones increases. These result in a significant increase in frictional pressure drop.

For all the channels examined, the friction factor is increased relative to the straight channel values with increasing Reynolds number. Figure 5.31 also shows that the effect of various channel geometries on pressure-drop penalty is significant. As seen from this figure, the pressure-drop penalties of channels Zigzag 1 and Sine 1, which have sharp bends and short straight sections, are much higher than those of other channels. The pressure-drop penalty increases due to two factors, Dean vortices and flow separation near the bends. As the corner becomes sharper, the growth of recirculation zones with Reynolds number increases pressure losses by reducing the areas of main flow passages. In addition, the pressure-drop penalty increases due to the formation of Dean vortices even when there is no recirculation formed at low Reynolds numbers (Rosaguti et al., 2007b). The strength of Dean vortices increases and the flow mixing and disturbance are more pronounced in channels with sharper bends, which result in higher pressure-drop penalty. It is also shown that the increase in e_f of zigzag channels is more pronounced than that of sinusoidal channels with the same half-unit length and amplitude. The absence of recirculation zones in channels Sine 2 and Sine 3 accounts for the small increase in the friction factor. These results are in agreement with the flow characteristics in the channels discussed in the above sections. The experimental data agree well with the simulated values.

5.6 Summary

The micro-PIV system allows detailed velocity profiles to be obtained in wavy microchannels across a range of Reynolds numbers. Data collected at low Reynolds numbers where the flow is steady were validated by the steady-state simulations. Then these were extended to higher Reynolds numbers and confirmed the existence of massive recirculation and unsteady flows.

The time-resolved velocity measurements in a base zigzag channel ($R_c/d = 0.51$, $L/d = 1.75$, and $\theta = 45°$) have revealed a transition from a steady flow to a time-dependent oscillatory flow having a dominant frequency and subsequently to a complex transient flow. The flow becomes unsteady at a relatively low Reynolds number in the zigzag channel in the laminar flow regime. Unsteadiness first appears at the end of the channel and moves upstream with increasing Reynolds number. In the chaotic regime, the flow was found to be very sensitive to the inlet condition. Small disturbances in the inlet flow trigger an early transition to unsteady flow. In the transient flow regime, the fluid velocity in the zigzag channel fluctuates randomly and the power spectrum of the velocity becomes broadband and continuous.

Comprehensive flow visualisation in the zigzag channel shows recirculation zones form immediately after the inner corner when the Reynolds number is larger than a value of around 135. The size and strength of the recirculation increase with increasing Reynolds numbers. High fluctuations in recirculation zones highlight the importance of the flow recirculation in leading to transient flow.

Using the present two-dimensional PIV and a continuity based technique, three-dimensional maps of the complex flow including the identification and localization of vortical structures in wavy microchannels were obtained, which provides a way to better understand the complex flow behaviour and evolution in wavy microchannels. The spatial and temporal evolution of secondary flow (Dean vortices) play important roles in generating chaotic advection, enhancing fluid mixing and heat transfer.

Flow visualisation experiments were conducted in five different channel geometries for a wide range of Reynolds numbers. In wavy channels, the steady flow exists at low Reynolds numbers but at a critical Reynolds number, which depends on the channel geometry, unsteady flow develops. The effects of channel geometries on the flow characteristics of wavy microchannels were investigated experimentally. It is shown that the zigzag geometry is always better than the sinusoidal channel in terms of flow mixing. In channels which have higher bend angles (θ) or amplitude to half-unit length ratio (A/L), flow recirculation zones form near the bends of the channel, even at low Reynolds numbers, leading to an earlier transition to unsteady regime as compared with smoother channel geometries.

This investigation also revealed the possibility of triggering sustained oscillatory flows in wavy channels. The critical Reynolds number for oscillatory flows, which is also the onset of unsteadiness of the velocity field, and the dominant frequency depend on the channel geometry. The oscillation might be caused by the unsteadiness of the Dean vortices which is trigged by the small disturbances from the inlet.

Consistent with the findings on flow structures, the pressure-drop penalty in wavy channels is always higher than that in a straight channel with the same length and it increases with increasing Reynolds number due to flow separation and the formation of Dean vortices. The pressure-drop penalty is higher in zigzag channels than that in sinusoidal channels due to the pronounced recirculation induced by the sharp bends. Higher bend angle (θ) or amplitude to half-unit length ratio (A/L) generally leads to increased friction factor. The pressure-drop penalty obtained from the experimental study agrees very well with the simulation predictions.

The transient effect generated by flow separation and Dean vortices by the presence of the bends plays important roles in heat transfer performance. The detailed heat transfer characteristics of wavy microchannels are studied in Chapter 6.

Chapter 6

Heat Transfer in Wavy Microchannels

In Chapter 5, flow visualisation experiments were carried out in different wavy channel geometries for a wide range of Reynolds numbers and the investigation of the detailed flow fields reveals the existence of flow recirculation and secondary flows. As a consequence of complex flow behaviours, the heat transfer performance of wavy microchannels is much superior to that of straight channels with the same cross-section, as evidenced by previous studies. However, as addressed in the literature review, the heat transfer performance of wavy microchannels similar to those used in this study has not been investigated experimentally in a systematic fashion. Only a limited number of experimental studies were conducted on the overall heat transfer coefficients of wavy channels in microscale (Sui et al., 2011, Anxionnaz-Minvielle et al., 2013, Karale et al., 2013). The experimental difficulties due to the restrictions imposed by the small length-scales involved in obtaining accurate, microscale measurements are still the main hindrance in the progress towards understanding the heat transfer characteristics in tortuous microchannels.

In this chapter, the heat transfer experiments are performed for the same wavy channels and working conditions as those used in the hydrodynamics study. The system design and calibration, data acquisition and data reduction procedures were detailed in Chapters 3 and 4. Three-dimensional conjugate simulations are also carried out for the corresponding experimental conditions to validate the experimental system and data processing procedures. The heat transfer performance together with pressure-drop penalty in different geometries is discussed to understand the mechanisms of heat transfer enhancement in wavy channels.

6.1 Numerical simulations

A generalized computational model has been described in Chapter 4 for the straight channel test section. A similar method was applied to the wavy channel test section. A "complete model" including the whole length of the channel (*n* repeating units together with jointed inlet and outlet sections), Kovar and glass substrates was applied for conjugate simulation of the wavy channel test section. This model also accounts for possible flow non-periodicity in tortuous channels by including all the repeating units. The geometrical dimensions, such as substrate thickness, channel wavelength, amplitude and wavy unit number, are all identical to those for the fabricated test section used in the experiments (listed in Chapter 3).

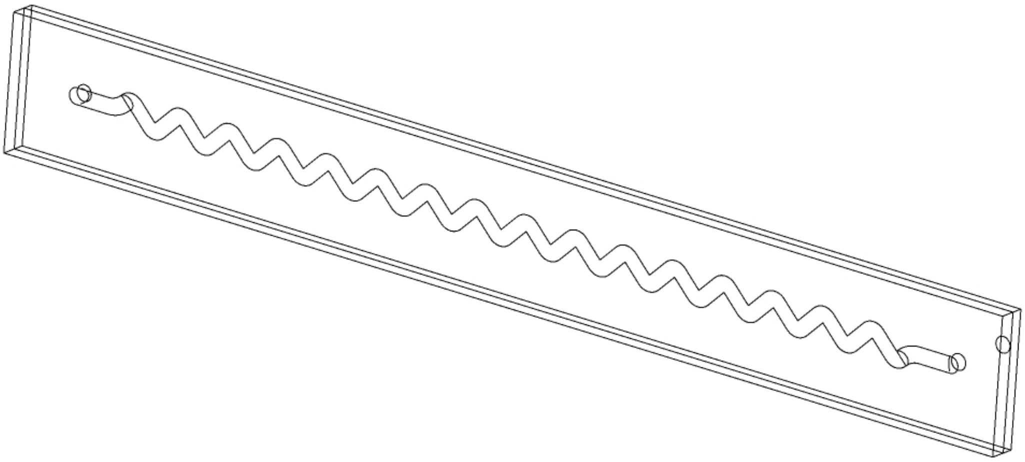

Figure 6.1: Schematic of the computational domain for Zigzag 1 channel.

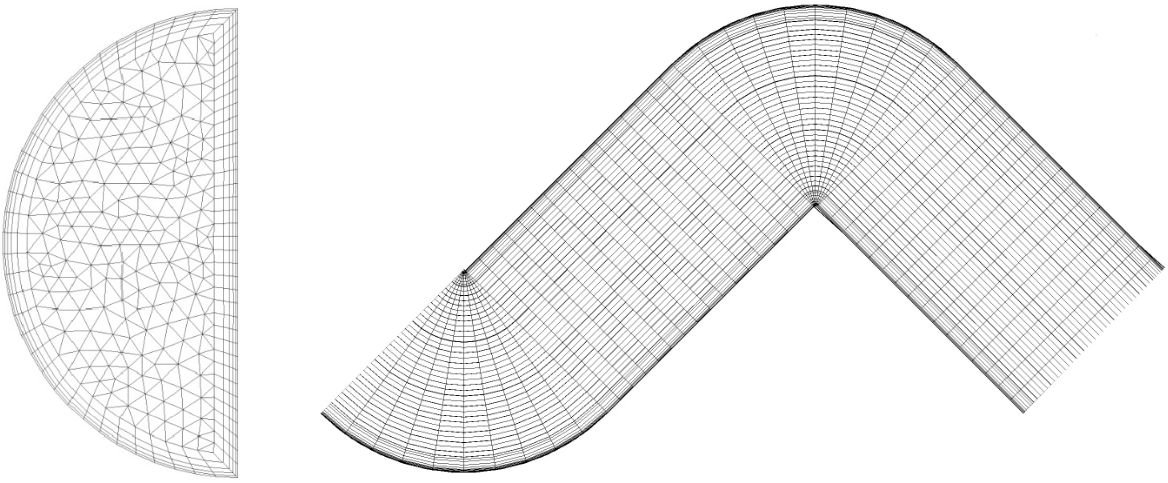

(a) **(b)**

Figure 6.2: Illustration of the computational mesh for one repeating unit of Zigzag 1 channel on: **(a)** the cross-section; and **(b)** the axial direction.

The entire computational domain for one of the wavy channels (Zigzag 1) is shown in Figure 6.1. The flow starts from the inlet section and goes through 16 repeating units, which provide a sufficiently long distance for flow development. The final unit (n^{th} unit) is then connected to the outlet section, allowing the flow to exit the channel smoothly. The computational mesh for one repeating unit of Zigzag 1 channel is shown in Figure 6.2. The cross-sectional mesh was constructed to provide the greatest resolution close to the walls where fluid velocity and temperature gradients are the highest, as shown in Figure 6.2 (a). The mesh on the inlet was extruded along the axial path to produce the swept mesh, as shown in Figure 6.2 (b).

A series of simulations was first carried out as a grid independence study. The initial mesh size was 332 elements in the channel cross-section and 50 elements per unit in the axial direction (332 × 50) and was increased to 742 × 50 and further to 1304 × 70. The simulation results of the local Nusselt number for *Re* = 158 and *Pr* = 6.13, which falls within the steady flow regime, are presented in Figure 6.3. The average Nusselt number changes by less than 0.4% during grid refinement, which indicates that the mesh density is sufficient for steady flow simulation. A final mesh size of 742 × 50 was employed for simulation of Zigzag 1 channel to ensure that the region where the secondary flows form is well resolved. The computational domain of the whole test section consists of 467,000 cells in the fluid domain and 482,000 cells in the solid domain. Similar model discretization and mesh resolutions were employed for other channels used in the present study except Sine 1 channel. The geometry for the Sine 1 channel was not sweepable so a tetrahedral mesh with inflation at the wall was used.

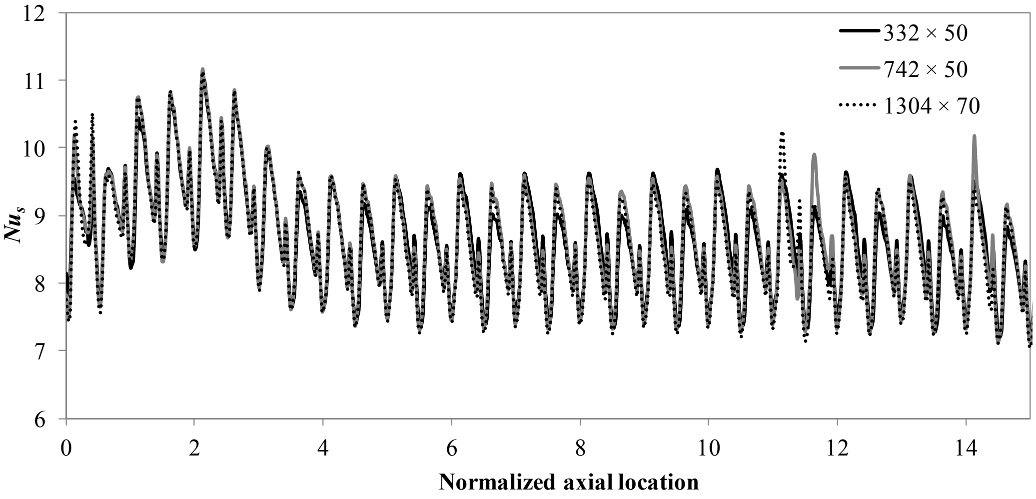

Figure 6.3: The Nusselt number in the flow direction of Zigzag 1 channel at *Re* = 158 for different mesh sizes. Results are for a Prandtl number of 6.13.

6.2 Heat transfer experiments in zigzag channels

6.2.1 System calibration

A series of experiments without fluid flow were conducted for system calibration. The heat loss coefficient was calibrated for each test section before the heat transfer measurements and the calibration curves are plotted in Figure 6.4. Due to the similar configuration all of the heat loss coefficients follow the same trend and can be expressed by Eq. (6.1) using curve-fits. The A, B and C values for each test section are listed in Table 6.1.

$$h_{loss} = A(T_w - T_a)^2 + B(T_w - T_a) + C \tag{6.1}$$

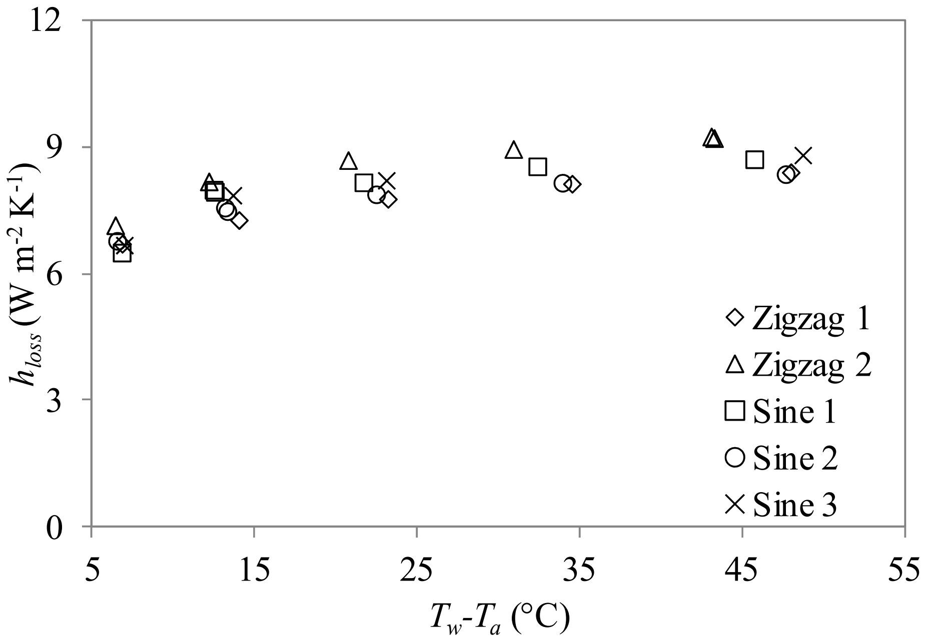

Figure 6.4: Heat loss coefficient calibration for wavy channel test sections.

Table 6.1: Heat loss coefficients for different test sections.

Test section	*A*	*B*	*C*
Straight	-0.0004	0.0558	6.486
Zigzag 1	-0.0009	0.0885	6.168
Zigzag 2	-0.0021	0.1536	6.389
Sine 1	-0.0020	0.1617	5.510
Sine 2	-0.0011	0.0946	6.287
Sine 3	-0.0018	0.1462	5.543

6.2.2 Heat transfer of single-phase flow

The heat transfer characterises of Zigzag 1 channel (R_c/d = 0.51, L/d = 1.75, and θ = 45°) which is the base case geometry was studied in detail. Single phase water flow heat transfer experiments were conducted for Reynolds numbers ranging from 42 to 960. The heater was attached more towards the outlet end, leaving a few un-heated units that served to enable the flow to become hydrodynamically fully-developed before entering the heating region (shown in Figure 6.6). The input power was adjusted for different Reynolds numbers so that the temperature rise from the inlet to the outlet was between 2 and 10 °C, due to the fact that the uncertainty of temperature measurement is relatively large for a small temperature change. For each test, the system was allowed to reach steady state prior to measuring and recording the flow rate and temperatures.

6.2.2.1 **Validity of experimental approaches**

As discussed in Chapter 4, the direct measurement of the inner wall temperature is impossible in the experiments. The average wall temperature at the wall-fluid interface was extrapolated from the measured outer wall temperatures through a simplified model of the heat conduction in the system, which provides good estimation with less than 10% error in the straight channel test section. The validity of Eq. (4.15) in predicting wall-fluid temperature difference was examined in the zigzag test section. Figure 6.5 shows the comparison of wall-fluid temperature difference, $\bar{T}_w - T_b$, between the simulation data and that predicted from Eq. (4.15). As can be seen, for the Reynolds number considered in this study, good agreement is achieved with predicted values of the local driving force falling within ±20% of the actual values obtained directly from the simulation.

However, the uncertainty of applying Eq. (4.15) to the zigzag channel is higher than that for the straight channel. This is because the temperature distribution is far more complicated in wavy channel test sections. Figure 6.6 shows a typical temperature distribution on the metal outer surface (Figure 6.6 (b)) and a cross-section inside the test section (x = 0.0825 m, Figure 6.6 (a)) for Re = 326 and Q_{in} = 17.8 W. The flow is from left to right in Figure 6.6 (b). The area of the heater is marked with the rectangular box. It can be seen that the temperature gradient over the plate is rather large over the cross-section. This large gradient is a result of the low thermal conductivity of Kovar (17 W K^{-1} m^{-1} compared with cooper (400 W K^{-1} m^{-1}) and silicon (149 W K^{-1} m^{-1}) which were used in many studies (Harms et al., 1999, Lelea et al., 2004, Tiselj et al., 2004)) and relatively large width of the plate compared with the diameter of the channel.

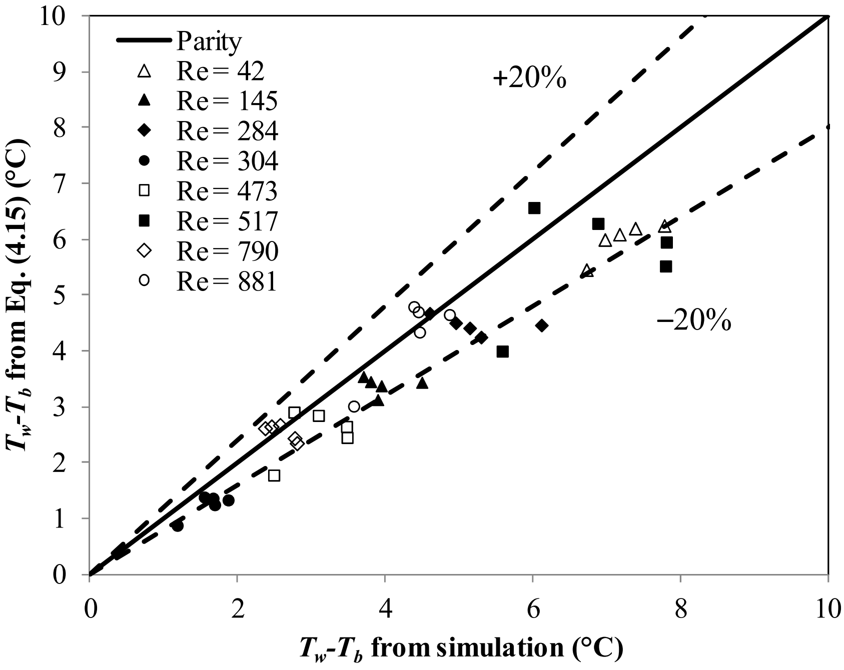

Figure 6.5: Comparisons of the temperature difference, $T_w - T_b$, between the simulation data and the predicted values obtained from Eq. (4.15) for Zigzag 1 channel.

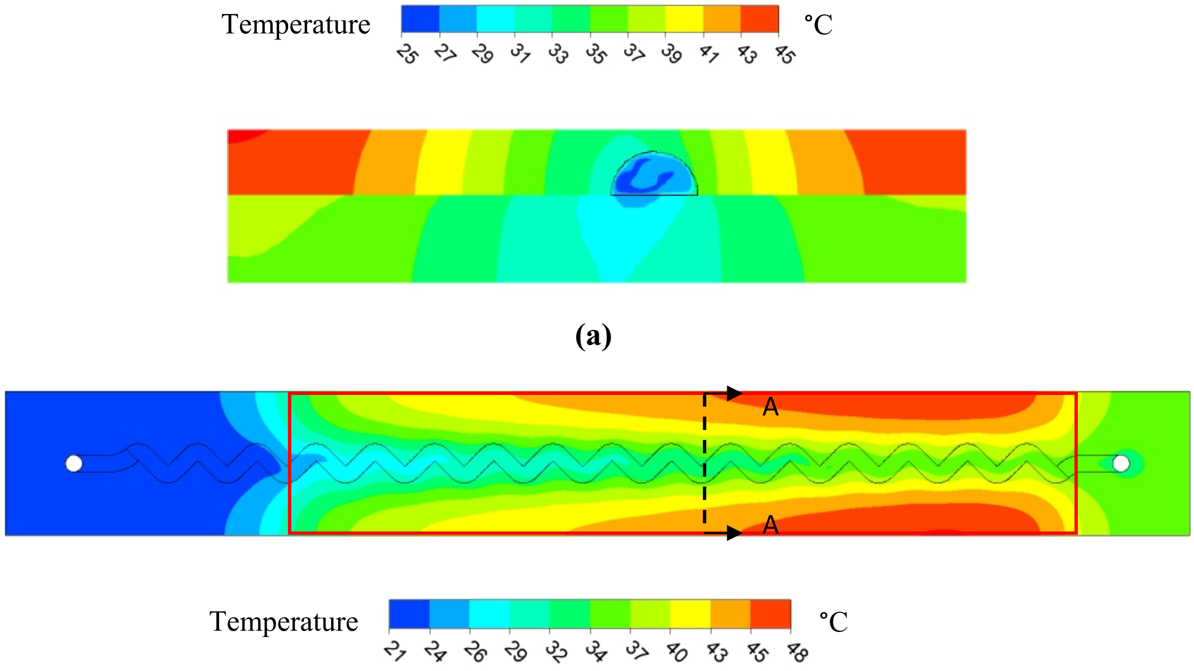

(a)

(b)

Figure 6.6: Temperature distribution on: **(a)** cross-section A-A at x = 0.0825 m; and **(b)** outer surface of the metal for Re = 326 and Q_{in} = 17.8 W.

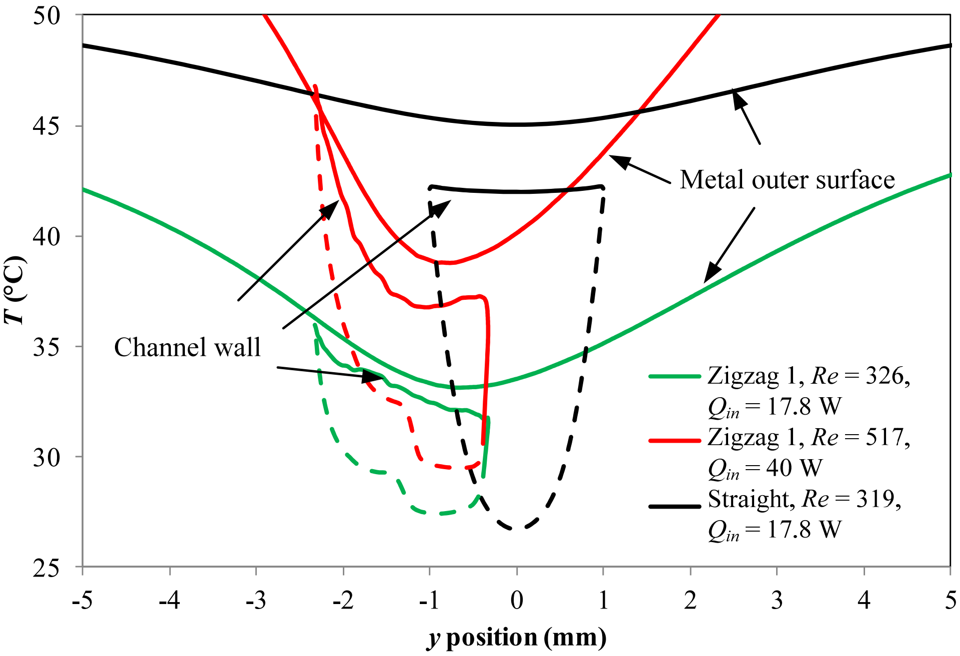

Figure 6.7: Temperature profiles on the cross-section at x = 0.0825 m (solid lines: metal wall; dashed lines: glass wall).

As indicated in Eq. (4.12), an assumption of a uniform temperature distribution on the metal inner surface at the channel cross-section was used in the model. Figure 6.7 shows the temperature profiles at a cross-section (x = 0.085 m) for both the Zigzag 1 channel and a straight channel. It is clear that the assumption is valid for the straight channel, where the temperature difference along the metal inner wall (solid line of the channel wall) is less than 0.3 °C. Although the temperature is not uniform on the glass wall, it will not influence the calculation since heat transfer between the glass wall and the fluid is neglected with an adiabatic boundary condition being assumed on the glass wall when calculating the wall-fluid temperature difference. However, the metal wall temperature is highly non-uniform in the circumference of the zigzag channel due to the complex flow behaviours. The temperature distribution on the channel wall depends on the design of the channel, the material of the substrate, and working conditions such as flow rate and heat flux. Therefore, the accuracy of Eq. (4.15) is influenced by the combined effect of these parameters. In addition, since the inner wall temperature was calculated from the measured outer surface temperature, the uncertainty in the measurement of the outer surface temperature plays an important role in the temperature calculations. As can be seen in both Figure 6.6 and Figure 6.7, the temperature gradient along the channel width is very large on the metal outer surface for the zigzag channel (it is more uniform in the straight channel as shown in Figure 6.7). The temperature measurement is therefore very sensitive to the location of the RTD sensors. Due to the limitation of physical size of the RTD sensors, it is difficult to resolve the temperature spatially down below 2 mm using the present technique; hence, caution should be used to locate the RTD sensors for the outer surface temperature measurements. To obtain the temperature on the heated wall with higher resolution, whole-field temperature measurement techniques might be needed, such as infrared thermology (Hetsroni et al., 2002). It is important to note that Eq. (4.15) provides a better prediction for the substrates with higher thermal conductivity, smaller thickness, relatively smaller width, and when the heat loss is minimized.

Typical temperature profiles measured from experiments are shown in Figure 6.8 and are compared with the simulation results. The outer surface temperatures were measured along the middle line of the substrates. The mean fluid temperature was calculated from Eq. (4.16) assuming a linear variation in the flow direction. It can be seen that the experimental temperatures of both the metal and glass outer surfaces agree well with the corresponding numerical predictions. The disparity between some points of the measured glass temperatures and simulation values may be caused by mis-location of the RTD sensors (such as the RTD sensors were not attached at exactly the middle line of the plate). The temperatures were found to agree well with the simulation results once the locations of the RTD sensors were corrected. It is also shown in Figure 6.8 that both the perimeter-averaged wall temperature (T_w) and bulk mean fluid temperatures (T_b) agree well with the simulation results, indicating that the heat transfer calculation model is still valid when applied to the wavy channels.

The local Nusselt number in the flow direction is examined and the typical results for Re = 246 and Q_{in} = 11.4 W are shown in Figure 6.9. The normalized channel axial location is written as

$$S = \frac{s}{S_0} \tag{6.2}$$

where s is the axial location and S_0 is the axial path length for one unit. Therefore, S = 0 corresponds to the inlet plane of the first unit and S = 16 to the exit plane of the last unit.

The experimental data are compared with the simulation values in Figure 6.9 and reasonably good agreement is achieved. The high value of the Nusselt number for the last measuring point is attributed to the uncertainty arising from the axial conduction effect at the end.

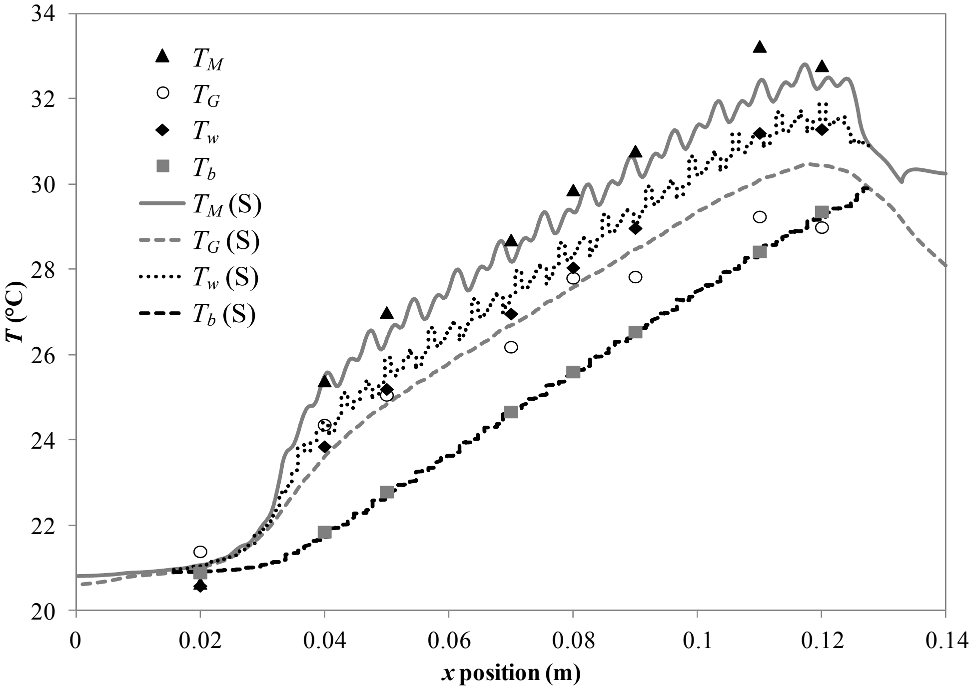

Figure 6.8: Comparison of the temperature distributions obtained from experiments (symbols, T_w is estimated using Eq. (4.15) and T_b is estimated using Eq. (4.16)) and simulations (lines) for *Re* = 246 and Q_{in} = 11.4 W.

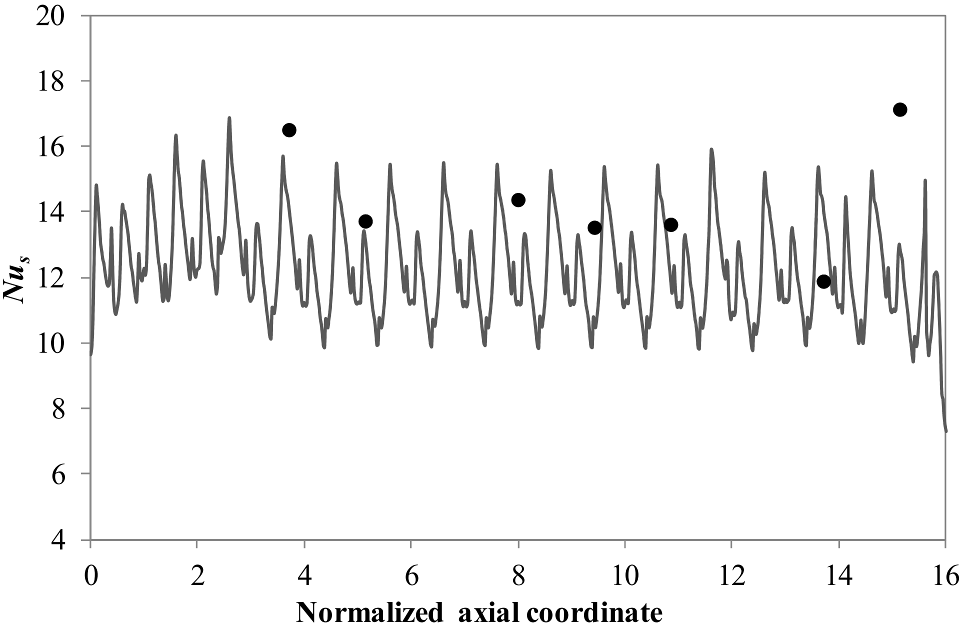

Figure 6.9: Comparison of the local Nusselt number obtained from experiments (symbols) and simulations (lines) for *Re* = 246 and Q_{in} = 11.4 W.

It should be clarified that the local Nusselt number is based on the averaged temperature over the area of the RTD sensors which gives a spatial resolution of ~2 mm. In the wavy channels, as shown from the simulation results in Figure 6.9, the Nusselt number changes dramatically along the channel and is very sensitive to the local position. It is very challenging to resolve it experimentally, considering the small scale of the channels. In addition, it is clear that the present apparatus actually provides mean values for the unsteady flows because of the temporal averaging of the measured data. As the three-dimensional conjugate simulation results agree reasonably well with the experiments, the detailed temperature distribution and heat transfer characteristics can be analysed through numerical simulations to get further understanding of the thermal performance of the wavy microchannels.

6.2.2.2 **Heat transfer enhancement**

The variation of the average Nusselt number with the Reynolds number for Zigzag 1 channel is presented in Figure 6.10. The average Nusselt number was calculated by averaging the local Nusselt numbers at axial positions along the flow direction (in the range between 40 and 90 mm from the inlet, so that the entrance effects and the uncertainties arising from the unheated end effects are minimized). The error bars represent one standard deviation for the local Nusselt numbers measured at different locations. The plot of the average Nusselt number for the straight channel is also presented in Figure 6.10 for comparison. The predicted values from simulations are presented as solid lines. It should be noted that for $Re < 390$ a converged state has always been reached with all the scaled residuals below 10^{-6}. However, it was found that the normalised residuals stayed above 10^{-4} after 1000 iterations for $Re = 397$, suggesting that there may not be a steady state solution and the flow has become transient. Therefore, the steady-state heat transfer results are limited to $Re < 400$, and the plots for transient flows (dashed line) are instructive only.

As expected, the Nusselt number increases with Reynolds number, as shown in Figure 6.10. Both the experimental and simulation results showed that the heat transfer performance of Zigzag 1 channel is much better than that of the straight channel with the same cross-section. The average Nusselt number in the zigzag geometry is about 6.1 times higher than that of the straight channel at $Re = 728$. The underlying physical mechanism was revealed by the detailed flow field analysis in Chapter 5, which showed that the flow recirculation and secondary flow structures present at the bend increase the heat transfer rates by constantly disrupting the thermal boundary layer. It can be also seen from Figure 6.10 that the experimental results match the numerical predictions quite well, with the largest difference being less than 18%. The experimental Nusselt numbers are slightly higher than the predicted values for 100 < *Re* < 300, while lower at higher Reynolds number (*Re* > 800). The mean value of the absolute error is 9.3%. Reasons for this disparity include uncertainties in temperature measurement in the experiments, as well as prediction of the average wall temperature.

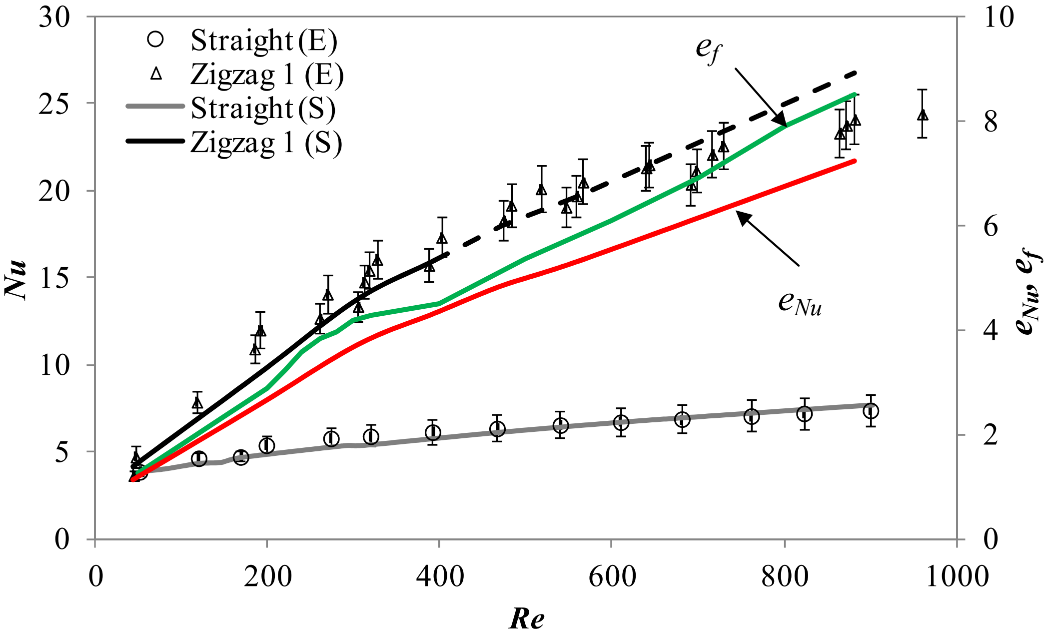

Figure 6.10: Variation of the average Nusselt number with Reynolds number obtained from experiments (symbols) and simulations (lines) for Zigzag 1 channel and the straight channel. The error bars represent one standard deviation for the local Nusselt numbers measured at different locations. The red and green lines denote e_{Nu} and e_f from simulations, respectively. Simulation results are for a Prandtl number of 6.13.

The simulated heat transfer enhancement (e_{Nu}) defined in Eq. (3.22) is plotted in Figure 6.10 (red line). As discussed in Chapter 4, for a straight channel with semi-circular cross-section, Nu_{str} = 3.7 was employed for hydrodynamically- and thermally-developed laminar flow with a thermal boundary condition representative of that achieved in the present study. Recall that the present experimental arrangement does not correspond strictly to any standard thermal boundary condition for laminar flow even though the perimeter-averaged wall heat flux in the heating zone is approximately constant. The simulated relative pressure-drop penalty, e_f, for Zigzag 1 channel has been discussed in Chapter 5 and is also presented in Figure 6.10 (green line) for convenience of comparison. It is shown that the heat transfer enhancement is obtained in the zigzag channel at the expense of a larger pressure drop penalty compared with the straight channel. For this particular case, the heat transfer enhancement is slightly lower than the pressure-drop penalty, which is opposite to the results obtained from Zheng (2013) for the same geometry but with a constant heat flux boundary condition. The different thermal performance might be attributed to the difference in the thermal boundary conditions.

6.3 Effect of channel geometry

The detailed flow fields and pressure drop penalty were investigated in five different geometries in Chapter 5. A heat transfer study for Zigzag 1 channel was presented in detail in the previous section. Heat transfer experiments were also conducted using the other four test sections. Three-dimensional conjugate simulations for similar experimental conditions were also carried out, and the steady-state solutions for water flow and heat transfer in these channels were obtained for Reynolds numbers up to 800.

The same experimental approach for the Nusselt number calculation was applied to all the wavy channels. The average Nusselt number obtained from experiments and simulations for the wavy channels Sine 1, Zigzag 2, Sine 2 and Sine 3 are presented in Figure 6.11. The e_{Nu} and e_f curves obtained from simulations are also plotted to facilitate comparison. As seen from the figures, the general trends of the dependence of Nusselt number on the Reynolds number are similar between the experimental results and simulation predictions for all the cases considered. In general, it is found that the heat transfer performance is better than that of the straight channel and that both e_{Nu} and e_f increase with increasing Reynolds number. This is because, as explained before, the secondary flow and/or recirculation are generated and the intensities of these vortices increase with Reynolds number. Similar to Zigzag 1 channel, the heat transfer enhancement and pressure-drop penalty augmentation in Sine 1 channel are similar in magnitude. For the other three channels, the heat transfer augmentation at higher Reynolds number rises relatively faster when compared with the increase in pressure-drop penalty.

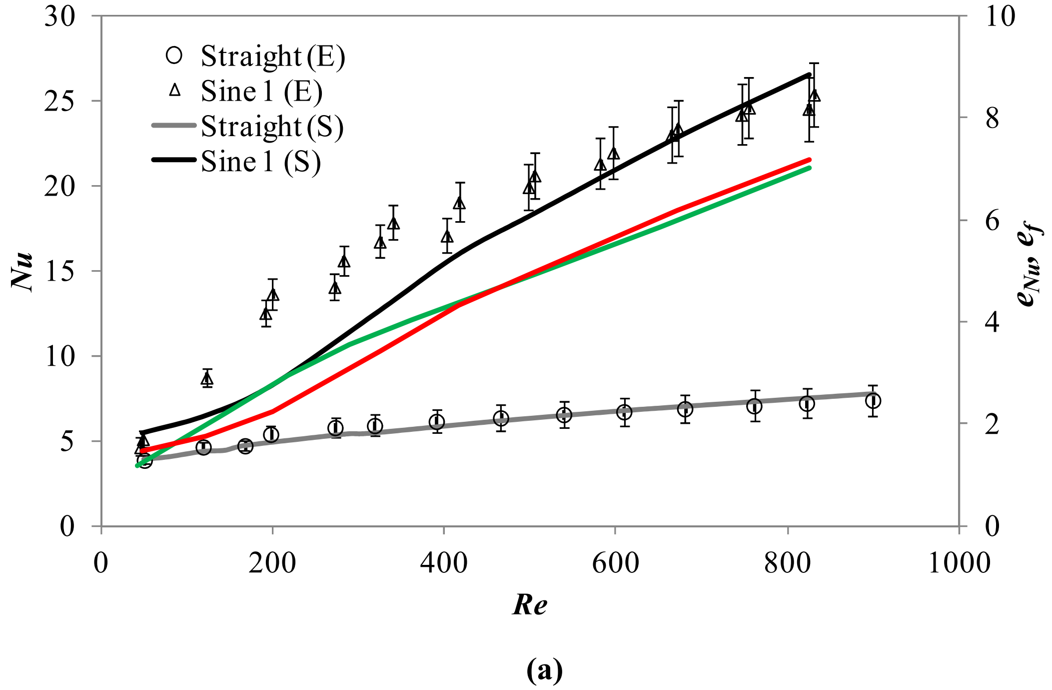

(a)

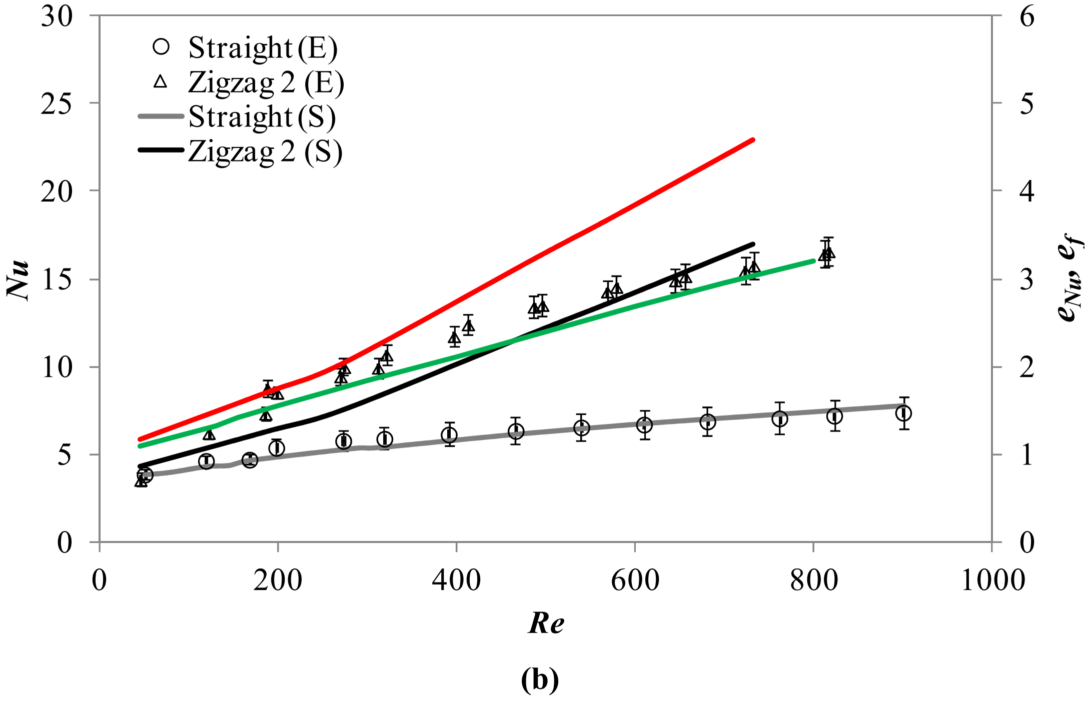

(b)

Figure 6.11 (a) and (b): Variation of average Nusselt numbers with Reynolds number obtained from experiments (symbols) and simulations (lines) for wavy microchannels: **(a)** Sine 1; **(b)** Zigzag 2. The error bars represent one standard deviation for the local Nusselt numbers measured at different locations. The red and green lines denote e_{Nu} and e_f from simulations, respectively.

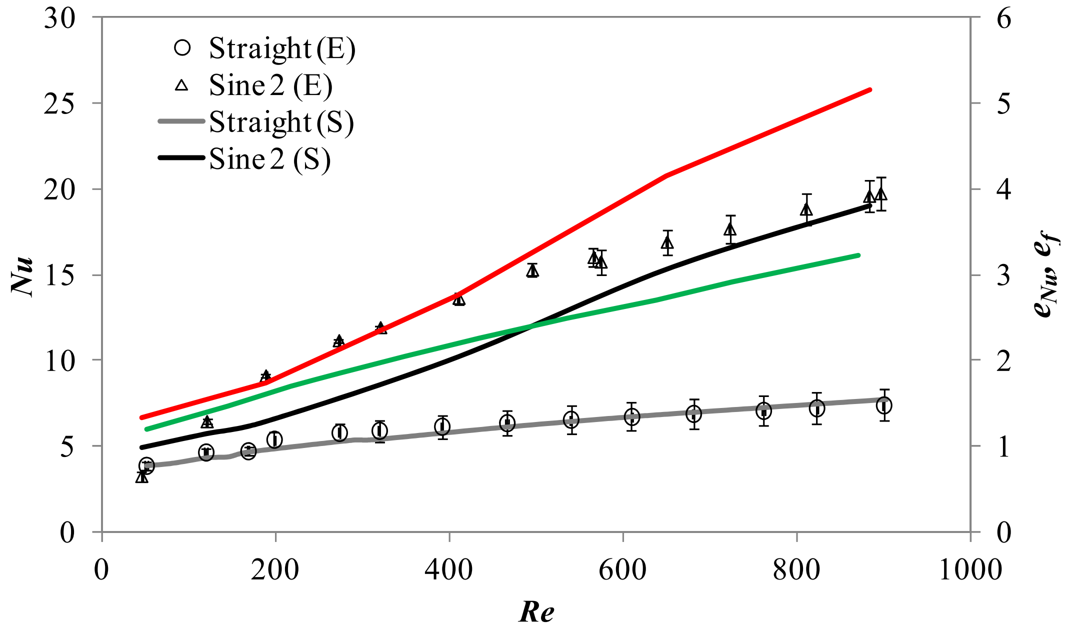

(c)

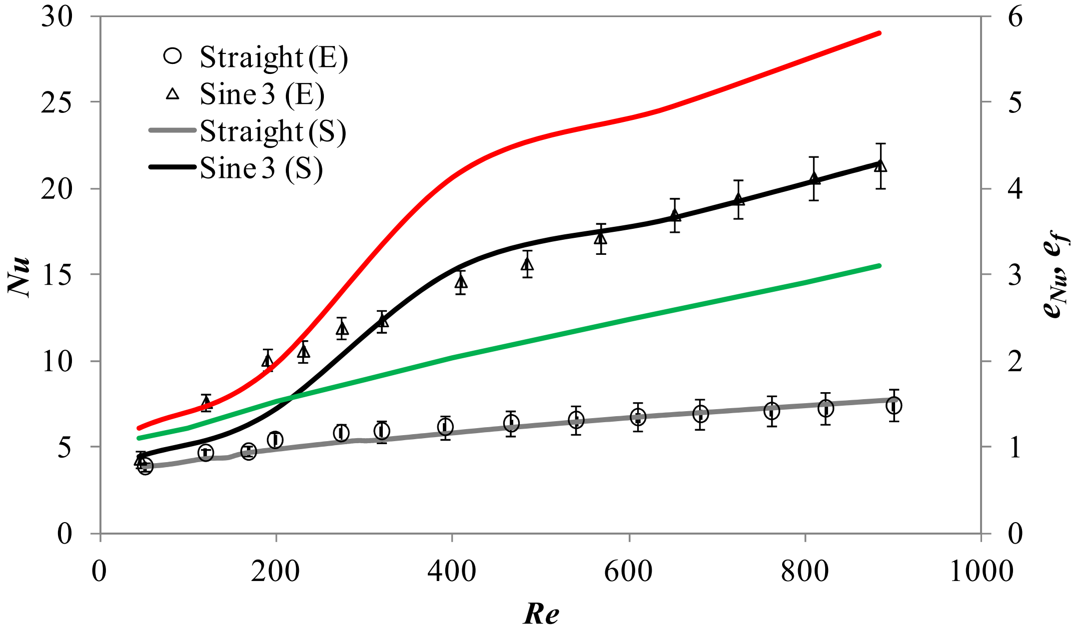

(d)

Figure 6.11 (c) and (d): Variation of average Nusselt numbers with Reynolds number obtained from experiments (symbols) and simulations (lines) for wavy microchannels: **(c)** Sine 2; and **(d)** Sine 3. The error bars represent one standard deviation for the local Nusselt numbers measured at different locations. The red and green lines denote e_{Nu} and e_f from simulations, respectively.

It is interesting to note that the deviation between the experimental and predicted Nusselt numbers is more significant for Reynolds number around 200-300 for most of the cases. This might be caused by the combined effect of the heat flux and flow conditions, so that the uncertainty using Eq. (4.15) is slightly higher under these working conditions. The average deviation between the experimental and simulation results are 16.7%, 14.5%, 20%, and 10.1% for Sine 1, Zigzag 2, Sine 2 and Sine 3 channels, respectively. Taking into account the experimental difficulties and the simplification of the model, the agreement of the experimental data with the simulation predictions is considered to be satisfactory.

To better compare the flow and heat transfer performance between different geometries, the heat transfer enhancement and relative pressure-drop penalty for all the five channels are plotted in Figure 6.12 (a) and 6.12 (b), respectively. Due to the reasonable agreement between the experimental and computational results, only results obtained from simulations are presented.

It can be seen that the Zigzag 1 and Sine 1 channels provide the highest heat transfer enhancement but also the highest pressure loss. This is explained by the investigation of the flow field which reveals the dominance of recirculation zones in these channels with tight bends and short straight sections.

For zigzag and sinusoidal channels with the same amplitude and half-unit length (Zigzag 1 and Sine 1, Zigzag 2 and Sine 2), the heat transfer enhancement is similar in magnitude for both channels across the range of Reynolds numbers studied, but the pressure drop is smaller in sinusoidal channels, which is attributed to the relatively smoother pathway in the sinusoidal channels.

Comparing Zigzag 1 ($\theta = 45°$) and Zigzag 2 ($\theta = 30°$) channels, and Sine 1 ($A/L = 0.5$) and Sine 2 ($A/L = 0.289$) channels, one can conclude that a larger bend angle or A/L ratio tends to result in more intensive heat transfer as well as increased pressure-drop penalty. The results obtained in the present experimental and numerical studies are in general agreement with the findings from Zheng et al. (2013b) and Rosaguti et al. (2007b), who conducted systematic simulations in wavy channels with various geometrical parameters. Zheng et al. (2013b) indicated that the heat transfer enhancement and pressure-drop penalty in zigzag channels increase noticeably at different Reynolds numbers as θ changes from 5 to 40 degrees, however the increase in heat transfer benefit becomes very limited when θ is further increased from 40 to 45 degrees. Similarly, for sinusoidal channels, Rosaguti et al. (2007b) reported that the greatest heat transfer augmentation is achieved at a higher A/L ratio.

However, their studies were mainly focus on a low Reynolds number range (usually *Re* < 400).

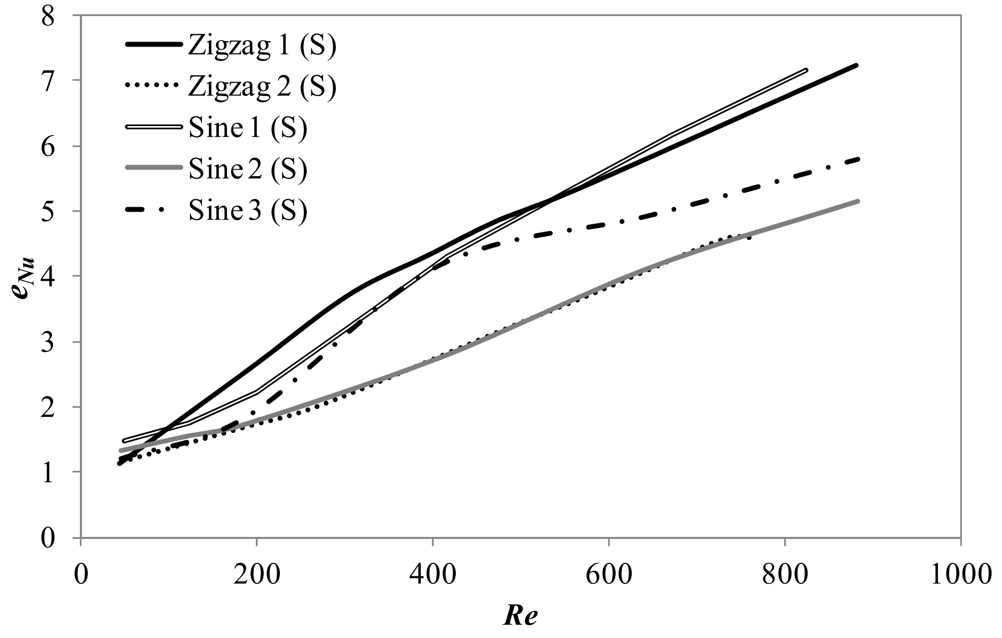

(a)

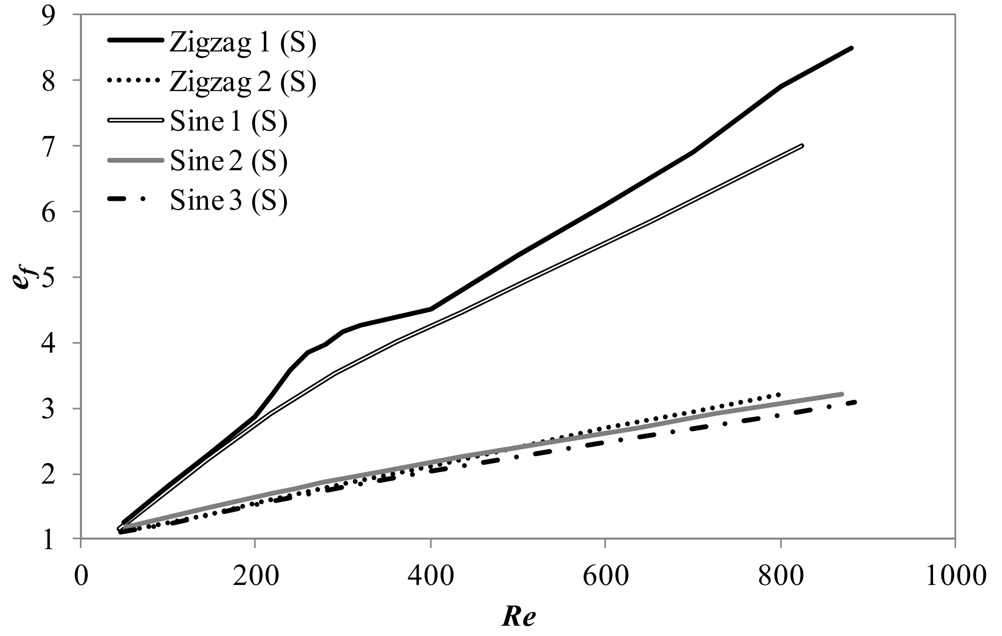

(b)

Figure 6.12: (a) Average heat transfer enhancement; and **(b)** relative pressure-drop penalty as a function of Reynolds number obtained from simulations ($Pr = 6.13$) for five wavy channels.

It is interesting to find that the Sine 3 channel, which has the same amplitude to half-unit length ratio ($A/L = 0.5$, $L/d = 3.5$) as Sine 1 ($A/L = 0.5$, $L/d = 1.75$) channel but is scaled up, presents significant heat transfer enhancement (comparable with that of the Sine 1 and Zigzag 1 channels at intermediate Reynolds numbers) with the lowest pressure drop. The heat transfer enhancement exceeds the relative pressure-drop penalty by a factor as large as 2.1 at Reynolds number around 400 for the Sine 3 channel. This is similar to the value (a factor of 1.8 at $Re = 200$) found in the work of Rosaguti et al. (2007b) for sinusoidal channels with $A/L = 0.444$, $L/d = 4.5$ and H2/T thermal boundary conditions. It has been shown in Chapter 5 that no obvious flow recirculation was found in the Sine 3 channel even at very high Reynolds numbers ($Re = 907$ in Figure 5.25 (e)). However, the counter-rotating (Dean) vortices (Figure 5.26) are formed in the cross-sections and promote cross-sectional mixing without causing a large pressure-drop. It is these structures that give rise to the heat transfer enhancement with comparatively low fraction factors (Rosaguti et al., 2007b). In addition, the direction of the Dean vortices alternates after every turning point in the sinusoidal flow path, potentially leading to chaotic advection with increasing Reynolds number, thus promoting further heat transfer enchantment.

6.4 Considerations for plate design

6.4.1 Stackability and heat transfer intensification

The performance of the wavy channels was analysed above based on criteria of heat transfer enhancement and relative pressure-drop penalty. However, these criteria do not directly indicate an overall performance of the systems using wavy channels when they are used separately. An “efficiency” or “enhancement” factor which is defined as the ratio of heat transfer enhancement and the relative pressure-drop penalty was used to relate thermal performance and hydraulic performance (Rosaguti et al., 2007b, Karale et al., 2013). This concept is well-suited for comparing single channels of the same axial length. However, it does not indicate how effectively the overall plate area in a heat exchanger is utilised when tortuous channels are introduced onto the plate surface. A tortuous path serves to enhance the heat transfer relative to the performance obtainable with straight channels, but also occupies more area on a plate.

Geyer et al. (2007) and Geyer (2008) introduced a broader concept of efficiency that includes not only the thermohydraulics of the channel but also the stackability of channels on a plate. The concept of area efficiency or area enhancement was introduced to define how well channels could be stacked onto a plate as a function of both their shape and the required separation distance. This, when multiplied by the heat transfer enhancement, gives a heat transfer intensification factor which provides a measure of the efficiency of using a plate with the given channel path, relative to equivalent straight channels. The same concept is used in this study to assess the intensification degree, combining the heat transfer enhancement and stackability on a plate.

The apparent area density which is defined as the ratio of the heat transfer surface area to the plate area is given by Eq. 6.3, considering a length of plate with straight channels of width *d*, separated by a wall thickness *t*.

$$(A_c/A_p)_{str} = \frac{P}{d+t} \tag{6.3}$$

where P is the perimeter of the channel cross-section; A_c and A_p are the surface areas of the channel and the plate, respectively.

The area utilisation e_A is defined as the ratio of area densities of the wavy channel to that of a straight channel via:

$$e_A = \frac{(A_c/A_p)_w}{(A_c/A_p)_{str}} \tag{6.4}$$

For tortuous channels, the apparent area density depends very much on the pathway and the minimum wall thickness required between channels. Geyer et al. (2007) provided equations to determine the channel pitch (the distance between a given point on one channel and the location of the same point on the next channel on the plate), thereby calculating the apparent area density for trapezoidal channels. However, these schemes are hard to apply to the sinusoidal channels with varying curvature. As seen in Figure 6.13, which presents the space arrangement of sinusoidal channels on a plate, the wall thickness between two adjacent channels varies along the channel. The structural rigidity of the system depends very much on the minimum distance between two channels ($t_{\min}$), which is usually determined by manufacturing and structural integrity requirements.

Due to the complexity in mathematically calculating the channel surface and plate areas for zigzag and sinusoidal channels, in this study, the apparent area density was obtained by calculating the areas using the CAD package ANSYS DesignModeler. As shown in Figure 6.13, the unit area of the plate ($A_{p,w}$) for wavy channels can be obtained through the summation of the channel project area ($A_{c,p}$) and the plate area between two adjacent channels (A_{adj}).

For wavy channels with the same channel diameter and minimum wall thickness as the straight channels, the area utilisation can be written as:

$$e_A = \frac{(A_c/A_p)_w}{(A_c/A_p)_{str}} = \frac{P.S_0/A_{p,w}}{P/(d+t)} = \frac{S_0(d+t_{min})}{(A_{c,p}+A_{adj})_w} \tag{6.5}$$

where S_0 is the path length along the centreline of one unit of the repeating geometry.

Since the straight passages have the best stackability, the area utilisation e_A is invariably below unity.

The heat transfer intensification relative to straight channels is given in Eq. (6.6):

$$i_A = \frac{Nu_{wavy}}{Nu_{str}} \cdot \frac{(A_c/A_p)_{wavy}}{(A_c/A_p)_{str}} = e_{Nu} \cdot e_A \tag{6.6}$$

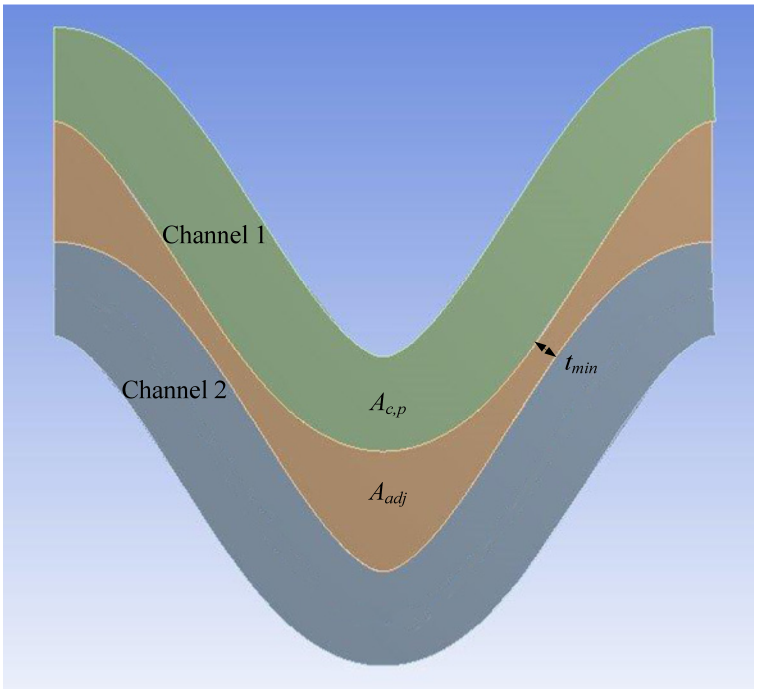

Figure 6.13: Sinusoidal channels (Sine 3) arrangement on a plate.

6.4.2 Results for plate based channels

Table 6.2 presents the area utilisation for four geometries used in this study, where t_{min} has been set to 0.5 mm. It is obvious that the zigzag channels have higher area utilisation than the sinusoidal passages. Figure 6.14 shows the area utilisation of Zigzag 2 and Sine 2 channels that have the same amplitude and half-unit length. The minimum channel distance between channels (t_{min}) are the same for the two channel configurations. As can be seen, Zigzag 2 provides significant area intensification ($e_A = 0.99$ from Table 6.2) since the channels can be nested almost as well as straight channels with only little loss of area utilisation caused by the bend curvature. However, Sine 2 channel yields a larger distance between rows of channels on a plate, so that it cannot utilise the plate very efficiently. The Sine 3 channel has the lowest area utilisation as indicated in Table 6.2. As shown in Figure 6.13 and Figure 6.14 (b), higher amplitude to half-unit length ratio (*A/L*) leads to a larger distance between the two channels at the crest and trough of the sine waves, which gives rise to a significant loss of area packing density.

Table 6.2: Area utilisation for different channel geometries.

Channel	e_A
Zigzag 1	0.91
Zigzag 2	0.99
Sine 1	0.86
Sine 2	0.89
Sine 3	0.81

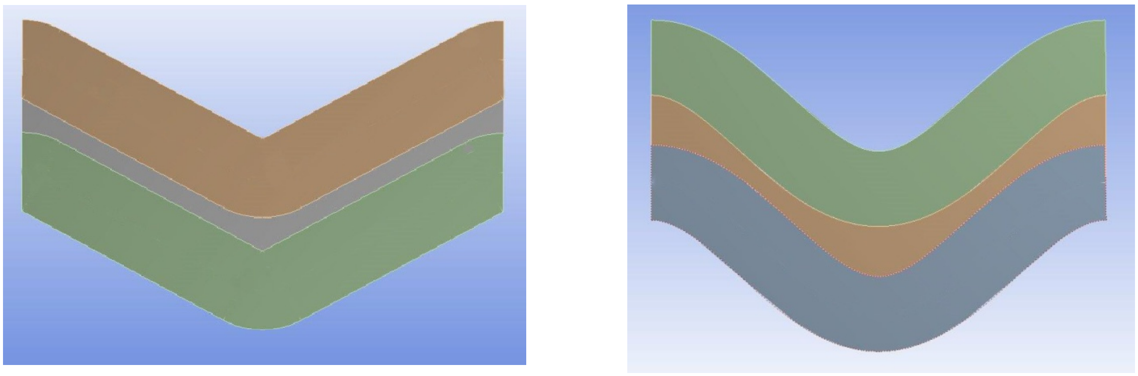

(a) **(b)**

Figure 6.14: Area utilisation of: **(a)** Zigzag 2 channel; and **(b)** Sine 2 channel.

Figure 6.15 shows the plots of heat transfer intensification for the five geometries. Since the heat transfer enhancement for the corresponding zigzag and sinusoidal channels is nearly the same, the heat transfer intensification of zigzag channels is higher than that of the sinusoidal passages due to the higher area utilisation. Sine 1 and Sine 3 channels, which provide heat transfer enhancement as good as Zigzag 1 channel at certain Reynolds number, give lower heat transfer intensification when considering the stackability on a plate. However, all the wavy channels still perform much better than the straight channels ($i_A > 1$). It is indicated that channels with a zigzag axial path configuration are well suited for use in compact plate heat exchangers, as their shape generally allows rows of them to be stacked close together. Due to the superior overall performance of zigzag channel geometries, they are more likely to be found on a printed circuit heat exchanger plate than other geometries.

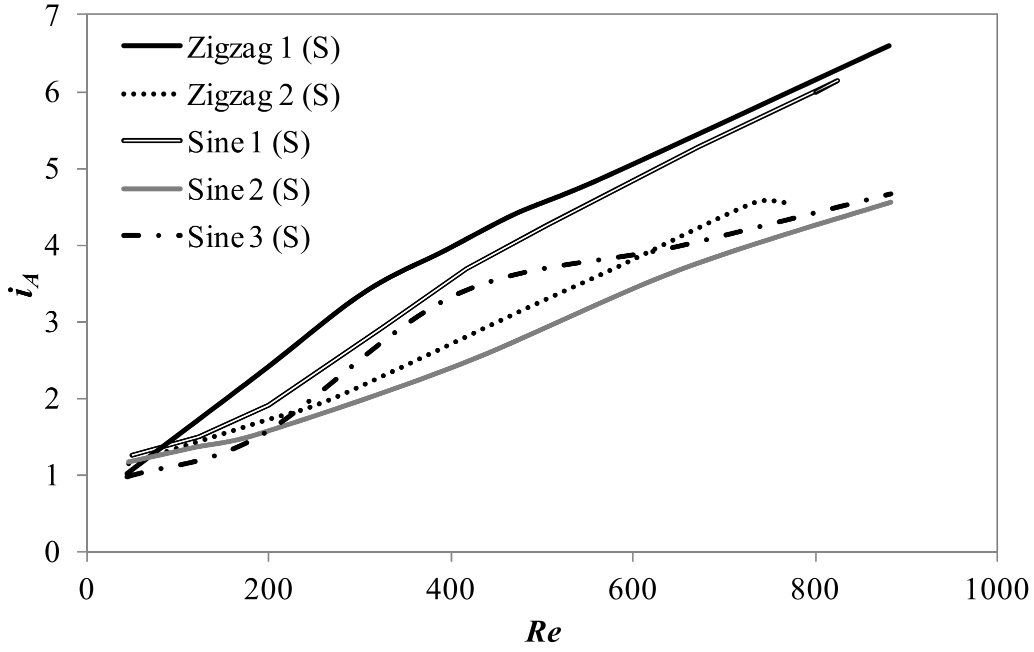

Figure 6.15: Heat transfer intensification (i_A) for different channel geometries.

6.5 Summary

An experimental investigation of the heat transfer characteristics in wavy microchannels of different geometries was performed over a wide range of Reynolds numbers (50 < *Re* < 900). Three-dimensional conjugate CFD simulations were also carried out for the corresponding experimental conditions. Despite the difficulties in temperature measurements in wavy microchannels, the present apparatus and experimental approaches provide heat transfer rates with satisfactory accuracy, which is indicated by the reasonably good agreement between the experimental results and simulation predictions. The average Nusselt numbers for water flowing through semi-circular wavy channels were experimentally determined and the effects of geometry and Reynolds number were discussed. Key conclusions obtained from this study are:

1. Compared with straight channels, wavy microchannels can significantly increase the heat transfer performance albeit accompanied by increased pressure-drop. Both the heat transfer enhancement and pressure drop penalty increase with increasing Reynolds number for all the channels considered. In spite of the pressure drop increase, the heat transfer enhancement significantly exceeds the increase in friction factor for most channels. The heat transfer enhancement exceeds the relative pressure-drop penalty by a factor as large as 2.1 for a sinusoidal channel with geometric parameters of $A/L = 0.5$ and $L/d = 3.5$.
2. The channels with higher bend angle (θ) or amplitude to half-unit length ratio (A/L) are found to provide higher heat transfer enhancement as well as pressure-drop penalty compared with the channels with lower values of θ or A/L.
3. The heat transfer enhancement is attributed to two effects based on the flow dynamics study: (1) flow recirculation (lateral vortices) along the channel and (2) Dean vortices in the cross-sections. Sinusoidal channels with smooth pathways offer similar level of heat transfer enhancement but with much lower pressure drop compared with the corresponding zigzag channels with sharp bends. This is mainly due to the absence of recirculation zones in the smooth pathways and the establishment of Dean vortices which promote cross-sectional mixing. Increased heat transfer performance is therefore obtained with a surprisingly low pressure drop penalty.
4. The channel geometries were evaluated by measuring of the improvement of heat transfer above that of a row of straight channels obtained by nesting tortuous paths on the same plate area. The swept zigzag pathway with lower bend angle was found to provide the greatest area utilisation ($e_A = 0.99$), which indicates the channel structure is better suited to stacking. When examining the geometrical configuration on the basis of an entire plate, sinusoidal channels provide lower heat transfer intensification because they cannot utilise the plate very efficiently. Zigzag channel configurations are well suited for the use in compact plate heat exchangers due to their significant heat transfer enhancement, as well as good stackability.

The results presented here will be useful for the design and optimization of micro-reactors and heat exchangers using wavy microchannels.

Chapter 7

Non-intrusive Temperature Measurements

As mentioned in the literature review, an accurate estimation of the fluid temperature is essential for the investigation of heat transfer coefficients. However, direct and accurate determination of temperature in microscale systems is quite challenging. The bulk temperature of the fluid is usually calculated, either by assuming a linear variation in the axial (flow) direction (Tso and Mahulikar, 2000, Lelea et al., 2004), or considering it to be constant and equal to the inlet bulk temperature. In Chapters 4 and 6, where the heat transfer in microchannels was studied, a linear variation for the local bulk temperature of the fluid was assumed in the heating zone where the heat flux was assumed constant. In this chapter, an experimental technique is developed to measure the fluid temperature in microchannels.

Laser Induced Fluorescence (LIF) was typically used to get a whole-field temperature distribution non-intrusively (based on variations in the emission intensity of a fluorophore dissolved in the fluid) due to its excellent spatial and temporal resolutions (Hanson, 1988, Coppeta and Rogers, 1998, Sakakibara and Adrian, 1999, Ross et al., 2001, Chamarthy et al., 2009, Dabiri, 2009, Kim and Yoda, 2010). A two-dye LIF technique, which uses a reference signal from a second dye or colour band, has been used to eliminate effects of the non-temperature dependent parameters (such as laser intensity fluctuations, non-uniform dye concentration and photobleaching) and to improve measurement accuracy (Sakakibara and Adrian, 2004, Sutton et al., 2008, Natrajan and Christensen, 2009, Kim and Yoda, 2010, Dunand et al., 2012). In the present study, temperature measurement was carried out using the two-dye LIF technique using a colour camera and a colour enhancement filter, instead of two monochrome cameras. The capability of the technique was verified through its applications in fluid temperature measurements in single-phase flow and Taylor flow. In the following sections the two-dye LIF technique using a colour camera is briefly described, along with a discussion of dye selection, spectral conflicts, measurement uncertainties and limitations.

7.1 Principle of Laser Induced Fluorescence (LIF)

The Laser Induced Fluorescence (LIF) technique is based on fluorescence of molecules and atoms, which is induced by absorption of a photon. This absorption causes a transition from ground state to an excited state. Part of the absorbed energy is released as light at longer wavelengths which is commonly known as fluorescence during spontaneous transition from the excited state to the ground state. When the laser beam illuminates the liquid solution seeded with an organic fluorescent dye, the fluorescence intensity is affected by the absorption of the incident laser beam and by the re-absorption of the fluorescence itself across the absorbing medium. For dilute solutions where the concentration is low enough and the re-absorption can be neglected, the fluorescence signal can be defined as

$$I_f(\lambda) = I_L \varepsilon_L C K_{opt}(\lambda) \phi(\lambda) V_{em} \tag{7.1}$$

where I_L is the intensity of the incident laser beam; ε_L is the molar extinction coefficient of the dye for the incident laser excitation; C is the molecular concentration of the fluorescent dye; $K_{opt}(\lambda)$ is a constant depending on the optical and spectral properties of the detection system; $\Phi(\lambda)$ is the fluorescence quantum efficiency and V_{em} is the emitted fluorescent signal collection volume (generally defined by the intersection of the liquid volume, laser sheet or beam and depth of field of the collection optics).

For most organic dyes, variations in the fluorescence intensity I_f with temperature are predominantly attributable to the temperature dependence of the quantum efficiency, which decreases due to increased quenching effects with increasing temperature. The absorption coefficient can be temperature dependent as well. For some dyes, such as Fluorescein 27, the fluorescence emission increases with increasing temperature. This positive temperature dependence is due to a temperature-dependent absorption curve, where the absorption coefficient increases with increasing temperatures (Sutton et al., 2008).

From Lemoine and Anotine (1999), the quantum yield can be represented by the following equation:

$$\phi(\lambda) = K_{spec}(\lambda) e^{\frac{\beta}{T}} \tag{7.2}$$

Then the fluorescence signal can be expressed as:

$$I_f(\lambda) = I_L \varepsilon_L C V_{em} K_{opt}(\lambda) K_{spec}(\lambda) e^{\frac{\beta}{T}} \tag{7.3}$$

where $K_{spec}(\lambda)$ depends on the spectroscopic and physical property of the fluorescent molecule and β is the temperature sensitivity of the dye, which can be determined during the calibration process. For a microscopy system with a camera as the detection device, the optical constant $K_{opt}(\lambda)$ can be determined by $K_{opt}(\lambda) = \Omega \eta_c(\lambda) \eta_f(\lambda)$, where Ω is the solid angle, η_c is the quantum efficiency of the camera sensor and η_f is the transmission efficiency of the filter used in the optical path.

Note that the fluorescence spectrum of the dye tracer is generally broadband and many quantities in Eq. (7.3) are wavelength dependent. The detected fluorescence signal S_f will be the integral of the fluorescence intensity $I_f(\lambda)$ over the detected wavelength [λ_1, λ_2].

$$S_f = I_L C V_{em} \varepsilon_L \int_{\lambda_1}^{\lambda_2} K_{opt}(\lambda) K_{spec}(\lambda) e^{\frac{\beta}{T}} \, d\lambda = I_L C \Omega V_{em} \varepsilon_L \int_{\lambda_1}^{\lambda_2} \eta_c(\lambda) \eta_f(\lambda) K_{spec}(\lambda) e^{\frac{\beta}{T}} \, d\lambda \tag{7.4}$$

The LIF technique can be applied in two ways, one-dye LIF technique and two-dye/colour LIF technique (known as ratiometric method), as described below.

7.1.1 One-dye LIF

In its simplest implementation, the temperature is estimated from the change in fluorescence intensity from one dye imaged over a single wavelength band by using Eq. (7.3) or (7.4). This procedure can be presented in terms of the following expression if the intensity is normalized by that at a reference temperature:

$$\ln\left[\frac{I_f(T)}{I_f(T_0)}\right] = \beta\left(\frac{1}{T} - \frac{1}{T_0}\right) \tag{7.5}$$

where T_0 is the reference temperature which is usually the ambient temperature. However, as mentioned in the literature review, the drawback of using one-dye LIF is that it is very difficult to maintain the incident laser intensity uniform both spatially and temporally throughout the process, which will result in inaccurate temperature measurements.

7.1.2 Two-dye LIF

Improvements of the LIF technique have been made by using a reference signal from a second dye or second spectrum allowing compensating for fluctuations in the illumination intensity. The two dyes usually have different emission spectra and the individual intensities can be measured by two monochrome cameras with optical filters; then the intensity ratio can be obtained from the cameras output. However, since the two cameras image the scene from different viewpoints, the recorded images are not characterized by the same correspondence between coordinates of points in physical and image space. Therefore, image registration is required to achieve a pixel by pixel correspondence between the two images (Sakakibara and Adrian, 1999, Natrajan and Christensen, 2009). Great effort has been put into the image registration and currently an alignment of both images with accuracy of sub-pixel can be reached. However, this procedure has to be repeated every time the optical setup (camera alignment, magnification, etc.) changes and it has to be performed prior to all other image processing steps (Vogt and Stephan, 2012).

In recent years, the use of colour cameras for microscopy imaging has become a valuable alternative to monochrome cameras. These cameras are based on the use of chips containing red/green/blue (RGB) channels that are sensitive to the red, green and blue light of the visible spectrum. The Funatani group (Funatani et al., 2004) were the first to try the two-colour LIF using a colour camera. The emissions of two dyes (Rhodamine B and Rhodamine 110) were filtered by the red and green channels of the colour CCD camera. Later on, Fischer and co-workers (Fischer et al., 2012, Meier et al., 2013) used a digital colour camera for the simultaneous imaging of barometric pressure and temperature. Three fluorescence signals with different emission wavelengths were separated by the colour camera with their emissions matching the blue, green and red channels, respectively. The advantage of using a colour camera is the simplicity of the system, since it does not require the calibration of image coordinates of the two monochrome cameras. Therefore, in this study, a colour camera was used for the two-dye LIF technique.

The principle of the two-dye LIF using a colour camera is similar to that used in the two-camera system. Emissions of two dyes (called Red A and Green B) are detected by RGB channels (e.g. red and green channels) in a colour camera instead of two cameras. The signals detected by the red channel and green channel can be expressed as

$$S^R = S_A^R + S_B^R = I_L \Omega V_{em} \left(C_A \varepsilon_{AL} F_A^R e^{\frac{\beta_A}{T}} + C_B \varepsilon_{BL} F_B^R e^{\frac{\beta_B}{T}} \right) \tag{7.6}$$

$$S^G = S_A^G + S_B^G = I_L \Omega V_{em} \left(C_A \varepsilon_{AL} F_A^G e^{\frac{\beta_A}{T}} + C_B \varepsilon_{BL} F_B^G e^{\frac{\beta_B}{T}} \right) \tag{7.7}$$

where F_A^R and F_A^G are fluorescence factors of dye A detected by the red channel and the green channel, respectively, and similarly for F_B^R and F_B^G. These factors will be constants after the dyes and the detection system are selected. They can be expressed as follows:

$$F_A^R = \int_{\lambda_1}^{\lambda_2} \eta_R(\lambda) \eta_f(\lambda) K_{Aspec}\,(\lambda) d\lambda \tag{7.8a}$$

$$F_A^G = \int_{\lambda_1}^{\lambda_2} \eta_G(\lambda) \eta_f(\lambda) K_{Aspec}\,(\lambda) d\lambda \tag{7.8b}$$

$$F_B^A = \int_{\lambda_1}^{\lambda_2} \eta_A(\lambda) \eta_f(\lambda) K_{Bspec}\,(\lambda) d\lambda \tag{7.8c}$$

$$F_B^G = \int_{\lambda_1}^{\lambda_2} \eta_G(\lambda) \eta_f(\lambda) K_{Bspec}\,(\lambda) d\lambda \tag{7.8d}$$

The signal ratio of two channels can be written as the following equation:

$$R = \frac{S^R}{S^G} = \frac{C_A \varepsilon_{AL} F_A^R e^{\frac{\beta_A}{T}} + C_B \varepsilon_{BL} F_B^R e^{\frac{\beta_B}{T}}}{C_A \varepsilon_{AL} F_A^G e^{\frac{\beta_A}{T}} + C_B \varepsilon_{BL} F_B^G e^{\frac{\beta_B}{T}}} = \frac{1 + F_1 e^{\frac{\beta_B - \beta_A}{T}}}{F_2 + F_3 e^{\frac{\beta_B - \beta_A}{T}}} \tag{7.9}$$

where $F_1 = \frac{F_B^R}{F_A^R} \cdot \frac{C_B}{C_A} \cdot \frac{\varepsilon_{BL}}{\varepsilon_{AL}}$, $F_2 = \frac{F_A^G}{F_A^R}$ and $F_3 = \frac{F_B^G}{F_A^R} \cdot \frac{C_B}{C_A} \cdot \frac{\varepsilon_{BL}}{\varepsilon_{AL}}$.

The ratio expression Eq. (7.9) is similar to that for a two-camera system described by Sakakibara and Adrian (1999). It cancels out not only the effect of laser intensity variation but also some effects of the optical detection parameters (e.g. solid angle, collection volume and imaging non-uniformities). Another benefit of using a colour camera rather than two cameras is that it also cancels the effect of variations in the sensitivity of the two cameras by taking the pixel by pixel ratio of the intensity values of two channels from one camera.

The temperature sensitivity of $\frac{S^R}{S^G}$ can be evaluated by Eq. (7.10).

$$\frac{\partial R}{\partial T}=\frac{\partial}{\partial T}\left(\frac{1+F_1e^{\frac{\beta_B-\beta_A}{T}}}{F_2+F_3e^{\frac{\beta_B-\beta_A}{T}}}\right)=\frac{(F_3-F_1F_2)\frac{\beta_B-\beta_A}{T^2}e^{\frac{\beta_B-\beta_A}{T}}}{\left(F_2+F_3e^{\frac{\beta_B-\beta_A}{T}}\right)^2} \tag{7.10a}$$

or

$$\frac{\partial \ln{(R)}}{\partial T}=\frac{(F_3-F_1F_2)\frac{\beta_B-\beta_A}{T^2}e^{\frac{\beta_B-\beta_A}{T}}}{\left(1+F_1e^{\frac{\beta_B-\beta_A}{T}}\right)\left(F_2+F_3e^{\frac{\beta_B-\beta_A}{T}}\right)} \tag{7.10b}$$

The temperature sensitivity is influenced by the combined effect of the concentration, spectroscopic properties and temperature sensitivity of the two dyes. It is straightforward to apply if the two dyes can be perfectly separated by the two channels, that is F_A^G and F_B^R are zero. The ratio of signals from the two channels is then simplified as

$$R=\frac{C_A\varepsilon_{AL}F_A^Re^{\frac{\beta_A}{T}}}{C_B\varepsilon_{BL}F_B^Ge^{\frac{\beta_B}{T}}}=\frac{C_A\varepsilon_{AL}F_A^R}{C_B\varepsilon_{BL}F_B^G}e^{\frac{\beta_A-\beta_B}{T}} \tag{7.11}$$

The concentration effect can be eliminated if a reference measurement at a known temperature (T_0) is recorded. The following equations can be obtained:

$$\frac{R(T)}{R(T_0)}=e^{(\beta_A-\beta_B)(\frac{1}{T}-\frac{1}{T_0})} \tag{7.12a}$$

or

$$\ln\left[\frac{R(T)}{R(T_0)}\right]=(\beta_A-\beta_B)\left(\frac{1}{T}-\frac{1}{T_0}\right) \tag{7.12b}$$

The temperature sensitivity of $\frac{S^R}{S^G}$ is defined as $\frac{d}{dT}(\ln Ra)$

$$\frac{d}{dT}(\ln Ra)=\frac{d}{dT}\ln\left[\frac{R(T)}{R(T_0)}\right]=\frac{-(\beta_A-\beta_B)}{T^2} \tag{7.13}$$

This indicates that the temperature sensitivity of $\frac{S^R}{S^G}$ only depends on the sensitivities of the selected dyes. It does not change even if the concentrations of the dyes change during the process. A way to have a high overall temperature sensitivity of $\frac{S^R}{S^G}$ is to choose two dyes whose temperature sensitivity differs significantly.

7.2 Technique development of two-dye LIF using a colour camera

7.2.1 Experimental setup of micro-PIV/LIF

The two-dye LIF technique using a colour camera briefly highlighted above was implemented in the present micro-PIV facility to carry out temperature measurements in microchannels. The system schematic is shown in Figure 7.1. The light source (Darwin-Duo, 527 nm) and filter setup (540DRLP + 540LP) used for PIV could also be used for the LIF application. However, the fluorescence light shorter than 540 nm will be blocked by the filter set. A different option for fluorescence excitation by using a continuous blue laser (iBeam, 0.2 W) at 488 nm was also explored. The advantage of this laser is that the excitation wavelength is spectrally easier to separate from the fluorescence, allowing more efficient detection. A new filter set was selected for the 488 nm laser system so that a wider range of fluorescence can be collected.

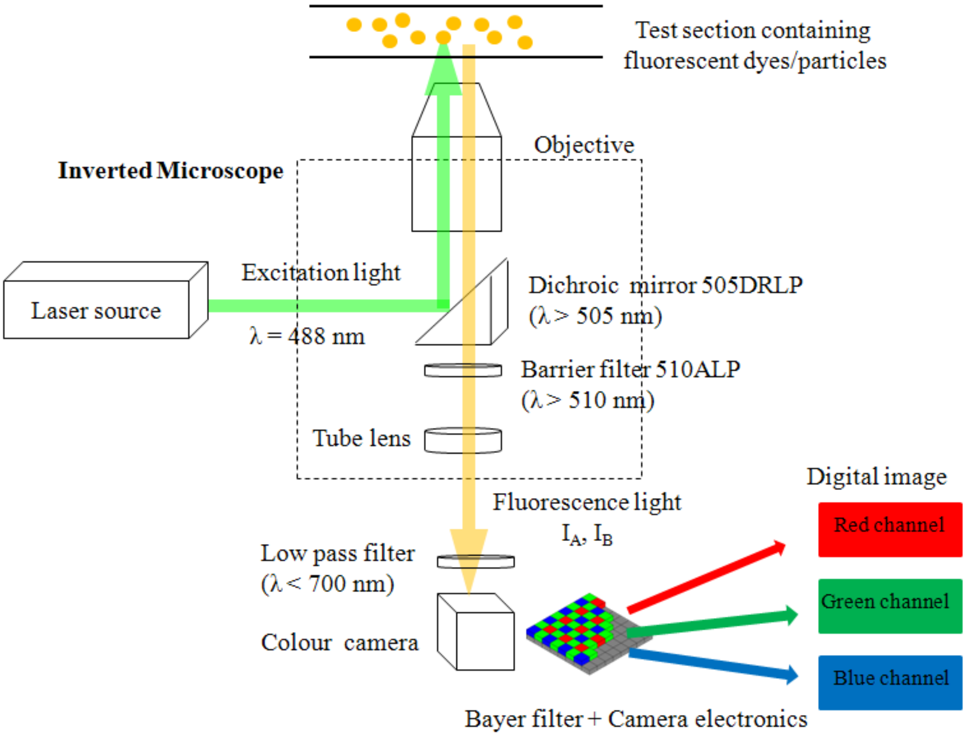

Figure 7.1: Schematic of the micro-PIV/LIF setup.

As shown in the epi-fluorescent microscope system (Figure 7.1), the laser light beam (488 nm) was shone through the fluorescence test section after being reflected by a dichroic mirror

(505DRLP-QuantaMAX, Omega optics) into a microscope objective. A long pass filter (510ALP, Omega optics) was added as the emission filter, which eliminated all remaining incident light. The fluorescence emission from the dyes was then collected by the objective and transmitted through the dichroic mirror. The fluorescence intensity was imaged using a colour camera (pco.edge scientific CMOS camera) with a full spatial resolution of 2560 × 2160 pixels and 16 bits for each channel. The spatial resolution of the measurement is determined by the microscope optics, and the temporal resolution is determined by the rate at which video frames can be captured by the camera. For the present setup, all light with a wavelength lower than 510 nm was blocked by the optical filters. Therefore, the blue channel was almost blank and the green and red channels were used for the ratiometric technique.

7.2.2 Dyes selection

The selection of the fluorescent dyes is a very important topic for the two-dye LIF technique. According to the principle, the implementation of the two-dye LIF ratiometric technique requires the selection of two dyes with different temperature sensitivity and spectral characteristics such that the separation of the emitted light by optical means is possible.

The most common fluorescent dyes or dye combinations used for LIF experiments in the literature are summarized in Table 7.1. Rhodamine B (RhB) and Kiton Red 620 (KR) are the most widely used temperature sensors due to their high temperature sensitivity and complete solubility in aqueous solutions (Coppeta and Rogers, 1998). Their fluorescence intensities decrease due to increased quenching effects with increasing temperature. Another dye, Fluorescein (Fluorescein 27 or disodium fluorescein), on the other hand, exhibits a positive temperature sensitivity due to the increase with temperature of its absorption. The interesting features of Fluorescein, such as anti-Stokes shifted spectrum, high quantum yield and very high temperature sensitivity (~3.5%/°C), make it a very good green emitter that can work with another negative sensitive dye (RhB or KR) to improve the temperature sensitivity (Sutton et al., 2008, Shafii et al., 2010, Estrada-Perez et al., 2011). However, a common problem quoted in the literature about using Fluorescein for quantitative purposes is the photo-instability due to “photobleaching” (Saylor, 1995). Another drawback that may limit its use is that the absorption of Fluorescein is very low at 527 nm compared with other possible excitation wavelengths.

A crucial criterion imposed upon the two-dye LIF system is that the dyes have non-conflicting absorption and emission characteristics (Coppeta and Rogers, 1998). The spectral overlaps give rise to the difficulty of separation of emissions and also produce an adverse effect on the overall temperature sensitivity. Three kinds of spectral conflicts (or overlaps between absorption and emission bands) were discussed in detail in Coppeta and Rogers (1998).

Another problem that would be encountered in the colour camera system is the overlap between colour channels (signal conflict). Generally, the colour signal is focused onto a CCD array: a two-dimensional array of light sensitive elements which convert the light energy into an electrical charge when light is incident. In front of these devices are placed one or more filter elements, the role of which is to preferentially transmit light energy at certain wavelengths. In most single-chip digital image sensors used in digital cameras, a Bayer filter array is used for arranging RGB colour filters to create a colour image. The red, green and blue channels are characterized by their responsivity, giving the proportion of incident photons that are converted to electrons (called quantum efficiency). The camera colour curves which show the spectral response of the sensor of pco.edge scientific CMOS camera (only red and green channels) are shown in Figure 7.2. As can be seen, each channel covers a broad band of the spectrum with the transmission peaks of 550 nm and 620 nm for the green and red channels, respectively. However, in the range of 570 to 600 nm where the red and green channels overlap, the signal will go to both channels. In this case, the fluorescence emissions which cover both the green and red spectra, such as the yellow emission of RhB (λ_{em} = 585 nm), will generate signals registered in both the green and red channels. Therefore, fluorescent dyes whose emissions in this wavelength region may not be good candidates for the colour camera system due to this signal conflict.

In the present work, several red-emitting and green-emitting dyes from Table 7.1 as potential ratiometric partners were evaluated based on their temperature sensitivities, quantum yields and spectral properties. The overall temperature sensitivity of the two dyes was estimated through Eqs.(7.4) - (7.10) by convolving the camera colour curves (or camera quantum efficiency curves) and filter transmission curves with the emission spectral data of the dyes, integrating the green and red channel signals over appropriate bandwidths, and taking the ratio of the signals from the red and green channels. The signal conflict between the colour channels was found to reduce the temperature sensitivity of the ratiometric measurement. After some preliminary tests and model prediction, the temperature sensitive red emitter Kiton Red (KR, λ_{em} = 600 nm) and the nearly temperature insensitive green-emitter Rhodamine 110 (Rh110, λ_{em} = 520 nm) were selected for the colour camera system.

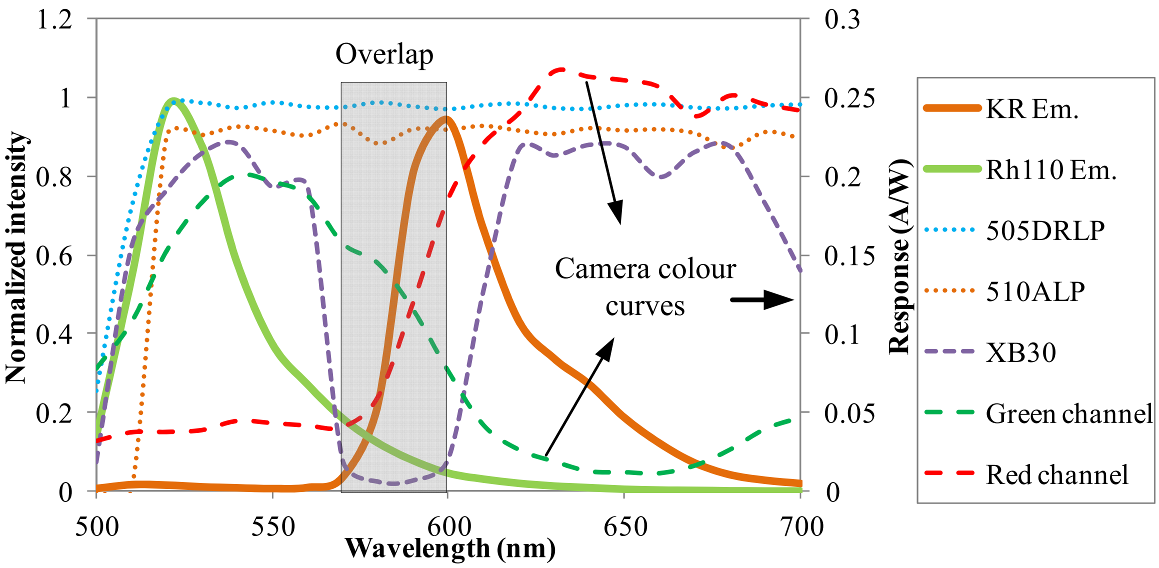

Figure 7.2: Emission spectra of Kiton Red and Rhodamine 110, camera colour curves and filter transmission curves (Excitation = 488 nm).

The emission spectra of KR and Rh110 measured by a luminescence spectrometer (Perkin Elmer, LS-50B) are plotted in Figure 7.2, together with the spectral characteristics (camera colour curves and filter transmission curves) of the detection system. As can been seen, the spectral overlap between two emissions is actually quite small. However, in the overlap range of the red and green channels (570-600 nm), the KR fluorescence would be detected by both channels (signal conflict as discussed before). In order to solve this problem, a triple band-pass, colour enhancement filter (XB30, Omega optics) was proposed to eliminate the overlap between each colour channel. The filter allows transmission of the three bands of pure colour - red, green and blue - while blocking those intermediate wavelengths that distort the recoding of colour. In this study it is very important that the dye fluorescence would not be totally blocked by this filter. Inclusion of the XB30 filter precludes the use of the dye Rhodamine B (λ_{em} = 585 nm) because the emission of this otherwise suitable dye is located largely in the blocking region. The emission spectrum of Kiton Red is shifted to the right in comparison with Rhodamine B which gives a higher signal in the red channel.

Table 7.1: Typical fluorescent dyes used for temperature measurements.

Excitation (nm)	Green emitter		Red emitter		Temperature range (°C)	Reference
	Dye	***S* (%/°C)**	**Dye**	***S* (%/°C)**		
One-dye/colour LIF						
514	Fluorescein	2.43			20-60	Coppeta and Rogers, (1998)
532	Fluorescein 27	3.5			20-75	Dunand et al., (2012)
514			Rhodamine B	-1.54	20-60	Coppeta and Rogers, (1998)
532			Rhodamine B	-3	20-60	(Coolen et al., 1999)
532			Rhodamine B	-2	30-55	Bogild et al., (2012)
514			Kiton Red	-1.55	20-60	Coppeta and Rogers, (1998)
488			LDS 698	-1.27	20-60	Coppeta and Rogers, (1998)
ultraviolet			Tris(bipyridine)ruthenium(II)	-3	24-61	Sato et al., (2003)
Two-dye/colour LIF						
488	Rhodamine 110	0.13	Rhodamine B	-2.3	15-40	Sakakibara and Adrian, (1999)
488	Rhodamine 110	-0.2	Rhodamine B	-2	20-70	Chamarthy et al., (2010)
488	Rhodamine 110	-	Rhodamine B	-	30-60	Funatani et al., (2004)
450-490	Rhodamine 110	-0.17	Rhodamine B	-0.75	45-100	Fogg et al., (2009)
514	Fluorescein	2.44	Sulforhodamine B	-1.54	20-60	Kim and Yoda, (2010)

532	Fluorescein 27	3.5	Rhodamine B	-1.59	20-80	Sutton et al., (2008)
526, 532	Fluorescein 27	-	Rhodamine B	-	20-80	Estrada-Perez et al., (2011)
532	Fluorescein 27	3.5	Kiton Red	-1.58	20-60	Sutton et al., (2008)
514.5	Fluorescein 27	-	Kiton Red	-	4-20	Shafii et al., (2010)
532	Rhodamine B	-2.6	Sulforhodamine 101	0.38	10-50	Natrajan and Christensen, (2009)
532	Rhodamine B $^{(1)}$	-1	Nile Red	-0.08	15-65	Yamaguchi et al., (2006)
370	Coumarin 500	-	Europium (III) thenoyltrifluoroacetonate (EuTTA)	-1.94	5-45	West (2012)
335	Perylene	-	Europium (III) thenoyltrifluoroacetonate (EuTTA)	-1.80	5-50	Basu and Venkatraman (2009)
532	Pyrromethene 567 $^{(2)}$	-	Pyrromethene 597-8C9	-0.5	20-50	Vogt and Stephan, (2012)

**S* is the temperature sensitivity; (1) Solvent is ethanol; (2) Solvent is hexadecane.

7.2.3 Colour camera considerations

Monochrome cameras are usually used in scientific applications due to their “true” pixel intensity and high resolution. Most colour cameras determine pixel colour with a combination of filters (such as the Bayer-type filter) and interpolation from the intensity values of neighbouring pixels which inevitably reduces resolution. This becomes less of a problem when modern cameras provide resolution that rivals that of a monochrome camera. The colour quality can be also improved by using a 3-chip CCD colour camera, where a separating prism mounted in front of the three sensors directs the red, green, and blue light to the appropriate detector chip. The colour can be truly recorded at each pixel without interpolation. However, the prism and additional sensors make this solution much more expensive. In this study, the scientific single-chip CMOS camera pco.edge with 5.5 megapixel capability provides excellent resolution for image recording and image analysis. It also has extremely low noise (1.1 electrons) and wide dynamic range so that the lowest level of light can be detected.

Another thing that has to be considered when using a colour camera is the white balance, which has to be set to match or “balance” the signals from the camera's red, green and blue channels so that whites and greys look neutral. The camera was balanced for a colour temperature of 3200 K and the setting was kept the same during the whole experiment.

7.2.4 Calibration

To obtain the relationship between the measured fluorescence intensity and the solution temperature, the calibration process was performed using the setup illustrated in Figure 7.1.

7.2.4.1 Camera sensitivity calibration

In the LIF technique, the solution temperature is estimated from the fluorescence intensity recorded by the camera. The response of the camera is therefore critical in accurately estimating the temperature of the solution.

A cuvette filled with the Kiton Red solution with a concentration of 1 mg L^{-1} was illuminated by the iBeam laser (488 nm). The fluorescence from KR solution was then imaged by the colour camera. The camera response to the fluorescence was calibrated by calculating the image intensity at various excitation levels controlled by adjusting the output power of the laser (I_L). Experiments were performed under different objectives. A spatially and temporally averaged image intensity was calculated over a rectangular region (300 × 400 pixels) in the middle of the image and over 10 images recorded in a sequence.

The averaged image intensity is normalized as follows:

$$I_n = \frac{I - I_b}{I_{max} - I_b} \tag{7.13}$$

where I_b is the background noise of the camera, determined by calculating the image intensity without laser excitation. Due to the low noise of the camera, I_b was found to be around 100 out of 65535. I_{max} is the saturated greyscale value (65535) for the 16 bits images.

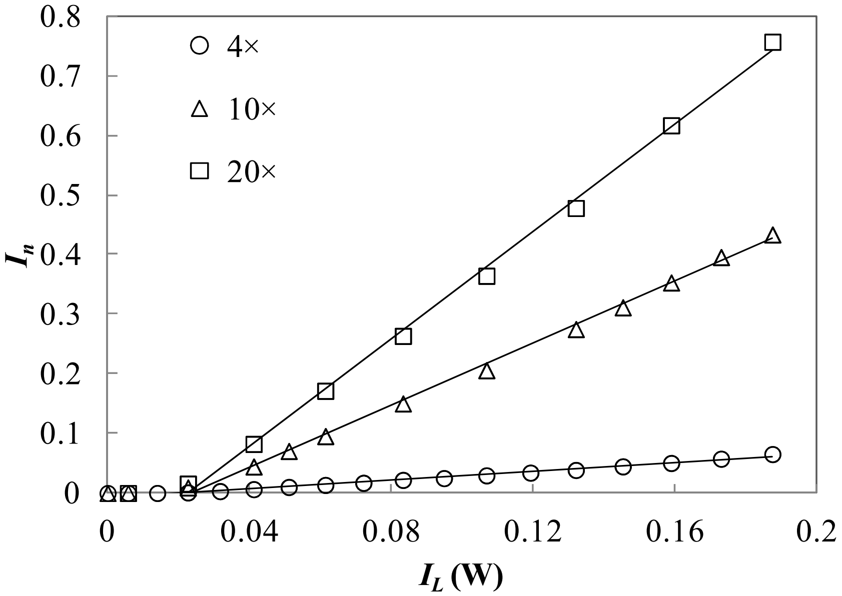

Figure 7.3: Camera calibration showing the normalized image intensity as a function of the laser output power.

Figure 7.3 shows the normalized intensity I_n as a function of the laser output power I_L under different objectives. Only the intensity of the red channel was calculated as Kiton Red occupied mainly the red channel. The straight lines are linear fits of the experimental data. Clearly, the relationship between the emission intensity incident on the sensor (which is proportional to the laser output) and the resultant image intensity recorded is linear for $I_L >$ 0.02 W, as indicated by the good agreement between the data and the fitting lines. Therefore, the pco.edge camera has a linear intensity response over most of its operating range. It can be also seen that for the same dye concentration, the signal is strongest by using the 20× objective, while it is very low under the 4× objective. Therefore, the dye concentration might need to be increased if using the 4× objective. It should be noted that no signal was detected for I_L < 0.02 W. One reason is that the fluorescence of the dye is too low to be detected by the camera under very low excitation. Another reason is the uncertainty in the laser power calibration which converts the current into power. The laser power calibration curve provided by the supplier was calibrated without fiber connection. However, the laser power was reduced after connecting to the fiber in the present experiments, due to the coupling efficient of the fiber. The offset was being corrected before taking ratios of the fluorescent signals during temperature measurement experiments.

7.2.4.2 **Effect of concentration**

The variation of intensity ratio $R = \frac{S^R}{S^G}$ against temperature was studied in a cuvette (45 mm × 12.5 mm × 12.5 mm) where the temperature was kept uniform. A transparent thermofoil heater was attached on the bottom of the cuvette and the temperature was controlled by adjusting the power supply connected to the heater. A K-type thermocouple of 0.5 mm diameter was inserted into the cuvette to monitor the solution temperature. For each experiment, the measurement was taken when the fluid temperature became steady and the standard deviation of the temperature measured by the thermocouple over 5 min was within 0.2 °C. The calibrations were carried out at different concentration ratios, $CR = C_{KR}/CR_{Rh110}$, using the colour camera with and without the colour enhancement filter. The 4× objective was used in the calibration because it was to be used in later experiments to get a large observation view. The concentrations of the fluorescent dyes were higher than the values used in camera calibration procedure to provide sufficient signal. A stock solution with concentration of 10 mg L^{-1} for each dye was prepared using distilled water. The concentration of KR was kept constant and the Rh110 solution was diluted to get a *CR* from 1 to 40.

A sequence of 10 images of the emissions from KR and Rh110 was recorded at a frame rate of 10 Hz and an exposure time of 50 ms. Figure 7.4 shows representative colour images of the fluorescing mixture at *CR* = 5 under different temperatures. The first row (Figure 7.4 (a) to (c)) and the second row (Figure 7.4 (d) to (e)) were recorded without and with colour enhancement filter XB30, respectively. As can be seen, for both cases, the image becomes greener and darker with increasing temperature. This is because the red channel intensity which is dominated by KR decreases due to the negative temperature dependence of KR. The images recorded with filter XB30 are darker and greener than those taken without the filter because the filter blocks the intermediate wavelengths between green and red colours.

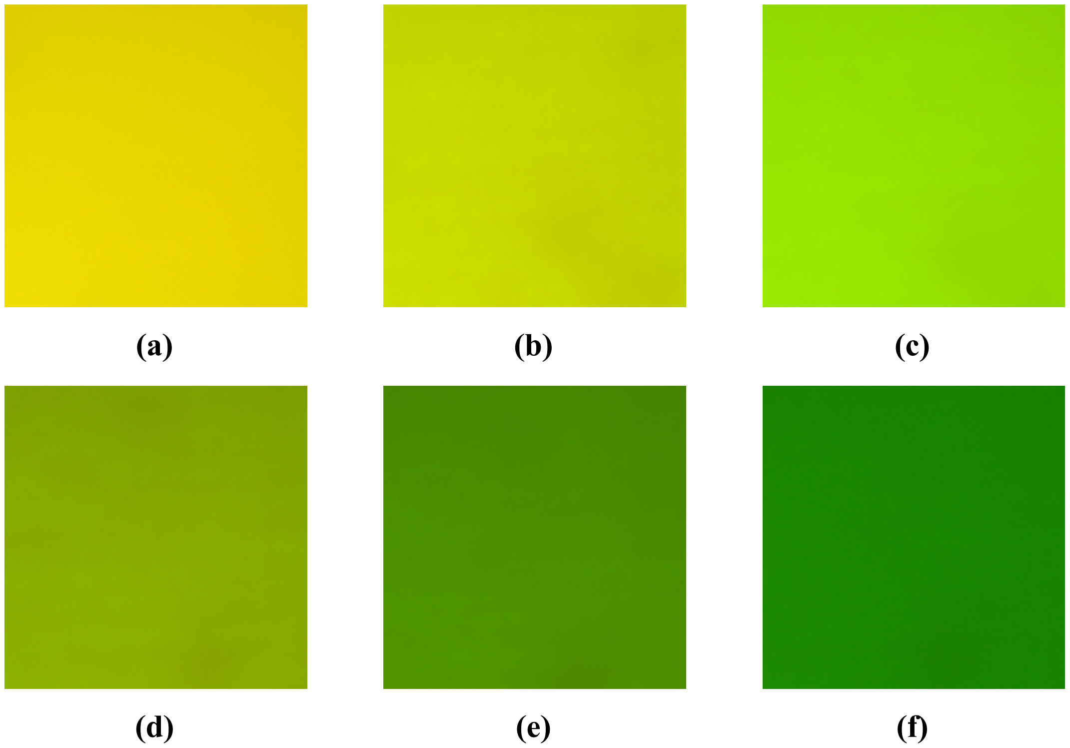

(a) **(b)** **(c)**

(d) **(e)** **(f)**

Figure 7.4: Colour images of fluorescing mixture (*CR* = 5, exposure time = 50 ms) at: **(a)** and **(d)**: 25 °C; **(b)** and **(e)**: 45 °C; **(c)** and **(f)**: 70 °C; (a) to (c) were taken without XB30 and (d) to (f) were taken with XB30.

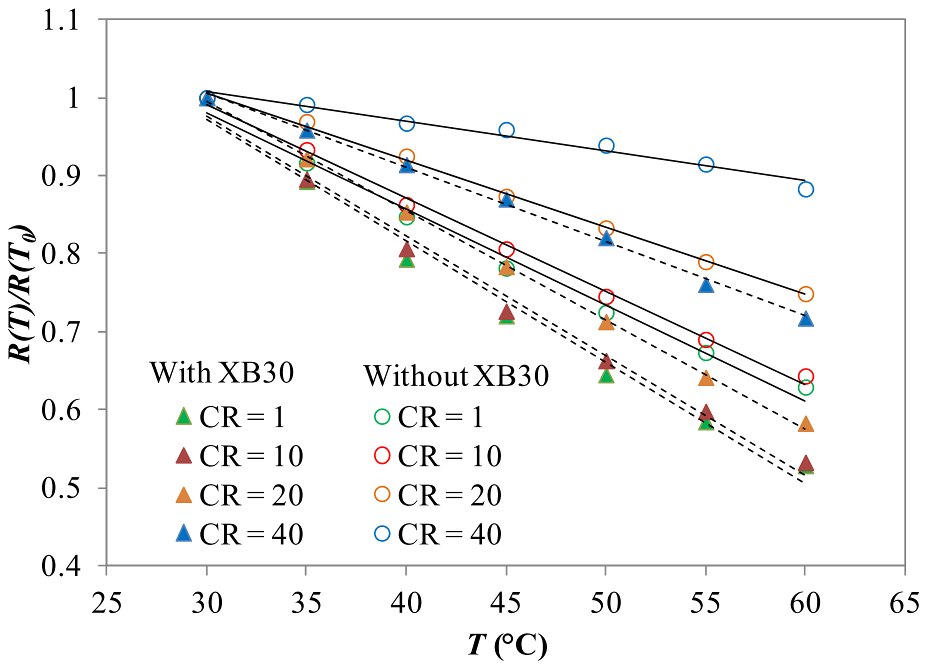

Figure 7.5: Variation of normalized intensity ratio with respect to temperature (solid lines: linear fitting of the experimental data without XB30; dashed lines: linear fitting of the experimental data with XB30).

The intensities of the red and green channels were extracted from each image and the ratio $R = \frac{S^R}{S^G}$ was normalized by that at T_0 = 21 °C, $R(T_0)$. The normalized intensity ratio $\frac{R(T)}{R(T_0)}$ as a function of temperature for each condition is plotted in Figure 7.5. It is shown that for the samples with the same *CR*, using the colour enhancement filter (XB30) gives a steeper slope and therefore a higher temperature sensitivity.

The overall sensitivity $S = \frac{\partial}{\partial T}\left(\ln\left[\frac{R(T)}{R(T_0)}\right]\right)$ against *CR* is shown in Figure 7.6 with solid lines representing the values evaluated from Eq. (7.10). It is observed that the sensitivity decreases with increasing concentration ratio. The temperature sensitivity with the XB30 filter is much higher than that without it. The experimental data agree reasonably well with the theoretical values predicated by the model.

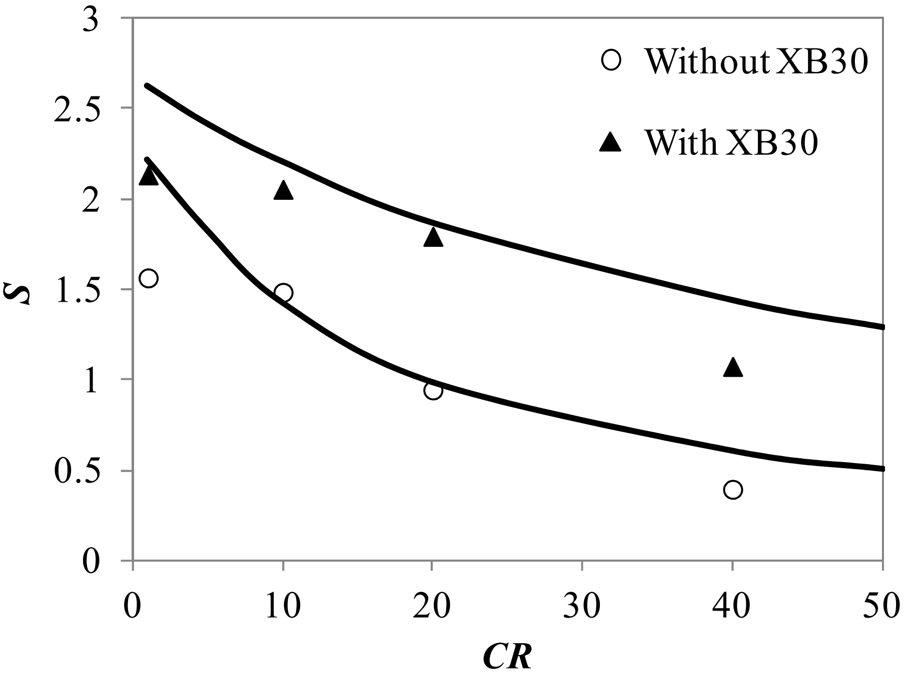

Figure 7.6: Variation of temperature sensitivity *S* with respect to concentration ratio *CR*. Solid lines were evaluated from Eq. (7.10).

Funatani et al., (2004) noted that the temperature sensitivity was reduced by 10% when using a colour camera for the two-colour LIF technique compared to the LIF using two cameras. This is caused by the spectral conflicts and overlaps between colour channels. By introducing the colour enhancement filter in this study, the overall temperature sensitivity is improved by at least 40%. The maximum sensitivity of 2.2%/°C can be achieved at *CR* = 1 with the filter XB30 while 1.6%/°C is the maximum without using the filter. Therefore, the colour camera with a colour enhancement filter can be used for two-dye LIF measurement without sensitivity reduction.

It should be noted that, at a very high or low *CR*, the fluorescence mixture will become either too red or too green. The measurement will depend on the low signal to noise ratio (*S/N*) of the darker channel (Sakakibara and Adrian, 1999). This leads to the big disparities between the experimental data and theoretical values at *CR* = 1 and *CR* = 40 as shown in Figure 7.6. In order to get a maximized *S/N* ratio, *CR* ~ 20 was selected in this study so that the intensity of each channel fills the same level of the dynamic range of the camera.

7.2.4.3 **Effect of geometry**

The calibration was taken under four optical conditions for *CR* = 20: rectangular cuvette (45 mm × 12.5 mm × 12.5 mm) at depth D_1 = 0.5 mm and D_2 = 1.5 mm, circular tube with diameter *d* = 2 mm, and circular tube with diameter *d* = 0.98 mm. Figure 7.7 shows that the normalized intensity ratios $\frac{R(T)}{R(T_0)}$ under four conditions are almost superimposed, indicating that the temperature sensitivity is independent of the optical detection parameters, such as collection volume and optical path. It confirms that the effects of the channel geometry and optical path have been cancelled out by this two-dye ratiometric LIF technique.

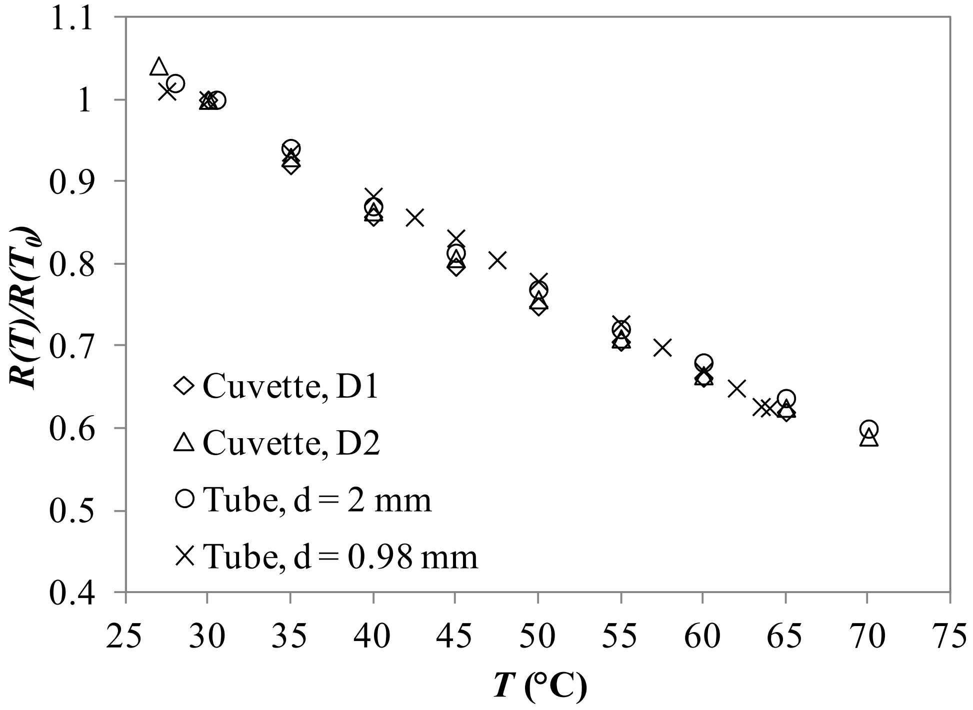

Figure 7.7: Variation of normalized intensity ratio with respect to temperature.

7.3 LIF applications

7.3.1 Depth-averaged temperature measurement in single-phase flow

Based on the calibration, the two-dye LIF method developed above was applied to measure the fluid temperature of single-phase flow in semi-circular microchannels. In the calibration section, it has been shown that the optical path and channel geometry have little effect on the calibration curve. However, in order to obtain the best accuracy and minimum error possible, for each experiment an appropriate calibration curve corresponding to its optical path and dye concentration was used to calibrate the temperature.

7.3.1.1 **LIF measurement in a straight channel**

The dye mixture of Kiton Red and Rhodamine 110 with CR = 20 was pumped through the "hybrid" test section with a straight channel. The test section was heated by the thermofoil heater attached on the metal surface. The fluid was volumetrically illuminated by the 488 nm iBeam laser. Two sequences of 20 images were recorded under a 4× objective by the colour camera (exposure time of 50 ms) with the colour enhancement filter along the channel at Re = 47 and 64. The first reference sequence was obtained at the reference temperature T_0 = 21 °C, while the second sequence of images was recorded once the flow reached steady state after the heating power was applied. The steady state was indicated by the wall temperatures measured by RTDs varying by no more than 0.2 °C over 5 min. The numerical model of the "hybrid" test section, as detailed in Chapter 4, was used to validate LIF results.

Figure 7.8 (a) and (b) show the typical colour images of KR and Rh110 emissions in the straight channel at Re = 47. They were recorded with the focal plane near the flat surface of the channel. The flow goes from bottom to top in all images and the centre-line of the region shown in all images is at axial location x = 0.054 m. The black region on the two sides of the images is the sidewall of the channel. Figure 7.8 (b) shows the flow image under heating input Q_{in} = 6.5 W, while Figure 7.8 (a) is the reference image taken at the room temperature (T_0) at the same location. As can be seen, the fluorescence intensity becomes lower when the flow is heated. However, the intensity fields are not uniform spatially as many streaks and dark spots can be seen in the images. The normalized intensity $\frac{R(T)}{R(T_0)}$ is shown in Figure 7.8 (c). Background subtraction and a median filter of 10 × 10 pixels were applied to each image to reduce the noise. This results in a spatial resolution of 43 μm × 43 μm. It is seen from the normalized intensity field that the two-dye LIF reduces the effects of the illumination and imaging non-uniformities, which again confirms the benefit of the ratiometric technique. The analysed fluid temperature distributions are shown in Figure 7.8 (d) and (e) which come from LIF measurement and simulation, respectively. An obvious temperature gradient can be seen across the channel with the high temperature near the wall and low one in the middle. The experimental data agree with the simulation predictions qualitatively.

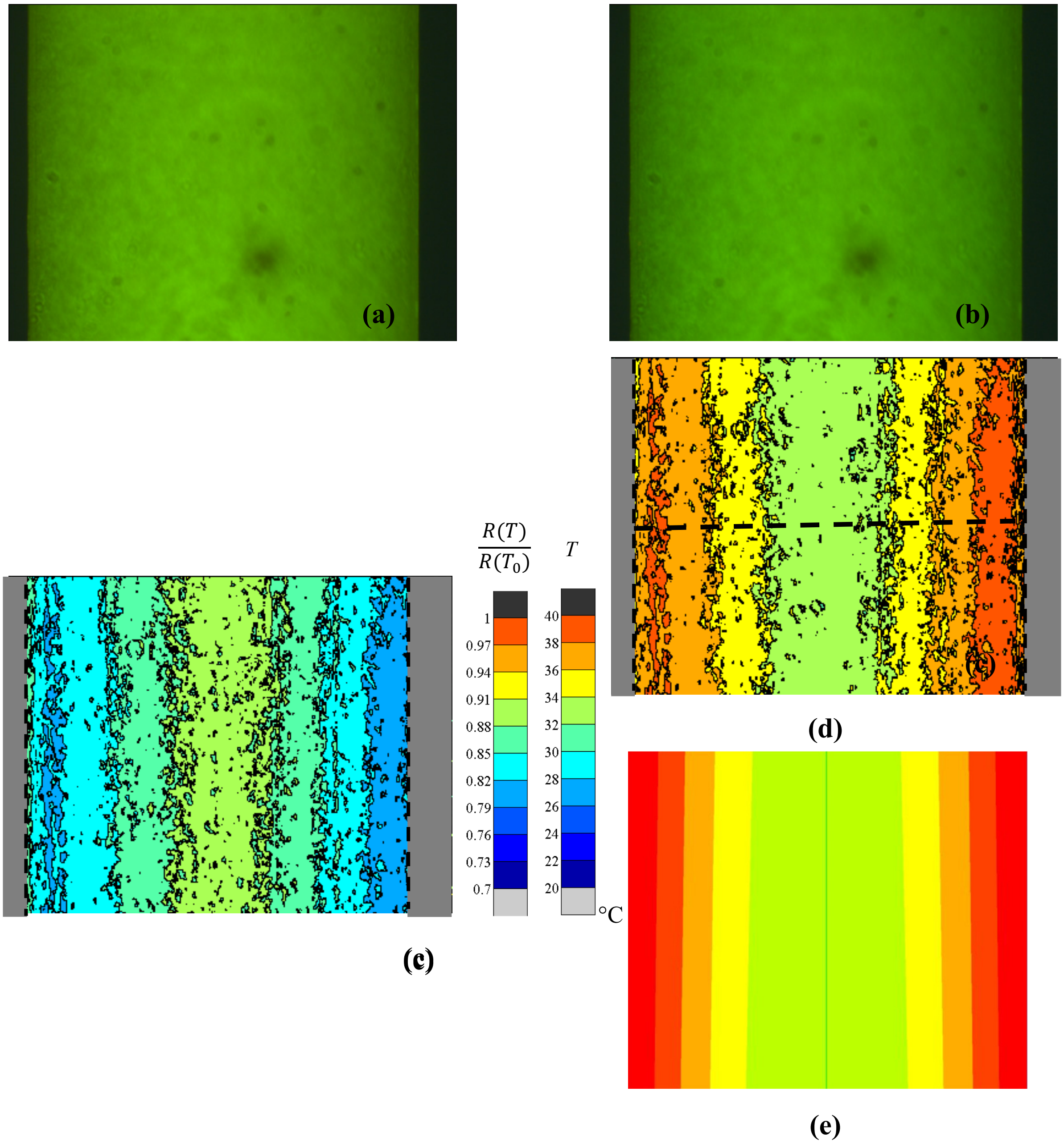

Figure 7.8: Raw colour images of KR and Rh110 for *Re* = 47 at: **(a)** Q_{in} = 0 W (T_0 = 21°C); **(b)** Q_{in} = 6.5 W. **(c)** Normalized intensity ratio field, $R(T)/R(T_0)$; **(d)** temperature field measured from LIF; and **(e)** temperature field obtained from simulation. The centre line of the region shown in all images is at x = 0.054 m.

It should be noted that in micro-LIF where volume illumination is usually applied and the dye is dissolved in the liquid, the signal from the measurement plane is superimposed upon the fluorescence from out-of-focus planes. It is hypothesized that the temperature information is averaged in the direction of the optical axis. Figure 7.9 shows the temperature profiles across the channel at x = 0.054 m (dashed line indicated in Figure 7.8 (d)) at different focal depths obtained from LIF and simulation. The experimental data were averaged over 20 pixels in the axial direction. As can be seen, the temperature profiles measured by LIF at different focal planes are nearly identical, while in fact those predicted by simulation are very different, with a temperature difference of more than 5 °C within a depth distance of 0.52 mm. The measured profiles are then compared with a simple un-weighted depth-averaged temperature from the simulation at the same position. Good agreement can be seen between the LIF measurements and the depth-averaged temperature. The largest disparities between LIF data and simulation results are observed near the wall, or in the region with the highest fluid temperatures. These variations are likely due to the relatively low level of fluorescence intensity at high temperatures.

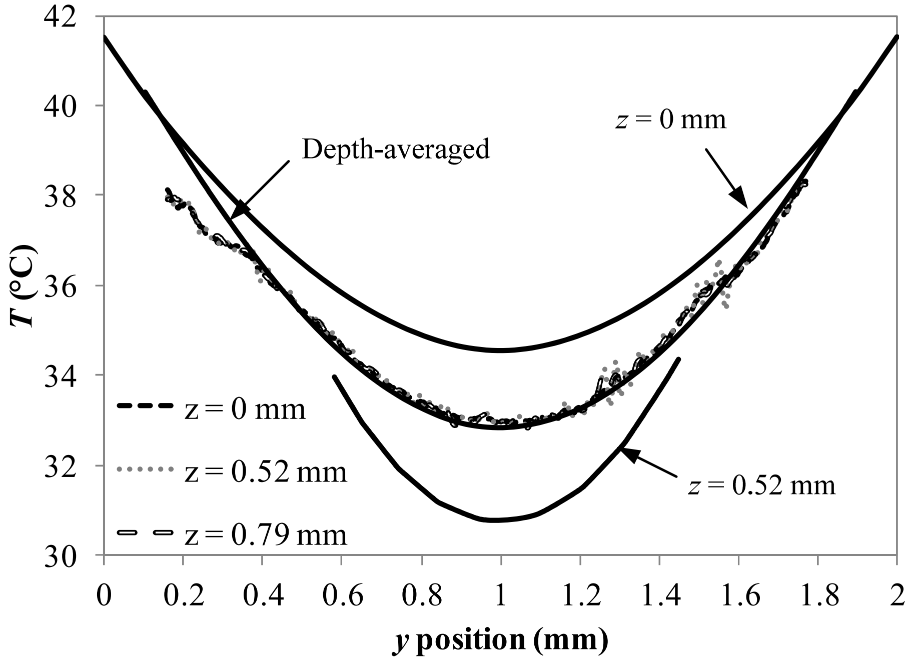

Figure 7.9: Temperature profiles measured by LIF at different focal depths (dashed lines) and those obtained from simulation (solid lines) at x = 0.054 m.

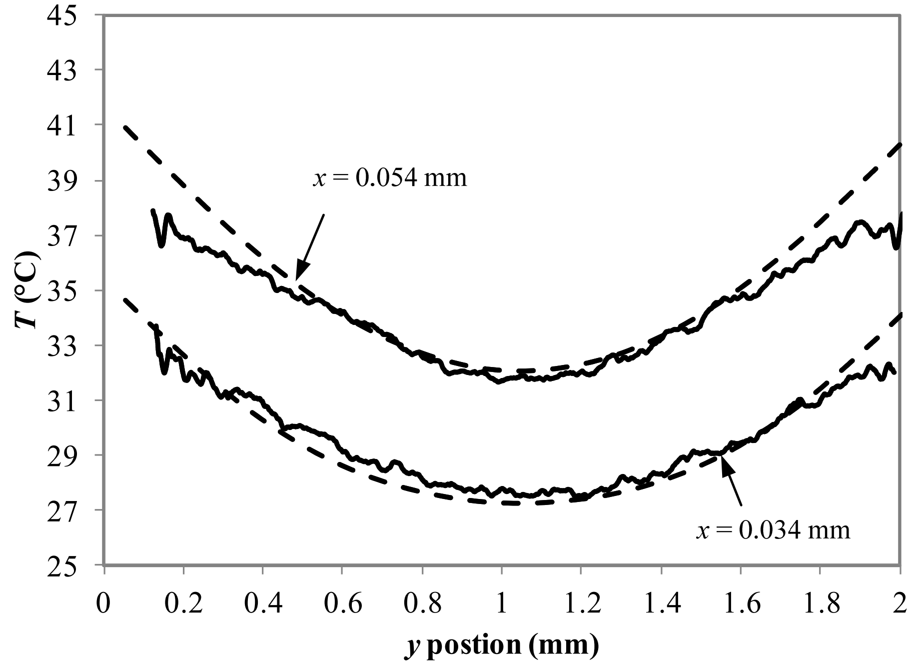

Figure 7.10: Measured temperature profiles at different axial locations compared with depth-averaged temperatures obtained from simulation (dashed lines).

Figure 7.10 compares the temperature profiles at different axial locations measured by LIF with the corresponding depth-averaged temperatures predicted by the simulation. Again, the LIF temperatures approach the depth-averaged temperature very closely with disparity within 1 °C except the near wall region.

Since the emission over the whole illuminated volume was collected, the image intensity is independent of the location of the focal plane of the imaging system within the channel. It is therefore believed that LIF technique cannot resolve the depth-wise temperature gradient when the entire channel is illuminated. Different from the micro-PIV, where the spatial resolution is usually determined by the imaging system (Wereley et al., 2002), such as the depth of field of a microscope (the distance between the nearest and farthest object planes that are considered to be in focus), the spatial resolution of micro-LIF along the optical axis is limited by the illumination system (Kim, 2010) .

Figure 7.11 presents the temperature distributions along the axial direction obtained from the experiment and simulation for *Re* = 47. The metal and glass surface temperatures were measured by the RTDs attached on the surfaces. The temperature T_{LIF} was calculated by averaging the intensity across the whole channel followed by averaging through a sequence of 20 images at a given axial location. The error bars indicate the standard deviation of the temperature variations over the image sequence. The measured T_{LIF} is compared with the bulk temperature predicted by the simulation. As can been seen from Figure 7.11, the temperature calibrated from image-averaged intensity across the channel gives a good estimate of the bulk temperature. The temperature discrepancy between the LIF temperature T_{LIF} and the bulk temperature T_b obtained from numerical predictions at different axial locations are listed in Table 7.2. As can be seen that an average temperature difference of 0.59 °C and 1.36 °C can be obtained for *Re* = 47 and *Re* = 64, respectively.

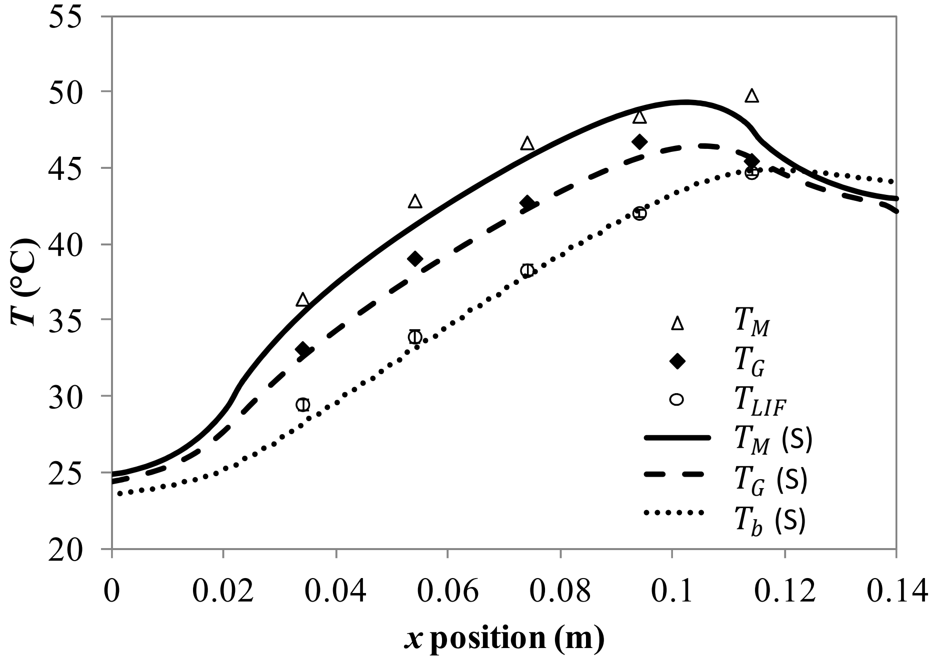

Figure 7.11: Comparison of the temperature distributions obtained from experiment (symbols) and simulation (lines) for *Re* = 47.

Table 7.2: Temperature discrepancy between the LIF temperature and the bulk temperature from numerical predictions at different axial locations.

Location	$|T_{LIF} - T_b|$ (°C) ***Re* = 47**	 ***Re* = 64**
x_1 = 0.034 m	1.32	1.43
x_2 = 0.054 m	0.62	0.27
x_3 = 0.074 m	0.35	1.53
x_4 = 0.114 m	0.09	2.21
Average	0.59	1.36

7.3.1.2 LIF measurement in a wavy channel

The LIF measurements were also taken place in a wavy channel (Sine 3). Figure 7.12 shows the fluorescence image taken at Bend 4 of Sine 3 channel and the corresponding temperature fields obtained from LIF and simulation at *Re* = 232. The black defects in Figure 7.12 (b) are caused by the contamination of some particles during the experiments as shown in Figure 7.12 (a). Comparing with the temperature field predicted by the simulation, the LIF technique provides quite a good temperature map showing that the flow temperature is no longer symmetric in the wavy channel, although the temperature information is averaged over the depth. In Figure 7.13, the measured T_{LIF} along the axial direction is compared with the bulk temperature obtained from the simulation and that predicted by Eq. (4.10). Again, the temperature calibrated from image-averaged intensity across the channel agrees well with the bulk mean temperature.

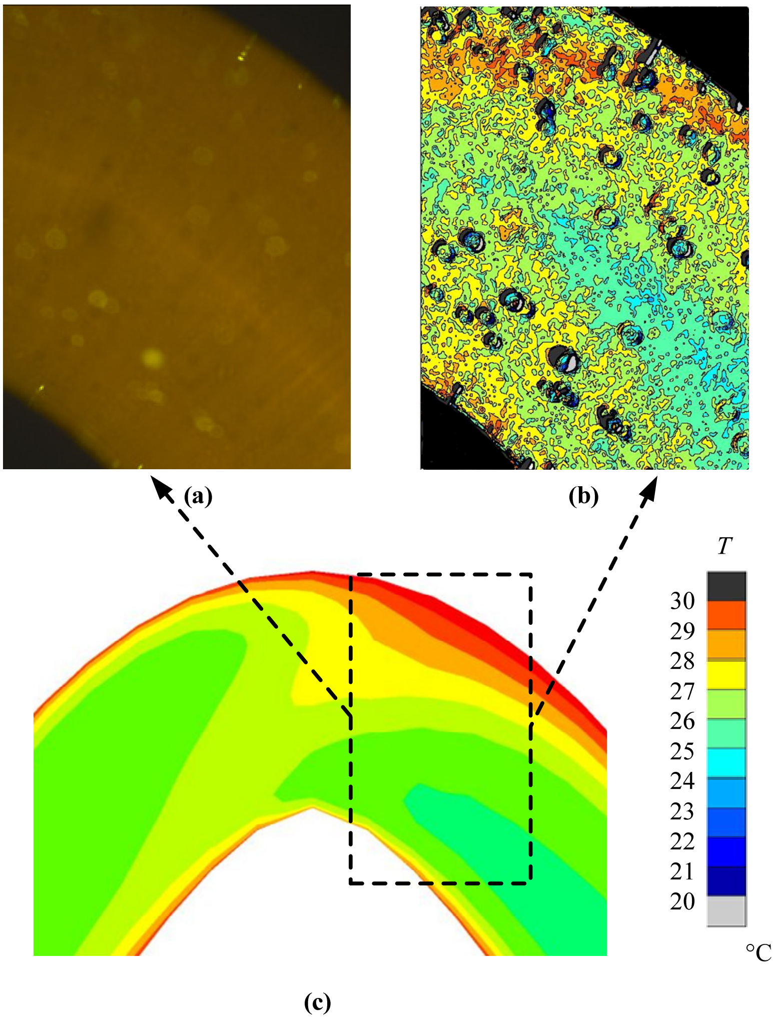

Figure 7.12: **(a)** Fluorescent image; **(b)** temperature field measured from LIF; and **(c)** temperature field obtained from simulation at Bend 4 of Sine 3 at *Re* = 232.

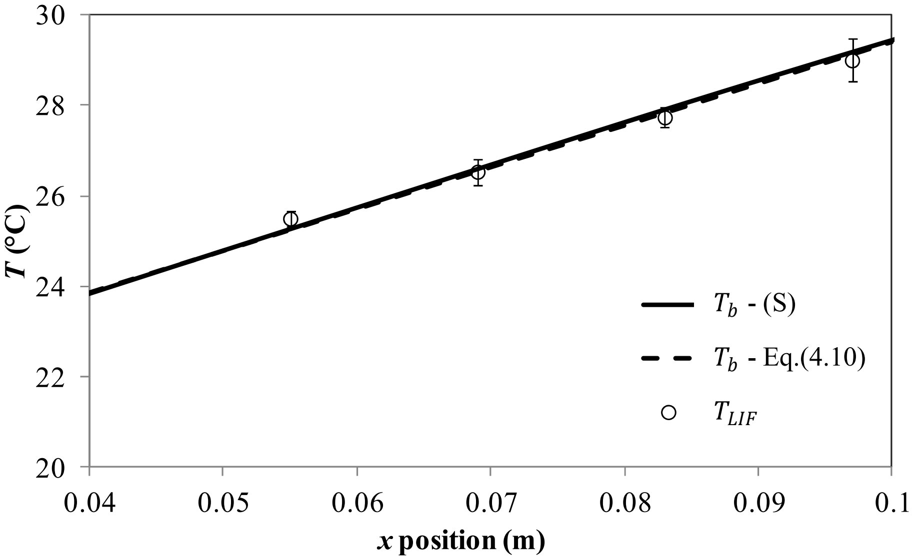

Figure 7.13: Temperatures measured by LIF compared with bulk mean temperatures obtained from simulation and Eq. (4.10) (solid and dashed lines) at different axial locations for *Re* = 232.

7.3.2 Film temperature measurement in Taylor flow

In the last section, the two-dye LIF technique using a colour camera was used to measure the depth-averaged temperature and the bulk temperature based on the fluorescent light that comes from the whole depth of channel. In this section, this technique is explored to measure the film temperature in Taylor bubble flow.

Taylor flow as a means of enhancing the mixing and heat transfer rates in microchannels is one of the important multi-phase flow patterns encountered in industrial applications. This flow regime is typically characterized by regular capsular gas bubbles separated by co-current liquid slugs and surrounded by a thin liquid film at the tube wall. Due to the introduction of gas, the flow characteristics of Taylor flow differ markedly from those of single-phase flow. Internal recirculation (in a reference frame moving with the bubble) within the liquid slug promotes radial mixing of the fluid, resulting in significant enhancements of heat and mass transfer rates (Gupta, 2010, Leung, 2012). Knowledge of local thermo-hydrodynamic characteristics of Taylor flow is vital for a complete understanding of the behaviour and improving the performance of micro-structured devices that operate in this regime.

While the hydrodynamics and mass transfer in Taylor flow have been studied extensively, heat transfer in Taylor flow is poorly understood. The liquid temperature cannot be measured at any point in the channel except for the inlet and outlet, which makes the calculation of the local heat transfer coefficient difficult. In a recent study of Majumder et al., (2013), thermocouples were inserted into the centre of the channel cross-section to measure the local fluid temperatures in Taylor flow. However, these thermocouples were found to disturb the liquid flow and the discrepancy between this measured temperature and the true bulk mean temperature was about 2 °C. Therefore, with the traditional measurement techniques, information inside a micro two-phase flow, such as the local temperature in the bubble film and slug fluid, is difficult to obtain without disturbing the flow. In contrast, LIF has a possibility to offer those quantities. When the LIF measurement is taken in the bubble region, the thin film results in an "optically thin" system, where the attenuation of the emitted fluorescence due to re-absorption is negligible and the effects of the temperature variation in the optical direction on the fluorescence are not as substantial (Hishida and Sakakibara, 2000). Therefore, a more accurate temperature can be obtained even with the volume illumination.

7.3.2.1 **Experimental setup for Taylor flow**

Taylor flow was generated in the same straight channel that used in single-phase experiments. Nitrogen and ethylene glycol were employed as the gas and liquid phases, respectively. The ethylene glycol was introduced using a HPLC pump (LC-20 AT) and the gas flow was regulated by a calibrated mass flow controller (Sierra Smart-Trak, C100L) to achieve steady flows. The gas and liquid were mixed in a T-junction prior to entering the semi-circular microchannel test section. The test section was heated by the thermofoil heater. The RTDs were attached on the metal and glass surfaces to monitor the wall temperatures. Table 7.3 shows the properties of the working fluids at 25 °C and atmospheric pressure.

Table 7.3: Physical properties of the working fluids at 25 °C and atmospheric pressure.

Fluid	Nitrogen	Ethylene glycol (EG)
Density (kg m^{-3})	-	1113
Viscosity (kg m^{-1} s^{-1})	2.10×10^{-5}	0.0171
Surface tension (N m^{-1})	-	0.048
Specific heat capacity (J kg^{-1} K^{-1})	1040	2405
Thermal conductivity (W m^{-1} K^{-1})	-	0.258
Prandtl number, *Pr*	-	163.3
Refractive index	-	1.432

The double pulse high power laser (Darwin-Duo, 527 nm) was used in this application to ensure that there were sufficient fluorescence signals from the thin film. The short pulse duration of the pulsed laser also allows for nearly instantaneous measurements of the desired flow. In order to reduce the smearing effect and get a clear interface of the bubble and liquid, the exposure time was set to be 1 ms and the camera operated at 250 fps under a reduced resolution (1440 × 374 pixels). The filter setup 540DRLP + 540LP had to be used to eliminate the excitation light. Therefore, only the fluorescence wavelengths longer than 540 nm were collected by the camera. New calibrations were performed for the above setup.

7.3.2.2 **Film and slug temperature measurements**

Figure 7.14 shows typical fluorescence images including the bubble head and tail captured by the colour camera at 250 fps. Images were recorded with an objective of 4× magnification when the flow achieved steady-state with periodic gas bubbles and liquid slugs of nearly constant lengths. The flow parameters and the related dimensionless numbers are given in Table 7.4. The flow structures were confirmed to be in the Taylor bubble regime. The liquid film between the channel wall and gas bubble was clearly visible in the "hybrid" test section since there is no optical distortion, which is usually encountered in a circular tube.

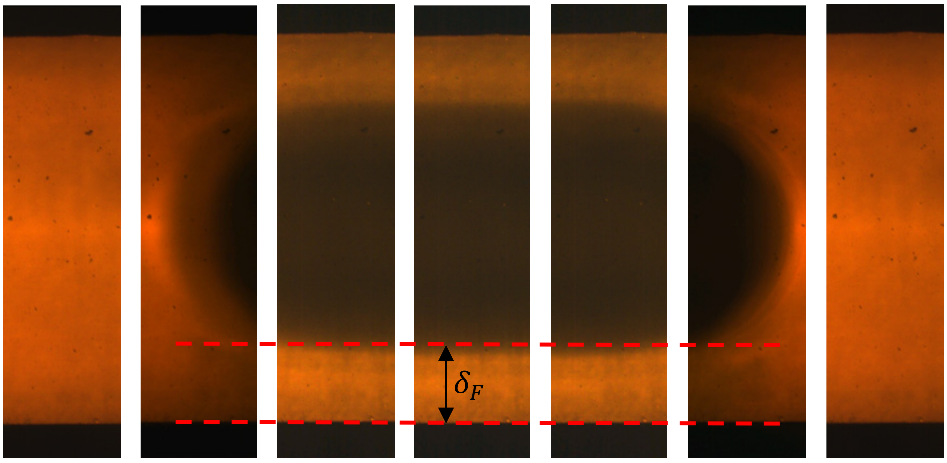

Figure 7.14: Typical fluorescence images of Taylor flow including bubble head and tail obtained by the colour camera at 250 fps.

The bubble velocity, U_B, bubble length, L_B, and slug length, L_S, were then determined by performing a frame-by-frame analysis of the recorded images using the following equations (Leung, 2012):

$$U_B = \frac{\Delta Z}{\tau} \tag{7.14}$$

$$L_B = U_B\left(f_{t,i} - f_{n,i}\right)\tau \tag{7.15}$$

$$L_S = U_B\left(f_{n,i+1} - f_{t,i}\right)\tau \tag{7.16}$$

where τ is the frame period; ΔZ is the distance moved by the bubble nose in a time of τ; $f_{t,i}$ and $f_{n,i}$ are the frame numbers when the bubble tail and bubble nose appear on the video image, respectively; $f_{n,i+1}$ is that when the bubble nose of the next bubble appears on the video image.

Due to the fact that the bubbles are not radially symmetric in the semi-circular cross-sectional tube, the film thickness, δ_F, was estimated approximately by measuring the distance between the wall and the gas-liquid interface from the images taken with the focal plane near the flat surface of the channel (as indicated in Figure 7.14). A thin film of thickness about 163 μm was obtained under the present working condition.

Table 7.4: Experimental conditions and the related dimensionless numbers.

Channel: Semi-circular *d* = 2mm		
	Nitrogen	**EG**
Superficial velocity, U_G or U_L (m s^{-1})	0.106	0.032
Bubble length, L_B, or slug length, L_S (mm)	6.73	2.02
Mixture velocity, $U_{TP} = U_G + U_L$ (m s^{-1})	0.137	
Bubble velocity, U_B (m s^{-1})	0.143	
Reynolds number, $Re = \frac{\rho_L U_{TP} d}{\mu_L}$	10.9	
Capillary number, $Ca = \frac{\mu_L U_{TP}}{\sigma}$	0.048	
Homogeneous void fraction, $\beta = \frac{U_G}{U_{TP}}$	0.77	
Film thickness, δ_F (μm)	163	

The temperature profiles across the channel in the bubble and slug regions for U_{TP} = 0.137 m s^{-1} and heat input of 5.44 W are shown in Figure 7.15. The values reported here were obtained by averaging the values over the entire recording period (3-10 bubbles per recording). As mentioned before, the measured slug temperature indicates a depth-averaged temperature over the whole channel depth. The temperature in the gas bubble is higher than that in the liquid slug, as seen in Figure 7.15. This is explained by the fact that the heat capacity rate of the gas is very low compared with that of the liquid. The bubble film temperature approaches the wall temperature with fluctuation less than 5% in the main region.

Large disparity can be seen at the interface of the bubble and liquid which is possibly caused by the blurry edge and large intensity gradient near the interface. The temperature fluctuation in the bubble film region is also higher than that in the slug region. The large uncertainty is due to the lower *S/N* ratio (higher temperature and less dye volume) in the bubble region than that in the slug region.

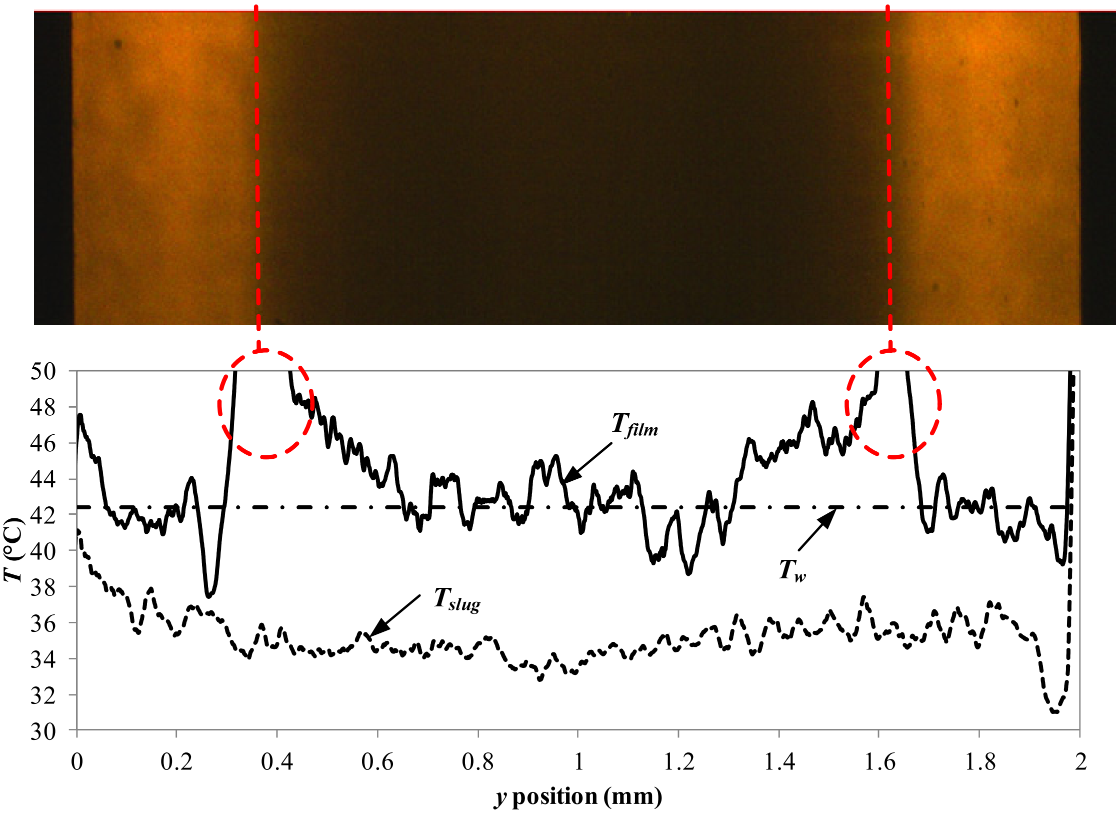

Figure 7.15: The temperature profiles across the channel in the bubble and slug regions for U_{TP} = 0.137 m s^{-1} and Q_{in} = 5.44 W.

Figure 7.16 shows the temporal variation of the fluid temperature (film temperature in the bubble region and the bulk mean temperature in the slug region) at x = 0.07 m and Q_{in} = 5.44 W. The value was calculated by averaging the temperature over the channel cross-section. The erroneous data near the interface were not taken into account when calculating the film temperature. The measured slug temperature represents the bulk mean temperature of the fluid as indicated in Section 7.3.1. The LIF measurements in the bubble region provide the film temperature directly since the temperature difference across such a thin film is negligible. The dashed line gives the time-averaged wall temperature as temporal fluctuations of the wall temperature were not detectable due to the thermal inertia of the channel wall and low time resolution of RTD measurement.

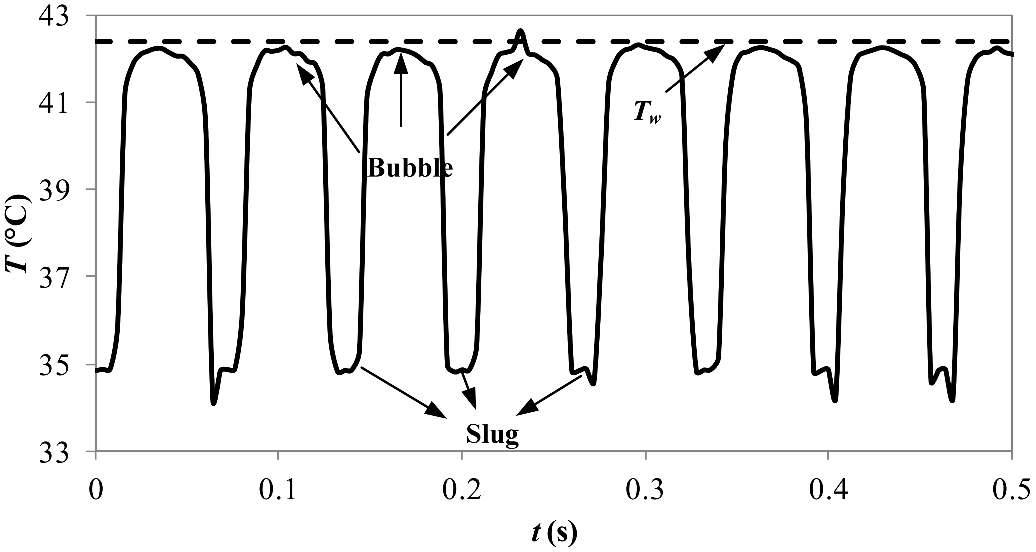

Figure 7.16: Temporal variation of the fluid temperature at x = 0.07 m for U_{TP} = 0.137 m s^{-1} and Q_{in} = 5.44 W.

It is obvious that the fluid temperature fluctuates periodically as the bubble passed through the recording point with a dominant frequency which matches with the bubble frequency. It is found from Figure 7.16 that the fluid temperature increases sharply when the bubble reaches the recording point then decreases immediately after the bubble passes through it. This profile is similar to that of the axial bulk temperature distribution obtained from numerical simulations (Gupta et al., 2010, Asadolahi et al., 2011, Asadolahi et al., 2012), which showed that the fluid temperature was highest at the tail of the bubble and decreased in the liquid slug region. The alternating pattern of liquid slug and bubble flow continually disrupts the formation of the thermal boundary layer, which gives an enhanced heat transfer.

The film temperatures at different axial locations along the channel for Q_{in} = 1.52 W and Q_{in} = 5.44 W are shown in Figure 7.17. The error bars on the T_{LIF} data represent the standard deviation of the film temperatures calculated from the individual images in the recording sequence. As can be seen, in both cases, there is a small difference between the film temperature measured by LIF and the wall temperature obtained from RTDs. The LIF data obtained in the thin film give a good estimate of the wall temperatures. The difference between the film temperature and the wall temperature lies in the range of 1-5 °C with the average difference being 1.2 °C. This is in accordance with the assumptions usually used in the literature that the liquid film has a uniform temperature that is close to the wall temperature at any given axial location (Fukagata et al., 2007, Gupta et al., 2010, Asadolahi et al., 2011, Asadolahi et al., 2012).

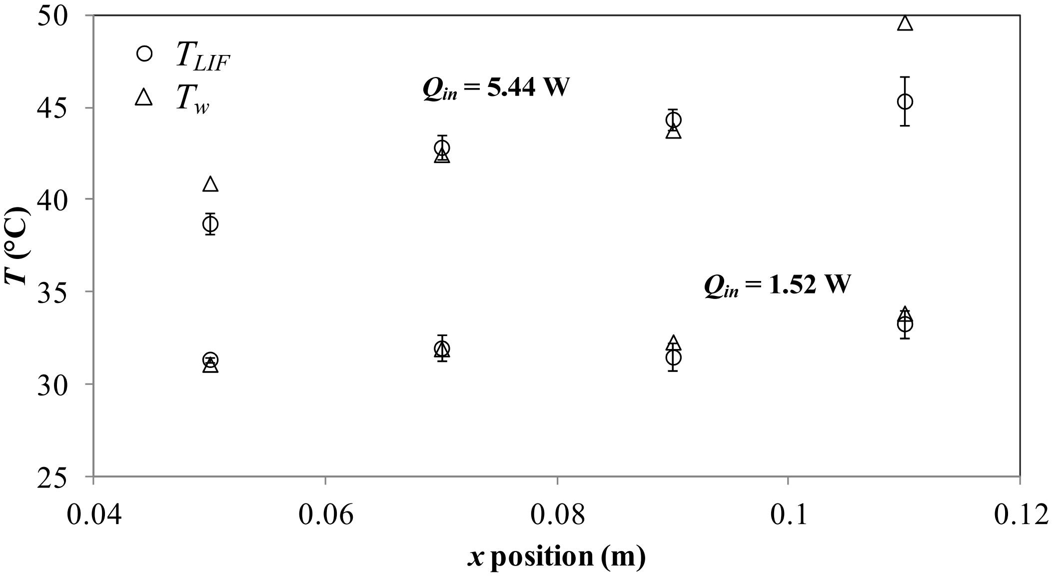

Figure 7.17: Comparison of film temperature and wall temperature in the axial direction.

The above analysis indicates that the LIF technique provides a non-intrusive way to measure the fluid temperature in Taylor flow. The volume-illuminated LIF tends to give a true film temperature in the bubble region where the thin film is nearly isothermal, while for slug temperatures the use of this technique is limited to the depth-averaged values. The LIF is also serving as a way to measure the wall temperature as usually the film temperature is approaching the wall temperature within 1 °C difference. The use of high-speed pulsed laser and high-speed camera also provides the ability to acquire "instantaneous" images in Taylor flow and temporally resolved measurements. These results are helpful for the development of Taylor flow models and verification of numerical simulations, which is important for a better understanding of the Taylor flow heat transfer mechanisms. This technique can be easily extended to annular flow and boiling flow.

7.4 Error analysis

In the LIF technique, the temperature measurement relies on the detection of the fluorescence intensity. The digital camera is the most important part of the LIF system and its resolution, bit depth and noise characteristics affect the accuracy of fluorescence intensity directly. For cameras, image resolution describes the detail an image can hold and colour/bit depth determines how many discrete colour values can be represented. Images with higher resolution and bit depths can encode more colours and provide more details under ideal circumstances. The bit depth (n) will determine the temperature measurement resolution (*dT*) of the LIF technique as expressed by the following equation:

$$dT = \frac{1}{2^n A} \times 100\% \qquad (7.18)$$

where A can be interpreted as the overall temperature sensitivity. Therefore, a 10 bit and 16 bit cameras will resolve the temperature by 0.1 ºC and 0.0015 ºC, respectively, if the temperature sensitivity is 1%/ºC.

The accuracy of the temperature measurement mainly relies on the noise characteristics of the camera and the temperature sensitivity of fluorescent dyes. The temperature will be estimated from the intensity ratio of two channels using the calibration curve. To make it simple, a linear relationship between $\ln(R)$ and *T* can be estimated through the model:

$$\ln(R) = AT + B \qquad (7.19)$$

The uncertainty in the intensity ratio *R*, associated with the noise of the camera, will result in an error of ΔT.

$$\Delta T = \frac{\partial T}{\partial R}\Delta R + \sigma = \frac{1}{A}\frac{\Delta R}{R} \qquad (7.20)$$

From Eq. (7.20) it can be found that 1% uncertainty in the intensity ratio ($\frac{\Delta R}{R}$) will result in a $\Delta T = \frac{1\%}{A} = 1$ ºC error in the measured temperature value if the temperature sensitivity is 1%/ºC. It can be also concluded from Eq. (7.20) that the higher the temperature sensitivity (*A*) is, the smaller the error is in the temperature estimation. Therefore, in order to have a higher resolution and accuracy in measuring the temperature by means of LIF, one should use a camera with higher resolution, higher bit depth and lower noise and select a dye combination with the highest temperature sensitivity. In addition, for the two-colour LIF system using a colour camera, the colour pick-up system has an impact on the signal separation, thereby influencing the overall temperature sensitivity. Due to the adverse effect of signal overlap it is necessary to improve the temperature sensitive and image quality of the camera if the overlaps are large.

It is important to point out that photobleaching caused by over-exposure to the excitation can bring enormous error into the temperature measurement over time. This effect was found to be negligible since a flowing dye solution was used in this study so that the fluorophore molecules were exposed to the excitation for only a brief interval 1-2 s. However, dye degradation due to heating was observed during the experiment. The dye solution became almost colourless after a long heating period. To reduce inaccuracies of this type, fresh florescent solutions were prepared before experiments and calibrations were performed frequently.

7.5 LIF limitations

The LIF technique has been used as a useful tool to measure the fluid temperature fields in microscale systems. However, as discussed above, it is also confirmed that the LIF with volume illumination has a very poor spatial resolution along the optical axis and cannot resolve the temperature gradient in the depth-wise direction. In many studies, the measured temperature was taken as the local temperature or bulk mean temperature without taking into account the averaging effect (Ross et al., 2001, Sato et al., 2003). This might give the right temperature when the temperature gradient along the penetration direction is small, but it needs more consideration when large temperature variation exists in the depth-wise direction. Consequently, for devices such as tortuous microchannels where three-dimensional flows develop, the conventional micro-LIF technique may have inherent limits and excessive measurement errors. Improving the spatial resolution of LIF along the optical axis will therefore require illuminating thinner “slices” of the channel or more advanced imaging techniques such as confocal microscopy. Based on the author’s best knowledge, very few previous studies have explored the 3D temperature fields in microchannels experimentally due to these limitations. To well understand the thermohydraulics in microchannels, accurate local temperature measurement is required. In the next chapter, temperature sensitive particles are proposed to replace the dye solution to achieve local temperature measurement and simultaneous measurement of temperature and velocity in microchannels.

7.6 Summary

An experimental method for non-intrusive temperature measurement in fluid flow was developed using Laser Induced Fluorescence (LIF) with a colour camera. A temperature sensitive dye (Kiton Red) and a temperature insensitive dye (Rhodamine 110) were chosen as temperature indicators and the temperature was evaluated from the intensity ratio of the red and green channels of colour images.

Calibrations performed with different concentration ratio and optical conditions demonstrate the feasibility of this unique technique and its ability to accurately determine fluid temperature despite variations in other non-temperature parameters such as illumination intensity and optical characteristics of the system. Colour enhancement filter has been introduced for the first time and has been shown to effectively reduce the spectral conflicts and significantly improve the temperature sensitivity. A maximum sensitivity of 2.2%/°C can be achieved at $C_{KR}/CR_{Rh110} = 1$ with the colour enhancement filter XB30 while 1.6%/°C is the maximum without using the filer.

Two-dimensional temperature measurement using the two-dye LIF was demonstrated in fully-developed laminar flows in both straight and wavy channels. The intensity of the recorded fluorescence light for the present setup is linked to the depth-averaged temperature so that the micro-LIF technique cannot resolve the temperature gradient over the optical axis. A detailed comparison of experimental findings on the depth-averaged temperature and corresponding numerical results shows good agreement. Comparisons between the LIF measurements and the numerical predictions also suggest that the LIF temperatures calibrated from image-averaged intensity across the channel are, on average, within 1 °C difference from the bulk mean temperature. These results suggest that LIF can be used to non-intrusively estimate the bulk temperature with reasonably good accuracy.

The two-dye LIF technique was also applied in measuring the film temperature in Taylor flows. The thin film in the bubble region generates an optically thin system where the temperature variation is negligible, so that the volume-illuminated LIF tends to give a true film temperature, while for slug temperatures the use of this technique is limited to the depth-averaged values. The film temperature also provides a reasonable estimation of the wall temperature as usually the film temperature is approaching the wall temperature within less than 1 °C difference. Temporally-resolved measurements in Taylor flow were achieved using the high-speed pulsed laser and high-speed camera. These results provide valuable information for the development of Taylor flow models and verification of numerical simulations.

Chapter 8

Temperature Sensitive Particles and Simultaneous Measurement of Temperature and Velocity

As discussed in Chapter 7, the LIF technique using dissolved fluorescent dyes reports more-or-less un-weighted average values over certain areas/depths of the samples, because the indicating fluorescence is not spatially located in volume illumination. Such a limitation can be overcome by encapsulating fluorescent molecules into microparticles or nanoparticles made from organic polymers. In this Chapter, a series of fluorescent dyes are incorporated into microparticles. The temperature sensitivity of the fabricated particles is evaluated. Two-dye particles for ratiometric temperature measurement are also prepared and evaluated, together with image processing methods for in-focus particle identification. Ultimately, the temperature sensitive particles are planned to be used as both temperature indicators and flow tracers. Simultaneous measurement of temperature and velocity can therefore be achieved by combining the two-dye LIF and PIV. It provides a non-intrusive tool to study the three-dimensional temperature and velocity fields in small-scale devices. It is hoped that the present work can be applied to the study of the thermohydraulics of complex microchannels.

8.1 LIF using particles

Different luminescent/fluorescent materials, such as rare-earth phosphors or fluorescent organic dyes, have been used for luminescence/fluorescence-based temperature measurements. The dyes are widely used in solution, but also in immobilized form (in an inert host polymer), for example in the form of solid-state thin films or particles. While there have been numerous studies of temperature measurements in fluids using the LIF technique with dissolved dyes, there is much less documentation about the use of temperature sensitive particles to measure local temperatures.

The rare-earth chelate europium thenoyltrifluoroacetonate $Eu(TTA)_3$ is known to possess good temperature sensitivity. It has been immobilized in polymers including polystyrene, poly (methyl methacrylate), polyurethane and model airplane dope, with fluorescence detected either as intensity or decay time (Someya et al., 2010, Someya et al., 2011, West, 2012). In the earlier days, it was widely used as temperature sensitive paint for temperature mapping in aerodynamic measurements (Gallery et al., 1994, Liu et al., 1997) and integrated circuit diagnostics (Kolodner and Tyson, 1982). The co-immobilization of a relatively inert reference dye (such as perylene) and the temperature sensitive Eu(TTA)$_3$ in a polystyrene matrix also enables ratiometric thermometry (Basu and Venkatraman, 2009).

Temperature sensitive particles were proposed by Simon (2000) in a United States Patent (No. US6132958 A). The invention disclosed a fluorescent bead that can be used for determining the temperature of a single cell contained in a cell/tissue sample. The temperature sensitive particles were tagged with the temperature sensitive fluorophore Eu(TTA)$_3$ and temperature insensitive fluorophore coumarin to correct the non-uniformities in lighting and particle size/shape. The beads are 80-90 nm in size and made of poly (methyl methacrylate). West (2012) reported the synthesis of polystyrene microspheres doped with the same dyes. These particles were used for flow visualisation and qualitative temperature measurements in natural convection in water.

Most recently, a particle image thermometry method based on microcapsules filled with a fluorescent dye solution was reported by Vogt and Stephan (2012). The microcapsules consisted of a solid polymer shell and a liquid core of hexadecane in which the temperature sensitive dye Pyrromethene 597-8C9 and temperature insensitive dye Pyrromethene 567 are dissolved. The applicability of the technique was demonstrated in a stationary temperature field drive by natural convection. However, a very high measurement uncertainty was observed.

Temperature sensitive particles using thermographic phosphor Mg_4FGeO_6:Mn was presented for high temperature gas thermometry by Omrane et al. (2008). The red shifted emission of phosphor particles was detected and analysed to infer temperature using calibration procedures for lifetime and emission spectra against temperature. The velocity fields were also achieved simultaneously by tracking the particles using PIV technique.

A thorough review of luminescent probes and sensors for temperature measurement can be found in (Wang et al., 2013), which provides a discussion of polymeric matrices for immobilizing temperature sensitive probes and an overview of the various application formats of temperature sensors. It showed that the currently used luminescent probes, especially rare-earth chelate complexes, display good sensing capabilities, but they are usually photoexcited in the 350-450 nm region only. The development of probes that can efficiently absorb visible light is highly desired.

In this study, some popular organic dyes used in traditional LIF are studied by investigating the feasibility of their being integrated into particles. Those dyes can be usually excited by blue or green lasers and provide opportunity for the LIF technique using a colour camera.

8.2 Development of temperature sensitive particles

In order to overcome the problems associated with the LIF technique with volume illumination, the temperature sensitive fluorescent dyes were presented in particle form, called temperature sensitive particles (TSPs). The local temperature field in the focal plane can be obtained by calculating the intensity of in-focus particles. By moving the focal plane, a 3-D temperature field can be reconstructed. The particles can also be used as a tracer particle for the PIV measurement. Thus, it combines the capabilities of LIF for high resolution temperature measurements with the possibility of measuring velocity simultaneously.

The encapsulation of fluorescent dyes into microparticles is a straightforward way to prepare temperature sensitive particles (Wang et al., 2013). Until now the most common approach for the immobilization is the physical entrapment of the sensitive probe in a polymer matrix. In this approach, the dye is usually placed in the outer shell of the particles where it maintains the photophysical properties of its dissolved form. However, physical entrapment of the dyes in the polymer matrix produces inhomogeneity in the material and gives stability problems due to the leaching of the fluorescent probe, reducing the lifetime and reproducibility of the sensor (Basabe-Desmonts et al., 2007).

To improve the stability of these materials, the alternative is the covalent attachment of the probes to the polymeric matrices. For instance, dyed microparticles can be produced through dispersion polymerization by several methods. Dyes can be dissolved in the monomer prior to polymerization or microspheres can also be dyed after polymerization using an organic solvent to swell the particles and transport the dye into the particles. Alternatively, the particles can be optically encoded by dyes (or smaller dyed particles) that are covalently bound to their surfaces (Hoffacker et al., 2013). Typically the homogeneously volume-stained particles made by processes that embed the fluorophores into the polymer matrix of the sphere, rather than just providing the coating on the surface, have little leaching of the internally incorporated fluorophores and show high stability in solvents. However, these solid particles may lose some of the temperature sensitivity of the original dyes due to loss of some conformational freedom.

The selection of proper polymer matrices is critical when immobilizing the temperature sensitive fluorophores (Basu and Venkatraman, 2009, Wang et al., 2013). The polymer has to be mechanically robust and transparent. Some functional groups, e.g. carboxy groups, can quench the luminescence of an indicator dye. Furthermore, some fluorophores are solvatochromic, meaning their spectral properties change depending on the matrix they are embedded in.

The seeding particles are an inherently critical component of the micro-LIF/PIV system. These particles need to have adequate temperature sensitivity so that the temperature can be detected with high accuracy and resolution. Their stability in an aqueous environment, stability during embedding into the polymer, and resistance to photobleaching (such resistance is required for long-term observations and subsequent calibrations) play significant roles in the implementation of the technique. Additionally, with the simultaneous measurements in mind, the particle size, density, and concentration should also meet the requirement for PIV application. Therefore, great effort and care must be devoted to the selection of particle material, probe immobilization methods, and fluorescent dyes.

8.2.1 TSPs fabrication

TSPs labelled with the two dye candidates (KR and Rh110) proposed before could be fabricated as their feasibility has been evaluated in Chapter 7. Ideally, to take full advantage of the two-dye LIF technique, the two verified dyes would be incorporated into one particle (two-dye, one-particle). In this case, the ratiometric technique could be applied at exactly the same location using the intensities of the red and green channels. Alternatively, two kinds of particles with each labelled with one dye (two-dye, two-particle) could be used at the cost of spatial resolution. As two fluorescence emissions come from two different particles at different positions (pixels), the intensity ratio can be only processed by averaging the intensities in an interrogation window. However, this method is beneficial to validate the feasibility of the corresponding particles working with a colour camera system by investigating their individual optical characteristics and temperature sensitivities after the integration of the dyes into the particles.

Fluorescent particles of various sizes and colours that are manufactured from different materials and manufacturing processes are currently commercially available. Typical applications of these fluorescent spheres include flow cytometry, flow visualisation, biomedical diagnostics and life sciences research. The stability of specific fluorescent colorants under environmental effects and photobleaching are important for the fluorescence detection, so that their fluorescence intensities are usually stable and resistant to the environment changes (temperature, pH, etc.).

Several different types of commercially-available fluorescent polymer microspheres, such as fluorescent microspheres labelled with Fluorescein and Rhodamine B (Bangs Laboratories. Inc.) were tested. Although the fluorophores are well-known to be temperature sensitive, the standard particles did not show any temperature sensitivity during examinations. Therefore, microparticles with the desired temperature sensitivity and specific spectral characteristics have to be custom-manufactured.

The TSPs were developed by microParticles GmbH (Berlin) using their novel manufacturing techniques. The fluorescent particles can be made with either poly (methyl methacrylate) (PMMA) or polystyrene (PS). The densities are 1.19 g cm^{-3} and 1.05 g cm^{-3} for PMMA and PS particles, respectively. As previously stated, Kiton Red and Rhodamine110 are preferred fluorescent dyes for the two-dye LIF technique using a colour camera. However, during the preparation it was found that Kiton Red dye leached out of the interior of the shells over time when it came together with PMMA or PS particles. Another material, melamine resin (MF), was therefore tried – in order to overcome the tendency of solid particles of MF (density 1.51 g cm^{-3}) to settle in water, hollow particles had to be produced. Eventually, 6 μm hollow melamine resin spheres with a shell thickness in the 100 nm range were prepared successfully. The dye was soaked into hollow MF spheres followed by evaporating the solvent. In this approach, the beads remain intact and contain the dye in quasi "free" form so that the dye retains its conformational degrees of freedom, in contrast to the encapsulated variety.

Other potential temperature sensitive dyes were also tested to determine their suitability to serve as components of the fluorescent particles for temperature measurements. Table 8.1 lists the particles fabricated by microParticles GmbH. Particularly, Pyrromethene 597-8C9 (PM597) and Europium (III) thenoyltrifluoroacetonate (EuTTA) which are temperature sensitive dyes were manufactured based on studies of Vogt and Stephan (2012) and West (2012).

Table 8.1: Summary of the developed fluorescent particles.

Labelled dye	Size (μm)	Peak Ex/Em (nm)	Temperature sensitivity (%/°C) measured by fluorimeter
PMMA-RhB	6	560/584	–0.84
PS-RhB	3	560/584	–2.72/–1.29 (measured by micro-LIF)
PMMA-NR	6	553/590	~0
PS-NR	1	553/570	–0.15
PMMA-LDS 698	6	476/668	-
PS-LDS 698	6	476/668	-
PS-NB	6	558/563, 625	–0.22
PS-EuTTA	6	310/620	-
MF-KR (hollow)	2.5	554/594	–0.12
MF-PM597 (hollow)	6	544/547	–0.48
PIV-P(1)	6	542/612	–0.28

RhB = Rhodamine B, NR = Nile Red, NB = Nile Blue, EuTTA = Europium (III) thenoyltrifluoroacetonate, KR = Kilton Red, PM597 = Pyrromethene 597-8C9, PIV-P(1) = PIV Particles (purchased from Duke Scientific); PMMA = Poly (methyl methacrylate), PS = Polystyrene, MF = Melamine resin.

8.2.2 Temperature sensitivity analysis

8.2.2.1 Spectroscopy study

The spectral property and temperature sensitivity of the manufactured TSPs were examined by using a fluorimeter (Varian Eclipse Fluorimeter) in the School of Chemistry at the University of Sydney. The seeding particles used for PIV in the present study (Duke Scientific) were also tested. The particles are polymer particles encapsulating a fluorescent dye which emits the orange-colour fluorescence when illuminated by a green laser (e.g. Nd:YAG, Nd:YLF).

The particle samples were excited at both 488 nm and 527 nm (the same as the laser wavelengths used in the micro-LIF system). Figure 8.1 shows the emission spectra of the tested particles excited at 488 nm. It can be seen that the emission peaks of most of the particles are located in the range of 540-600 nm. As mentioned in Chapter 7, the yellow emission (570-600 nm) might not be ideal for the LIF system using a colour camera; however, these particles still provide potential for temperature measurements using traditional LIF setup. It is interesting that PS-NB shows two emission peaks located at 563 nm and 625 nm, respectively. It should be noted here that insufficient light was detected for the EuTTA particles and LDS 698 particles when being excited by 488 nm or 527 nm light. In Figure 8.1, the PS-EuTTA particles were excited by 310 nm light and it displays a sharp emission with the peak located at 620 nm, which is ideal for colour separation. The PS-LDS 698 particles have a very large Stokes shift with a peak emission at approximately 670 nm when they were excited by 570 nm light. Due to the low quantum efficiency of these two kinds of particles under the excitation wavelengths of 488 nm and 527 nm, no further study was performed for them.

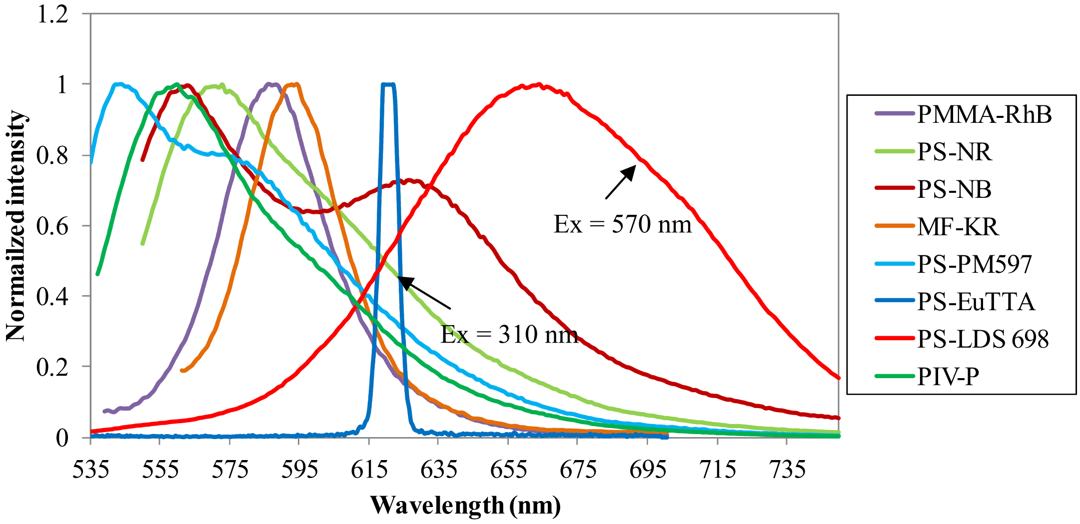

Figure 8.1: Emission spectra of TSPs at excitation wavelength of 488 nm.

The temperature sensitivity was determined by recording fluorescent intensity changes during temperature changes. The cuvette holder of the fluorimeter was connected to a thermostatically-controlled water-bath and the temperature of the particles was controlled by the temperature of the circulating water. A plot of the normalized fluorescent intensities against temperature for the tested particles is shown in Figure 8.2. The data have been fitted with linear regressions for a better comparison to other dyes. The average temperature sensitivities of the particles are summarized in Table 8.1. It is shown in Figure 8.2 that the PS-RhB particles show the greatest temperature sensitivity of –2.72%/°C and the PMMA-RhB particles display a temperature sensitivity of –0.84%/°C. The fluorescence intensity of other particles, however, did not change much with temperature as the temperature sensitivity is less than 0.5%/°C.

The temperature sensitivity study of these TSPs shows that the matrix-immobilized dyes do not show the same extent of temperature sensitivity as their free counterparts in solution. The thermal sensitivity properties of the fluorophores might have been altered after being incorporated into the particles.

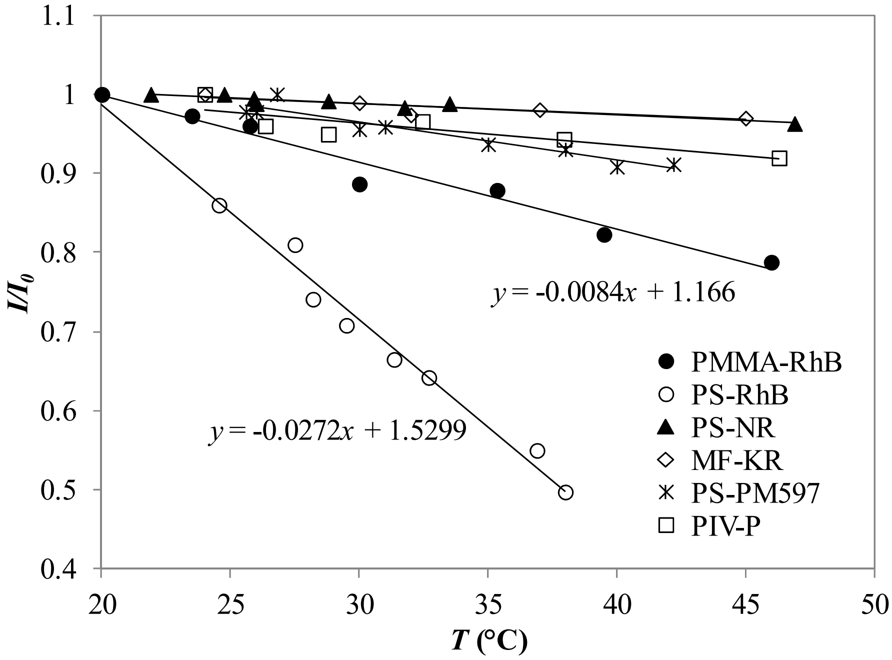

Figure 8.2: Variation of normalized intensity ratio, I/I_0 (T_0 = 20°C), with respect to temperature for the tested particles.

8.2.2.2 Micro-LIF study

Since the particles would be used in the microchannels for the temperature measurements, they were further examined using the micro-LIF system. Imaging of the TSPs under different temperatures was performed using the the micro-LIF setup shown in Figure 7.1. The temperature calibration was performed using a static sample of particles. A drop of particle suspension was placed on a glass coverslip. A thin layer of particles were coated on the glass by evaporating the solvent. The particle temperature was controlled by a transparent thermofoil heater attached on the coverslip. A RTD sensor was attached on the coverslip to monitor the particle temperature.

Figure 8.3 presents the colour images of PS-RhB particles at two different temperatures using the pco.edge scientific CMOS camera. As can be seen, the particles became darker with increasing temperature. To measure the fluorescence intensity quantitatively, the particle intensity was extracted using the technique described in Section 8.3. The intensity was determined by averaging over the particles in a region of interest (ROI) over 10 images.

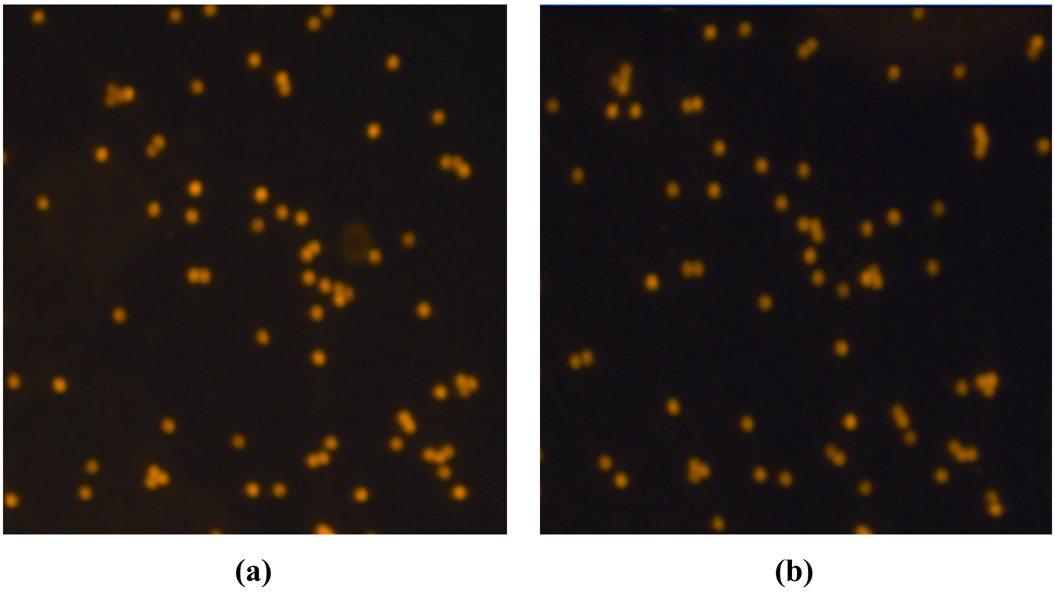

Figure 8.3: Fluorescence images of PS-RhB particles at: **(a)** 24 °C; and **(b)** 48 °C.

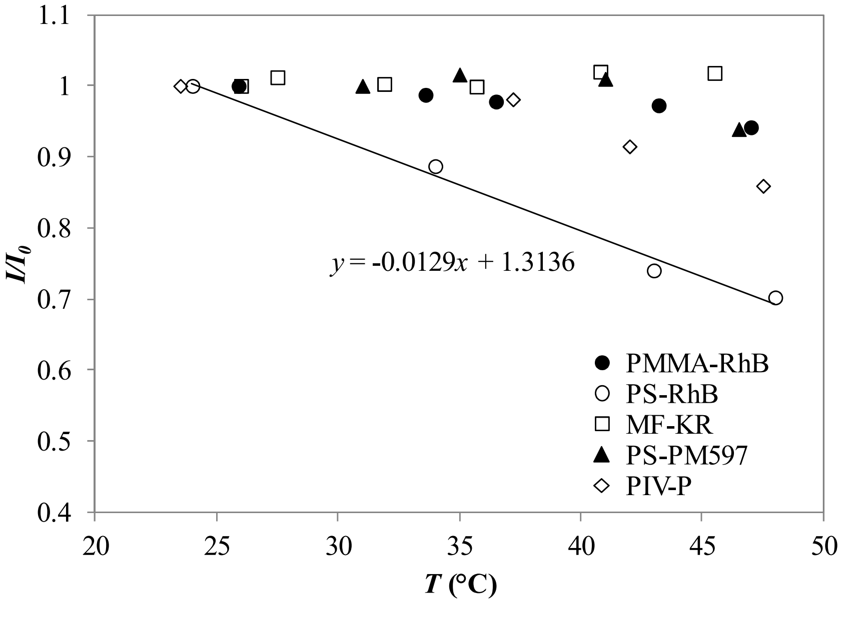

Figure 8.4: Variation of normalized intensity ratio, I/I_0 (T_0 = 20°C), with respect to temperature for the tested particles measured by the micro-LIF system.

The fluorescence intensity calculated from the particle images against temperature for the interested particles is shown in Figure 8.4. The calibration shows a temperature sensitivity of approximately –1.29%/°C for PS-RhB, which is lower than that detected by the fluorimeter (–2.72%/°C). Although a reasonable temperature sensitivity of PMMA-RhB and PS-PM597 particles was tested by the fluorimeter, neither of them was adequately detectable with the high-sensitivity camera. Again, for other particles, the effect of temperature on fluorescence intensity was negligibly small. Of the various TSPs fabricated and tested, the best results were achieved with PS-RhB particles.

The stability of particles was tested by recording the average fluorescent signal over time. Unfortunately, for almost all particles, photobleaching was encountered with the fluorescence intensity decreasing with time. Intensity measurements at different temperatures were done over a heating run followed by a cooling run for PS-RhB particles. The particles' performance was not reversible for the heating and cooling cycles. The particles were not stable and the results were not repeatable. This was even worse in the micro-LIF system where high power laser excitation was used. Therefore, the PS-RhB particles are not satisfactory for high-accuracy temperature measurement with the micro PIV/LIF setup.

From the temperature sensitivity analysis of the particles, it was found that a general problem of using TSPs is that fluorescent dyes lose their temperature sensitivity after being incorporated into the particles. A thorough literature survey showed that the loss of temperature sensitivity had been encountered in most studies when the fluorescent particles were used to measure the temperature. Vogt and Stephan (2012) found that the temperature sensitivity of the PM597 dropped from approximately –1.75%/°C in solution form to –0.5%/°C for microcapsules. The temperature sensitivity of the microcapsules is therefore very low compared with LIF with dissolved dyes (–2.7%/°C) (Natrajan and Christensen, 2009).

8.2.3 Two-dye one-particle

Based on the temperature sensitivity study of particles tagged with one dye, an attempt was made to incorporate a temperature-insensitive fluorescent reference dye into the particles. Although the spectral characteristics of the proposed KR+Rh110 particles are favourable, KR could not be used due to the loss of temperature sensitivity in the polymer matrix. Accordingly, particles tagged with Rhodamine B (RhB) and Rhodamine 110 (Rh110) were developed.

Due to problems of losing temperature sensitivity and photobleaching encountered in the previous particle manufacture, the two-dye particle development was carried out by Surflay Nanotec GmbH (Berlin) using their patent-protected Layer-by-Layer (LbL) technology with charged polymers (polyelectrolytes). Highly uniform 6 µm PMMA microparticles labelled with RhB and Rh110 were fabricated successfully. The confocal laser scanning images and transmission electron micrographs of TSPs taken with 60× oil immersion objective are shown in Figure 8.5. The emission spectrum of the two-dye particles excited at 488 nm is displayed in Figure 8.6. Two emission peaks (529 nm and 585 nm) can be seen from the spectrum of PMMA-RhB+Rh110 particles which correspond to the emission peaks of Rh110 and RhB, respectively.

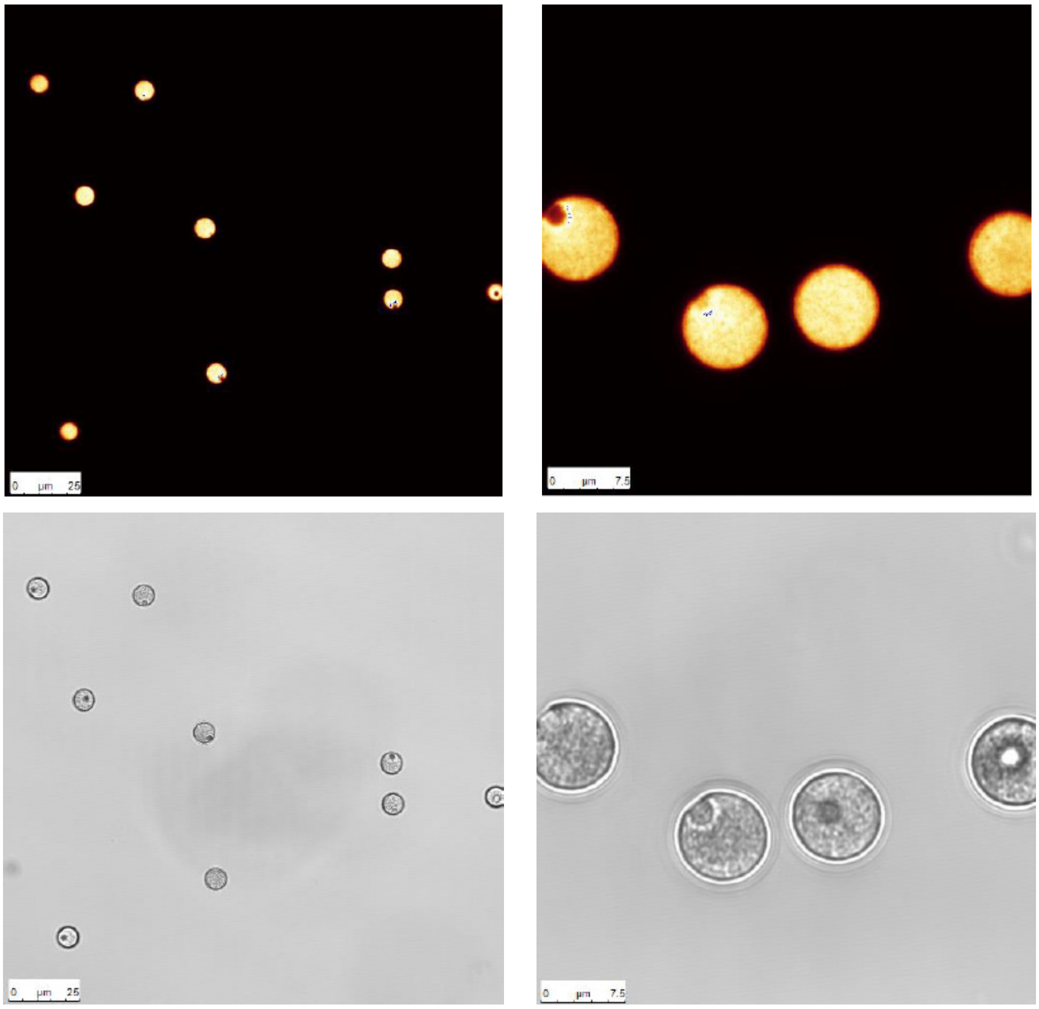

Figure 8.5: Confocal laser scanning images (top) and transmission electron micrographs (bottom) of PMMA-RhB+Rh110 (provided by Surflay Nanotec GmbH).

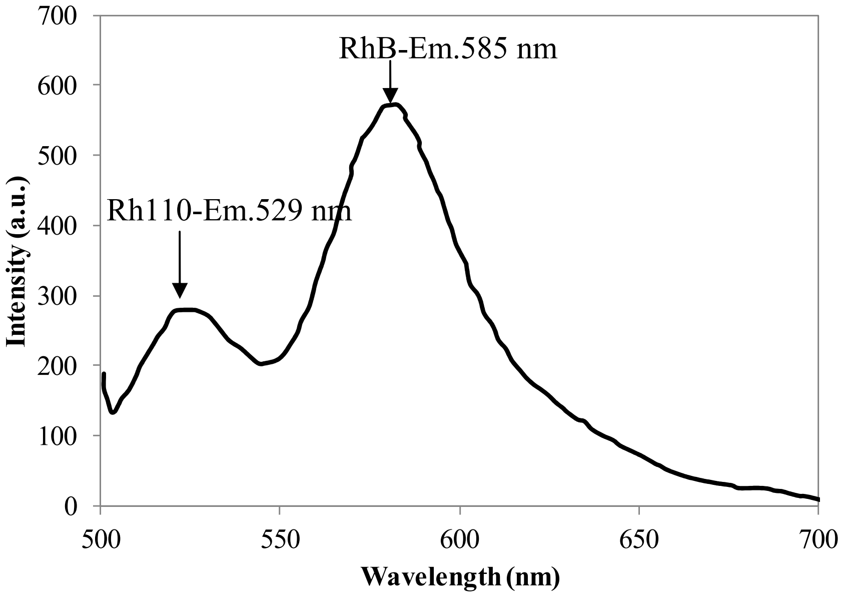

Figure 8.6: Fluorescent emission spectrum of PMMA-RhB+Rh110 excited at 488 nm.

The intensity of each peak as a function of temperature is plotted in Figure 8.7. As expected, the intensity of Rh110 does not change much with temperature, whereas the intensity of RhB at 585 nm is significantly decreased with the temperature. Figure 8.7 (b) shows the normalized intensity ratio of the two dyes. A linear fit of the data reveals a temperature sensitivity of –1.7%/°C for the intensity ratio of RhB and Rh110.

The temperature sensitivity test was also undertaken using the micro-LIF system with 527 nm laser using the signal ratio of the red and green channels. The high power laser was used so that the particles could provide sufficient fluorescence signals to be detected by the camera. The variation of the signal ratio with respect to temperature is shown in Figure 8.8. As can be seen, a slightly higher temperature sensitivity of –1.88%/°C was obtained.

The stability of PMMA-RhB+Rh110 particles was tested at constant (room) temperature over time. Similar to one-dye particles, the most noticeable effect is photobleaching caused by the high power of excitation. Figure 8.9 shows the normalized average fluorescence intensity recorded at different times while the 527 nm laser was exciting with a power of I_L = 1.23 W at 1 kHz. It can be seen that the fluorescence intensity decreases more than 15% within 4 min. This significant photobleaching will cause large inaccuracies in temperature measurements over time if it is not corrected for in the analysis.

To minimize photobleaching the excitation time was reduced during the experiments. As it takes the laser about 5-10 s to stabilize, the maximum excitation time during one measurement was therefore chosen to be 50 s which also allows image recording. In this case, the photobleaching would be less than 5%. In addition, photobleaching can also be reduced by using a flowing sample which will decrease the time it is exposed to the excitation. The low level of photobleaching may explain the slight higher temperature sensitivity under 527 nm high power laser than that detected by the fluorimeter.

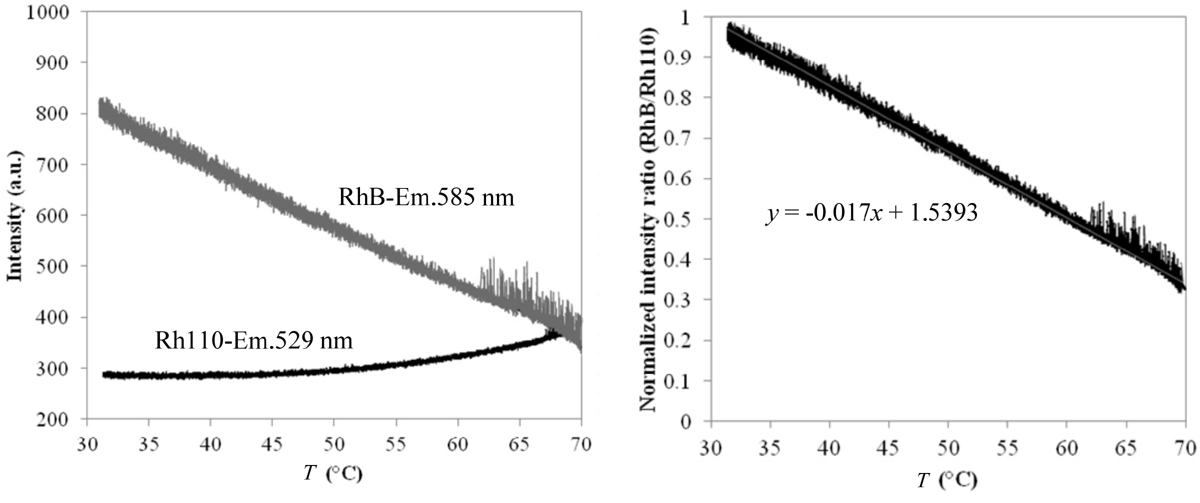

(a) **(b)**

Figure 8.7: **(a)** Variation of fluorescence intensity of PMMA-RhB+Rh110 particles with respect to temperature; and **(b)** Variation of normalized intensity ratio of RhB and Rh110 with respect to temperature.

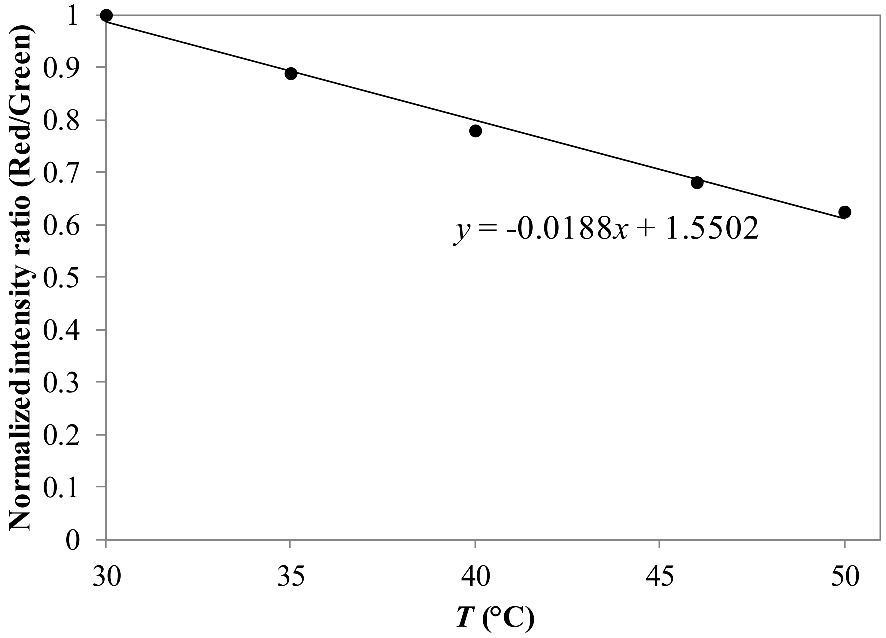

Figure 8.8: Variation of normalized intensity ratio of red and green channels with respect to temperature for PMMA-RhB+Rh110 particles.

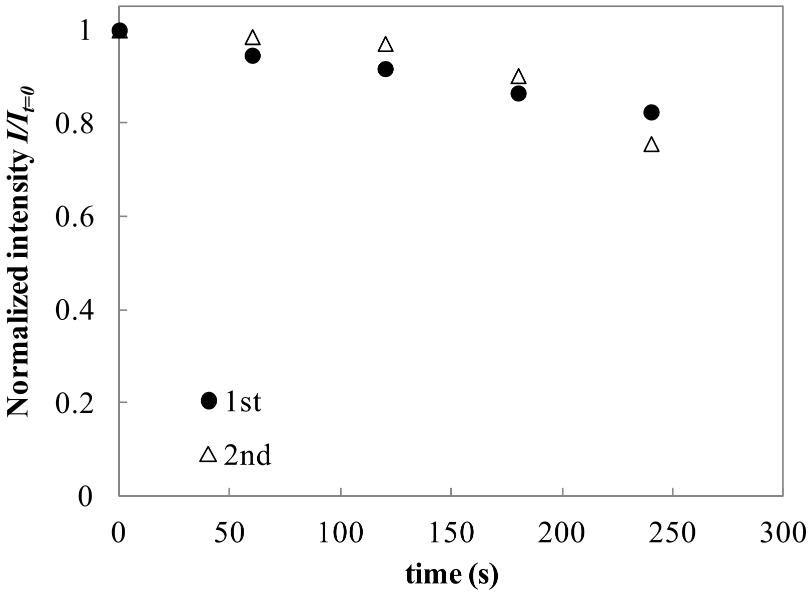

Figure 8.9: Variation of normalized intensity of PMMA-RhB+Rh110 particles with respect to excitation time.

8.3 Image processing: identification of in-focus particles

As the entire volume of fluid is illuminated in micro-PIV/LIF, all of the particles throughout the depth of the flow field will contribute to the resulting particle images. Those particles close to the focal plane (in-focus particles) usually exhibit bright intensity and sharp edge, while particles further from the focal plane (out-of-focus particles) are darker with blurry edge. Out-of-focus particles contribute negatively to the image by effectively varying the particle image size and luminous intensity, reducing the signal-to-noise ratio, and ultimately affecting the temperature and velocity measurements. Therefore, an essential part of using the particles to measure the temperature is to locate the particles and extract the intensity information from the in-focus particle images.

Threshold or contrast enhancement and background subtraction can help to highlight the in-focus particles according to intensities (Lim et al., 2012, Vogt and Stephan, 2012). These methods however may lead to loss of information in the image by eliminating the dark in-focus particles. For example, a particle at high temperature with a well-defined outline, deemed to be an in-focus particle, has a lower intensity than a brighter particle with a blurred outline, regarded as an out-of-focus particle. This means that the particle intensity itself may not be appropriate as a criterion for identifying the in-focus particles, especially when a temperature difference exists in the measurement plane. Kim and Yoo (2008) used the slope of the image-intensity gradient as a criterion to select particles with well-defined outlines as a particle with well-defined outline has a steeper slope than that of particle with blurred outline. In Vogt and Stephan (2012), the in-focus particles were detected using a threshold filter and all detected objects were checked for roundness and size to remove objects that do not show the form and dimensions of a typical particle.

In this study, the ImageJ software (NIH, Bethesda, MD) which is an open source image analysis package was used to process the particle images and identify in-focus particles. For the particle images taken at a given focal plane, an image threshold was automatically set using an iterative procedure based on the isodata algorithm (Lim et al., 2012). A specific size and circularity filter were applied based on the typical dimensions of the in-focus particles. The particle analysis technique generated a table of potential in-focus particles. All particles were marked in the set of images and referenced numerically in the table, and each particle was characterized based on a user-defined set of parameters (e.g., *x-y* coordinates, particle area, circularity, channel, max, min and mean signal intensities). The particle coordinates and intensities of the red and green channels were imported into Matlab for conversion into temperature and data presentation. The image analysis procedures were written in an ImageJ macro and Matlab code to provide fast and quantitative analysis of particle image data.

8.4 Uncertainties

The above discussed TSPs development and image processing technique allow for the global mapping of the temperature distribution within a fluid flow. The uncertainty in temperature measurement using the two-dye TSPs (PMMA-RhB+Rh110) by the present micro-LIF setup was evaluated from the experimental data taken in a uniform temperature field by comparing the temperature measured by the TSPs and that by a RTD sensor.

Figure 8.10 shows the instantaneous fluorescent particle images and the corresponding temperature maps at 30 °C and 46 °C. The particles were picked up with outlines marked in red using the image processing technique descried in Section 8.3. As seen in Figure 8.10, the fluorescent intensities of the particles are very uniform and decrease with increasing temperature. Very uniform temperature fields were obtained with big disparity coming from aggregate particles and very dim particles. The standard deviation of the temperature evaluated from individual particles are 2.5 °C and 2.4 °C for the 30 °C and 46 °C temperature fields, respectively. It should be mentioned that the low seeding density resulted in pixel areas with a lack of valid temperature data in the single shot images. A higher seeding density or a larger sample would be required to produce a temperature field with higher resolution and accuracy.

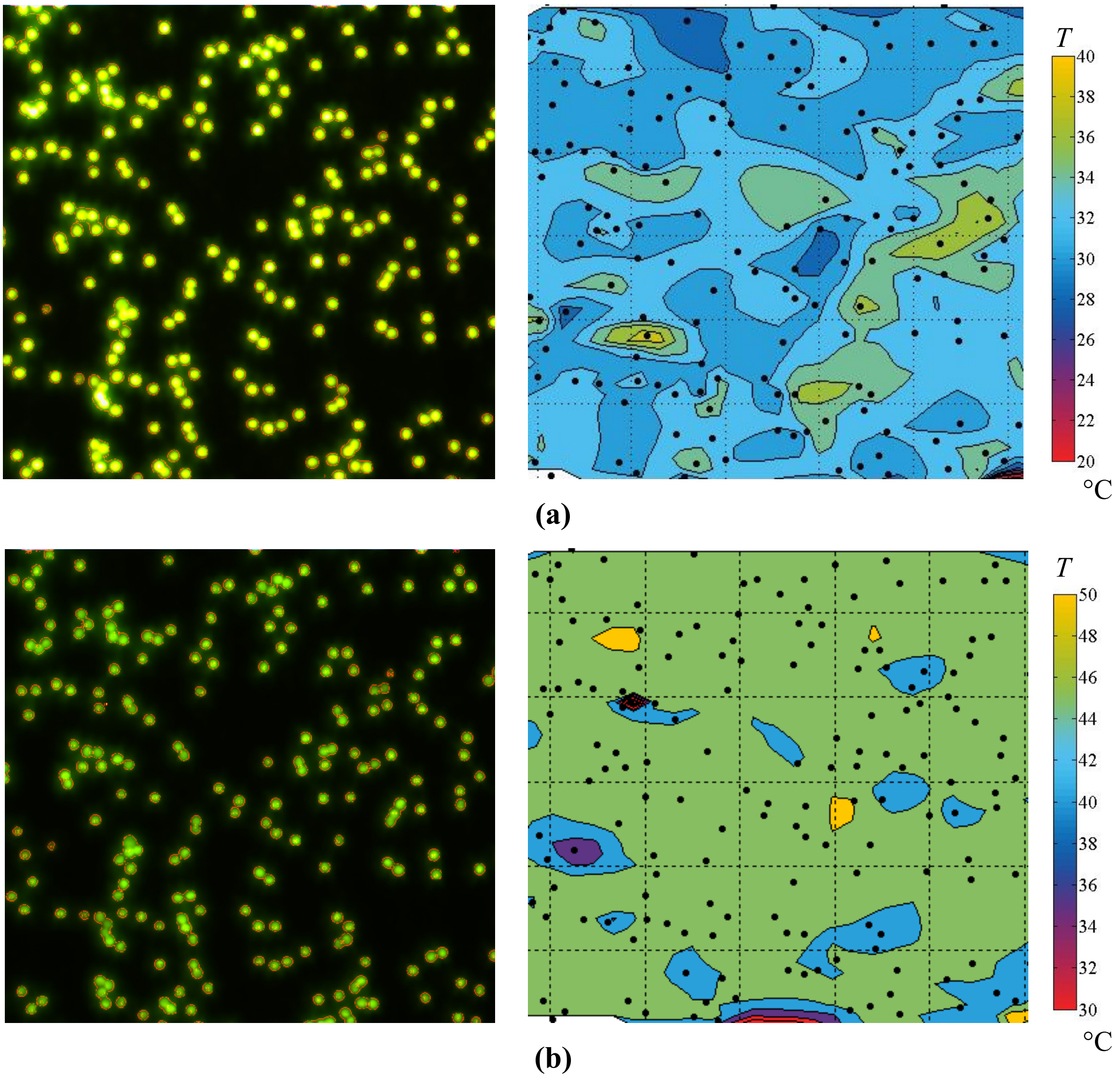

Figure 8.10: Instantaneous fluorescent particle images (left) and the corresponding temperature maps (right) at: **(a)** 30 °C; and **(b)** 46 °C.

It is apparent from Figure 8.10 that large uncertainties are encountered when the temperature is measured from individual TSPs. Vogt and Stephan (2012) found that the temperature measured from the particles showed significant variance. Their technique using particles labelled with EuTTA showed an uncertainty ranging from ±1.6 to ±9.4 °C (depending on the averaging performed) which is at least ten times higher than the uncertainty reported for LIF measurements using dissolved dyes (Sakakibara and Adrian, 2004, Natrajan and Christensen, 2009). This high measurement uncertainty can be attributed to the low temperature sensitivity and poor photostability (photobleaching) of the particles. The measurement uncertainty is also partially attributed to statistical errors that can be minimized by averaging over many images, but with the price of reduction in spatial resolution.

Notwithstanding these results, the use of TSPs for temperature measurements is affected by problems such as limited long-term stability, undesired and unpredictably effects of surface chemistry, irreversible dye degradation, and small signal changes with temperature. To use this technique quantitatively, several challenges have to be overcome including the right choice of labelled fluorescent dyes, the selection of proper polymer matrices and calibration of the fluorescent signal and the system, etc. There is still a large potential to improve these new fluorescent microparticles for the purpose of temperature measurements.

8.5 Simultaneous measurement of temperature and velocity

As mentioned in the literature review presented in Chapter 2, various studies have been carried out to develop effective techniques for whole-field, simultaneous velocity and temperature measurements. In this study, the developed TSPs which are labelled with two dyes can be used as temperature indicators, as well as PIV tracers. Both the temperature and velocity can be obtained from the particle images captured by a colour camera at the focal plane. Figure 8.11 shows the flowchart for the simultaneous measurement of temperature and velocity. The colour images are split into three channels (R, G and B). The particle intensities in the red and green channels are used for ratiometric temperature measurement, while the position of the particles in two sequential images demonstrate the velocity distribution at the same instant by means of the standard PIV. The PIV analysis is carried out using greyscale images converted from the colour images. Three-dimensional temperature and velocity distributions can be reconstructed through the sliced measurement planes while shifting the focal plane of the objective.

In the study of Funatani et al. (2004), simultaneous measurement was achieved by adding tracer particles to the fluorescent dye solution. However, the particles would deteriorate the accuracy of temperature measurement by influencing the fluorescence intensity used for temperature calculation if they cannot be filtered out from the LIF images. Attention has to be paid to the optimum concentration ratio of the dyes corresponding to the amount of tracer particles for the velocity measurement. This problem can be overcome by the application of TSPs without extra tracer particles. The PIV analysis can be applied on any channel image or greyscale image. In this case, a high-speed colour camera may be need to be synchronized with the high-speed laser for PIV measurements. With the aid of a high-speed camera, the technique could be extended with potential application in the study of transient systems.

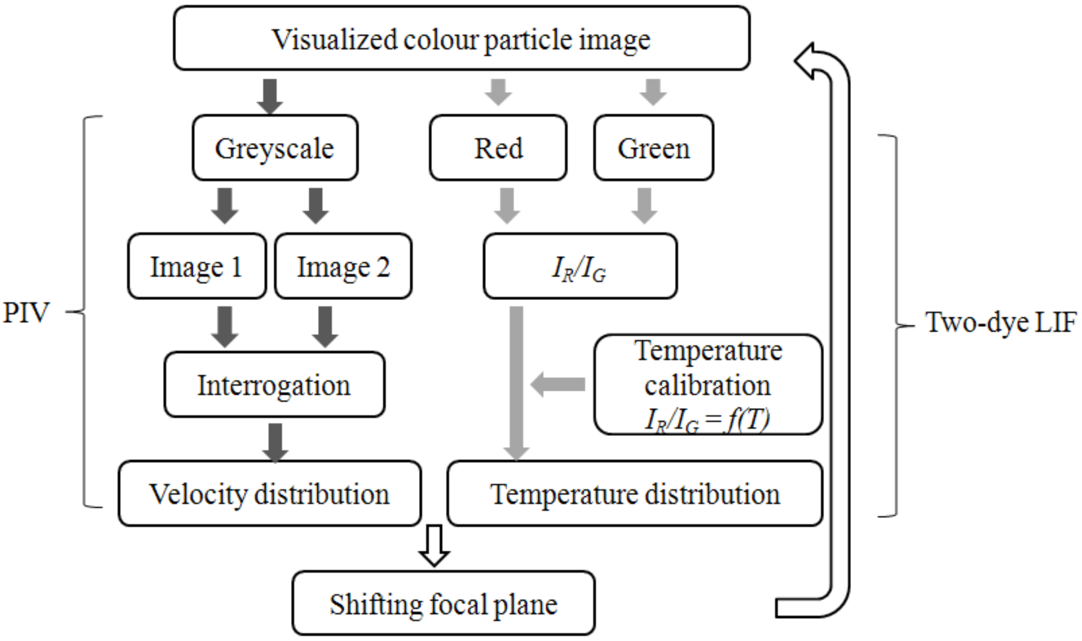

Figure 8.11: Flowchart of simultaneous measurement of temperature and velocity using TSPs.

The pco.edge scientific CMOS camera used in the present study has a frame rate of 100 fps at full resolution of 2560 × 2160 pixels and 450 fps at a reduced resolution of 640 × 480 pixels. However, it is not able to be synchronized with the high-speed laser (usually 1 kHz) in the present setup. Before purchasing a new high-speed colour camera, the simultaneous measurement can be achieved by using two detection systems alternatively. The particles can be imaged by two cameras: a colour camera for LIF and a monochrome camera (high-speed) for PIV. The colour images taken by the colour camera will be used for temperature measurements while the greyscale images captured by the monochrome camera will be processed to measure velocities, as in the standard micro-PIV. The two LIF and PIV cameras are brought to observe the same field-of-view by means of beam splitter optics and geometrical calibration.

Finally, it has to be mentioned that all examined concepts and techniques in this study can easily be transferred and adapted to other LIF methods where the LIF signal represents, e.g., species concentration, pressure, pH etc. with the potential to broaden the insight for a wide range of dynamic processes.

8.6 Summary

Temperature sensitive particles (TSPs) were proposed with promising characteristics for local temperature measurement and the capability for simultaneous measurement of temperature and velocity fields in microscale systems. One-dye particles made of different polymers and labeled with different dyes were prepared and the temperature sensitivity was examined by both the fluorimeter and micro-LIF system. The temperature sensitivity study showed that most of the particles lost their thermal sensitivity compared with their free counterparts in solution. Of the various TSPs fabricated and tested, the best results were achieved with PS-RhB particles with a temperature sensitivity of –2.72%/°C and –1.29%/°C for spectroscopy and micro-LIF studies, respectively.

Two-dye particles labelled with RhB and Rh110 have been successfully fabricated by collaborators through Layer-by-Layer technology. The calibration showed that a temperature sensitivity of –1.88%/°C could be obtained using the present micro-LIF system.

An image processing technique was developed for identification of the in-focus particles and extraction of quantitative temperature information from particle images. The temperature measurement using the two-dye particles under uniform temperature fields has proved the applicability of the present technique to the measurement of temperature. The uncertainties were found to be 2.5 °C for a single shot image analysis.

The application of TSPs in the micro-PIV/LIF system with a colour camera provides a simple and convenient system to process the particle images into instant whole-field velocity and temperature maps. Simultaneous measurement of temperature and velocity can be achieved using a one colour camera system or two-camera system. The TSPs development and corresponding imaging processes will be beneficial for the study of detailed thermohydraulics of micro-devices. Particles with high temperature sensitivity and photostability are still required to obtain reliable and high accuracy data for temperature measurements.

Chapter 9

Conclusions and Recommendations

This thesis presented a comprehensive experimental study of the hydrodynamics and heat transfer characteristics of single-phase flow in tortuous microchannels. With the aid of advanced experimental techniques, the thermohydraulic performance of the various channels was presented, making an important contribution to the validation of the computational models and engineering design of compact heat exchangers. The high quality experimental data collected through non-intrusive optical techniques fill an important gap in the field by bringing new insights into the thermohydraulics of wavy passages. The techniques developed in this thesis would be beneficial for the study of the detailed temperature and velocity fields in various micro-devices. This chapter summarizes the conclusions drawn from this work and provides recommendations for future research in the field.

9.1 Conclusions

9.1.1 Experimental design

1. Test section

Flow visualisation and heat transfer measurements are required to understand the thermohydraulic characteristics of tortuous channels. “Hybrid test sections” which are suitable to carry out experimental work for both purposes were designed and manufactured. The test sections were constructed by milling semi-circular channels in Kovar plates and anodically bonding Pyrex glass on to the plate to provide a high quality seal and good optical access for visualisation. These materials have very similar coefficients of thermal expansion, meaning that the test sections could be heated without breaking the seal. The heating was supplied by an electrical thermofoil heater fixed to the back of the metal plate. The design of using a flat optical surface prevented the optical distortion associated with the use of a curved geometry. A key conclusion of this thesis is that this technique is feasible and provides channels that can be heated and provide good optical access.

2. Micro-PIV technique

A high-speed micro-Particle Image Velocimetry (micro-PIV) system was applied to measure the whole-field two-dimensional velocity distributions. Whole-volume velocity measurements in a three-dimensional domain were achieved through scanning-based visualisation technique and image processing. The technique was validated by comparing the time-averaged velocity profiles with the simulation results in both straight and wavy microchannels, showing that detailed velocity profiles could be obtained with high accuracy in most regions of the flow, except near the wall region.

A three-dimensional reconstruction technique was developed using the present two-dimensional PIV data and the continuity equation. Three-dimensional maps of the complex flow, including the identification and localization of vortical structures (Dean vortices) in wavy microchannels were obtained.

The time-resolved capabilities of the micro-PIV system were demonstrated by recording velocity fluctuations over time, which was validated by determining the Reynolds number for the transition to turbulence in a straight channel. High sampling rate data measurements (up to 3,000 Hz) were used to study the transient behaviour in wavy channels using the high-speed camera associated with the micro-PIV system.

3. Pressure drop measurements

To evaluate the frictional pressure drops in wavy channels more accurately, the additional pressure losses due to the inlet and outlet effects were taken into account by calculating the additional losses using a straight channel. Measured data were in very good agreement with computed pressure losses obtained from CFD simulations.

9.1.2 Numerical methodology

A numerical methodology was developed to simulate steady flow and heat transfer in test sections identical to those used in the present experiments. A complete model including the whole length of the channel (*n* repeating units together with the inlet and outlet sections for wavy channels), Kovar and glass substrates was applied to solve the conjugate heat transfer involved in the current experimental design. The conservation equations were solved using the ANSYS CFX code with the necessary boundary conditions to simulate the experimental setup.

The three-dimensional conjugate simulations enabled the complex thermal behaviour of the experiments to be understood and interpreted. It was found that the conjugate effects in microchannels induced non-uniform temperature and heat flux distributions at the channel wall. In the present study the microchannels did not correspond strictly to any standard thermal boundary condition for laminar flow even though the perimeter-averaged wall heat flux in the heating zone is approximately constant.

9.1.3 Thermohydraulic performance of wavy microchannels

Investigations have been made into the thermohydraulic characteristics of single-phase flow in channels following zigzag and sinusoidal channels. Comprehensive flow visualisation using the micro-PIV technique and heat transfer experiments were performed in five tortuous channels with various geometries for a wide range of Reynolds number ($50 < Re < 900$). Three-dimensional conjugate simulations were carried out for the corresponding experimental conditions to validate the experimental approaches and to provide data to compare with experimental results.

1. Onset of unsteadiness

The time-resolved velocity measurements have revealed a transition from a steady flow to a time-dependent oscillatory flow having a dominant frequency and subsequently to a complex transient flow in both zigzag and sinusoidal channels. It was observed that the flow transition from steady to unsteady flow occurred at a relatively low Reynolds number in the laminar regime compared with that in a straight channel. The critical Reynolds number (Re_c) for the onset of unsteadiness (or the onset of oscillatory flow) depended on the channel geometry. A detailed study in a zigzag channel with geometric parameters of $R_c/d = 0.51$, $L/d = 1.75$, and $\theta = 45°$ revealed that unsteadiness first appeared at the end of the channel and moved upstream with increasing Reynolds number.

Experimental results showed that transition to a transient flow occurred at much lower Reynolds numbers than predicted numerically. Time-dependent flow was observed in the experiments over the range of Reynolds number where steady chaotic advection (the flow pattern was still steady but not spatially periodic) occurred in previous simulations of the same geometry (Zheng, 2013). However, it was observed that in the experiments the inlet flow was never completely steady, possibly explaining this early transition. Simulations that introduced fluctuating inlet boundary conditions demonstrated a similar early transition to unsteady flow. It revealed that the flow was very sensitive to the inlet conditions at a high enough Reynolds number, and small fluctuations can trigger transient behaviour.

2. Oscillatory flow

An interesting phenomenon observed in the experiments was the sustained oscillatory flows in the wavy channels. Periodic or quasi-periodic flow oscillation occurred before the flow became transient with the critical Reynolds number and the dominant frequency depending on the channel geometry. A possible reason for this was proposed to be the unsteadiness of Dean vortices being trigged by the small disturbances from the inlet.

3. Heat transfer enchantment and pressure-drop penalty

The thermohydraulic performance of the wavy channels was examined in terms of heat transfer enhancement and relative pressure-drop penalty, the values of which were calculated as the ratio of Nusselt numbers and pressure drops, respectively, to those in equivalent straight channels. The results are summarised by the following points:

- Significant heat transfer enhancement was achieved in wavy channels albeit accompanied by increased pressure-drop penalty. For the zigzag channel with geometric parameters of $R_c/d = 0.51$, $L/d = 1.75$, and $\theta = 45°$ and a thermal boundary condition representative of that achieved in the present study, the heat transfer rate was 6.1 times that in a straight channel, while the pressure drop increased by a factor of 7 at $Re = 728$. Both the heat transfer enhancement and pressure-drop penalty increased with increasing Reynolds number, although the heat transfer enhancement levels significantly exceeded the pressure-drop penalty levels for most channels considered in this thesis. The heat transfer enhancement exceeded the relative pressure-drop penalty by a factor as large as 2.1 for a sinusoidal channel with $A/L = 0.5$ and $L/d = 3.5$ at $Re = 400$.
- The underlying physical mechanism of the heat transfer enhancement was revealed by the detailed flow dynamics study, which showed that the flow recirculation and secondary flow structures (Dean vortices) present at the bend section helped to increase the heat transfer rates by constantly disrupting the thermal boundary layer. The intensities of the secondary flow and/or recirculation increased with Reynolds number, leading to further heat transfer enhancement.

- The flow and heat transfer characteristic of wavy channels were affected greatly by geometrical parameters. Higher bend angle (*θ)* or amplitude to half-unit length ratio (*A/L*) generally lead to increased heat transfer enhancement, as well as a relatively greater friction factor increase. Flow visualisation revealed that the recirculation size and strength were bigger in channels with higher *θ* or *A/L* values compared with the channels with lower values.

  It was found that zigzag geometries were prone to the generation of recirculation zones, while the sinusoidal geometry was remarkably resistant to flow separations. However, the heat transfer performance of the sinusoidal channels was as good as the corresponding zigzag channel (with the same amplitude and half-unit length), while the pressure drop was smaller in the sinusoidal channels. Close investigation showed that the high heat transfer enhancement at the expense of low pressure-drop penalties was caused by the absence of recirculation formation and the presence of Dean vortices that enhanced cross-sectional mixing without incurring great pressure drop.
- The pressure-drop penalty obtained from experiments agreed very well with the simulation values. Reasonably good agreement between the experimental Nusselt numbers and simulation predictions was also achieved using the present apparatus and experimental approaches, despite the difficulties in temperature measurements and conjugate problems involved in the present test sections.

4. Stackability and heat transfer intensification

The channel geometries were evaluated from the point of view of stackability on a plate structure with the interest of their usage in compact heat exchangers. A heat transfer intensification factor, which quantifies the improvement in heat transfer rate for a plate by using a tortuous geometry compared with using straight channels, was used to access the effects of the tortuosity of the channel. It was found that, overall, the best performing channels were those with zigzag pathways which provide both significant heat transfer enhancement and good stackability. Sinusoidal channels cannot utilise the plate very efficiently due to their poor stackability, although they provide equivalent heat transfer enhancement as the corresponding zigzag channels. Therefore zigzag channels are a preferred design option.

9.1.4 Non-intrusive temperature measurement

True insight into thermohydraulics of wavy microchannel must be achieved through detailed velocity and temperature information. However, measurement of the temperature fields in fine passages poses specific challenges due to the small channel dimensions and three-dimensional characteristics. In this thesis, an experimental method for non-intrusive temperature measurement in fluid flow was developed based on Laser Induced Fluorescence (LIF).

A novel two-dye LIF technique was developed by choosing two fluorescent dyes with different temperature sensitivities (Kiton Red and Rhodamine 110), and using a colour camera with a colour enhancement filter. The advantages of this system include the simplicity of setup by using a colour camera instead of two monochrome cameras, and higher accuracy obtained by taking the pixel by pixel ratio of the intensity values of two channels from one camera to compensate for fluctuations of incident light and variations of optical system. The introduction of the colour enhancement filter (XB30) was shown to effectively reduce the spectral conflicts and significantly improve the overall temperature sensitivity. A maximum sensitivity of 2.2%/°C was achieved at C_{KR}/CR_{Rh110} = 1 with the colour enhancement filter versus 1.6%/°C without using the filter.

The capability of this technique was verified through its applications in fluid temperature measurements in single-phase flow and Taylor flow in semi-circular microchannels. A detailed comparison of experimental measurements and numerical results indicated that the measured temperature corresponded to a depth-averaged value with the entire channel volumetrically illuminated, suggesting that micro-LIF with volume illumination has a poor spatial resolution along the optical axis. However, this technique served as a way to measure the bulk temperature with reasonably good accuracy (within 1 °C).

This technique provided a better estimation of film temperature in the bubble region of Taylor flow, where the temperature variation is negligible, while for slug temperatures the use of this technique was still limited to the depth-averaged values. The film temperature also provided a reasonable estimation of the wall temperature due to the small temperature difference between them in Taylor flow. The use of the high-speed pulsed laser and high-speed camera provided the ability to acquire temporally-resolved measurements. These results would be helpful for the development of Taylor flow models and verification of numerical simulations, which is important for a better understanding of the Taylor flow heat transfer mechanisms.

9.1.5 Simultaneous measurement of velocity and temperature

Temperature sensitive particles (TSPs) based on the two-dye LIF technique were developed to increase the depth-wise resolution of the micro-LIF technique. Two-dye particles labelled with RhB and Rh110 were successfully fabricated by collaborators through Layer-by-Layer technology. A temperature sensitivity of –1.88%/°C was obtained using the present micro-LIF system. An image processing technique was developed for identification of the in-focus particles and extraction of quantitative temperature information from particle images. Preliminary tests in uniform temperature fields showed that the temperature measurement using the two-dye particles could be achieved with uncertainties of 2.5 °C for a single shot image analysis. Since the TSPs could be used as both temperature indicators and flow tracers, simultaneous measurement of temperature and velocity could therefore be achieved by combining the two-dye LIF and PIV.

9.2 Recommendations for future work

While this thesis has made an important contribution to the understanding of the hydrodynamics and heat transfer in tortuous passages, there are areas that require further investigation. Suggestions for future work are given below.

9.2.1 Measurements of local temperature and local heat transfer rate

- Two-dye temperature sensitive particles have been developed and manufactured in this thesis. However, uncertainty arising from photobleaching is still a big concern for temperature measurements. Development of particles with higher temperature sensitivity and photostability is crucial for further study.
- Application of the temperature sensitive particles for the measurement of local temperature or three-dimensional temperature field in wavy microchannels would be the next step to obtain the local heat transfer rate and thus a greater understanding of the detailed thermal performance of wavy microchannels.
- Although the present experimental system provides the capability for simultaneous measurement of velocity and temperature, the present flow visualisation and heat

transfer experiments were carried out separately before the development of the temperature sensitive particles. To link the velocity and temperature distributions via simultaneous study would provide an important step for better understanding of the transport phenomenon and fundamental mechanisms for heat transfer enhancement in tortuous channels.

9.2.2 Oscillatory flow

In tortuous channels, it was found in the experimental work that oscillatory flow, instead of steady chaotic predicted by CFD, occurs before the flow becomes transient. A further investigation of the oscillatory flow is needed to identify the fundamental mechanisms. Given that the inlet flow is never completely steady in experiments, simulations with introduced fluctuating inlet boundary conditions are worthwhile due to its practical relevance. The effect of random disturbance on flow behaviour in wavy channels, especially in the chaotic regime may be of importance in controlling the onset of unsteady flow and is worthy of analysis.

9.2.3 Turbulent flow

This thesis studied the flow and heat transfer in wavy channels for Reynolds numbers up to 1,000. There is an apparent interest to continue this to higher Reynolds numbers, from transient unsteady to fully turbulent flow. Since turbulent simulations are potentially computationally very expensive (if a wide range of turbulence scales are to be resolved rather than modelled) and different models have their own limitations, it would be valuable to carry out experiments in the turbulent regime. With the help of experimental feedback, it would be possible to validate the turbulence models and introduce necessary modifications to numerical codes.

9.2.4 Test section

Complex conjugate problem in the microchannels with heat sink brings difficulties for heat transfer measurements. Test sections with higher thermal conductivity (e.g. silicon), smaller thickness and relatively smaller width might be of preference for further study of heat transfer. In addition, experimental technique which can measure the wall surface temperature with higher resolution and accuracy could be valuable to develop local heat transfer correlations in geometries that include the effects of thermal coupling at these small scales.

9.2.5 Multiphase flow

The flow in micro-structured devices can be single phase gas or liquid flow or a multiphase flow, for example, gas-liquid, liquid-liquid and flow boiling. It has been shown that the mixing and therefore heat transfer rate is enhanced in two-phase flow and boiling flow compared with that for fully-developed laminar single-phase flow (Leung et al., 2010, Asadolahi et al., 2011, Gupta et al., 2013, Liu et al., 2013). Since heat transfer enhancement is also achieved in wavy channels, it would be interesting to examine the effect of curvature for the Taylor flow regime and flow boiling, as in this geometry flow mixing caused by Dean vortices would be added to that already brought by multiphase flow. The test section design and experimental techniques developed in this thesis would provide important tools for this investigation.

References

Adams, T. M., Abdel-Khalik, S. I., Jeter, S. M. & Qureshi, Z. H. 1998. An experimental investigation of single-phase forced convection in microchannels. *International Journal of Heat and Mass Transfer,* 41**,** 851-857.

Adrian, R. J. & Westerweel, J. 2011. *Particle image velocimetry* New York: Cambridge University Press.

Ahmad, T. & Hassan, I. 2010. Experimental analysis of microchannel entrance length characteristics using microparticle image velocimetry. *Journal of Fluids Engineering-Transactions of the ASME,* 132**,** 041102.

Amon, C. H., Guzman, A. M. & Morel, B. 1996. Lagrangian chaos, Eulerian chaos, and mixing enhancement in converging-diverging channel flows. *Physics of Fluids,* 8**,** 1192-1206.

Anxionnaz-Minvielle, Z., Cabassud, M., Gourdon, C. & Tochon, P. 2013. Influence of the meandering channel geometry on the thermo-hydraulic performances of an intensified heat exchanger/reactor. *Chemical Engineering and Processing: Process Intensification,* 73**,** 67-80.

Aref, H. 1984. Stirring by chaotic advection. *Journal of Fluid Mechanics,* 143**,** 1-21.

Aref, H. 2002. The development of chaotic advection. *Physics of Fluids,* 14**,** 1315-1325.

Asadolahi, A. N., Gupta, R., Fletcher, D. F. & Haynes, B. S. 2011. CFD approaches for the simulation of hydrodynamics and heat transfer in Taylor flow. *Chemical Engineering Science,* 66**,** 5575-5584.

Asadolahi, A. N., Gupta, R., Leung, S. S. Y., Fletcher, D. F. & Haynes, B. S. 2012. Validation of a CFD model of Taylor flow hydrodynamics and heat transfer. *Chemical Engineering Science,* 69**,** 541-552.

Asthana, A., Zinovik, I., Weinmueller, C. & Poulikakos, D. 2011. Significant Nusselt number increase in microchannels with a segmented flow of two immiscible liquids: An experimental study. *International Journal of Heat and Mass Transfer,* 54**,** 1456-1464.

Barz, D. P. J., Zadeh, H. F. & Ehrhard, P. 2008. Laminar flow and mass transport in a twice-folded microchannel. *Aiche Journal,* 54**,** 381-393.

Basabe-Desmonts, L., Reinhoudt, D. N. & Crego-Calama, M. 2007. Design of fluorescent materials for chemical sensing. *Chemical Society Reviews,* 36**,** 993-1017.

Basu, B. J. & Venkatraman, S. 2009. Fabrication of a Bi-luminophore temperature sensitive coating by embedding Europium thenoyltrifluoroacetonate (EuTTA) and Perylene in polystyrene. *Journal of Fluorescence,* 19**,** 479-485.

Bogild, M. R., Poulsen, J. L., Rath, E. Z., Sorensen, H. & Iop 2012. Investigation of heat transfer in mini channels using Planar Laser Induced Fluorescence. *6th European Thermal Sciences Conference.*

Bottausci, F., Mezic, I., Meinhart, C. D. & Cardonne, C. 2004. Mixing in the shear superposition micromixer: three-dimensional analysis. *Philosophical Transactions of the Royal Society a-Mathematical Physical and Engineering Sciences,* 362**,** 1001-1018.

Bown, M. R., MacInnes, J. M. & Allen, R. W. K. 2007. Three-component micro-PIV using the continuity equation and a comparison of the performance with that of stereoscopic measurements. *Experiments in Fluids,* 42**,** 197-205.

Briand, D., Weber, P. & de Rooij, N. F. 2004. Bonding properties of metals anodically bonded to glass. *Sensors and Actuators A: Physical,* 114**,** 543-549.

Celata, G. P., Cumo, M., Marconi, V., McPhail, S. J. & Zummo, G. 2006. Microtube liquid single-phase heat transfer in laminar flow. *International Journal of Heat and Mass Transfer,* 49**,** 3538-3546.

Chamarthy, P., Garimella, S. V. & Wereley, S. T. 2009. Non-intrusive temperature measurement using microscale visualization techniques. *Experiments in Fluids,* 47**,** 159-170.

Chamarthy, P., Garimella, S. V. & Wereley, S. T. 2010. Measurement of the temperature non-uniformity in a microchannel heat sink using microscale laser-induced fluorescence. *International Journal of Heat and Mass Transfer,* 53**,** 3275-3283.

Chang, S. M., Humphrey, J. A. C. & Modavi, A. 1983. Turbulent-flow in a strongly curved U-bend and downstream tangent of square cross-sections. *Physicochemical Hydrodynamics,* 4**,** 243-269.

Cheng, K. C., Lin, R. C. & Ou, J. W. 1976. Fully developed laminar flow in curved rectangular channels. *Trans. ASME C: J . Fluids Engineering,* 98**,** 41-48.

Cheng, K. C., Mok, S.Y. 1986. Flow visualization studies on secondary flow patterns and centrifugal instability phenomena in curved tubes. *Fluid Control and Measurement,* 2**,** 765-733.

Chintada, S., Ko, K. H. & Anand, N. K. 1999. Heat transfer in 3-D serpentine channels with right-angle turns. *Numerical Heat Transfer: Part A: Applications,* 36**,** 781-806.

Choi, J. M. & Anand, N. K. 1993. Heat transfer in a serpentine channel with a series of right-angle turns. *Numerical Heat Transfer: Part A: Applications,* 23**,** 189-210.

Choi, J. M. & Anand, N. K. 1995. Turbulent heat transfer in a serpentine channel with a series of right-angle turns. *International Journal of Heat and Mass Transfer,* 38**,** 1225-1236.

Choi, S. B., Barron, R. F. & Warrington, R. O. Fluid flow and heat transfer in microtubes. ASME DSC, 1991. 123-134.

Christensen, K. T. 2004. The influence of peak-locking errors on turbulence statistics computed from PIV ensembles. *Experiments in Fluids,* 36**,** 484-497.

Comini, G., Croce, G. & Nonino, C. 2004. Modeling of convection enhancement mechanisms. *International Journal of Numerical Methods for Heat and Fluid Flow,* 14**,** 66-84.

Comini, G., Nonino, C. & Savino, S. 2002. Convective heat and mass transfer in wavy finned-tube exchangers. *International Journal of Numerical Methods for Heat & Fluid Flow,* 12**,** 735-755.

Coolen, M. C. J., Kieft, R. N., Rindt, C. C. M. & van Steenhoven, A. A. 1999. Application of 2-D LIF temperature measurements in water using a Nd : YAG laser. *Experiments in Fluids,* 27**,** 420-426.

Coppeta, J. & Rogers, C. 1998. Dual emission laser induced fluorescence for direct planar scalar behavior measurements. *Experiments in Fluids,* 25**,** 1-15.

Dabiri, D. 2009. Digital particle image thermometry/velocimetry: a review. *Experiments in Fluids,* 46**,** 191-241.

Dabiri, D. & Gharib, M. 1991. Digital particle image thermometry: The method and implementation. *Experiments in Fluids,* 11**,** 77-86.

Dean, W. R. 1928. Fluid motion in a curved channel. *Proceedings of the Royal Society of London Series a-Containing Papers of a Mathematical and Physical Character,* 121**,** 402-420.

Dennis, S. C. R. & Ng, M. 1982. Dual solutions for steady laminar-flow through a curved tube *Quarterly Journal of Mechanics and Applied Mathematics,* 35**,** 305-324.

Dunand, P., Castanet, G. & Lemoine, F. 2012. A two-color planar LIF technique to map the temperature of droplets impinging onto a heated wall. *Experiments in Fluids,* 52**,** 843-856.

Elsinga, G. E., Scarano, F., Wieneke, B. & van Oudheusden, B. W. 2006. Tomographic particle image velocimetry. *Experiments in Fluids,* 41**,** 933-947.

Estrada-Perez, C. E., Hassan, Y. A. & Tan, S. C. 2011. Experimental characterization of temperature sensitive dyes for laser induced fluorescence thermometry. *Review of Scientific Instruments,* 82**,** 074901.

Eustice, J. 1910. Flow of water in curved pipes. *Proceedings of the Royal Society of London Series A,* 84**,** 107-118.

Eustice, J. 1911. Experiments on stream-line motion in curved pipes. *Proceedings of the Royal Society of London Series A,* 85**,** 119-131.

Fedorov, A. G. & Viskanta, R. 2000. Three-dimensional conjugate heat transfer in the microchannel heat sink for electronic packaging. *International Journal of Heat and Mass Transfer,* 43**,** 399-415.

Finlay, W. H., Keller, J. B. & Ferziger, J. H. 1988. Instability and transition in curved channel flow. *Journal of Fluid Mechanics,* 194**,** 417-456.

Fischer, L. H., Karakus, C., Meier, R. J., Risch, N., Wolfbeis, O. S., Holder, E. & Schaeferling, M. 2012. Referenced dual pressure- and temperature-sensitive paint for digital color camera read out. *Chemistry-A European Journal,* 18**,** 15706-15713.

Fogg, D., David, M. & Goodson, K. E. 2009. Non-invasive measurement of void fraction and liquid temperature in microchannel flow boiling. *Experiments in Fluids,* 46**,** 725-736.

Foong, A. J. L., Ramesh, N. & Chandratilleke, T. T. 2009. Laminar convective heat transfer in a microchannel with internal longitudinal fins. *International Journal of Thermal Sciences,* 48**,** 1908-1913.

Fouilland, T. S. 2008. *Micro-PIV measurement and modelling of Gas-Liquid flows in microchannels.* PhD Thesis, The University of Sydney.

Fouras, A., Lo Jacono, D., Nguyen, C. V. & Hourigan, K. 2009. Volumetric correlation PIV: a new technique for 3D velocity vector field measurement. *Experiments in Fluids,* 47**,** 569-577.

Fujisawa, N. & Funatani, S. 2000. Simultaneous measurement of temperature and velocity in a turbulent thermal convection by the extended range scanning liquid crystal visualization technique. *Experiments in Fluids,* 29**,** S158-S165.

Fujisawa, N., Funatani, S. & Watanabe, Y. 2008. Simultaneous imaging techniques for temperature and velocity fields in thermal fluid flows. *Journal of Visualization,* 11**,** 247-255.

Fukagata, K., Kasagi, N., Ua-arayaporn, P. & Himeno, T. 2007. Numerical simulation of gas-liquid two-phase flow and convective heat transfer in a micro tube. *International Journal of Heat and Fluid Flow,* 28**,** 72-82.

Funatani, S., Fujisawa, N. & Ikeda, H. 2004. Simultaneous measurement of temperature and velocity using two-colour LIF combined with PIV with a colour CCD camera and its application to the turbulent buoyant plume. *Measurement Science & Technology,* 15**,** 983-990.

Gallery, J., Gouterman, M., Callis, J., Khalil, G., McLachlan, B. & Bell, J. 1994. Luminescent thermometry for aerodynamic measurements. *Review of Scientific Instruments,* 65**,** 712-720.

Gao, P., Le Person, S. & Favre-Marinet, M. 2002. Scale effects on hydrodynamics and heat transfer in two-dimensional mini and microchannels. *International Journal of Thermal Sciences,* 41**,** 1017-1027.

Generalova, A. N., Oleinikov, V. A., Sukhanova, A., Artemyev, M. V., Zubov, V. P. & Nabiev, I. 2013. Quantum dot-containing polymer particles with thermosensitive fluorescence. *Biosens Bioelectron,* 39**,** 187-93.

Geyer, P. E. 2008. *Simulations of laminar and turbulent thermohydraulics in tortuous passages.* PhD Thesis, The University of Sydney.

Geyer, P. E., Fletcher, D. F. & Haynes, B. S. 2007. Laminar flow and heat transfer in a periodic trapezoidal channel with semi-circular cross-section. *International Journal of Heat and Mass Transfer,* 50**,** 3471-3480.

Geyer, P. E., Rosaguti, N. R., Fletcher, D. F. & Haynes, B. S. 2006a. Laminar flow and heat transfer in periodic serpentine mini-channels. *Journal of Enhanced Heat Transfer,* 13**,** 309-320.

Geyer, P. E., Rosaguti, N. R., Fletcher, D. F. & Haynes, B. S. 2006b. Thermohydraulics of square-section microchannels following a serpentine path. *Microfluidics and Nanofluidics,* 2**,** 195-204.

Giron-Palomares, B., Hernandez-Guerrero, A., Romero-Mendez, R. & Oviedo-Tolentino, F. 2009. An experimental analysis of the flow pattern in heat exchangers with an egg carton configuration (parallel, convergent and divergent cases). *International Journal of Heat and Fluid Flow,* 30**,** 158-171.

Gong, L., Kota, K., Tao, W. Q. & Joshi, Y. 2011a. Parametric numerical study of flow and heat transfer in microchannels with wavy walls. *Journal of Heat Transfer-Transactions of the ASME,* 133**,** 051702.

Gong, L., Kota, K., Tao, W. Q. & Joshi, Y. 2011b. Thermal performance of microchannels with wavy walls for electronics cooling. *Ieee Transactions on Components Packaging and Manufacturing Technology,* 1**,** 1029-1035.

Grafsronningen, S. & Jensen, A. 2012. Simultaneous PIV/LIF measurements of a transitional buoyant plume above a horizontal cylinder. *International Journal of Heat and Mass Transfer,* 55**,** 4195-4206.

Guasto, J. S. & Breuer, K. S. 2008. Simultaneous, ensemble-averaged measurement of near-wall temperature and velocity in steady micro-flows using single quantum dot tracking. *Experiments in Fluids,* 45**,** 157-166.

Guasto, J. S., Huang, P. & Breuer, K. S. 2006. Statistical particle tracking velocimetry using molecular and quantum dot tracer particles. *Experiments in Fluids,* 41**,** 869-880.

Gui, L. & Wereley, S. T. 2002. A correlation-based continuous window-shift technique to reduce the peak-locking effect in digital PIV image evaluation. *Experiments in Fluids,* 32**,** 506-517.

Guo, Z. Y. & Li, Z. X. 2003. Size effect on microscale single-phase flow and heat transfer. *International Journal of Heat and Mass Transfer,* 46**,** 149-159.

Gupta, R. 2010. *CFD simulations of gas-liquid flow in microchannels.* PhD Thesis, The University of Sydney.

Gupta, R., Fletcher, D. F. & Haynes, B. S. 2010. CFD modelling of flow and heat transfer in the Taylor flow regime. *Chemical Engineering Science,* 65**,** 2094-2107.

Gupta, R., Geyer, P. E., Fletcher, D. F. & Haynes, B. S. 2008. Thermohydraulic performance of a periodic trapezoidal channel with a triangular cross-section. *International Journal of Heat and Mass Transfer,* 51**,** 2925-2929.

Gupta, R., Leung, S. S. Y., Manica, R., Fletcher, D. F. & Haynes, B. S. 2013. Hydrodynamics of liquid-liquid Taylor flow in microchannels. *Chemical Engineering Science,* 92**,** 180-189.

Guzman, A. M., Beiza, M. P., Diaz, A. J., Fischer, P. F. & Ramos, J. C. 2013. Flow and heat transfer characteristics in micro and mini communicating pressure driven channel flows by numerical simulations. *International Journal of Heat and Mass Transfer,* 58**,** 568-577.

Guzman, A. M. & Del Valle, M. 2006. Heat transfer enhancement in grooved channels due to flow bifurcations. *Heat and Mass Transfer,* 42**,** 967-975.

Hanson, R. K. 1988. Planar Laser-Induced Fluorescence imaging *Journal of Quantitative Spectroscopy & Radiative Transfer,* 40**,** 343-362.

Hardison, D., Deepthike, H. U., Senevirathna, W., Pathirathne, T. & Wells, M. 2008. Temperature-sensitive microcapsules with variable optical signatures based on incorporation of quantum dots into a highly biocompatible hydrogel. *Journal of Materials Chemistry,* 18**,** 5368-5375.

Harms, T. M., Kazmierczak, M. J. & Gerner, F. M. 1999. Developing convective heat transfer in deep rectangular microchannels. *International Journal of Heat and Fluid Flow,* 20**,** 149-157.

Hetsroni, G., Mosyak, A., Pogrebnyak, E. & Rozenblit, R. 2011. Infrared temperature measurements in micro-channels and micro-fluid systems. *International Journal of Thermal Sciences,* 50**,** 853-868.

Hetsroni, G., Mosyak, A., Pogrebnyak, E. & Yarin, L. P. 2005. Heat transfer in micro-channels: Comparison of experiments with theory and numerical results. *International Journal of Heat and Mass Transfer,* 48**,** 5580-5601.

Hetsroni, G., Mosyak, A., Segal, Z. & Ziskind, G. 2002. A uniform temperature heat sink for cooling of electronic devices. *International Journal of Heat and Mass Transfer,* 45**,** 3275-3286.

Hille, P., Vehrenkamp, R. & Schulzdubois, E. O. 1985. The development and structure of primary and secondary flow in a curved square duct. *Journal of Fluid Mechanics,* 151**,** 219-241.

Hishida, K. & Sakakibara, J. 2000. Combined planar laser-induced fluorescence-particle image velocimetry technique for velocity and temperature fields. *Experiments in Fluids,* 29**,** S129-S140.

Hoffacker, K. D., Lugade, A. G. & Terpetschnig, E. 2013. Methods for forming dyed microspheres and populations of dyed microspheres. Google Patents.

Hossain, M. Z. & Islam, A. K. M. S. 2004. Fully developed flow structures and heat transfer in sine-shaped wavy channels. *International Communications in Heat and Mass Transfer,* 31**,** 887-896.

Huang, H., Dabiri, D. & Gharib, M. 1997. On errors of digital particle image velocimetry. *Measurement Science & Technology,* 8**,** 1427-1440.

Huo, X., Chen, L., Tian, Y. S. & Karayiannis, T. G. 2004. Flow boiling and flow regimes in small diameter tubes. *Applied Thermal Engineering,* 24**,** 1225-1239.

Hwang, S. D., Jang, I. H. & Cho, H. H. 2006. Experimental study on flow and local heat/mass transfer characteristics inside corrugated duct. *International Journal of Heat and Fluid Flow,* 27**,** 21-32.

Ichiyanagi, M., Sasaki, S., Sato, Y. & Hishida, K. 2009. Micro-PIV/LIF measurements on electrokinetically-driven flow in surface modified microchannels. *Journal of Micromechanics and Microengineering,* 19**,** 045021.

Ichiyanagi, M., Sato, Y. & Hishida, K. 2007. Optically sliced measurement of velocity and pH distribution in microchannel. *Experiments in Fluids,* 43**,** 425-435.

Ichiyanagi, M., Tsutsui, I., Kakinuma, Y., Sato, Y., Hishida, K. 2012. Three-dimensional measurement of gas dissolution process in gas-liquid microchannel flow *International Journal of Heat and Mass Transfer,* 55**,** 2872-2878.

Incropera, F. P., De Witt, D.P. 1996. *Fundamentals of Heat and Mass Transfer*, Wiley, New York.

Islamoglu, Y. 2008. Effect of rounding of protruding edge on convection heat transfer in a converging-diverging channel. *International Communications in Heat and Mass Transfer,* 35**,** 643-647.

Islamoglu, Y. & Parmaksizoglu, C. 2003. The effect of channel height on the enhanced heat transfer characteristics in a corrugated heat exchanger channel. *Applied Thermal Engineering,* 23**,** 979-987.

Islamoglu, Y. & Parmaksizoglu, C. 2006. Comparison of CFD simulation to experiment for convection heat transfer in an enhanced channel. *Heat Transfer Engineering,* 27**,** 53-59.

Ismagilov, R. F., Stroock, A. D., Kenis, P. J. A., Whitesides, G. & Stone, H. A. 2000. Experimental and theoretical scaling laws for transverse diffusive broadening in two-phase laminar flows in microchannels. *Applied Physics Letters,* 76**,** 2376-2378.

Jiang, F., Drese, K. S., Hardt, S., Kupper, M. & Schönfeld, F. 2004. Helical flows and chaotic mixing in curved micro channels. *AICHE Journal,* 50**,** 2297-2305.

Johnston, A. M. & Haynes, B. S. Design considerations for compact heat exchangers. In proceedings of the International symposium on compact heat exchangers, 2002 Greenoble, France.

Joseph, B., Smith, E. P. & Adler, R. J. 1975. Numerical treatment of laminar flow in helically coiled tubes of square cross-secion. 1. Stationary helically coiled tubes. *AICHE Journal,* 21**,** 965-974.

Kandlikar, S. G., Joshi, S. & Tian, S. R. 2003. Effect of surface roughness on heat transfer and fluid flow characteristics at low reynolds numbers in small diameter tubes. *Heat Transfer Engineering,* 24**,** 4-16.

Karale, C. M., Bhagwat, S. S. & Ranade, V. V. 2013. Flow and Heat Transfer in Serpentine Channels. *AIChE Journal,* 59**,** 1814-1827.

Keane, R. D., Adrian, R. J. & Zhang, Y. 1995. Superresolution particle imaging velocimetry *Measurement Science & Technology,* 6**,** 754-768.

Kim, B. J., Liu, Y. Z. & Sung, H. J. 2004. Micro PIV measurement of two-fluid flow with different refractive indices. *Measurement Science & Technology,* 15**,** 1097-1103.

Kim, H. J. 2005. Measurements of temperature and flow fields with sub-millimeter spatial resolution using two-color laser induced fluorescence (LIF) and micro-particle image velocimetry (PIV). *Journal of Mechanical Science and Technology,* 19**,** 716-727.

Kim, M. 2010. *Microscale optical thermometry techniques for measuring liquid-phase and wall surface temperatures.* PhD Thesis, Georgia Institute of Technology.

Kim, M. & Yoda, M. 2010. Dual-tracer fluorescence thermometry measurements in a heated channel. *Experiments in Fluids,* 49**,** 257-266.

Kim, S. K. 2001. An experimental study of developing and fully developed flows in a wavy channel by PIV. *Ksme International Journal,* 15**,** 1853-1859.

Kim, Y. W. & Yoo, J. Y. 2008. The lateral migration of neutrally-buoyant spheres transported through square microchannels. *Journal of Micromechanics and Microengineering,* 18**,** 065015.

Kimura, I., Hyodo, T., Ozawa, M. 1998. Temperature and Velocity Measurement of a 3-D Thermal Flow Field using Thermo-sensitive Liquid Crystals. *Journal of Visualization* 1**,** 145-152.

Kinoshita, H., Kaneda, S., Fujii, T. & Oshima, M. 2007. Three-dimensional measurement and visualization of internal flow of a moving droplet using confocal micro-PIV. *Lab on a Chip,* 7**,** 338-346.

Knowles, K. M. & van Helvoort, A. T. J. 2006. Anodic bonding. *International Materials Reviews,* 51**,** 273-311.

Kolodner, P. & Tyson, J. A. 1982. Microscopic fluorescent imaging of surface temperature profiles with 0.01 degrees resolution. *Applied Physics Letters,* 40**,** 782-784.

Koo, J. & Kleinstreuer, C. 2004. Viscous dissipation effects in microtubes and microchannels. *International Journal of Heat and Mass Transfer,* 47**,** 3159-3169.

Korichi, A. & Oufer, L. 2007. Heat transfer enhancement in oscillatory flow in channel with periodically upper and lower walls mounted obstacles. *International Journal of Heat and Fluid Flow,* 28**,** 1003-1012.

Korichi, A., Oufer, L. & Polidori, G. 2009. Heat transfer enhancement in self-sustained oscillatory flow in a grooved channel with oblique plates. *International Journal of Heat and Mass Transfer,* 52**,** 1138-1148.

Kosar, A. 2010. Effect of substrate thickness and material on heat transfer in microchannel heat sinks. *International Journal of Thermal Sciences,* 49**,** 635-642.

Kumar, V. & Nigam, K. D. P. 2005. Numerical simulation of steady flow fields in coiled flow inverter. *International Journal of Heat and Mass Transfer,* 48**,** 4811-4828.

Kumar, V., Paraschivoiu, M. & Nigam, K. D. P. 2011. Single-phase fluid flow and mixing in microchannels. *Chemical Engineering Science,* 66**,** 1329-1373.

Lang, N. & Limberg, W. 1999. Construction of three-dimensional flow structure out of two-dimensional steady flow field velocity measurements. *Experiments in Fluids,* 27**,** 351-358.

Lasbet, Y., Auvity, B., Castelain, C. & Peerhossaini, H. 2007. Thermal and hydrodynamic performances of chaotic mini-channel: Application to the fuel cell cooling. *Heat Transfer Engineering,* 28**,** 795-803.

Lavieille, P., Lemoine, F., Lavergne, G. & Lebouche, M. 2001. Evaporating and combusting droplet temperature measurements using two-color laser-induced fluorescence. *Experiments in Fluids,* 31**,** 45-55.

Lavieille, P., Lemoine, F., Lavergne, G., Virepinte, J. F. & Lebouche, M. 2000. Temperature measurements on droplets in monodisperse stream using laser-induced fluorescence. *Experiments in Fluids,* 29**,** 429-437.

Lee, P. S., Garimella, S. V. & Liu, D. 2005. Investigation of heat transfer in rectangular microchannels. *International Journal of Heat and Mass Transfer,* 48**,** 1688-1704.

Lelea, D., Nishio, S. & Takano, K. 2004. The experimental research on microtube heat transfer and fluid flow of distilled water. *International Journal of Heat and Mass Transfer,* 47**,** 2817-2830.

Lemoine, F., Antoine, Y., Wolff, M. & Lebouche, M. 1999. Simultaneous temperature and 2D velocity measurements in a turbulent heated jet using combined laser-induced fluorescence and LDA. *Experiments in Fluids,* 26**,** 315-323.

Leung, S. S. Y. 2012. *Heat transfer in microchannels - Taylor flow.* PhD Thesis The University of Sydney.

Leung, S. S. Y., Liu, Y., Fletcher, D. F. & Haynes, B. S. 2010. Heat transfer in well-characterised Taylor flow. *Chemical Engineering Science,* 65**,** 6379-6388.

Li, J., Peterson, G. P. & Cheng, P. 2004. Three-dimensional analysis of heat transfer in a micro-heat sink with single phase flow. *International Journal of Heat and Mass Transfer,* 47**,** 4215-4231.

Li, L., Yang, M. & Zhang, Y. W. 2008. Numerical study of periodically fully-developed convection in channels with periodically grooved parts. *International Journal of Heat and Mass Transfer,* 51**,** 3057-3065.

Li, S., Zhang, K., Yang, J. M., Lin, L. W. & Yang, H. 2007. Single quantum dots as local temperature markers. *Nano Letters,* 7**,** 3102-3105.

Li, Z. X., Du, D. X. & Guo, Z. Y. 2003. Experimental study on flow characteristics of liquid in circular microtubes. *Microscale Thermophysical Engineering,* 7**,** 253-265.

Ligrani, P. M. & Niver, R. D. 1988. Flow visualization of Dean vortices in a curved channel with 40 to 1 aspect ratio. *Physics of Fluids,* 31**,** 3605-3617.

Lim, E. J., Ober, T. J., Edd, J. F., McKinley, G. H. & Toner, M. 2012. Visualization of microscale particle focusing in diluted and whole blood using particle trajectory analysis. *Lab on a Chip,* 12**,** 2199-2210.

Lindken, R., Rossi, M., Grosse, S. & Westerweel, J. 2009. Micro-Particle Image Velocimetry (mu PIV): Recent developments, applications, and guidelines. *Lab on a Chip,* 9**,** 2551-2567.

Liu, R. H., Stremler, M. A., Sharp, K. V., Olsen, M. G., Santiago, J. G., Adrian, R. J., Aref, H. & Beebe, D. J. 2000. Passive mixing in a three-dimensional serpentine microchannel. *Journal of Microelectromechanical Systems,* 9**,** 190-197.

Liu, T., Campbell, B. T., Burns, S. P. & Sullivan, J. P. 1997. Temperature- and pressure-sensitive luminescent paints in aerodynamics. *Applied Mechanics Reviews,* 50**,** 227-246.

Liu, Y. 2011. *Boiling flow in microchannels.* PhD Thesis, The University of Sydney.

Liu, Y., Fletcher, D. F. & Haynes, B. S. 2013. On the importance of upstream compressibility in microchannel boiling heat transfer. *International Journal of Heat and Mass Transfer,* 58**,** 503-512.

Majumder, A., Mehta, B. & Khandekar, S. 2013. Local Nusselt number enhancement during gas-liquid Taylor bubble flow in a square mini-channel: An experimental study. *International Journal of Thermal Sciences,* 66**,** 8-18.

Manglik, R. M., Zhang, J. H. & Muley, A. 2005. Low Reynolds number forced convection in three-dimensional wavy-plate-fin compact channels: fin density effects. *International Journal of Heat and Mass Transfer,* 48**,** 1439-1449.

Marakkos, K. & Turner, J. T. 2006. Vortex generation in the cross-flow around a cylinder attached to an end-wall. *Optics and Laser Technology,* 38**,** 277-285.

Maranzana, G., Perry, I. & Maillet, D. 2004. Mini- and micro-channels: influence of axial conduction in the walls. *International Journal of Heat and Mass Transfer,* 47**,** 3993-4004.

Matsumoto, R., Zadeh, H. F. & Ehrhard, P. 2005. Quantitative measurement of depth-averaged concentration fields in microchannels by means of a fluorescence intensity method. *Experiments in Fluids,* 39**,** 722-729.

Mees, P. A. J., Nandakumar, K. & Masliyah, H. 1996. Secondary instability of flow in a curved duct of square cross-section. *Journal of Fluid Mechanics,* 323**,** 387-409.

Meier, R. J., Fischer, L. H., Wolfbeis, O. S. & Schaferling, M. 2013. Referenced luminescent sensing and imaging with digital color cameras: A comparative study. *Sensors and Actuators B-Chemical,* 177**,** 500-506.

Meinhart, C. D., Wereley, S. & Gray, M. 2000. Volume illumination for two-dimensional particle image velocimetry. *Measurement Science and Technology,* 11**,** 809-814.

Mereu, R., Colombo, E. & Inzoli, F. 2013. Numerical analysis of fluid dynamics and thermal characteristics inside a wavy channel. *International Journal of Numerical Methods for Heat & Fluid Flow,* 23**,** 1049-1062.

Metwally, H. M. & Manglik, R. M. 2004. Enhanced heat transfer due to curvature-induced lateral vortices in laminar flows in sinusoidal corrugated-plate channels. *International Journal of Heat and Mass Transfer,* 47**,** 2283-2292.

Mohammed, H. A., Gunnasegaran, P. & Shuaib, N. H. 2011. Influence of channel shape on the thermal and hydraulic performance of microchannel heat sink. *International Communications in Heat and Mass Transfer,* 38**,** 474-480.

Mokrani, O., Bourouga, B., Castelain, C. & Peerhossaini, H. 2009. Fluid flow and convective heat transfer in flat microchannels. *International Journal of Heat and Mass Transfer,* 52**,** 1337-1352.

Nandakumar, K. & Masliyah, J. H. 1982. Bifurcation in steady laminar flow through curved tubes. *Journal of Fluid Mechanics,* 119**,** 475-490.

Naphon, P. 2007. Heat transfer characteristics and pressure drop in channel with V corrugated upper and lower plates. *Energy Conversion and Management,* 48**,** 1516-1524.

Naphon, P. 2008. Effect of corrugated plates in an in-phase arrangement on the heat transfer and flow developments. *International Journal of Heat and Mass Transfer,* 51**,** 3963-3971.

Naphon, P. & Wongwises, S. 2006. A review of flow and heat transfer characteristics in curved tubes. *Renewable & Sustainable Energy Reviews,* 10**,** 463-490.

Natrajan, V. K. & Christensen, K. T. 2009. Two-color laser-induced fluorescent thermometry for microfluidic systems. *Measurement Science & Technology,* 20**,** 015401.

Natrajan, V. K. & Christensen, K. T. 2010. Non-intrusive measurements of convective heat transfer in smooth- and rough-wall microchannels: laminar flow. *Experiments in Fluids,* 49**,** 1021-1037.

Natrajan, V. K. & Christensen, K. T. 2011. Non-intrusive measurements of transitional and turbulent convective heat transfer in a rectangular microchannel. *Journal of Micromechanics and Microengineering,* 21**,** 085001.

Ngo, T. L., Kato, Y., Nikitin, K. & Ishizuka, T. 2007. Heat transfer and pressure drop correlations of microchannel heat exchangers with S-shaped and zigzag fins for carbon dioxide cycles. *Experimental Thermal and Fluid Science,* 32**,** 560-570.

Ngo, T. L., Kato, Y., Nikitin, K. & Tsuzuki, N. 2006. New printed circuit heat exchanger with S-shaped fins for hot water supplier. *Experimental Thermal and Fluid Science,* 30**,** 811-819.

Nikitin, K., Kato, Y. & Ngo, L. 2006. Printed circuit heat exchanger thermal-hydraulic performance in supercritical CO2 experimental loop. *International Journal of Refrigeration,* 29**,** 807-814.

Nikolaidis, N. M. & Mathioulakis, D. S. 2002. Axial and secondary flow study in a 90 deg bifurcation under pulsating conditions using PIV. *Journal of Fluids Engineering-Transactions of the ASME,* 124**,** 505-511.

Nishimura, T. & Matsune, S. 1998. Vortices and wall shear stresses in asymmetric and symmetric channels with sinusoidal wavy walls for pulsatile flow at low Reynolds numbers. *International Journal of Heat and Fluid Flow,* 19**,** 583-593.

Nishimura, T., Oka, N., Yoshinaka, Y. & Kunitsugu, K. 2000. Influence of imposed oscillatory frequency on mass transfer enhancement of grooved channels for pulsatile flow. *International Journal of Heat and Mass Transfer,* 43**,** 2365-2374.

Nogueira, J., Lecuona, A. & Rodriguez, P. A. 2001. Identification of a new source of peak locking, analysis and its removal in conventional and super-resolution PIV techniques. *Experiments in Fluids,* 30**,** 309-316.

Oishi, M., Kinoshita, H., Fujii, T. & Oshima, M. 2011. Simultaneous measurement of internal and surrounding flows of a moving droplet using multicolour confocal micro-particle image velocimetry (micro-PIV). *Measurement Science & Technology,* 22**,** 105401.

Olsen, M. G. & Adrian, R. J. 2000. Brownian motion and correlation in particle image velocimetry. *Optics and Laser Technology,* 32**,** 621-627.

Omrane, A., Petersson, P., Aldén, M. & Linne, M. A. 2008. Simultaneous 2D flow velocity and gas temperature measurements using thermographic phosphors. *Applied Physics B: Lasers and Optics,* 92**,** 99-102.

Oosthuizen, P. H. Development of unsteady flow in a wavy minichannel system. ASME 2008 6th International Conference on Nanochannels, Microchannels, and Minichannels, 2008. 7-14.

Oviedo-Tolentino, F., Romero-Mendez, R., Hernandez-Guerrero, A. & Giron-Palomares, B. 2008. Experimental study of fluid flow in the entrance of a sinusoidal channel. *International Journal of Heat and Fluid Flow,* 29**,** 1233-1239.

Oviedo-Tolentino, F., Romero-Mendez, R., Hernandez-Guerrero, A. & Giron-Palomares, B. 2009. Use of diverging or converging arrangement of plates for the control of chaotic mixing in symmetric sinusoidal plate channels. *Experimental Thermal and Fluid Science,* 33**,** 208-214.

Owhaib, W., Palm, B. & Martin-Callizo, C. 2006. Flow boiling visualization in a vertical circular minichannel at high vapor quality. *Experimental Thermal and Fluid Science,* 30**,** 755-763.

Ozawa, M., Muller, U., Kimura, I. & Takamori, T. 1992. Flow and temperature measurement of natural convection in Hele-Shaw cell using a thremosensitive liquid-crystal tracer *Experiments in Fluids,* 12**,** 213-222.

Park, H. G., Dabiri, D. & Gharib, M. 2001. Digital particle image velocimetry/thermometry and application to the wake of a heated circular cylinder. *Experiments in Fluids,* 30**,** 327-338.

Park, J. S., Choi, C. K. & Kihm, K. D. 2004. Optically sliced micro-PIV using confocal laser scanning microscopy (CLSM). *Experiments in Fluids,* 37**,** 105-119.

Peerhossaini, H., Castelain, C. & Leguer, Y. 1993. Heat-exchanger design based on chaotic advection. *Experimental Thermal and Fluid Science,* 7**,** 333-344.

Pehl, M., Werner, F. & Delgado, A. 2000. First visualization of temperature fields in liquids at high pressure using thermochromic liquid crystals. *Experiments in Fluids,* 29**,** 302-304.

Peng, X. F. & Peterson, G. P. 1996. Convective heat transfer and flow friction for water flow in microchannel structures. *International Journal of Heat and Mass Transfer,* 39**,** 2599-2608.

Popiel, C. O. & vanderMerwe, D. F. 1996. Friction factor in sine-pipe flow. *Journal of Fluids Engineering-Transactions of the ASME,* 118**,** 341-345.

Pouya, S., Koochesfahani, M., Snee, P., Bawendi, M. & Nocera, D. 2005. Single quantum dot (QD) imaging of fluid flow near surfaces. *Experiments in Fluids,* 39**,** 784-786.

Prasad, A. K., Adrian, R. J., Landreth, C. C. & Offutt, P. W. 1992. Effect of resolution on the speed and accuracy of particle image velocimetry interrogation. *Experiments in Fluids,* 13**,** 105-116.

Qu, W. L., Mala, G. M. & Li, D. Q. 2000. Heat transfer for water flow in trapezoidal silicon microchannels. *International Journal of Heat and Mass Transfer,* 43**,** 3925-3936.

Qu, W. L. & Mudawar, I. 2002. Experimental and numerical study of pressure drop and heat transfer in a single-phase micro-channel heat sink. *International Journal of Heat and Mass Transfer,* 45**,** 2549-2565.

Raffel, M., Willert, C.E., Wereley, S.T., Kompenhans, J. 1998. *Particle Image Velocimetry: A practical guide* Cambridge University Press.

Rahman, M. M. 2000. Measurements of heat transfer in microchannel heat sinks. *International Communications in Heat and Mass Transfer,* 27**,** 495-506.

Ramgadia, A. G. & Saha, A. K. 2012. Fully developed flow and heat transfer characteristics in a wavy passage: Effect of amplitude of waviness and Reynolds number. *International Journal of Heat and Mass Transfer,* 55**,** 2494-2509.

Ramgadia, A. G. & Saha, A. K. 2013. Numerical study of fully developed flow and heat transfer in a wavy passage. *International Journal of Thermal Sciences,* 67**,** 152-166.

Ramshaw, C. 1983. Higee distillation-an example of process intensification. *Chemical Engineer-London,* 389**,** 13-14.

Ray, S. & Date, A. W. 2001. Laminar flow and heat transfer through square duct with twisted tape insert. *International Journal of Heat and Fluid Flow,* 22**,** 460-472.

Ray, S. & Date, A. W. 2003. Friction and heat transfer characteristics of flow through square duct with twisted tape insert. *International Journal of Heat and Mass Transfer,* 46**,** 889-902.

Revellin, R., Dupont, V., Ursenbacher, T., Thome, J. R. & Zun, I. 2006. Characterization of diabatic two-phase flows in microchannels: Flow parameter results for R-134a in a 0.5 mm channel. *International Journal of Multiphase Flow,* 32**,** 755-774.

Robinson, O. & Rockwell, D. 1993. Construction of 3-Dimensional images of flow structure via particle tracking techniques. *Experiments in Fluids,* 14**,** 257-270.

Roesgen, T. 2003. Optimal subpixel interpolation in particle image velocimetry. *Experiments in Fluids,* 35**,** 252-256.

Rogers, T. & Kowal, J. 1995. Selection of glass, anodic bonding conditions and material compatibility for silicon-glass capacitive pressure sensor. *Sensors and Actuators A-Physical,* 46-47**,** 113-120.

Rosaguti, N. R., Fletcher, D. F. & Haynes, B. S. 2005. Laminar flow and heat transfer in a periodic serpentine channel. *Chemical Engineering & Technology,* 28**,** 353-361.

Rosaguti, N. R., Fletcher, D. F. & Haynes, B. S. 2006. Laminar flow and heat transfer in a periodic serpentine channel with semi-circular cross-section. *International Journal of Heat and Mass Transfer,* 49**,** 2912-2923.

Rosaguti, N. R., Fletcher, D. F. & Haynes, B. S. 2007a. A general implementation of the H1 boundary condition in CFD simulations of heat transfer in swept passages. *International Journal of Heat and Mass Transfer,* 50**,** 1833-1842.

Rosaguti, N. R., Fletcher, D. F. & Haynes, B. S. 2007b. Low-Reynolds number heat transfer enhancement in sinusoidal channels. *Chemical Engineering Science,* 62**,** 694-702.

Ross, D., Gaitan, M. & Locascio, L. E. 2001. Temperature measurement in microfluidic systems using a temperature-dependent fluorescent dye. *Analytical Chemistry,* 73**,** 4117-4123.

Rush, T. A., Newell, T. A. & Jacobi, A. M. 1999. An experimental study of flow and heat transfer in sinusoidal wavy passages. *International Journal of Heat and Mass Transfer,* 42**,** 1541-1553.

Rütten, F., Schroder, W. & Meinke, M. 2005. Large-eddy simulation of low frequency oscillations of the Dean vortices in turbulent pipe bend flows. *Physics of Fluids,* 17**,** 035107.

Sakakibara, J. & Adrian, R. J. 1999. Whole field measurement of temperature in water using two-color laser induced fluorescence. *Experiments in Fluids,* 26**,** 7-15.

Sakakibara, J. & Adrian, R. J. 2004. Measurement of temperature field of a Rayleigh-Benard convection using two-color laser-induced fluorescence. *Experiments in Fluids,* 37**,** 331-340.

Sakakibara, J., Hishida, K. & Maeda, M. 1997. Vortex structure and heat transfer in the stagnation region of an impinging plane jet (simultaneous measurements of velocity and temperature fields by digital particle image velocimetry and laser-induced fluorescence). *International Journal of Heat and Mass Transfer,* 40**,** 3163-3176.

Sankar, S. R., Nandakumar, K. & Masliyah, J. H. 1988. Oscillatory flows in coiled square ducts. *Physics of Fluids* 31**,** 1410-1421.

Santiago, J. G., Wereley, S. T., Meinhart, C. D., Beebe, D. J. & Adrian, R. J. 1998. A particle image velocimetry system for microfluidics. *Experiments in Fluids,* 25**,** 316-319.

Sato, Y., Irisawa, G., Ishizuka, M., Hishida, K. & Maeda, M. 2003. Visualization of convective mixing in microchannel by fluorescence imaging. *Measurement Science and Technology,* 14**,** 114-121.

Saylor, J. R. 1995. Phtotobleaching of disodium fluorescein in water *Experiments in Fluids,* 18**,** 445-447.

Schönfeld, F. & Hardt, S. 2004. Simulation of helical flows in microchannels. *AICHE Journal,* 50**,** 771-778.

Shafii, M. B., Lum, C. L. & Koochesfahani, M. M. 2010. In situ LIF temperature measurements in aqueous ammonium chloride solution during uni-directional solidification. *Experiments in Fluids,* 48**,** 651-662.

Shah, R. K. & London, A. L. 1978. *Laminar flow forced convection in ducts: A source book for compact heat exchanger analytical data,* New York, Academic Press.

Shinohara, K., Sugii, Y., Aota, A., Hibara, A., Tokeshi, M., Kitamori, T. & Okamoto, K. 2004. High-speed micro-PIV measurements of transient flow in microfluidic devices. *Measurement Science & Technology,* 15**,** 1965-1970.

Sillekens, J. J. M., Rindt, C. C. M. & van Steenhoven, A. A. 1998. Development of laminar mixed convection in a horizontal square channel with heated side walls. *International Journal of Heat and Fluid Flow,* 19**,** 270-281.

Sim, D. Y., Kurabayashi, T. & Esashi, M. 1996. A bakable microvalve with a Kovar-glass-silicon-glass structure. *Journal of Micromechanics and Microengineering,* 6**,** 266-271.

Simon, S. M. 2000. Fluorescent bead for determining the temperature of a cell and methods of use thereof. Google Patents.

Sobhan, C. B. & Garimella, S. V. 2001. A comprehensive analysis of studies on heat transfer and fluid flow in micro-channels. *Microscale Thermophysical Engineering,* 5**,** 293-311.

Someya, S., Li, Y. R., Ishii, K. & Okamoto, K. 2011. Combined two-dimensional velocity and temperature measurements of natural convection using a high-speed camera and temperature-sensitive particles. *Experiments in Fluids,* 50**,** 65-73.

Someya, S., Ochi, D., Li, Y., Tominaga, K., Ishii, K. & Okamoto, K. 2010. Combined two-dimensional velocity and temperature measurements using a high-speed camera and luminescent particles. *Applied Physics B-Lasers and Optics,* 99**,** 325-332.

Someya, S., Yoshida, S., Li, Y. R. & Okamoto, K. 2009. Combined measurement of velocity and temperature distributions in oil based on the luminescent lifetimes of seeded particles. *Measurement Science & Technology,* 20**,** 025403.

Sousa, J. M. M. 2002. Turbulent flow around a surface-mounted obstacle using 2D-3C DPIV. *Experiments in Fluids,* 33**,** 854-862.

Stankiewicz, A. I. & Moulijn, J. A. 2000. Process intensification: Transforming chemical engineering. *Chemical Engineering Progress,* 96**,** 22-34.

Sudo, K., Sumida, M. & Hibara, H. 1998. Experimental investigation on turbulent flow in a circular-sectioned 90-degree bend. *Experiments in Fluids,* 25**,** 42-49.

Sudo, K., Sumida, M. & Hibara, H. 2001. Experimental investigation on turbulent flow in a square-sectioned 90-degree bend. *Experiments in Fluids,* 30**,** 246-252.

Sugiyama, S., Hayashi, T. & Yamazaki, K. 1983. Flow characteristics in the curved rectangular channels (Visualization of secondary flow) *Bulletin of the JSME-Japan Society of Mechanical Engineers,* 26**,** 964-969.

Sui, Y., Lee, P. S. & Teo, C. J. 2011. An experimental study of flow friction and heat transfer in wavy microchannels with rectangular cross section. *International Journal of Thermal Sciences,* 50**,** 2473-2482.

Sui, Y., Teo, C. J. & Lee, P. S. 2012. Direct numerical simulation of fluid flow and heat transfer in periodic wavy channels with rectangular cross-sections. *International Journal of Heat and Mass Transfer,* 55**,** 73-88.

Sui, Y., Teo, C. J., Lee, P. S., Chew, Y. T. & Shu, C. 2010. Fluid flow and heat transfer in wavy microchannels. *International Journal of Heat and Mass Transfer,* 53**,** 2760-2772.

Sutton, J. A., Fisher, B. T. & Fleming, J. W. 2008. A laser-induced fluorescence measurement for aqueous fluid flows with improved temperature sensitivity. *Experiments in Fluids,* 45**,** 869-881.

Syuto, T., Fujisawa, N., Takasugi, T. & Yamagata, T. 2010. Flow visualization and scanning PIV measurement of three-dimensional structure in near field of strongly buoyant jet. *Journal of Visualization,* 13**,** 203-211.

Thomson, J. 1876. On the origin of windings of rivers in alluvial plains with remarks on the flow of water round bends in pipes. *Proceedings of the Royal Society of London,* 25**,** 5-8.

Tiselj, I., Hetsroni, G., Mavko, B., Mosyak, A., Pogrebnyak, E. & Segal, Z. 2004. Effect of axial conduction on the heat transfer in micro-channels. *International Journal of Heat and Mass Transfer,* 47**,** 2551-2565.

Tso, C. P. & Mahulikar, S. P. 2000. Experimental verification of the role of Brinkman number in microchannels using local parameters. *International Journal of Heat and Mass Transfer,* 43**,** 1837-1849.

Tsuzuki, N., Kato, Y. & Ishiduka, T. 2007. High performance printed circuit heat exchanger. *Applied Thermal Engineering,* 27**,** 1702-1707.

Tsuzuki, N., Kato, Y., Nikitin, K. & Ishizuka, T. 2009. Advanced Microchannel Heat Exchanger with S-shaped Fins. *Journal of Nuclear Science and Technology,* 46**,** 403-412.

Tuckerman, D. B. & Pease, R. F. W. 1981. High-performance heat sinking for VLSI *Electron Device Letters,* 2**,** 126-129.

Tunstall, M. J. & Harvey, J. K. 1968. On the effect of a sharp bend in a fully developed turbulent pipe-flow. *Journal of Fluid Mechanics,* 34**,** 595-608.

van Helvoort, A. T. J., Knowles, K. M., Holmestad, R. & Fernie, J. A. 2004. Anodic oxidation during electrostatic bonding. *Philosophical Magazine,* 84**,** 505-519.

Vashisth, S., Kumar, V. & Nigam, K. D. P. 2008. A review on the potential applications of curved geometries in process industry. *Industrial & Engineering Chemistry Research,* 47**,** 3291-3337.

Vogt, J. & Stephan, P. 2012. Using microencapsulated fluorescent dyes for simultaneous measurement of temperature and velocity fields. *Measurement Science and Technology,* 23**,** 105306.

Walker, G. W., Sundar, V. C., Rudzinski, C. M., Wun, A. W., Bawendi, M. G. & Nocera, D. G. 2003. Quantum-dot optical temperature probes. *Applied Physics Letters,* 83**,** 3555-3557.

Wallis, G. & Pomerant, D. I. 1969. Field assisted glass-metal sealing. *Journal of Applied Physics,* 40**,** 3946-3949.

Wang, B. X. & Peng, X. F. 1994. Experimental investigation on liquid forced-convection heat transfer through microchannels *International Journal of Heat and Mass Transfer,* 37**,** 73-82.

Wang, G. & Vanka, S. P. 1995. Convective heat-transfer in periodic wavy passages *International Journal of Heat and Mass Transfer,* 38**,** 3219-3230.

Wang, X.-d., Wolfbeis, O. S. & Meier, R. J. 2013. Luminescent probes and sensors for temperature. *Chemical Society Reviews,* 42**,** 7834-7869.

Wereley, S., Meinhart, C., Gui, L. C., Tretheway, D. & Sud, A. 2005. Single pixel evaluation of microchannel flows. *ASME International Mechanical Engineering Congress and Exposition.*

Wereley, S. T., Gui, L. & Meinhart, C. D. 2002. Advanced algorithms for microscale particle image velocimetry. *AiIAA Journal,* 40**,** 1047-1055.

Wereley, S. T. & Meinhart, C. D. 2005. Micron-resolution particle image velocimetry. *Micro- and Nano- Scale Diagnostic Techniques.* Springer Berlin Heidelberg.

West, T. J. 2012. *Development and testing of temperature-sensitive beads for simultaneous thermometry and velocimetry.* Master Thesis, University of Washington.

Westerweel, J. 1997. Fundamentals of digital particle image velocimetry. *Measurement Science & Technology,* 8**,** 1379-1392.

Willert, C. E. & Gharib, M. 1992. 3-Dimensional particle imaging with a single camera. *Experiments in Fluids,* 12**,** 353-358.

Williams, G., Hubbell, C. & Finkell, G. 1902. Experiments at Detroit, Michigan on the effect of curvature on the flow of water in pipes. *Trans. ASCE,* 47**,** 1-196.

Williams, S. J., Park, C. & Wereley, S. T. 2010. Advances and applications on microfluidic velocimetry techniques. *Microfluidics and Nanofluidics,* 8**,** 709-726.

Xin, R. C. & Tao, W. Q. 1988. Numerical prediction of laminar-flow and heat transfer in wavy channels of uniform cross-sectional area *Numerical Heat Transfer,* 14**,** 465-481.

Xiong, R. Q. & Chung, J. N. 2007. Flow characteristics of water in straight and serpentine micro-channels with miter bends. *Experimental Thermal and Fluid Science,* 31**,** 805-812.

Xiong, R. Q. & Chung, J. N. 2008. Effects of miter bend on pressure drop and flow structure in micro-fluidic channels. *International Journal of Heat and Mass Transfer,* 51**,** 2914-2924.

Yamagishi, A., Inaba, T. & Yamaguchi, Y. 2007. Chaotic analysis of mixing enhancement in steady laminar flows through multiple pipe bends. *International Journal of Heat and Mass Transfer,* 50**,** 1238-1247.

Yamaguchi, E., Natrajan, V. K. & Christensen, K. T. 2006. Development of a two-dye LIF technique for measuring fluid temperature fields in microfluidic devices. *ASME 2006 2nd Joint US-European Fluids Engineering Summer Meeting Collocated With the 14th International Conference on Nuclear Engineering-ASME.*

Yanase, S., Goto, N. & Yamamoto, K. 1989. Dual solutions of the flow through a curved tube. *Fluid Dynamics Research,* 5**,** 191-201.

Yang, C. Y. & Lin, T. Y. 2007. Heat transfer characteristics of water flow in microtubes. *Experimental Thermal and Fluid Science,* 32**,** 432-439.

Yang, G., Dong, Z. F. & Ebadian, M. A. 1995. Lanimar forced -convection in a helicoidal pipe with finite pitch *International Journal of Heat and Mass Transfer,* 38**,** 853-862.

Yang, L. C., Asako, Y., Yamaguchi, Y. & Faghri, M. 1997. Numerical prediction of transitional characteristics of flow and heat transfer in a corrugated duct. *Journal of Heat Transfer-Transactions of the ASME,* 119**,** 62-69.

Yen, T. H., Shoji, M., Takemura, F., Suzuki, Y. & Kasagi, N. 2006. Visualization of convective boiling heat transfer in single microchannels with different shaped cross-sections. *International Journal of Heat and Mass Transfer,* 49**,** 3884-3894.

Zhang, J. H., Kundu, J. & Manglik, R. M. 2004. Effect of fin waviness and spacing on the lateral vortex structure and laminar heat transfer in wavy-plate-fin cores. *International Journal of Heat and Mass Transfer,* 47**,** 1719-1730.

Zheng, Z. 2013. *CFD simulations and design methodologies for tortuous channel heat exchangers.* PhD Thesis, The University of Sydney.

Zheng, Z., Fletcher, D. F. & Haynes, B. S. 2013a. Chaotic advection in steady laminar heat transfer simulations: Periodic zigzag channels with square cross-sections. *International Journal of Heat and Mass Transfer,* 57**,** 274-284.

Zheng, Z., Fletcher, D. F. & Haynes, B. S. 2013b. Laminar heat transfer simulations for periodic zigzag semicircular channels: Chaotic advection and geometric effects. *International Journal of Heat and Mass Transfer,* 62**,** 391-401.

Zheng, Z. Y., Fletcher, D. F. & Haynes, B. S. 2014. Transient laminar heat transfer simulations in periodic zigzag channels. *International Journal of Heat and Mass Transfer,* 71**,** 758-768.